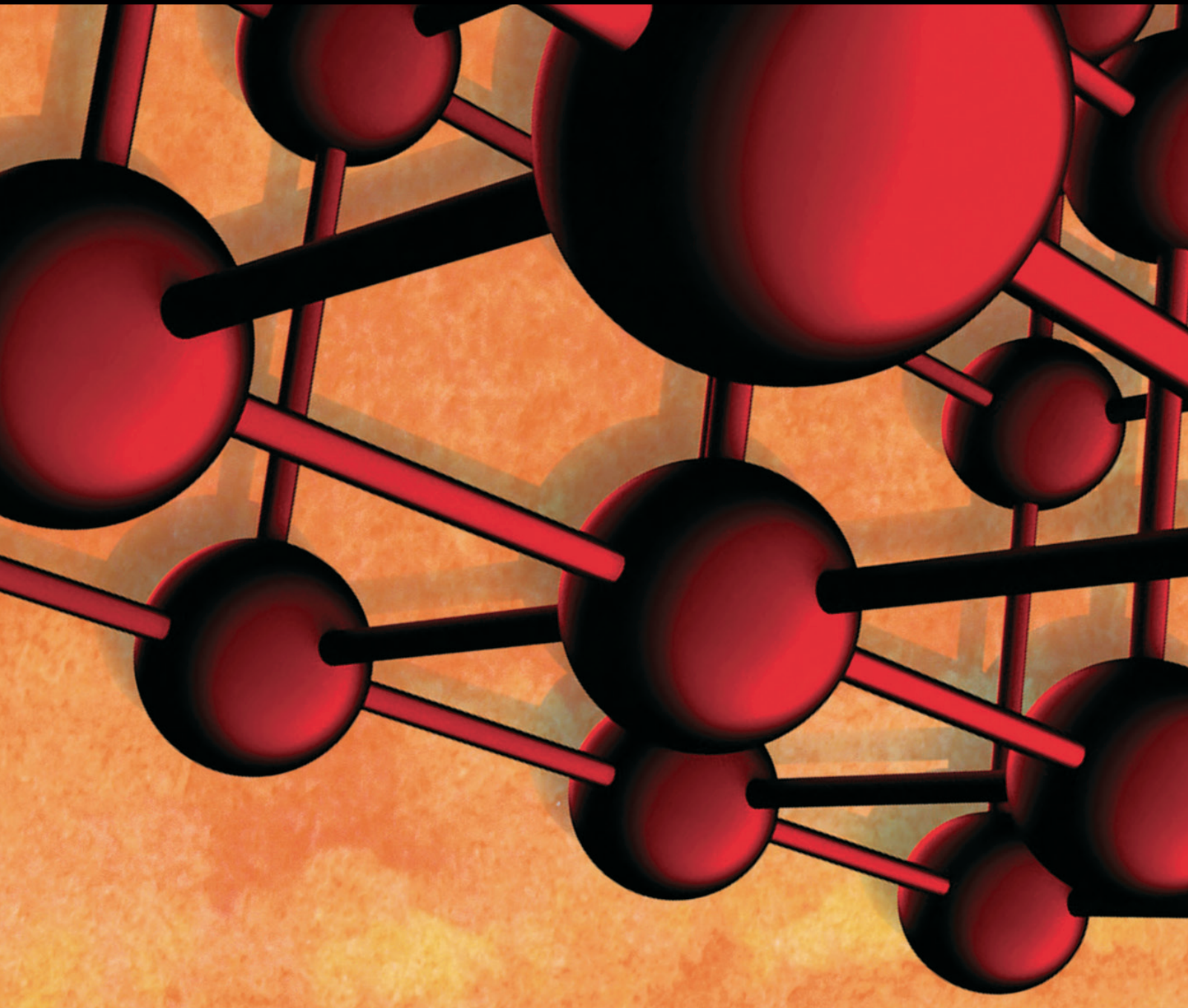


Advances in Materials Science and Engineering

Alternative Cementitious Materials and Their Composites

Lead Guest Editor: Kedsarin Pimraksa

Guest Editors: Prinya Chindaprasirt, Jay Sanjayan, and Tung-Chai Ling





Alternative Cementitious Materials and Their Composites

Advances in Materials Science and Engineering

Alternative Cementitious Materials and Their Composites

Lead Guest Editor: Kedsarin Pimraksa

Guest Editors: Prinya Chindaprasirt, Jay Sanjayan,
and Tung-Chai Ling



Copyright © 2018 Hindawi. All rights reserved.

This is a special issue published in “Advances in Materials Science and Engineering.” All articles are open access articles distributed under the Creative Commons Attribution License, which permits unrestricted use, distribution, and reproduction in any medium, provided the original work is properly cited.

Editorial Board

- Michael Aizenshtein, Israel
Jarir Aktaa, Germany
K. G. Anthymidis, Greece
Santiago Aparicio, Spain
Farhad Aslani, Australia
Renal Backov, France
Markus Bambach, Germany
Amit Bandyopadhyay, USA
Massimiliano Barletta, Italy
Mikhael Bechelany, France
Avi Bendavid, Australia
Jamal Berakdar, Germany
Jean-Michel Bergheau, France
G. Bernard-Granger, France
Giovanni Berselli, Italy
Patrice Berthod, France
Federica Bondioli, Italy
Susmita Bose, USA
Heinz-Günter Brokmeier, Germany
Steve Bull, UK
Gianlorenzo Bussetti, Italy
Antonio Caggiano, Germany
Veronica Calado, Brazil
Marco Cannas, Italy
Peter Chang, Canada
Daolun Chen, Canada
Gianluca Cicala, Italy
Francesco Colangelo, Italy
Marco Consales, Italy
José A. Correia, Portugal
María Criado, UK
Gabriel Cuello, France
Narendra B. Dahotre, USA
João P. Davim, Portugal
Angela De Bonis, Italy
Abílio De Jesus, Portugal
Luca De Stefano, Italy
Francesco Delogu, Italy
Maria Laura Di Lorenzo, Italy
Marisa Di Sabatino, Norway
Luigi Di Sarno, Italy
Ana María Díez-Pascual, Spain
Guru P. Dinda, USA
Nadka Tzankova Dintcheva, Italy
Frederic Dumur, France
Stanislaw Dymek, Poland
Kaveh Edalati, Japan
Philip Eisenlohr, USA
Claude Estournès, France
Michele Fedel, Italy
Paolo Ferro, Italy
Massimo Fresta, Italy
Pasquale Gallo, Japan
Germà Garcia-Belmonte, Spain
Santiago Garcia-Granda, Spain
Carlos Garcia-Mateo, Spain
Georgios I. Giannopoulos, Greece
Ivan Giorgio, Italy
Antonio Gloria, Italy
Vincenzo Guarino, Italy
Daniel Guay, Canada
Gianluca Gubbiotti, Italy
Xuchun Gui, China
Benoit Guiffard, France
Ivan Gutierrez-Urrutia, Japan
Hiroki Habazaki, Japan
Simo-Pekka Hannula, Finland
David Holec, Austria
Satoshi Horikoshi, Japan
David Houivet, France
Rui Huang, USA
Michele Iafisco, Italy
Saliha Ilican, Turkey
Ilia Ivanov, USA
kenji Kaneko, Japan
Katsuyuki Kida, Japan
Akihiko Kimura, Japan
Soshu Kirihara, Japan
Paweł Kłosowski, Poland
Fantao Kong, China
Hongchao Kou, China
krzysztof Kurzydłowski, Poland
Andrea Lamberti, Italy
Luciano Lamberti, Italy
Marino Lavorgna, Italy
Laurent Lebrun, France
Joon-Hyung Lee, Republic of Korea
Pavel Lejcek, Czech Republic
Cristina Leonelli, Italy
Ying Li, USA
Yuanshi Li, Canada
Jun Liu, China
Meilin Liu, Georgia
Shaomin Liu, Australia
Yunqi Liu, China
Zhiping Luo, USA
Fernando Lusquiños, Spain
Peter Majewski, Australia
Enzo Martinelli, Italy
Yoshitake Masuda, Japan
Bobby Kannan Mathan, Australia
Roshan Mayadunne, Australia
Philippe Miele, France
Andrey E. Miroshnichenko, Australia
Hossein Moayedi, Iran
Jose M. Monzo, Spain
Michele Muccini, Italy
Alfonso Muñoz, Spain
Rufino M. Navarro, Spain
Miguel Navarro-Cia, UK
Luigi Nicolais, Italy
Hiroshi Noguchi, Japan
Chérif Nouar, France
Olanrewaju Ojo, Canada
Laurent Orgéas, France
Togay Ozbakkaloglu, Australia
Davide Palumbo, Italy
Gianfranco Palumbo, Italy
Anna Maria Paradowska, Australia
Matthew Peel, UK
Gianluca Percoco, Italy
Claudio Pettinari, Italy
Giorgio Pia, Italy
Daniela Pilone, Italy
Fabrizio Pirri, Italy
Alain Portavoce, France
Simon C. Potter, Canada
Manijeh Razeghi, USA
Yuri Ribakov, Israel
Aniello Riccio, Italy
Anna Richelli, Italy
Antonio Riveiro, Spain



Marco Rossi, Italy
Pascal Roussel, France
Fernando Rubio-Marcos, Spain
Francesco Ruffino, Italy
Antti Salminen, Finland
F.H. Samuel, Canada
Hélder A. Santos, Finland
Carlo Santulli, Italy
Fabrizio Sarasini, Italy
Michael J. Schütze, Germany
Raffaele Sepe, Italy
Fridon Shubitidze, USA
Donato Sorgente, Italy
Charles C. Sorrell, Australia
Andres Sotelo, Spain
Costas M. Soukoulis, USA

Damien Soulat, France
Adolfo Speghini, Italy
Antonino Squillace, Italy
Manfred Stamm, Germany
Koichi Sugimoto, Japan
Baozhong Sun, China
Sam-Shajing Sun, USA
Kohji Tashiro, Japan
Miguel Angel Torres, Spain
Laszlo Toth, France
Achim Trampert, Germany
Luca Valentini, Italy
Ashkan Vaziri, USA
Lijing Wang, Australia
Rui Wang, China
Lu Wei, China

Jörg M. K. Wiezorek, USA
Guoqiang Xie, Japan
Dongmin Yang, UK
Hemmige S. Yathirajan, India
Yee-wen Yen, Taiwan
Wenbin Yi, China
Ling Yin, Australia
Belal F. Yousif, Australia
Michele Zappalorto, Italy
Jinghuai Zhang, China
Li Zhang, China
Ming-Xing Zhang, Australia
Wei Zhou, China
You Zhou, Japan

Contents

Alternative Cementitious Materials and Their Composites

K. Pimraksa , P. Chindapasirt , J. Sanjayan, and T.-C. Ling 

Volume 2018, Article ID 5074636, 2 pages

Influence of Pb Dosage on Immobilization Characteristics of Different Types of Alkali-Activated Mixtures and Mortars

Jan Koplík , Jaromír Pořízka, Lukáš Kalina, Jiří Másilko, and Matěj Březina

Volume 2018, Article ID 4026127, 6 pages

Improvement of the Early-Age Compressive Strength, Water Permeability, and Sulfuric Acid Resistance of Scoria-Based Mortars/Concrete Using Limestone Filler

Aref Al-Swaidani, Andraos Soud, and Amina Hammami

Volume 2017, Article ID 8373518, 17 pages

Flexural Behaviour of Combined FA/GGBFS Geopolymer Concrete Beams after Exposure to Elevated Temperatures

Jun-ru Ren, Hui-guo Chen, Tao Sun, Hao Song, and Miao-shuo Wang

Volume 2017, Article ID 6854043, 9 pages

Long-Term Properties of Cement-Based Composites Incorporating Natural Zeolite as a Feature of Progressive Building Material

Alena Sičáková, Matej Špak, Mária Kozlovská, and Marek Kováč

Volume 2017, Article ID 7139481, 8 pages

The Role of Various Powders during the Hydration Process of Cement-Based Materials

Shuhua Liu, Hongling Wang, and Jianpeng Wei

Volume 2017, Article ID 8394834, 9 pages

Development and Characterization of Norite-Based Cementitious Binder from an Ilmenite Mine Waste Stream

Mahmoud Khalifeh, Arild Saasen, Helge B. Larsen, and Helge Hodne

Volume 2017, Article ID 6849139, 7 pages

Properties and Internal Curing of Concrete Containing Recycled Autoclaved Aerated Lightweight Concrete as Aggregate

Teewara Suwan and Pitiwat Wattanachai

Volume 2017, Article ID 2394641, 11 pages

Optimising the Performance of Cement-Based Batteries

Aimee Byrne, Shane Barry, Niall Holmes, and Brian Norton

Volume 2017, Article ID 4724302, 14 pages

Effect of Calcined Hard Kaolin Dosage on the Strength Development of CPB of Fine Tailings with Sulphide

Juanrong Zheng, Lijie Guo, and Zhenbo Zhao

Volume 2017, Article ID 8631074, 7 pages

Strengths and Failure Characteristics of Self-Compacting Concrete Containing Recycled Waste Glass Aggregate

Rahman Khaleel AL-Bawi, Ihsan Taha Kadhim, and Osamah AL-Kerttani

Volume 2017, Article ID 6829510, 12 pages

Experimental Study and Application of Inorganic Solidified Foam Filling Material for Coal Mines

Hu Wen, Duo Zhang, Zhijin Yu, Xuezhao Zheng, Shixing Fan, and Bin Laiwang

Volume 2017, Article ID 3419801, 13 pages

An Investigation on Self-Compacting Concrete Using Ultrafine Natural Steatite Powder as Replacement to Cement

P. Kumar, K. Sudalaimani, and M. Shanmugasundaram

Volume 2017, Article ID 8949041, 8 pages

Compression Behavior of Confined Columns with High-Volume Fly Ash Concrete

Sung-Won Yoo, Young Cheol Choi, and Wonchang Choi

Volume 2017, Article ID 8208079, 11 pages

Modifying Cement Hydration with NS@PCE Core-Shell Nanoparticles

Yue Gu, Qianping Ran, Wei She, and Jiaping Liu

Volume 2017, Article ID 3823621, 13 pages

Flexural and Shear Behaviors of Reinforced Alkali-Activated Slag Concrete Beams

Kwang-Myong Lee, Sung Choi, Jinkyoo F. Choo, Young-Cheol Choi, and Sung-Won Yoo

Volume 2017, Article ID 5294290, 12 pages

Influence of Palm Oil Fuel Ash and W/B Ratios on Compressive Strength, Water Permeability, and Chloride Resistance of Concrete

Wachilakorn Sanawung, Tieng Cheewaket, Weerachart Tangchirapat, and Chai Jaturapitakkul

Volume 2017, Article ID 4927640, 8 pages

Editorial

Alternative Cementitious Materials and Their Composites

K. Pimraksa ¹, **P. Chindapasirt** ², **J. Sanjayan**,³ and **T.-C. Ling** ⁴

¹Department of Industrial Chemistry, Faculty of Science, Chiang Mai University, Chiang Mai 50200, Thailand

²Sustainable Infrastructure Research and Development Center, Khon Kaen University, Khon Kaen 40002, Thailand

³Center for Sustainable Infrastructure, Faculty of Science Engineering and Technology, Swinburne University of Technology, Hawthorn, VIC 3122, Australia

⁴College of Civil Engineering, Hunan University, Hunan 410082, China

Correspondence should be addressed to K. Pimraksa; kedsarin.p@cmu.ac.th

Received 28 January 2018; Accepted 28 January 2018; Published 27 February 2018

Copyright © 2018 K. Pimraksa et al. This is an open access article distributed under the Creative Commons Attribution License, which permits unrestricted use, distribution, and reproduction in any medium, provided the original work is properly cited.

Research and development of alternative cementitious materials as well as supplementary cementing materials (SCMs) become mandatory for construction industry to manage global warming as well as energy scarcity due to huge energy consumptions and greenhouse gas emissions entailed by the conventional cement technology. The improvement in durability of materials is inevitably aimed to be achieved for resource efficiency and safety factor. Researchers are trying to replace Portland cement (PC) with SCMs and low-temperature cementitious materials such as special cements and geopolymeric binders. Besides using alternative cements and SCMs instead of pure Portland cement, their composites with other inorganic materials can work as smart building materials and work for environmental aspects. In this special issue on alternative cementitious materials and their composites, we have invited a few papers that address such issues.

The first paper of this special issue addresses the immobilization of harmful Pb using alkali-activated materials made of industrial wastes, blast furnace slag (BFS) and coal fly ash. The Pb immobilization was accomplished at 99%. The best recipe for Pb solidification was alkali-activated BFS blended with sand, when compared to pure BFS and pure fly ash systems. This was due to the lowest porosity of the sand-blended system. The high dosage of Pb lowered the strength of materials. The second paper proposed the use of natural SCMs such as volcanic rock (scoria) and limestone for economic benefit and early-strength and durability improvements, respectively. The accelerated strength performance was due to the acceleration in precipitation of hydration products

when limestone powders were added. The combination of limestone and volcanic scoria created the best environment for H₂SO₄ protection due to many reasons: calcium hydroxide reduction, gypsum formation, and more Ca ions in the system, which assisted retardation of acid attack. The third paper attempted to address the fire resistance issue of conventional cement by introduction of the geopolymer as an alternative. The fire resistance and mechanical tests were carried out on geopolymer concrete made of class F fly ash and ground-granulated blast furnace slag and compared to normal concrete made of ordinary Portland cement (OPC). With the proposed formula, geopolymer concrete was less fire resistant than OPC concrete because of its higher shrinkage. The results showed the limitation of starting materials containing high alkali contents. However, the issue has to be deeply investigated for more understanding of the fire-resistant geopolymer. The fourth paper proposed the use of SCMs such as natural zeolite in concrete mix. It was worth to note here that zeolite, a kind of the porous material, could improve mechanical properties of concrete in the long term due to its pozzolanic reaction. The fifth paper described hydration of OPC in the presence of various powders such as glass powder, limestone powder, and steel slag powder. They behaved differently when met with OPC in that glass powder consumed calcium hydroxide (CH) due to its pozzolanic reaction, while limestone and steel slag powder did not react with CH and provided more CH for the system, respectively.

The sixth paper addressed the feasibility of natural rock, a kind of inert material, to synthesize the alkali-activated binder. This paper showed a successful case for using silicate minerals in groups of inosilicate and tectosilicate to produce

the geopolymeric binder. The seventh paper addressed the utilization of autoclaved aerated lightweight concrete wastes as an aggregate in concrete mix, aiming strength improvement by internal curing. The experiments provided positive results in introduction of such wastes for concrete mix as they could supply additional water for internal curing. The eighth paper proposed new direction of cementitious materials for energy storage due to their ionic and highly porous characteristics. The challenging perspective of this cement-based battery is how to improve its power output and service life. The ninth paper addressed the difficulty in strength and durability improvements of cement paste backfill for environmental cleaning-up, especially solidification of heavy metals in fine tailings containing sulphide from zinc mine. A use of calcined kaolin for cement replacement gave positive results both in short and long terms in aspects of strength and durability. The release of toxic elements shall be further investigated to confirm the potential of solidification. The tenth paper investigated an impact of glass waste aggregate contents on mechanical properties of concrete, especially fracture parameters, aiming to promote waste utilization for construction industry. In a replacement of the natural fine aggregate, a use of glass cullet provided negative effect on fracture behavior.

The eleventh paper addressed the problem of air leakage to improve coal mining safety. This paper offered a kind of new and affordable airtight filling material which composed various kinds of cementing materials. The best recipe for sealing composed of high amount of sulfoaluminate cement due to its highly expansive behavior and fast strength development. The twelfth paper proposed the possibility for a use of very fine steatite powder as cement replacement in self-compacting concrete. This paper showed that the natural clay mineral was possible to work as a supplementary cementing material. The thirteenth paper promoted a use of high-volume fly ash in concrete in structural application such as column. It showed a good sign to adopt high-volume fly ash for construction. The fourteenth paper described the modification of hydration of Portland cement in the presence of nano-SiO₂-polycarboxylate compounds which were combinations of pozzolan and superplasticizer. This paper achieved the introduction of this new composite material for controlling hydration of Portland cement. The fifteenth paper proposed the mechanical properties of alkali-activated slag concrete compared to those of Portland cement concrete. The flexural and shear behaviors of reinforced slag concrete were not significantly different from those of conventional Portland concrete. The last paper achieved the utilization of palm oil fuel ash for Portland cement replacement in terms of water permeability and chloride resistance.

*K. Pimraksa
P. Chindapasirt
J. Sanjayan
T.-C. Ling*

Research Article

Influence of Pb Dosage on Immobilization Characteristics of Different Types of Alkali-Activated Mixtures and Mortars

Jan Koplík , Jaromír Pořízka, Lukáš Kalina, Jiří Másilko, and Matěj Březina

Faculty of Chemistry, Materials Research Centre, Brno University of Technology, Purkyňova 118, 612 00 Brno, Czech Republic

Correspondence should be addressed to Jan Koplík; koplik@fch.vutbr.cz

Received 9 June 2017; Revised 31 October 2017; Accepted 28 November 2017; Published 11 January 2018

Academic Editor: Kedsarin Pimraksa

Copyright © 2018 Jan Koplík et al. This is an open access article distributed under the Creative Commons Attribution License, which permits unrestricted use, distribution, and reproduction in any medium, provided the original work is properly cited.

Alkali-activated matrices are suitable materials for the immobilization of hazardous materials such as heavy metals. This paper is focused on the comparison of immobilization characteristics of various inorganic composite materials based on blast furnace slag and on the influence of various dosages of the heavy metal Pb on the mechanical properties and fixation ability of prepared matrices. Blast furnace slag (BFS), fly ash, and standard sand were used as raw materials, and sodium water glass was used as an alkaline activator. $\text{Pb}(\text{NO}_3)_2$ served as a source of heavy metal and was added in various dosages in solid state or as aqueous solution. The immobilization characteristics were determined by leaching tests, and the content of Pb in the eluate was measured by inductively coupled plasma optical emission spectroscopy (ICP-OES). The microstructure of matrices and distribution of Pb within the matrix were determined by scanning electron microscopy (SEM) equipped with energy dispersive X-ray spectroscopy (EDS). Increasing the dosage of the heavy metal had negative impacts on the mechanical properties of prepared matrices. The leaching tests confirmed the ability of alkali-activated materials to immobilize heavy metals. With increasing addition of Pb, its content in eluates increased.

1. Introduction

Heavy metals such as Pb belong to hazardous materials, which are harmful to the human beings. Lead is highly toxic element, which attacks mainly the nervous system. Lead exposure mostly occurs through the ingestion of contaminated water or food. Therefore, it is important to prevent its leakage into the environment by stabilization or solidification of waste materials before their deposition into the landfill [1]. A possible way on how to immobilize heavy metals is using alkali-activated materials (AAMs). AAMs present a broad range of materials (geopolymers, activated blast furnace slag, etc.), but all of them are activated by high pH during their preparation. The AAMs can be divided into two big groups: high-calcium alkali-activated materials (HCAAMs) and low-calcium alkali-activated materials (LCAAMs). HCAAMs are represented mainly by activated BFS, and LCAAMs are represented mainly by activated fly ash or metakaolin. The structure of HCAAMs consists of the C-A-S-H gel as

a major hydration product. This gel has a similar structure as the C-S-H gel in hydrated ordinary Portland cement and is made up of tetrahedrally coordinated silicate chains, where aluminium is located in the bridging position instead of silicon. The structure and composition of the C-A-S-H gel depend on the nature and concentration of the used activator. AFm-type phases (NaOH-activated binders), hydrotalcite (BFS with high content of MgO), and zeolites (binders with high content of Al_2O_3) are usually formed as secondary hydration products [2–4].

Heavy metals can be immobilized by two types of fixation—physical and chemical. Mostly, both types of immobilization occur together. Physical fixation is linked with mechanical properties and porosity of the matrix. Chemical fixation means that there is a chemical bond between the heavy metal and the matrix. Heavy metals can be inhibited by transformation into a less soluble form as well. After alkali activation, the heavy metals usually occur in the form of silicate or hydroxide [5–7]. The

TABLE 1: Particle size distribution of raw materials.

	x (10%) μm	x (50%) μm	x (90%) μm	x (99%) μm
BFS	0.88	10.73	33.97	59.57
Fly ash	4.18	44.56	236.89	486.20

TABLE 2: The nomenclature of samples.

Mixture	Mixture name
BFS; 1% Pb added as solid	S1
BFS; 2.5% Pb added as solid	S2
BFS; 5% Pb added as solid	S5
BFS + sand; 1% Pb added as solid	M1
BFS + sand; 2.5% Pb added as solid	M2
BFS + sand; 5% Pb added as solid	M5
BFS + fly ash; 1% Pb added as solid	P1
BFS + fly ash; 2.5% Pb added as solid	P2
BFS + fly ash; 5% Pb added as solid	P5
BFS; 1% Pb added as liquid	SR1
BFS; 2.5% Pb added as liquid	SR2
BFS + sand; 1% Pb added as liquid	MR1
BFS + sand; 2.5% Pb added as liquid	MR2
BFS + fly ash; 1% Pb added as liquid	PR1
BFS + fly ash; 2.5% Pb added as liquid	PR2

TABLE 3: The mixture design of prepared matrices.

	BFS matrices	Matrices with sand	Matrices with fly ash
BFS	100 wt.%	25 wt.%	50 wt.%
Fly ash	—	—	50 wt.%
Sand	—	75 wt.%	—
Activator/binder	8%	8%	8%
Water/binder	0.33	0.42	0.33

immobilization of heavy metals within AAMs can be influenced by various factors, such as the composition of the matrix, the type of alkaline activator, the immobilized heavy metal, and the leaching medium [8, 9]. Previous researches proved that Pb reached high efficiency of immobilization in AAMs, but there is only little information about the influence of Pb dosage on immobilization characteristics of AAMs [10–13].

The aim of this work was to compare the ability of three different alkali-activated matrices based on BFS to immobilize Pb within their structure. The influence of different Pb dosages on the immobilization efficiency was also investigated.

2. Materials and Methods

2.1. Materials, Sample Preparation, and Leaching Tests. BFS and high-temperature fly ash were used as raw materials. The particle size distribution of both raw materials is listed in Table 1. Liquid sodium silicate with the $\text{SiO}_2/\text{Na}_2\text{O}$ ratio of

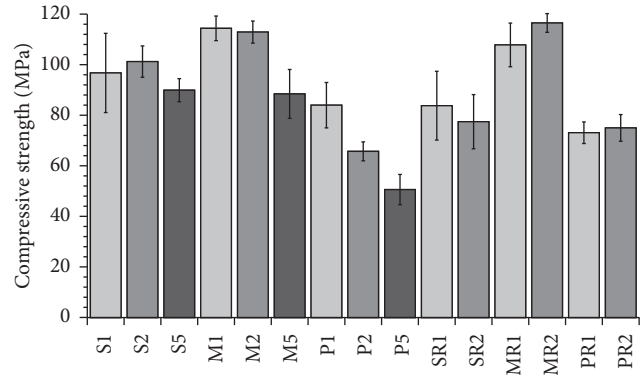


FIGURE 1: Compressive strength of prepared matrices (28 days).

1.85 served as an alkaline activator. As fine aggregates, three different fractions of siliceous Czech standard sand complying with ČSN EN 196-1 were used (the mass ratio of the fractions was 1 : 1 : 1). Pb was used in the form of $\text{Pb}(\text{NO}_3)_2$.

Three types of matrices were prepared. The first one was based only on BFS. In the second one, 50 wt.% of BFS was replaced by fly ash. And the third one consisted of BFS and standard sand. The sample nomenclature and the mixture designs are listed in Tables 2 and 3, respectively. Pb was added in the dosages of 1, 2.5, and 5 wt.% to binder mass and was added in two ways: as a solution and as a solid. In both cases, the water-to-binder ratios were the same.

The whole mixing procedure took four minutes. In the beginning, all materials without aggregates were put together and sand, if needed, was added after 30 s of mixing. The samples were cast in steel molds measuring $20 \times 20 \times 100$ mm. All analyses were performed after 28 days of moist curing (98% relative humidity) at laboratory temperature ($23 \pm 2^\circ\text{C}$).

The leaching tests were based on ČSN EN 12457-4. The demineralized water served as leaching agent. The solid/liquid ratio was 1 : 10, and the mixture was agitated for 24 hours. After the leaching time ended, the mixture was filtered by a membrane filter with the pore size of $0.45 \mu\text{m}$, and the concentration of Pb in solution was determined by ICP-OES.

2.2. Methods. The compressive strength was measured according to the ČSN EN 196-1 using Betonsystem Desttest 3310. To determine the porosity, prepared matrices were investigated by mercury intrusion porosimetry using Quantachrome instrument PoreMaster 33. The surface tension of mercury was 480 mN/m , and the contact angle was 140° based on the recommendation. The pore sizes were determined in the range from over $170 \mu\text{m}$ to $0.0064 \mu\text{m}$. The ICP-OES data were obtained using Horiba Jobin Yvon Ultima II Spectrometer. The parameters of measurement were as follows: RF power, 1350 W ; gas, argon; plasma gas, $13 \text{ L}\cdot\text{min}^{-1}$; auxiliary gas, $0.1 \text{ L}\cdot\text{min}^{-1}$; nebuliser gas, $0.85 \text{ L}\cdot\text{min}^{-1}$; plasma view, radial; nebuliser, Meinhard; and nebuliser pressure, 3 bar. The scanning electron microscopy (SEM) and the energy dispersive X-ray spectroscopy (EDS)

TABLE 4: Compressive strength of prepared matrices (7 days).

Mixture	S1	S2	S5	M1	M2	M5	P1	P2
MPa	62.3	61.8	58.3	75.0	74.8	59.7	56.7	49.7
Mixture	P5	SR1	SR2	MR1	MR2	PR1	PR2	—
MPa	40.1	55.4	53.2	70.5	76.3	50.3	52.7	—

TABLE 5: The porosity of matrices.

Total intruded volume (cm ³ /g)	P1	P5	PR1	M1	M5	MR1	S1	S5	SR1
	0.130	1.312	0.117	0.034	0.050	0.036	0.022	0.035	0.023

analyses were performed using Zeiss EVO LS 10 equipped with an Oxford X-Max 80 mm² detector in the backscattering mode. The working distance for all samples was 12 mm and the accelerate voltage was 30 kV. All samples were sputtered by carbon to obtain good surface conductivity.

3. Results and Discussion

3.1. Compressive Strength. The compressive strength of prepared matrices is shown in Figure 1 and Table 4. Following the results, the type of matrix had the highest influence on the compressive strength. The highest values had the matrix with aggregates, and the lowest values reached the matrix with fly ash. The results correspond with the findings in literature that, by replacing BFS with fly ash, the compressive strength decreases [2]. No clear behavior correlation was observed between the Pb dosage amount and mechanical properties. Increasing the dosage of Pb from 1 up to 2.5 wt.% led, in some cases, to the compressive strength increase and in some cases to the strength decrease. The addition of 5 wt.% of Pb caused the decrease of compressive strength in all types of matrices.

3.2. Porosity. The porosity of the prepared materials depended mainly on the type of the matrix. The total porosity of chosen samples is listed in Table 5. The matrix with fly ash showed the highest porosity. High-temperature fly ash consists of spherical particles, which can be filled in with similar smaller particles or can be hollow. Hence, partially reacted fly ash particles increased the porosity. The lowest porosity was observed in the matrix based on BFS. It is due to a very compact microstructure of this matrix, which was confirmed by SEM analysis (Figure 2). The dosage of Pb influenced the porosity of matrices too. The total porosity of matrices increased with increasing Pb content. As can be seen in Figure 3, around the areas, where Pb was cumulated, the matrix was not compact and the cracks and pores were formed. This caused the increase in porosity. The state of Pb addition—liquid/solid—did not affect the porosity.

3.3. Leaching Tests. To determine the efficiency of Pb immobilization, the leaching test based on ČSN EN 12457-4

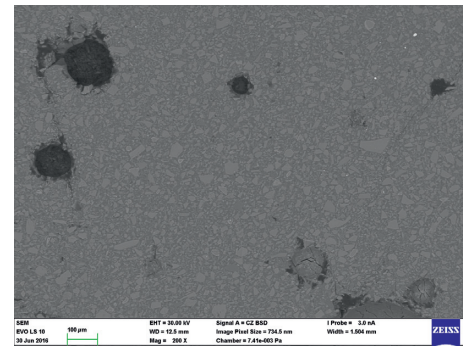


FIGURE 2: The microstructure of SR2 matrix.

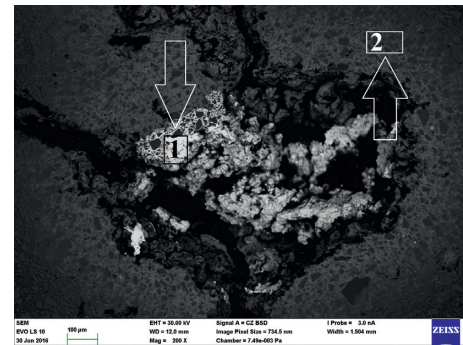


FIGURE 3: The microstructure of S2 matrix.

was performed. This test serves to determine whether the material is suitable for landfilling and whether it does not represent any hazard for the environment. Figure 4 shows the concentration of Pb in eluates from the prepared matrices. The immobilization of Pb in all matrices was very high and reached up to 99%. The results correspond with previous research and correlate with the total porosity of the matrices [11]. The highest Pb release occurred from matrices with fly ash, which also had the highest porosity and the lowest mechanical properties. The dosage of Pb had the influence on immobilization too. With increasing Pb addition, the content of Pb released into the leaching medium increased as well. It should be taken into consideration that when the Pb addition rose five times, the release increased only maximally three times. The efficiency of Pb immobilization was better with higher dosages of Pb.

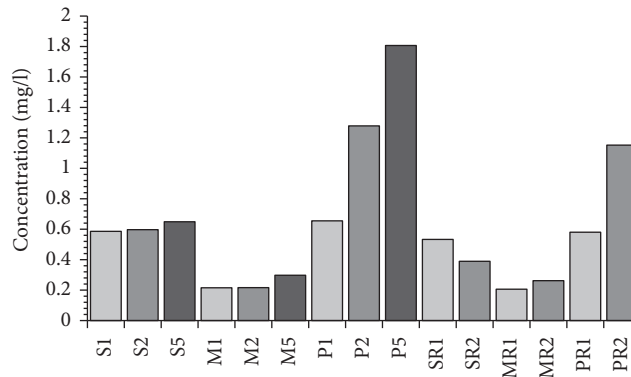


FIGURE 4: Concentration of Pb in eluates from matrices.

TABLE 6: The pH of eluates from matrices.

Mixture	S1	S2	S5	M1	M2	M5	P1	P2
pH	11.92	11.89	11.77	11.32	11.29	11.15	11.63	11.60
Mixture	P5	SR1	SR2	MR1	MR2	PR1	PR2	—
pH	11.51	11.89	11.88	11.31	11.31	11.63	11.58	—

TABLE 7: EDS analysis of S2 matrix.

Area 1											
Element	O	Na	Mg	Al	Si	Ca	Pb	—	—	—	—
Atomic (%)	57.85	3.29	0.76	0.95	12.32	1.64	23.20	—	—	—	—
Area 2											
Element	O	Na	Mg	Al	Si	Ca	Pb	S	K	Ti	Mn
Atomic (%)	58.13	4.62	3.93	3.00	15.23	12.80	0.97	0.88	0.19	0.07	0.18

TABLE 8: EDS analysis of P2 matrix.

Area 3											
Element	O	Si	Ca	Al	Pb	—	—	—	—	—	—
Atomic (%)	81.61	3.95	3.61	1.03	9.79	—	—	—	—	—	—
Area 4											
Element	O	Si	Ca	Al	Pb	Na	Mg	K	Ti	Fe	
Atomic (%)	59.10	18.91	5.96	7.57	0.12	4.89	1.86	0.57	0.30	0.72	

The pH of eluates is listed in Table 6. The matrices with sand reached the lowest pH, because they contained the smallest amount of the binder. The presence of fly ash led to the decrease of pH. The highest dosage of Pb (5 wt.%) caused the decrease of pH as well.

3.4. SEM. The SEM analysis showed three different microstructures depending on the type of matrix. The samples S2, P2, M2, and SR2 were investigated. The matrix based on BFS had a compact structure with unreacted particles of BFS and hydration products between them (Figure 3, Area 2; Table 7). A similar structure was observed in the matrix containing fly ash, but moreover, unreacted particles of fly ash were identified. The addition of fly ash led to the increase in the content of Si and Al and the decrease in the

content of Ca (Table 8). A quite different microstructure occurred in the matrix with aggregates. The unreacted aggregates filled the major area of the sample and in between them there was the matrix with the same composition as observed in the S2 sample (Figure 5, Table 9, and Area 6). The aggregates were composed of quartz (Table 9 and Area 7).

When Pb was added as a solid, it behaved in the same manner in all types of matrices. Pb was cumulated in pores and formed specific structures (Figures 3, 5, and 6). These structures consisted mainly of Pb and O. It can be assumed that Pb transformed into its insoluble salt $Pb(OH)_2$ after the alkali activation. These findings correspond to previous research [14]. Minor amount of Pb was dispersed throughout the matrix. A quite different situation came up with the addition of Pb as a solution. Pb was dispersed

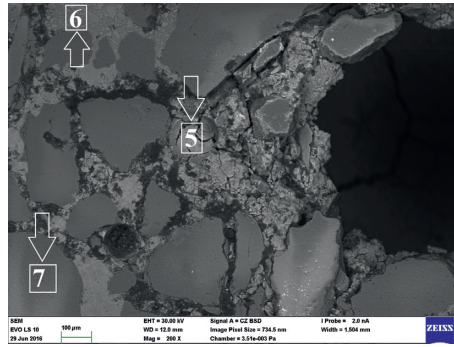


FIGURE 5: The microstructure of M2 matrix.

TABLE 9: EDS analysis of M2 matrix.

Area 5											
Element	O	Si	Ca	Pb	—	—	—	—	—	—	—
Atomic (%)	73.26	7.61	5.21	13.92	—	—	—	—	—	—	—
Area 6											
Element	O	Si	Ca	Pb	Na	Mg	Al	S	K	Ti	Mn
Atomic (%)	59.02	15.38	12.87	0.14	3.93	4.17	3.52	0.44	0.21	0.13	0.19
Area 7											
Element	O	Si	—	—	—	—	—	—	—	—	—
Atomic (%)	63.65	36.35	—	—	—	—	—	—	—	—	—

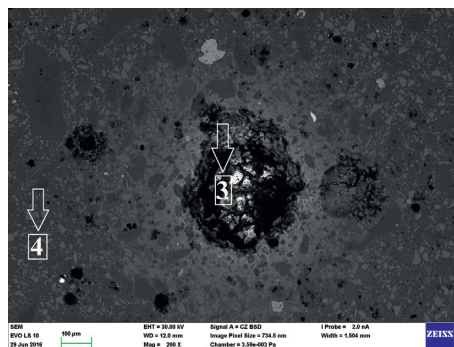


FIGURE 6: The microstructure of P2 matrix.

TABLE 10: EDS mapping of SR2 matrix.

Element	O	Si	Ca	Al	Pb	Na	Mg	K	Ti	Mn
Atomic (%)	58.96	15.39	13.06	3.08	0.27	4.65	3.86	0.18	0.07	0.15

equally throughout the matrix and did not create any specific structures (Figure 2, Table 10).

4. Conclusions

The immobilization of Pb in three different matrices was investigated. All matrices showed good ability to immobilize Pb. The increase in the Pb dosage led to the increase of Pb concentration in eluates, but the immobilization efficiency remained up to 99% in all cases. After

the alkali activation, Pb formed its insoluble salt $Pb(OH)_2$. Both the compressive strength and the porosity were influenced by the Pb dosage. The decrease of mechanical properties after the addition of higher Pb dosage (5 wt.%) was observed. The concentration of Pb in eluates correlated with the porosity: when the porosity was higher, more Pb was released in eluates. It can be assumed that Pb was fixed by physical fixation, which was linked with the mechanical properties of matrices. Pb was also well immobilized, thanks to the formation of its insoluble

salt. There was a difference in Pb behavior when added either as a solid or as a solution. In the case of solution, Pb was dispersed throughout the matrix equally, but when added as a solid, it formed specific structures, which cumulated in pores.

Conflicts of Interest

The authors declare that there are no conflicts of interest regarding the publication of this paper.

Acknowledgments

This outcome has been achieved with the financial support by the project Materials Research Centre at FCH BUT-Sustainability and Development (REG LO1211), National Programme for Sustainability I (Ministry of Education, Youth and Sports), and “Development of shrinkage reducing agents designed for alkali activated systems” (GA17-03670S, Czech Science Foundation).

References

- [1] J. M. Stellman, *Encyclopaedia of Occupational Health and Safety*, International Labour Office, Geneva, Switzerland, 4th edition, 1998.
- [2] J. L. Provis and J. S. J. van Deventer, *Alkali Activated Materials: State-of-the-Art Report*, Springer, Dordrecht, Netherlands, 2014.
- [3] L. Chao, S. Henghu, and L. Longtu, “A review: the comparison between alkali-activated slag (Si + Ca) and metakaolin (Si + Al) cements,” *Cement and Concrete Research*, vol. 40, no. 9, pp. 1341–1349, 2010.
- [4] F. Puertas, M. Palacios, H. Manzano, J. S. Dolado, A. Rico, and J. Rodríguez, “A model for the C-A-S-H gel formed in alkali-activated slag cements,” *Journal of the European Ceramic Society*, vol. 31, no. 12, pp. 2043–2056, 2011.
- [5] J. G. S. van Jaarsveld, J. S. J. van Deventer, and L. Lorenzen, “Factor affecting the immobilization of metals in geopolymerized fly ash,” *Metallurgical and Materials Transactions B*, vol. 29, no. 1, pp. 283–291, 1998.
- [6] J. W. Phair and J. S. J. van Deventer, “Effect of silicate activator pH on the leaching and material characteristic of waste-based inorganic polymer,” *Minerals Engineering*, vol. 14, no. 3, pp. 289–304, 2001.
- [7] A. Palomo and M. Palacios, “Alkali-activated cementitious materials: alternative matrices for the immobilisation of hazardous wastes part II. Stabilisation of chromium and lead,” *Cement and Concrete Research*, vol. 33, no. 2, pp. 289–295, 2003.
- [8] J. W. Phair, J. S. J. van Deventer, and J. D. Smith, “Effect of Al source and alkali activation on Pb and Cu immobilisation in fly-ash based “geopolymers,”” *Applied Geochemistry*, vol. 19, no. 3, pp. 423–434, 2004.
- [9] L. Zheng, W. Wang, and Y. Shi, “The effects of alkaline dosage and Si/Al ratio on the immobilization of heavy metals in municipal solid waste incineration fly ash-based geopolymer,” *Chemosphere*, vol. 79, no. 6, pp. 665–671, 2010.
- [10] J. Zhang, J. L. Provis, D. Feng, and J. S. J. van Deventer, “Geopolymers for immobilization of Cr⁶⁺, Cd²⁺ and Pb²⁺,” *Journal of Hazardous Materials*, vol. 157, no. 2-3, pp. 587–598, 2008.
- [11] J. Deja, “Immobilization of Cr⁶⁺, Cd²⁺, Zn²⁺ and Pb²⁺ in alkali-activated slag binders,” *Cement and Concrete Research*, vol. 32, no. 12, pp. 1971–1979, 2002.
- [12] J. G. S. van Jaarsveld and J. S. J. van Deventer, “The effect of metal contaminants on the formation and properties of waste-based geopolymers,” *Cement and Concrete Research*, vol. 29, no. 8, pp. 1189–1200, 1999.
- [13] L. Kalina, J. Koplík, F. Šoukal, J. Másilko, and L. Jaskowicová, “Potential uses of geopolymers to immobilize toxic metals from by-products material,” *Environmental Engineering and Management Journal*, vol. 11, no. 3, pp. 579–584, 2012.
- [14] J. Koplík, L. Kalina, J. Másilko, and F. Šoukal, “The characterization of fixation of Ba, Pb, and Cu in alkali-activated fly ash/blast furnace slag matrix,” *Materials*, vol. 9, no. 7, p. 533, 2016.

Research Article

Improvement of the Early-Age Compressive Strength, Water Permeability, and Sulfuric Acid Resistance of Scoria-Based Mortars/Concrete Using Limestone Filler

Aref Al-Swaidani,¹ Andraos Soud,² and Amina Hammami²

¹Faculty of Architectural Engineering, Arab International University, Damascus, Syria

²Transportation Engineering Department, Faculty of Civil Engineering, Damascus University, Damascus, Syria

Correspondence should be addressed to Aref Al-Swaidani; aydlswaidani@yahoo.fr

Received 9 June 2017; Accepted 26 September 2017; Published 8 November 2017

Academic Editor: Tung-Chai Ling

Copyright © 2017 Aref Al-Swaidani et al. This is an open access article distributed under the Creative Commons Attribution License, which permits unrestricted use, distribution, and reproduction in any medium, provided the original work is properly cited.

Natural pozzolan is being widely used as cement replacement. Despite the economic, ecological, and technical benefits of its adding, it is often associated with shortcomings such as the need of moist-curing for longer time and a lower early strength. This study is an attempt to investigate the effect of adding limestone filler on the compressive strength and durability of mortars/concrete containing scoria. Sixteen types of binders with different replacement levels of scoria (0, 10, 20, and 30%) and limestone (0, 5, 10, and 15%) were prepared. The development of the compressive strength of mortar/concrete specimens was investigated after 2, 7, 28, and 90 days' curing. In addition, the acid resistance of the 28 days' cured mortars was evaluated after 90 days' exposure to 5% H₂SO₄. Concrete permeability was also evaluated after 2, 7, 28, and 90 days' curing. Test results revealed that there was an increase in the early-age compressive strength and a decrease in water penetration depths with adding limestone filler. Contrary to expectation, the best acid resistance to 5% H₂SO₄ solution was noted in the mortars containing 15% limestone. Based on the results obtained, an empirical equation was derived to predict the compressive strength of mortars.

1. Introduction

Natural pozzolan is being widely used as cement replacement due to its ecological, economic, and performance-related advantageous properties [1–6]. However, its use caused longer setting times and lower early strengths compared with plain Portland cement [7, 8]. To overcome the disadvantages of low early strengths of binders containing natural pozzolans, adding limestone filler could be a solution.

During the last decade, limestone has proven to be an effective partial replacement for OPC. The effect of limestone filler on OPC is twofold. Replacing part of the OPC with limestone filler will provide additional surface for precipitation of hydration products, thereby promoting the early-age hydration of the OPC [9, 10]. Besides the aforesaid physical effect or what is called the filler effect, there is also a chemical effect: the calcium carbonate of the limestone filler can interact with the aluminate hydrates formed by OPC

hydration [9, 11, 12]. Calcium monosulfoaluminate hydrate is unstable in the presence of calcium carbonate, and instead calcium mono- and hemicaluminate hydrate will form. This leads to the stabilization of the ettringite and will result in an increase in the total volume of the hydration products [9, 12, 13], which potentially might result in a decrease in porosity and thus an increase in strength. The effect of this chemical interaction in an OPC-limestone system is, however, not so pronounced due to the limited aluminate content in the anhydrous clinker. In OPC the limestone filler is therefore often considered inert. The chemical interaction between calcium aluminate hydrates (CAH) and calcium carbonate (CC) might therefore be of greater importance in binders containing supplementary cementitious materials of significant contents of aluminates such as fly ash, metakaolin, and natural pozzolan. The CAH formed during the pozzolanic reaction react with the CC of the limestone filler and form calcium carboaluminate hydrates [9].

Portland cement concrete is vulnerable to acid erosion because of its high content of alkaline hydrates. In recent years, Portland cement concrete often incorporates pozzolans due to various benefits. One of these important benefits is the higher acidic resistance due to the dense microstructure and reduced calcium hydroxide, $\text{Ca}(\text{OH})_2$ [1]. However, the main composition of limestone filler is calcium carbonate, CaCO_3 , which easily suffers from acid attack.

Syria is rich in both limestone and volcanic scoria with estimated reserves of about 12 billion cubic meters and one billion tonnes, respectively [14, 15]. Although there are numerous studies on using natural pozzolan and limestone filler as cement replacement, very little works have been carried out in the past to investigate the influence of adding limestone filler on the mechanical and durability properties of volcanic scoria-based binder mortar/concrete. In addition, literature did not cover the wide area of durability and did not give answers in many areas regarding the growing use of limestone filler-volcanic scoria-OPC system.

The objective of this paper is to investigate the influence of adding limestone filler on some properties of mortars/concrete containing volcanic scoria-based binders. Compressive strength, acid resistance, and water permeability have particularly been investigated. Sixteen binders with different replacement levels of volcanic scoria (0, 10, 20, and 30%) and limestone filler (0, 5, 10, and 15%) have been produced for this investigation.

The study is of particular importance for the following points:

(i) Studying the strength development of both mortars and concrete with the same (w/b) ratio was not probably tackled before. Therefore, to predict the compressive strength of concrete depending on the mortar results could be considered a good approach.

(ii) Replacement of OPC by volcanic scoria and limestone filler could significantly minimize CO_2 released into atmosphere and save energy.

(iii) This study is the first of its kind in Syria. However, it is not limited to the country. It can be applied to other countries of similar geology, for example, Harrat Al-Shaam, a volcanic field which covers a total area of some 45,000 km^2 ; about 15,000 km^2 is located in the country, Figure 1. The rest covers parts of Jordan and KSA.

(iv) As our country begins preparations for the huge reconstruction after the war comes to its end, the encouraging results can be considered a motivation of other studies, such as using these local supplementary cementing materials in enhancement of properties of recycled concrete which are expected to be inevitable building material during the postwar reconstruction in Syria.

It is worth mentioning that, in previously published papers on studying Syrian volcanic scoria as cement replacement, the scoria was quarried from Dirat-at-Tulul (it is currently out of the governmental control) and ground with all other binder components (i.e., clinker and gypsum) together (i.e., intergrinding) into a specific fineness [1, 16, 17]. However, in the present study, another supplementary cementitious material (i.e., limestone filler) was added as cement replacement. In addition, the used volcanic scoria was quarried

from Tal Shihan (it is under control of the government), which is about 75 km far from the Dirat-at-Tulul quarry. This was clearly seen from the varying chemical and mineralogical compositions. All binder components (i.e., scoria, limestone, and OPC) were separately ground into specific levels of fineness. This grinding process was adopted because it ensures achieving the required level of supplementary cementitious materials fineness. In addition, more attention was paid to investigating the effects of adding limestone filler to the scoria-based cement on the physical, mechanical, and some durability-related properties of paste/mortar/concrete. The microstructure of ternary binder pastes was investigated thoroughly, as well. Furthermore, prediction of mechanical strength of mortars/concrete containing both volcanic scoria and limestone filler can be of considerable benefit. Despite the large number of studies which dealt with the natural pozzolan and limestone filler containing concrete, there is a lack of such a prediction.

2. Materials and Methods

2.1. Volcanic Scoria. Volcanic scoria (VS) used in the experiments was collected from a Tal Shihan' quarry, 70 km southeast of Damascus, as shown in Figure 1. Mineralogical and petrographic properties of VS were identified under the polarizing microscope by using their thin sections (Figure 2(a)) and X-ray powder diffraction (XRD) analysis of the powdered bulk samples was carried out (Figure 2(b)). The petrographic examination showed that VS consisted of amorphous glassy ground mass, vesicles, plagioclase, olivine, and pyroxene. The chemical analysis of VS used in the study is summarized in Table 1. This analysis was carried out by means of wet chemical analysis specified in EN 196-2(1989).

2.2. Limestone. Limestone was quarried from Hama governance, 210 km north of Damascus. Chemical and some physical properties of limestone are presented in Table 1. Its total organic carbon (TOC) and clay contents have been determined in accordance with EN 13639 and EN 933-9, respectively. Limestone sample has been dried and ground to the required size. SEM of the limestone filler (LF) with EDX analysis were shown in Figure 3.

2.3. Binder Samples. Sixteen binder samples have been prepared; one plain Portland cement CEM I (control), three binary binders with three replacement levels of 10%, 20%, and 30% VS (EN 197-1), three binary binders with three replacement levels of 5%, 10%, and 15% LF (EN 197-1), and nine ternary binders containing both VS and LF as illustrated in Table 2. 5% of gypsum were added to all the binder samples. All replacements were made by mass of cement. The clinker has been obtained from Adra Cement Plant, Damascus, Syria. All binder constituents have been ground by a laboratory grinding ball mill of 25 kg raw mix capacity. Limestone and volcanic scoria have separately been ground to $4100 \pm 100 \text{ cm}^2/\text{g}$ Blaine fineness, while the clinker and gypsum have been interground into $3600 \pm 50 \text{ cm}^2/\text{g}$. The Blaine fineness was measured using air permeability method in accordance with the European standard (EN 196-6). The particle size

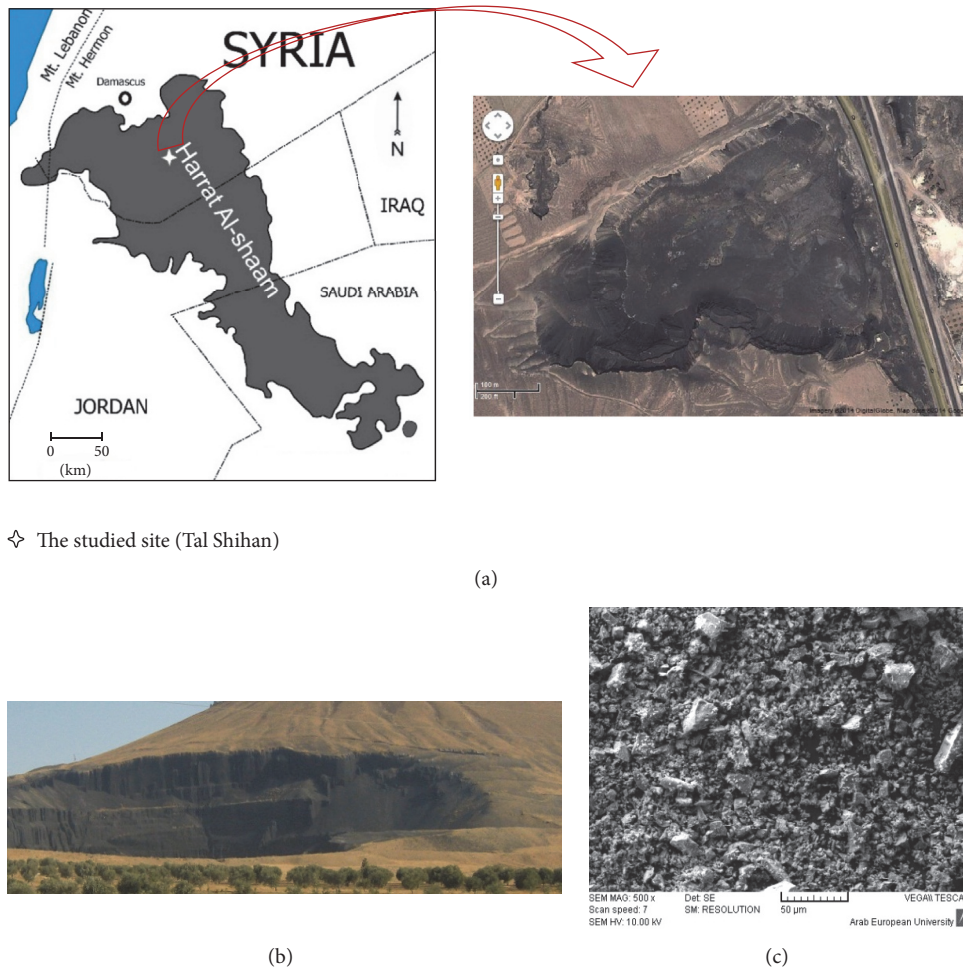


FIGURE 1: Map of Harrat Al-Shaam with a satellite view of the quarry. Photos of the studied quarry and the studied ground volcanic scoria. (a) Map of Harrat Al-Shaam with a satellite view of the studied area. (b) The studied volcanic scoria quarry. (c) SEM of the studied ground volcanic scoria.

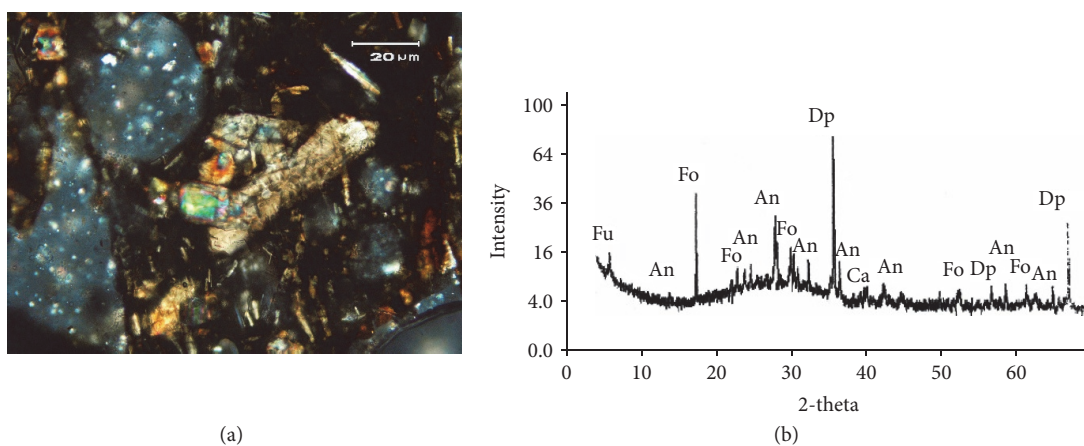


FIGURE 2: Petrographical examination and XRD analysis of the studied VS. (a) Microphenocrysts of olivine, pyroxene, and elongated plagioclase in volcanic glass matrix with vesicles, some of which are filled with white minerals. (b) XRD pattern of the studied VS. (Fo: Forsterite; An: Anorthite; Ca: Calcite; Dp: Diopside; Fu: Faujasite).

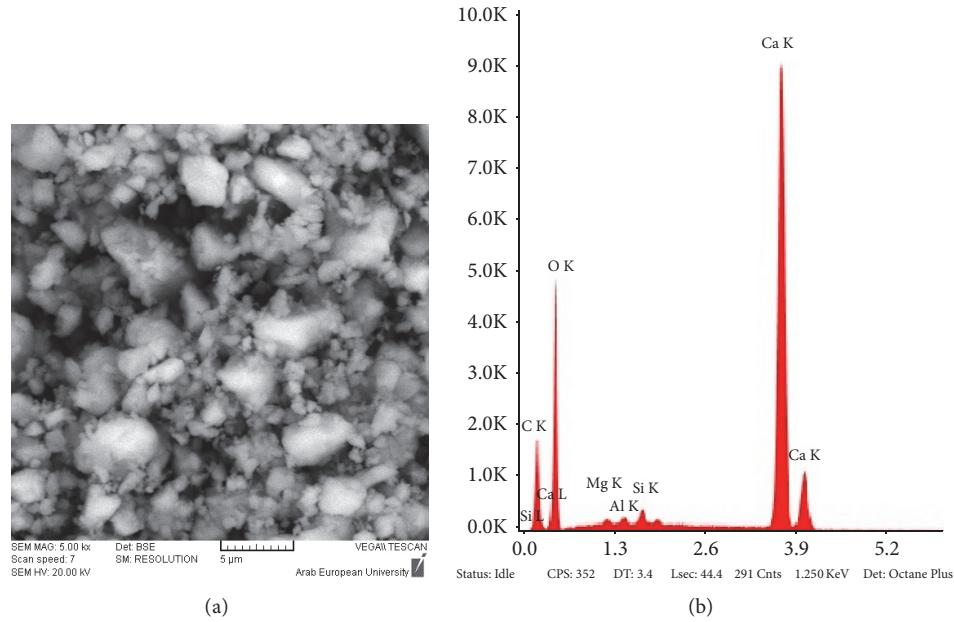


FIGURE 3: SEM and EDX of the studied ground limestone; (a) and (b), respectively.

distributions of the constituents have been obtained using Malvern Mastersizer 2000, a laser particle size analyzer, as shown in Figure 4. The median particle sizes of LF, VS, and OPC were about 9, 13, and 15 μm, respectively. All binders were designated according to the replacement levels. For instance, VS30LF5 refers to the binder containing 30% and 5% of VS and LF, respectively.

2.4. Mortars. Mortar specimens of all binders used in the experiments have been prepared using these binders and sand meeting the requirements of ASTM C778. In all mixtures, binder : sand and water : binder (w/b) ratios were kept constant as 1:2.75 and 0.5 by weight, respectively. After being kept in (RH ~ 95%) for 24 hours, the mortar specimens were demolded and kept in water at 22 + 2°C until the time of testing. No admixtures were used, as all mortar mixtures were mixable at this water-to-binder ratio.

2.5. Concrete. Sixteen concrete mixes have been prepared using grading of aggregate mixtures kept constant for all concrete mixes. Aggregates used in the study were crushed dolomite with natural sand added. Their quantities in 1 m³ concrete mix based on the oven-dry condition were as follows: 585.5 kg of coarse aggregate, 585.5 kg of medium-size aggregate, 467.5 kg of crushed stone sand, and 312.5 kg of natural sand. All concrete mixes were designed to have a water-binder ratio of 0.5 and a slump of 150 ± 20 mm. Superplasticizer of “type F” (ASTM C494) was added. Concrete cubes (150 mm) were cast for the determination of compressive strength and water permeability.

2.6. Physical and Mechanical Properties of Pastes/Mortars. Water requirements, setting times, and soundness of all

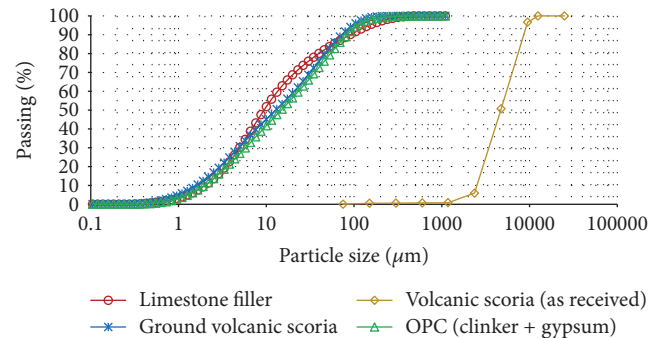


FIGURE 4: Particle size distribution of the materials used in the experimental part.

binder paste specimens have been determined in accordance with EN 196-3. Six-halved specimens obtained from the three mortar specimens used in the flexural strength tests have been tested for the determination of compressive strength of mortars under the same laboratory conditions as those applied in the flexural strength test. The compressive and flexural strength development was determined on 40 × 40 × 160 mm prismatic specimens, in accordance with EN 196-1, at ages of 2, 7, 28, and 90 days, respectively. The values reported in the results represent the average of six readings for compressive strength test and the average of three readings for all other tests.

2.7. Acid Attack Test. The relative acid resistance has been determined in accordance with ASTM C267 (2001). The aggressive acid environmental condition was simulated using 5% sulfuric acid (H₂SO₄) of pH ~ 0.5. The 28 days' cured

TABLE 1: Chemical composition of the materials used in the study.

Chemical composition (%)	Cementitious materials		
	OPC (clinker + gypsum)	Volcanic scoria	Limestone filler
SiO ₂	19.57	44.91	1.57
Al ₂ O ₃	4.86	16.98	0.69
Fe ₂ O ₃	3.50	8.64	0.33
CaO	62.21	9.39	54.37
MgO	2.78	8.87	0.43
SO ₃	2.12	0.01	0.01
Loss on ignition (LOI)	1.36	0.36	42.22
Na ₂ O	0.22	2.76	0.02
K ₂ O	0.34	1.75	0.01
TiO ₂	0.6	0.9	0.07
Cl ⁻	0.03	—	0.01
Insoluble residue	1.67	5.01	—
Total	99.26	99.58	99.73
Pozzolan activity index (ASTM C618)		78 (at 7 days)	
		89 (at 28 days)	
Main compounds of ordinary Portland cement calculated according to Bogue's formulas			
C ₃ S	60.82		
C ₂ S	10.22		
C ₃ A	6.96		
C ₄ AF	10.65		

TABLE 2: Mixtures used in the experimental investigation.

Mix type	Sample mixture (%)		
	Clinker + gypsum	Limestone filler (LF)	Volcanic scoria (VS)
VS0LF0	100	0	0
VS0LF5	95	5	0
VS0LF10	90	10	0
VS0LF15	85	15	0
VS10LF0	90	0	10
VS10LF5	85	5	10
VS10LF10	80	10	10
VS10LF15	75	15	10
VS20LF0	80	0	20
VS20LF5	75	5	20
VS20LF10	70	10	20
VS20LF15	65	15	20
VS30LF0	70	0	30
VS30LF5	65	5	30
VS30LF10	60	10	30
VS30LF15	55	15	30



FIGURE 5: Photo of the Plexiglas containers with immersed mortar specimens.

mortar cubes were immersed in the aggressive acid environment for 90 days. The Plexiglas containers with immersed mortar specimens were kept covered throughout the testing period to minimize the evaporation, as shown in Figure 5. At 2, 7, 14, 28, 56, and 90 days of exposure, the mortar specimens were cleaned with distilled water; then the acid resistance was evaluated through measurement of the weight loss of the specimens determined as follows:

$$\text{Weight loss (\%)} = \left[\frac{(W_1 - W_t)}{W_1} \right] \times 100, \quad (1)$$

where W_1 is the weight (grams) of the specimens before immersion and W_t is the weight (grams) of cleaned specimens after t day immersion. The average weight losses for each mortar specimens have been reported.

2.8. Concrete Permeability. Concrete permeability measured in terms of depth of water penetration has been carried out as per the standard EN 12390-8. The results shown in this paper are the average penetration depth.

3. Results and Discussion

3.1. Properties of Volcanic Scoria and Limestone Filler. As seen from Table 1, volcanic scoria is considered as suitable material for use as cement replacement. It satisfied the standards requirements for such a material by having a combined SiO_2 , Al_2O_3 , and Fe_2O_3 of more than 70%, a SO_3 content of less than 4%, and a loss on ignition of less than 10% (ASTM C618:2001). $\text{SiO}_{2\text{reactive}}$ content is more than 25%, as well (EN 197-1). In addition, it has a strength activity index with PC higher than the values specified in ASTM C618 (2001).

The chemical composition of limestone filler has been found to be 55% CaO (CaCO_3 ratio is about 97%) with a loss on ignition value of 43%. Furthermore, some impurities such as MgO, Fe_2O_3 , SO_3 , SiO_2 , and Al_2O_3 have been determined where their total amount is about 3%. The total organic content and clay content of the studied limestone have been

determined as 0.36% and 0.56%, respectively. According to EN 197-1 standard, it is possible to classify these cements as CEM II/A-L (group L: TOC is between 0.5% and 0.2%). In addition, according to this standard, the CaCO_3 ratio of limestone employed in the production of blended cement should be at least 75%, and the clay content of limestone should not exceed 1.2%. Based on the analysis results, the studied limestone can be used as ingredient in cement production.

3.2. Physical Properties of Binder Pastes

3.2.1. Water Requirements. The results of water requirements are given in Figure 6(a). Binary binders containing VS have, to some extent, a greater water demand. However, as it can be seen from Figure 6(a), there is no significant change in the water content even for the binder containing 30% VS which increased only by less than 3% compared to CEM I. This could be explained by the lubricant effect of natural pozzolan on paste when finely divided [1, 18] and the effect of VS shape which was characterized by shape-edged grain [19]. The limestone filler, despite its higher fineness, generally demands less water than the corresponding pure cement. This is due to the wider particle size distribution of limestone filler [20]. The particle size distribution of the clinker, which is harder to grind, is narrower, with a slope equal to 0.88 on a Rosin-Rammler diagram, as shown in Figure 6(b). That of the more easily ground limestone, on the other hand, is wider, with a slope of 0.69. These results are in good agreement with those reported by Sprung and Siebel [21]. Further, no significant change in water demand was observed in the ternary binders as compared with the control.

3.2.2. Setting Times. Figure 7 illustrates the setting times of the control paste and pastes containing VS, LF, or both. The results showed that the setting times slightly increased with VS replacement level. This could be due to the increase of water demand [7, 22] and the pozzolanic reaction between the glassy phase in VS and CH liberated during hydration of C_3S and C_2S of clinker, which is, usually, slower than the hydration of cement [7].

The initial setting times, by contrast, decreased with the increase of LF replacement ratio indicating the acceleration effect of CaCO_3 on the hydration of C_3A to form sulfoaluminate and of C_3S to form CSH and CH in cement. The acceleration of setting times reached a maximum of 50 min when 5% LF was used. This is in well agreement with the results reported by Kenai et al. [23]. The influence of adding LF can easily be seen in Figure 7. While VS30LF0-based paste has initial setting time of 194 min, the VS30LF5- and VS30LF10-based pastes showed a significant reduction in initial setting times of about 17 and 23 min, respectively.

It is worthwhile to note that all the investigated binders are seen to comply with the standard requirements (initial setting time ≥ 45 min and final setting time ≤ 420 min) according to ASTM C595.

A plot of the initial setting time against the final setting time for the whole tested samples as shown in Figure 8 indicates that there is a strong correlation between the parameters as the coefficient of determination (R^2) was calculated to be

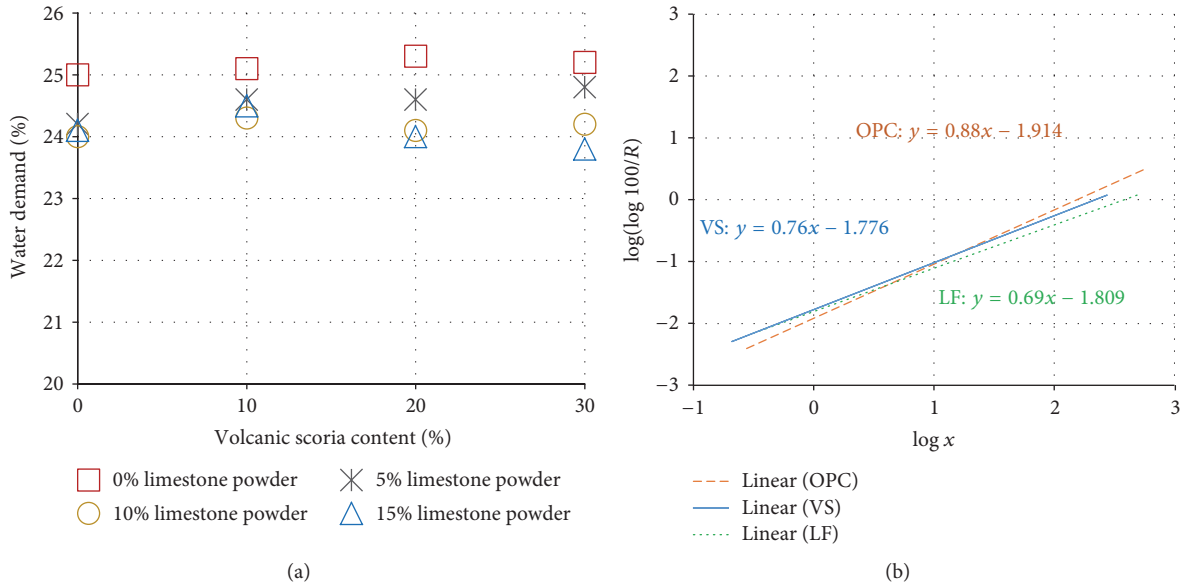


FIGURE 6: Water demand of the investigated binder pastes and Rosin-Rammler diagram. (a) Water demand of the investigated pastes. (b) Rosin-Rammler diagram (x : particle size; R : cumulative retained).

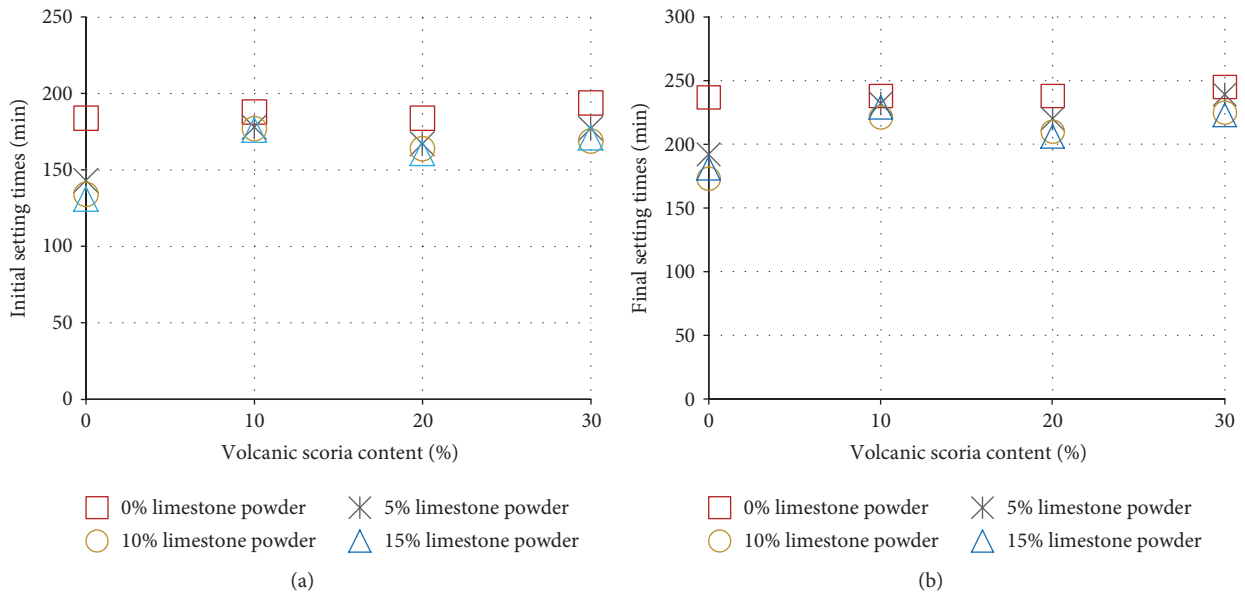


FIGURE 7: Initial and final setting times of the investigated binder pastes. (a) Initial setting times of the investigated pastes; (b) final setting times of the investigated pastes.

0.95. A strong relationship exists between two variables when $R^2 \geq 0.85$ [24]. Thus, an estimate of the final setting time can be predicted from (2) when the initial setting time has been obtained.

$$FST = 1.14IST + 27.43 \quad (R^2 = 0.95), \quad (2)$$

where FST is final setting time (min) and IST is initial setting time (min).

3.2.3. *Soundness.* According to the experimental results of volume stability determined by the Le Chatelier accelerated test, the soundness of all studied binders was satisfactory. It can be said that most of them recorded values of less than 0.5 mm which is much less than the maximum value of 10 mm allowed by En 197-1. Interpretation of these results is currently beyond the author’s understanding and needs further investigation. Nevertheless, these results could be attributed, to some extent, to the reduction in CaO_{free} and $MgO_{reactive}$ compounds which create the swelling effect.

TABLE 3: Compressive strength development of mortars.

Mix type	Compressive (f_{cm}) strength of mortars (MPa), normalized			
	2 days' curing	7 days' curing	28 days' curing	90 days' curing
VS0LF0	20.6–100%	39.6–100%	48.7–100%	54.9–100%
VS0LF5	20.5–100%	38.9–98%	48.9–100%	54.5–99%
VS0LF10	19.9–97%	37.1–94%	46.6–96%	52.8–96%
VS0LF15	14.8–72%	32.6–82%	44.1–91%	49.1–89%
VS10LF0	16.2–79%	32.1–81%	45.9–94%	54.2–99%
VS10LF5	15.7–76%	31.7–80%	45.5–93%	53.4–97%
VS10LF10	14.6–71%	29.1–73%	42.1–86%	50.5–92%
VS10LF15	10.4–51%	27.3–69%	36.8–76%	45.4–83%
VS20LF0	11.9–58%	28.9–73%	39.1–81%	49.1–89%
VS20LF5	11.9–58%	28.0–71%	37.9–78%	48.2–88%
VS20LF10	11.6–56%	27.6–70%	37.5–77%	48.1–88%
VS20LF15	8.8–43%	23.1–58%	33.5–69%	43.3–79%
VS30LF0	8.3–40%	24.1–61%	34.4–71%	47.8–87%
VS30LF5	8.4–41%	23.3–59%	33.5–69%	44.2–81%
VS30LF10	7.8–38%	21.8–55%	31.4–64%	42.3–77%
VS30LF15	6.9–34%	18.6–47%	26.8–55%	38.8–71%

TABLE 4: Compressive strength development of concrete.

Mix type	Compressive (f_c) strength of concrete (Mpa), normalized			
	2 days' curing	7 days' curing	28 days' curing	90 days' curing
VS0LF0	18.1–100%	34.3–100%	42.1–100%	47.9–100%
VS0LF5	18.2–101%	34.2–100%	41.3–98%	46.5–97%
VS0LF10	17.8–98%	33.3–97%	40.0–95%	45.5–95%
VS0LF15	13.3–73%	27.2–79%	35.9–85%	49.1–86%
VS10LF0	14.6–80%	28.1–82%	40.1–95%	46.9–98%
VS10LF5	13.9–77%	28.0–82%	39.4–94%	46.0–96%
VS10LF10	13.2–73%	26.0–76%	36.8–87%	43.2–90%
VS10LF15	9.7–54%	22.7–66%	31.3–74%	37.8–79%
VS20LF0	10.5–58%	23.3–68%	34.2–81%	43.7–91%
VS20LF5	10.8–60%	24.7–72%	34.5–82%	43.6–91%
VS20LF10	10.7–59%	23.4–68%	33.7–80%	43.1–90%
VS20LF15	8.1–45%	19.0–55%	30.4–72%	38.6–81%
VS30LF0	7.7–43%	20.6–60%	32.3–77%	47.8–89%
VS30LF5	7.7–43%	19.3–56%	30.3–72%	40.1–84%
VS30LF10	7.4–41%	17.6–51%	29.1–69%	38.6–81%
VS30LF15	6.7–37%	14.9–43%	24.9–59%	35.6–74%

3.3. Mechanical Strengths of Mortars/Concrete

3.3.1. Compressive Strength of Mortars/Concrete. The results of compressive strength development for all mortar/concrete mixes containing varying amounts of VS, LF, or both are given in Tables 3 and 4, respectively. As expected, all mortars/concrete show an increase in strength with curing time. Mortar/concrete specimens containing CEM I have almost higher compressive strengths at any curing time compared to binary or ternary binders. Also, it is seen that the compressive strength of mortars/concrete containing VS decreases with the replacement level for all curing times. For instance, the compressive strength of plain mortars and

mortars containing 30% VS after 7 days' curing decreased from 39.6 to 24.1 MPa, respectively. This could be explained by (i) the reduction of cement content in the mix with the increase of VS content, that is, the dilution effect [25], and (ii) the slowness of the pozzolanic reaction between the glassy phase in VS and the CH released during cement hydration. However, due to the continuation of this reaction and the formation of a secondary CSH, a greater degree of hydration is achieved resulting in strengths after 90 days' curing which are comparable to those of plain mortars [1]. For instance, the compressive strength of VS30LF0-based mortar was found to be 39% lower than plain mortar at 7 days' curing, but this reduction was only 13% after 90 days' curing. The significant

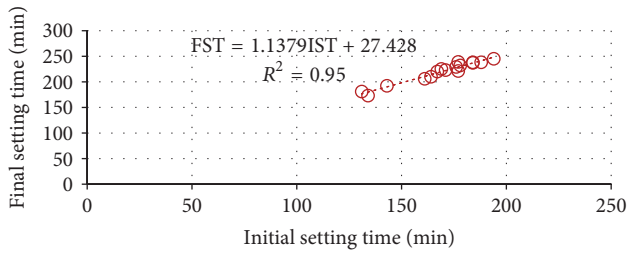


FIGURE 8: Correlation between initial and final setting times of the investigated binders.

gain in strength in mortars containing VS occurred when moving from 28 to 90 days' curing times while in plain mortar specimens this was noted during the first 28 days. This could be explained by the slow pozzolanic reaction and its progress with age in VS-based binder mortars.

The strengths of mortars containing LF were not affected by replacement of cement with LF content up to 10%. The early strength was improved by substituting 5% LF while after 90 days of curing the strength of mortars prepared with 5% LF was slightly lower than those prepared without LF. The increase in the early strength of the mortar due to the addition of 5% LF can be attributed to its active participation in cement hydration and filler effect of the fine particles of LF [13]. The additional surface area supplied by the limestone particles may provide sites for the nucleation and growth of hydration products that leads to further increase in strength [13, 26]. Further, despite the fact that the limestone filler has no pozzolanic property (i.e., it does not produce CSH) [27, 28], limestone particles contribute to the strength development by forming new hydration products like carboaluminate phases and by reducing the pore ratio [26]. According to Vuk et al. [29], Schmidt [30], and Voglis et al. [31], early strength increased with the use of 5% limestone; however, later strengths either remained the same or decreased relatively to the control. When LF is included in large quantities (15%) it acts as a diluent, so that strengths are lower than for comparable Portland cements. This is consistent with the findings reported by Sprung and Siebel [21] and Celik et al. [32].

The positive effect of adding LF on the early strength of 2 days' cured mortar can easily be seen in Table 3. For instance, the compressive strength increased from 8.3 MPa to 11.6 MPa when replacing 10% VS by 10% LF in the VS30LF0 mix and from 11.9 MPa to 14.6 MPa when replacing 10% VS by 10% LF in the VS20LF0 mix. On the other hand, the positive effect of VS on the later-age strength can also be observed from Table 3. For instance, replacing 10% LF by 10% VS in the VS0LF15 resulted in an increase in compressive strength by about 8%. This substitution confirmed the contribution of VS in the strength development through the pozzolanic reaction. Such positive synergy with regard to mechanical strength of concrete has also been reported by other researchers who studied ternary blended mixtures of OPC, limestone powder and fly ash, metakaolin, slag, or natural pozzolan [9, 28, 33–38].

Further, an interesting result has also to be reported. The binder containing 20% VS has compressive strengths similar

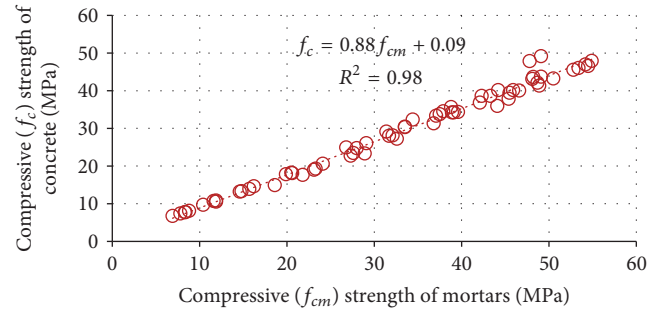


FIGURE 9: Correlation between the compressive strength of concrete and that of mortar of the same w/b ratio.

to that containing 20% VS and 5 or 10% LF. This means that replacing 5 or 10% of OPC with 5 or 10% LF does not impair the compressive strength even at later ages. The result shows that the cement producers could burn 5 or 10% less clinker and instead add LF. This is both economically and ecologically beneficial, as less energy is needed and less CO₂ will be emitted.

Strength of concrete is commonly considered its most valuable property, although, in many practical cases, other characteristics, such as durability and permeability, may in fact be more important [39]. Compressive strengths of concrete presented in Table 4 have a trend similar to that noted in mortars. The correlation between the compressive strength of VS-based mortars and the compressive strength of VS-based concrete is given in Figure 9. The compressive strength of VS-based concrete seems to have a close relationship with that of volcanic-scoria-based mortars. A linear regression analysis was conducted to determine the best-fit relationship between all the measured compressive strengths of mortars and concrete for all curing times. The following linear equation was derived based on the analysis with a regression coefficient of 0.98:

$$f_c = 0.88f_{cm} + 0.09, \quad (3)$$

where f_c , f_{cm} are compressive strength of concrete and mortars in MPa, respectively. So, the compressive strength of concrete at a given curing time can be predicted from a knowledge of the compressive strength of mortar prepared with the same w/b ratio. This linear equation is in good agreement with that reported by Neville [39] for plain mortar and concrete. Such similar relationships may need to be developed for other types of aggregates, different w/c ratios, and other curing conditions.

3.3.2. Flexural Tensile Strength of Mortars. Results of flexural tensile strength of the prisms prepared from the produced binder mortars and cured in water until the test dates are arranged in Table 5. The values given in Table 5 show the average of flexural tensile strength for 3 samples. A similar trend to that observed for compressive strength seems to be followed by the flexural strength results. However, the results show that flexural strength is less sensitive than the compressive strength to the addition of VS, LF, or both.

TABLE 5: Flexural strengths of the investigated mortars after various curing times.

Mix type	Flexural strength (MPa)			
	2 days' curing	7 days' curing	28 days' curing	90 days' curing
VS0LF0	4.8	6.8	7.6	8.1
VS0LF5	3.8	6.4	8	8
VS0LF10	3.5	6.9	7.7	7.6
VS0LF15	2.7	6.1	7.1	7.8
VS10LF0	4.3	5.9	7.4	7.8
VS10LF5	3.6	5.5	7.2	7.6
VS10LF10	3.8	6.0	7.1	7.6
VS10LF15	2.3	5.4	6.5	7.2
VS20LF0	2.8	5.4	6.8	7.3
VS20LF5	3.5	5.1	7.1	7.5
VS20LF10	2.7	5.4	6.7	7.4
VS20LF15	2.2	4.7	6.5	7.5
VS30LF0	2.2	4.9	6.4	7.4
VS30LF5	2.1	4.1	6.3	7.4
VS30LF10	2.2	4.4	6.6	7.3
VS30LF15	1.8	3.8	5.6	7.2

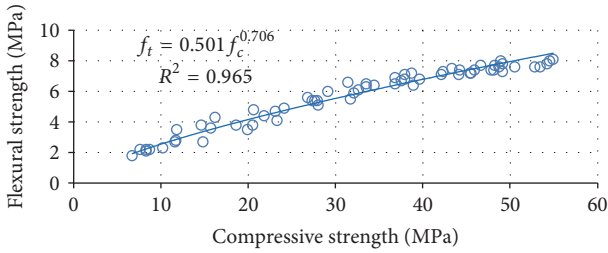


FIGURE 10: Correlation between flexural and compressive strength of the investigated mortars.

3.3.3. *Correlation between Compressive and Flexural Strength of Mortars.* The correlation between the flexural strength and the compressive strength results were calculated for the entire population of mortar test results as shown in Figure 10, and hence the relation obtained is

$$f_t = 0.5 (f_c)^{0.7} \quad (4)$$

with a correlation factor (R^2) of 0.97. So, knowing the compressive strength f_c of mortar, the flexural strength f_t can be predicted using (4). This relation is similar to those reported in the literature [39].

3.3.4. *Correlation between Mechanical Strengths and Supplementary Materials Content.* According to the test results, the mechanical strength of mortars containing VS, LF, or both seems to have a close relationship with the content of these additions. For each testing age, linear regression analysis was conducted to determine the best-fit relationship between measured mechanical strengths (compressive and flexural strengths) for all mixtures prepared according to the experimental design and the varying parameters. The independent variables of VS percentage and LF percentage

were employed in the following two estimation equations (5) derived by the authors:

$$f_c; f_t = a_1 + a_2 \times VS + a_3 \times LF + a_4 \times VS \times LF, \quad (5)$$

where f_c, f_t are compressive and flexural strength of mortars in (MPa), respectively; VS is the volcanic scoria content; LF is the limestone filler content; a_1, a_2, a_3, a_4 are constants. So, the compressive and flexural strengths of mortars at a given curing time can be predicted from knowledge of VS content and LF content.

Table 6 presents the constants (a_1, a_2, a_3, a_4) with regression coefficients (R^2) of the correlation between the experimental data and the proposed equation. However, it should be emphasized that additional factors including the type of natural pozzolan or limestone, composition and strength of clinker, w/b ratio, and fineness of the mix ingredients may also be important parameters.

From the values shown in Table 6, it should be noted that the highest R^2 values were found in the correlation between compressive strengths and the supplementary materials contents.

Generally, as can be seen from the correlation values, the predicted values were in good agreement with the measured values obtained in the study.

3.4. *Acid Attack.* Most investigations have considered weight loss as acceptable indicator for evaluating the resistance of concrete to acid attack. Weight change was determined for all mortars stored in 5% sulfuric acid solution. The results of weight losses of 28 days' cured mortar specimens according to exposure time are presented in Figure 11.

As expected, the acid resistance of the mortars improves with increasing the replacement level of VS. All mortars containing VS had lower weight loss than the control mortar at the ages of 2, 7, 14, 28, 56, and 90 days. This improvement

TABLE 6: Constants a_1 , a_2 , a_3 , and a_4 and regression coefficient (R^2) of the correlation between the experimental data and the proposed equations.

Curing time (day)	Mechanical strength	a_1	a_2	a_3	a_4	R^2
2	f_c	21.5	-44	-40.1	94.8	0.927
	f_t	4.9	-8.5	-13.9	39.4	0.856
7	f_c	39.3	-51.1	-41.7	35	0.959
	f_t	6.7	-6.6	-2.2	-10	0.914
28	f_c	50.3	-51.1	-39.9	-18.6	0.958
	f_t	7.9	-4.5	-4.2	1.2	0.811
90	f_c	56.5	-29.7	-42	-37	0.930
	f_t	8	-2.4	-2.9	8.2	0.671

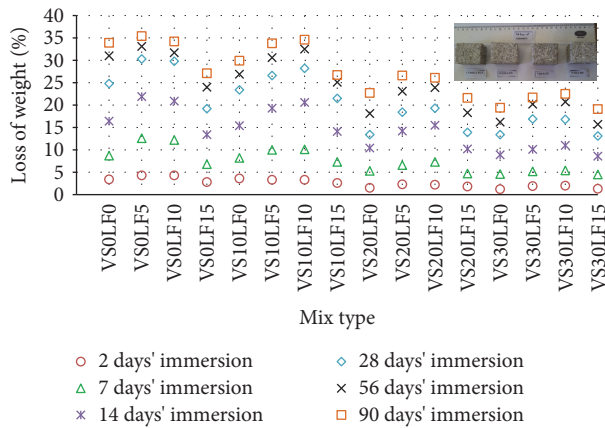


FIGURE 11: Weight losses over time of 28 days' cured mortars immersed in 5% H_2SO_4 .

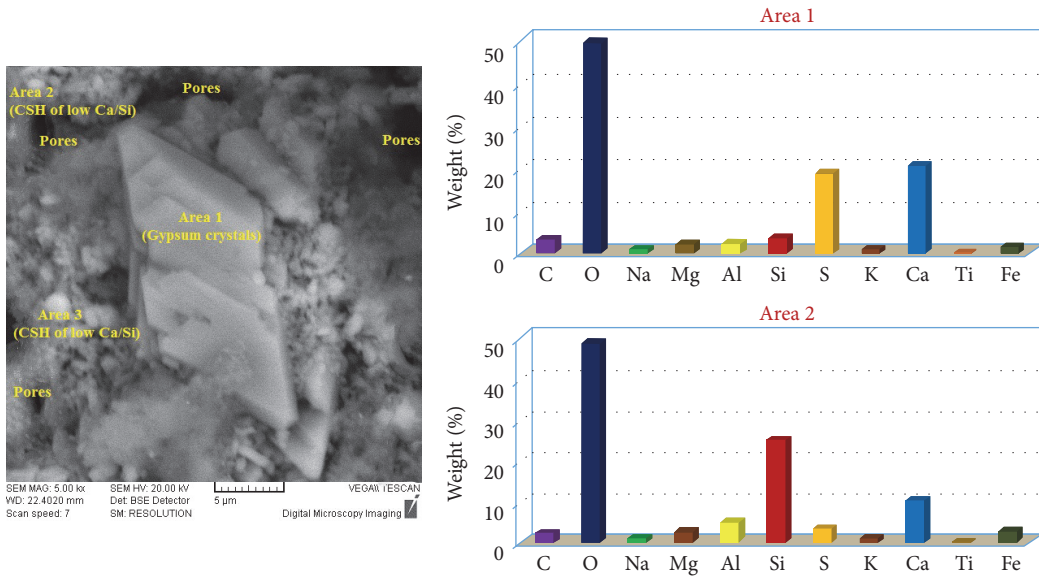
of acid resistance is higher at early ages and decreases with increasing the immersion time. The weight loss of the mortars containing 30% VS was much less than half of the weight loss of plain mortar at the first 2 and 7 days of exposure. The better performance of VS-based cements can be due to the pozzolanic reaction [40, 41]. This reaction between VS and calcium hydroxide liberated during the hydration of cement led to a refinement of the pore structure resulting in a highly impermeable matrix [1, 40, 41]. This was confirmed by the results of concrete permeability test. The pozzolanic reaction also fixes $Ca(OH)_2$, which is usually the most vulnerable product of hydration of cement in so far as acid attack is concerned [39]. In addition, as highly alkaline cements are good willing partners for acid attack [42], replacing a portion of cement with a less-alkaline pozzolanic material decreases the total amount of the present alkali. Further, pozzolans react with calcium hydroxide to form calcium silicate hydrate with a low CaO/SiO_2 ratio. The creation of calcium aluminate hydrates (CASH-ASH, CAH) in the VS-based mortar also contributes in increasing the chemical resistance of such a mortar. It is believed that CAH may be more chemically stable in highly acidic environments than CSH [43, 44].

Mortars containing up to 10% limestone filler showed higher loss of weight values at all immersion times. This could be due to the presence of calcium carbonate, $CaCO_3$, the main compound in the limestone, which easily suffers

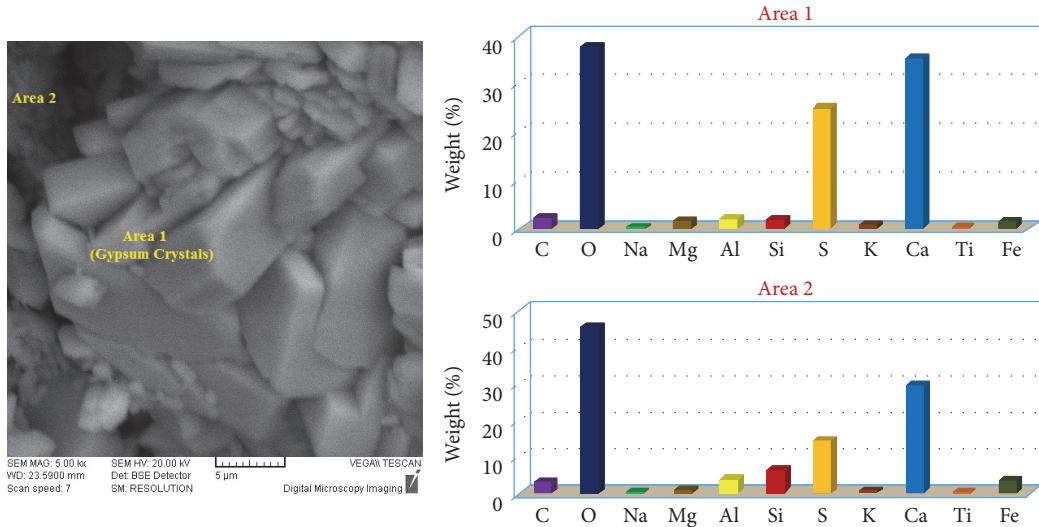
from acid attack. This result, which is in good agreement with the result of Bassuoni et al. (2007) [45], can also be attributed to the highly aggressive sulfuric acid solution (i.e., 5% concentration) and the relatively high fineness of LF (i.e., $4100 \text{ cm}^2/\text{g}$). As clearly seen in Figure 12(a), after 14 days of exposure to 5% H_2SO_4 , the deteriorated VS0LF5-based mortar showed a structure of relatively high porosity with some crystals of gypsum and CSH phases of low Ca/Si ratio. This relatively low ratio, according to the authors, might be due to the partial decalcification of CSH.

However, contrary to expectation, the weight loss of mortars containing 15% limestone filler was much less than the plain mortar when exposed to 5% H_2SO_4 . Moreover, the better performance with regard to the sulfuric acid resistance was noted when adding 15% LF to the VS-based mortars. This can be attributed to the following main factors: (i) LF was finer than OPC. It filled the micropores in mortar and the ability of mortar to resist acidic attack was improved by the reduced permeability and porosity, (ii) the presence of high calcium carbonate ($CaCO_3$) content increased the capacity of limestone mortars to consume more aggressive acid, (iii) the decreased proportion of cement reduced the portlandite (CH) content, (iv) addition of calcium carbonate will bring the calcium and thus maintain the protection of CSH of decalcification [46], (v) as LF content of 15% is the highest, a lot of gypsum from reaction between $CaCO_3$ and sulfuric acid will form [47]. This layer of gypsum can be capable of retarding the deterioration process by acting as a surface sealing layer [48]. Moreover, this layer has very low solubility in water [49]. This result was confirmed by SEM and EDX analysis, as shown in Figure 12(b), and (vi) carbonate ions from limestone compete against sulfate ions to react with C3A of cement [50]. As generally expected, none of the binders used can provide a long-term resistance when exposed to strong acids.

3.5. Water Permeability of Concrete. Permeability of concrete to water is closely related to the durability of concrete. Water penetration depth can be considered as an indication of permeable and impermeable concrete [39]. A depth of less than 50 mm classifies the concrete as impermeable and a depth of less than 30 mm as impermeable under aggressive conditions [39]. Figure 13 shows the water penetration depth test results for all binder types. Concrete containing VS-, LF-, or VSLF-based binders is supposed to have lower



(a) SEM and EDX of VS0LF5-based mortar after 14 days of exposure to 5% H₂SO₄



(b) SEM and EDX of VS30LF15-based mortar after 14 days of exposure to 5% H₂SO₄

FIGURE 12: SEM and EDX of (a) VS0LF5-based mortar and (b) VS30LF15-based mortar after 14 days of exposure to 5% H₂SO₄.

permeability than CEM I concrete. But in this research, it has been observed that, after 2-day curing, water penetration depth of 10% VS-based concrete was higher than that of CEM I. Increasing the moist-curing period of concrete from 28 to 90 days' reduced water penetration depths of all VS-based concrete. No concrete was found to be impermeable under aggressive conditions, before 28-day curing. The only mix that can be considered as impermeable under aggressive environments after 28-day curing, according to Neville [39], is VS30LF15-based concrete. However, all concrete containing VS contents $\geq 20\%$ and LF contents $\geq 5\%$ recorded water penetration depths less than 30 mm. This can be attributed to the filling effect of limestone filler and the pozzolanic reaction of volcanic scoria.

3.6. Microstructure Observations of the Hydration Products. Fragments of VS0LF0-, VS30LF0-, VS0LF15-, and VS30LF15-based paste specimens broken off and washed with acetone were examined and analyzed by SEM and EDX techniques. Figures 14, 15, 17, and 18 present the SEM photos and the EDX analysis of the studied pastes after 28 days' curing. The effect of adding limestone filler is clearly seen in modifying the microstructure of plain and VS-based pastes.

As shown in Figure 14, the SEM and EDX microanalysis of VS30LF0-based paste showed a very dense structure and indicated that the examined fractured sections mainly consist of CSH and CASH-ASH phases with very low CH content which might be consumed through the pozzolanic reaction. Different phases, by contrast, were detected when adding 15%

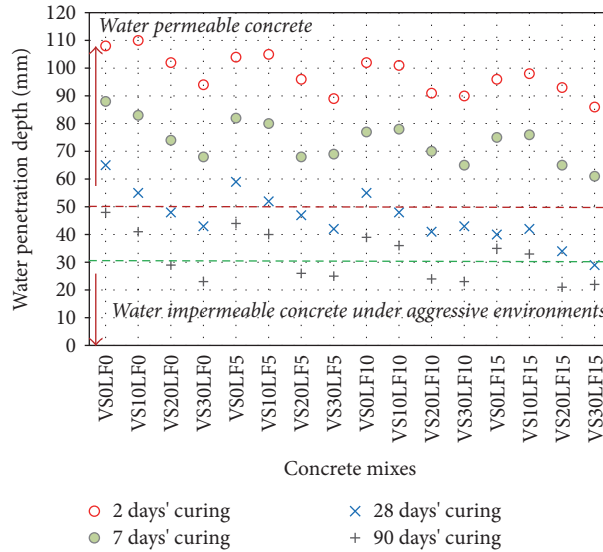


FIGURE 13: Water penetration depths measured in different concrete mixes cured for 2, 7, 28, and 90 days.

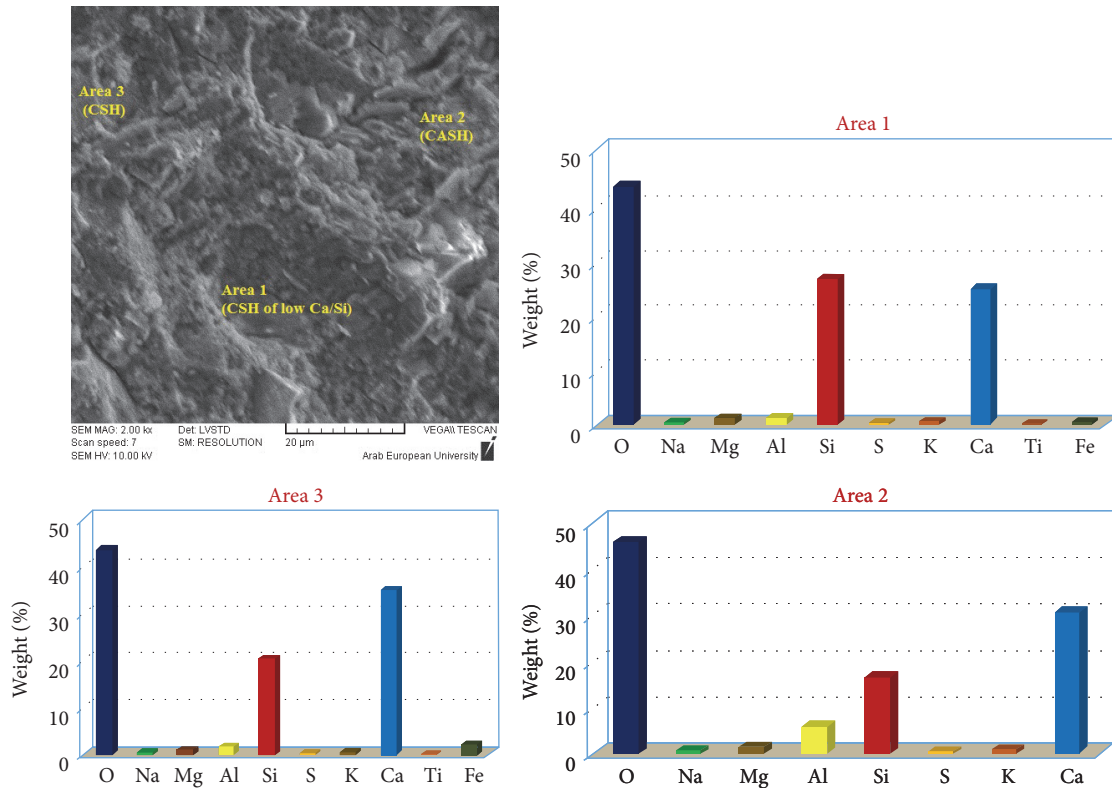


FIGURE 14: SEM and EDX analysis of 28 days' cured VS30LF0-based paste.

LF, as seen in Figure 15. EDX analysis of VS30-LF15-based paste showed major elements such as Ca, O, Si, C, and Al confirming the identification of carboaluminate hydrate and CSH formation. This, which was further confirmed by XRD analysis, as shown in Figure 16, is in agreement with the results reported in the literature [9, 31, 51]. Presence of LF could also fill the pores between the cement particles due to the formation of carboaluminate phases.

On the other hand, in Figure 17 a large number of needle-like crystals of ettringite in VS0LF15 can be seen. This confirms that limestone filler seems to stabilize ettringite as reported by other researchers [9, 11, 13]. This also confirms the role of limestone filler in chemically interacting with the aluminate phases in cement to stabilize a carboaluminate phase at the expense of monosulfoaluminate [13]. In addition, this action can increase the quantity of ettringite formed

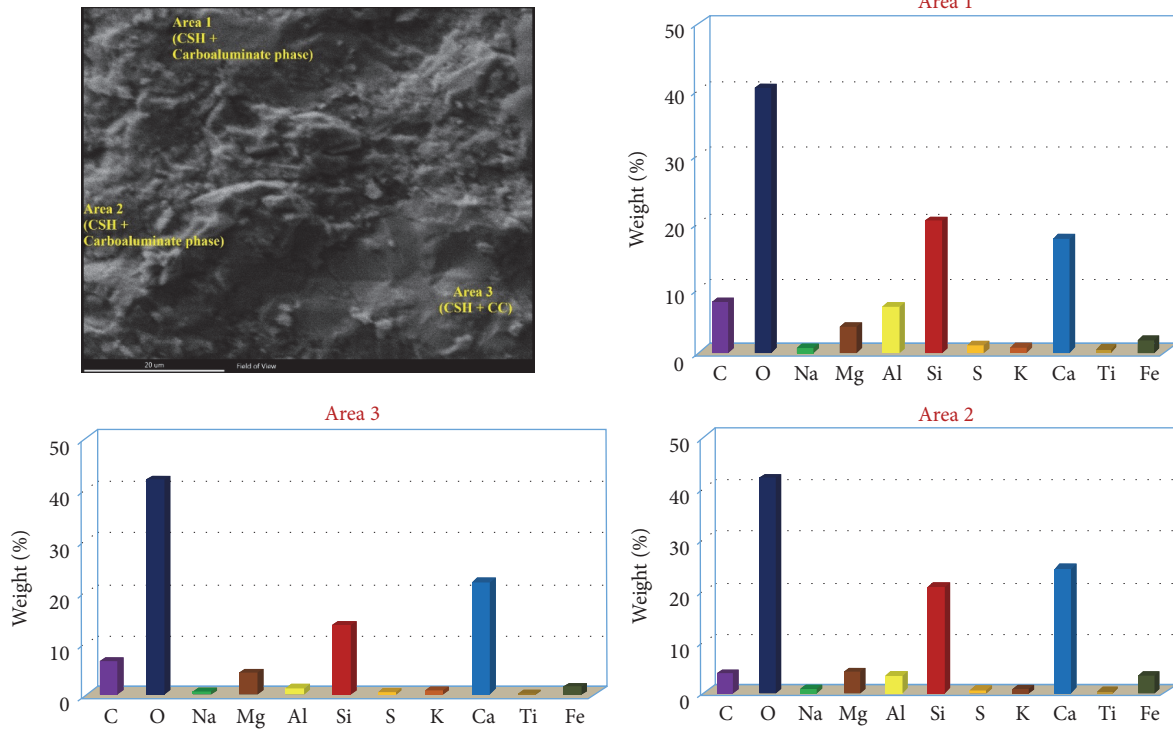


FIGURE 15: SEM and EDX analysis of 28 days' cured VS30LF15-based paste.

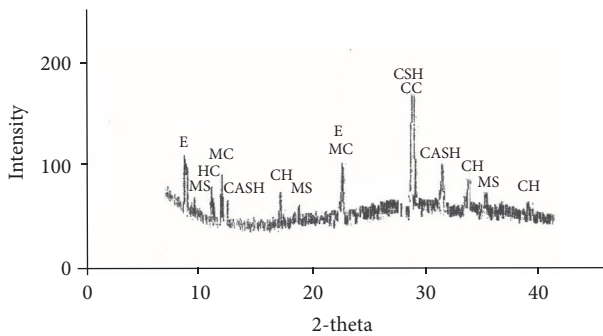


FIGURE 16: XRD of 28 days' cured VS30LF15-based paste (E: ettringite; MS: Monosulfate; HC: hemicarboaluminate; MC: monocarboaluminate; CH: calcium hydroxide; CSH: calcium silicate hydrates; CASH: calcium aluminate silicate hydrates; CC: calcium carbonate).

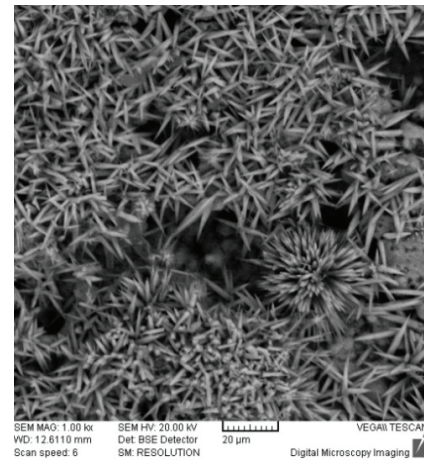


FIGURE 17: SEM of 28 days' cured VS30LF15-based paste.

which leads to an increase in solid volume and thus decreased porosity and slightly improved mechanical strength [9]. Further, as clearly seen in Figure 18, darker areas were more frequent in case of VS0LF0-based paste, indicating its higher porosity when compared with the others.

4. Conclusions

From the experimental results, the following conclusions could be drawn:

(i) The compressive strength of mortar/concrete containing VS-based binders was lower than that of plain cement mortar at all ages. At early ages, the mortars containing 30%

VS had compressive strengths much lower than that of plain cement mortar. However, after 90 days' curing, the compressive strengths of VS-based mortars were comparable to those of plain cement mortar. Adding up to 10% LF content, by contrast, develops almost the same compressive strength as the corresponding plain cement.

(ii) The negative effect of VS on the early strength of mortars can be compensated by using LF, while the negative effect of LF on the compressive strength of mortars at later ages can be compensated by using VS. This positive synergy effectively counters the dilution effect on the strength performance of blended cements. So, it is expected that the future

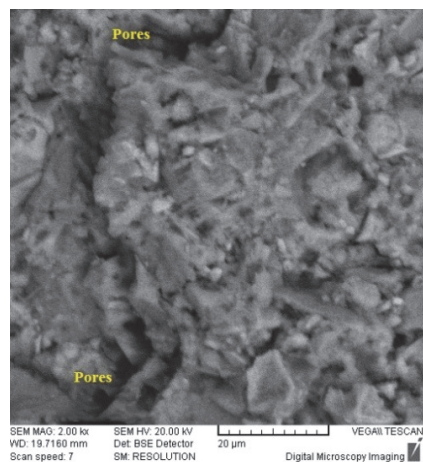


FIGURE 18: SEM of 28 days' cured VSOLF0-based paste.

world production and use of ternary blended cements will significantly be extended.

(iii) A strong correlation was observed between the compressive strength of concrete and that of mortars with a similar w/b ratio, such that one can be estimated from knowledge of the other.

(iv) Limestone filler is not solely an inert additive; CaCO_3 reacts with aluminates to form carboaluminate phases. This has been confirmed by the results obtained and the microstructural analysis.

(v) Results of loss in weight after (H_2SO_4) acidic exposure indicate generally superior performance of VS-based mortars and inferior performance of LF-based mortars compared to the respective control mortar. However, adding LF in a significant quantity (15%) considerably improved sulfuric acid resistance of the mortars investigated.

(vi) Based on the results obtained, the authors derived an estimation equation of both compressive and flexural strength development incorporating the effects of VS and LF contents at a given curing time. The mechanical strength of mortar containing VS, LF, or both could be adequately predicted using (5). Development of such a good relationship between mechanical strengths and the supplementary cementing materials could be of considerable benefit. However, more parameters such as type and fineness of the materials used and w/b ratio should be taken into consideration.

(vii) Water permeability of VSOLF0-based concrete mixes was much lower than those of either plain concrete or VS-based concrete, especially at longer curing time and high replacement levels. This has also been confirmed by SEM/EDX analysis.

(viii) Use of ternary cements containing an adequate combination of limestone filler and volcanic scoria can lead to an efficient use of natural resources, saving energy consumption and reducing gaseous emissions without compromising the mechanical properties of cement. So, production of a green concrete could be promoted.

Conflicts of Interest

The authors declare no conflicts of interest.

Acknowledgments

The authors gratefully acknowledge the technical and financial support of this research from Damascus University. Thanks are also expressed to Eng. Amjad Bernieh (Lafarge Co.) and Professor Tamer al-Hajeh, Vice-President of AIU, for their appreciated help.

References

- [1] A. M. al-Swaidani and S. D. Aliyan, "Effect of adding scoria as cement replacement on durability-related properties," *International Journal of Concrete Structures and Materials*, vol. 9, no. 2, pp. 241–254, 2015.
- [2] N. Kouloumbi, G. Batis, and P. Pantazopoulou, "Efficiency of natural Greek pozzolan in chloride-induced corrosion of steel reinforcement," *Cement, Concrete and Aggregates*, vol. 17, no. 1, pp. 18–25, 1995.
- [3] M. I. Khan and A. M. Alhozaimy, "Properties of natural pozzolan and its potential utilization in environmental friendly concrete," *Canadian Journal of Civil Engineering*, vol. 38, no. 1, pp. 71–78, 2011.
- [4] M. R. Moufti, A. A. Sabtan, O. R. El-Mahdy, and W. M. Shehata, "Assessment of the industrial utilization of scoria materials in central Harrat Rahat, Saudi Arabia," *Engineering Geology*, vol. 57, no. 3–4, pp. 155–162, 2000.
- [5] G. K. Al-Chaar, M. Alkadi, and P. G. Asteris, "Natural pozzolan as a partial substitute for cement in concrete," *The Open Construction & Building Technology Journal*, vol. 7, pp. 33–42, 2013.
- [6] Y. Senhadji, G. Escadeillas, H. Khelafi, M. Mouli, and A. S. Benosman, "Evaluation of natural pozzolan for use as supplementary cementitious material," *European Journal of Environmental and Civil Engineering*, vol. 16, no. 1, pp. 77–96, 2012.
- [7] A. M. al-Swaidani, S. D. Aliyan, and N. Adarnaly, "Mechanical strength development of mortars containing volcanic scoria-based binders with different fineness," *Engineering Science and Technology, an International Journal*, vol. 19, no. 2, pp. 970–979, 2016.
- [8] C. Shi, "An overview on the activation of reactivity of natural pozzolans," *Canadian Journal of Civil Engineering*, vol. 28, no. 5, pp. 778–786, 2001.
- [9] K. De Weerd, K. O. Kjellsen, E. Sellevold, and H. Justnes, "Synergy between fly ash and limestone powder in ternary cements," *Cement and Concrete Composites*, vol. 33, no. 1, pp. 30–38, 2011.
- [10] V. Bonavetti, H. Donza, V. Rahhal, and E. Irassar, "Influence of initial curing on the properties of concrete containing limestone blended cement," *Cement and Concrete Research*, vol. 30, no. 5, pp. 703–708, 2000.
- [11] V. L. Bonavetti, V. F. Rahhal, and E. F. Irassar, "Studies on the carboaluminate formation in limestone filler-blended cements," *Cement and Concrete Research*, vol. 31, no. 6, pp. 853–859, 2001.
- [12] B. Lothenbach, G. Le Saout, E. Gallucci, and K. Scrivener, "Influence of limestone on the hydration of Portland cements," *Cement and Concrete Research*, vol. 38, no. 6, pp. 848–860, 2008.
- [13] T. Matschei, B. Lothenbach, and F. P. Glasser, "The role of calcium carbonate in cement hydration," *Cement and Concrete Research*, vol. 37, no. 4, pp. 551–558, 2007.
- [14] GEMGR, "The General Establishment of Geology and Mineral Resources" in Syria (in Arabic), Official document no. (3207/T/9), 2007.

- [15] GEMGR, “The General Establishment of Geology and Mineral Resources” in Syria (in Arabic), A Guide for Mineral Resources in Syria, 2011.
- [16] A. M. Al-Swaidani, “Prediction of compressive strength and some permeability-related properties of concretes containing volcanic scoria as cement replacement,” *Revista Romana de Materiale/Romanian Journal of Materials*, vol. 46, no. 4, pp. 505–514, 2016.
- [17] A. M. Al-Swaidani, S. D. Aliyan, and N. Adarnaly, “Production of more sustainable mortar using finer volcanic scoria-based blended cements,” *Journal of Sustainable Architecture and Civil Engineering*, vol. 13, no. 4, pp. 49–61, 2015.
- [18] Ş. Yetgin and A. Çavdar, “Study of effects of natural pozzolan on properties of cement mortars,” *Journal of Materials in Civil Engineering*, vol. 18, no. 6, pp. 813–816, 2006.
- [19] A. R. Pourkhorshidi, M. Najimi, T. Parhizkar, F. Jafarpour, and B. Hillemeier, “Applicability of the standard specifications of ASTM C618 for evaluation of natural pozzolans,” *Cement and Concrete Composites*, vol. 32, no. 10, pp. 794–800, 2010.
- [20] S. Tsivilis, E. Chaniotakis, E. Badogiannis, G. Pahoulas, and A. Ilias, “A study on the parameters affecting the properties of Portland limestone cements,” *Cement and Concrete Composites*, vol. 21, no. 2, pp. 107–116, 1999.
- [21] S. Sprung and E. Siebel, “Assessment of the suitability of limestone for producing Portland limestone cement,” *Zement-Kalk-Gips*, vol. 44, no. 1, pp. 1–11, 1991.
- [22] A. Çolak, “Characteristics of pastes from a Portland cement containing different amounts of natural pozzolan,” *Cement and Concrete Research*, vol. 33, no. 4, pp. 585–593, 2003.
- [23] S. Kenai, W. Soboyejo, and A. Soboyejo, “Some engineering properties of limestone concrete,” *Materials and Manufacturing Processes*, vol. 19, no. 5, pp. 949–961, 2004.
- [24] D. C. Montgomery and E. A. Peck, *Introduction to Linear Regression Analysis*, John Wiley & Sons, New York, NY, USA, 1982.
- [25] K. M. A. Hossain, “Blended cement using volcanic ash and pumice,” *Cement and Concrete Research*, vol. 33, no. 10, pp. 1601–1605, 2003.
- [26] K. Tosun, B. Felekoglu, B. Baradan, and I. A. Altun, “Portland limestone cement, Part I-Preparation of cements,” in *Digest*, pp. 1337–1355, 2009.
- [27] V. Rahhal and R. Talero, “Early hydration of portland cement with crystalline mineral additions,” *Cement and Concrete Research*, vol. 35, no. 7, pp. 1285–1291, 2005.
- [28] G. Menéndez, V. Bonavetti, and E. F. Irassar, “Strength development of ternary blended cement with limestone filler and blast-furnace slag,” *Cement and Concrete Composites*, vol. 25, no. 1, pp. 61–67, 2003.
- [29] T. Vuk, V. Tinta, R. Gabrovšek, and V. Kaučič, “The effects of limestone addition, clinker type and fineness on properties of Portland cement,” *Cement and Concrete Research*, vol. 31, no. 1, pp. 135–139, 2001.
- [30] M. Schmidt, “Cement with interground additives capabilities and environmental relief, part 1,” *Zement Kalk-Gips*, vol. 45, pp. 64–69, 1992.
- [31] N. Voglis, G. Kakali, E. Chaniotakis, and S. Tsivilis, “Portland-limestone cements. Their properties and hydration compared to those of other composite cements,” *Cement and Concrete Composites*, vol. 27, no. 2, pp. 191–196, 2005.
- [32] K. Celik, M. D. Jackson, M. Mancio et al., “High-volume natural volcanic pozzolan and limestone powder as partial replacements for portland cement in self-compacting and sustainable concrete,” *Cement and Concrete Composites*, vol. 45, pp. 136–147, 2014.
- [33] K. Githachuri and M. G. Alexander, “Durability performance potential and strength of blended Portland limestone cement concrete,” *Cement and Concrete Composites*, vol. 39, pp. 115–121, 2013.
- [34] D. P. Bentz, T. Sato, I. De La Varga, and W. J. Weiss, “Fine limestone additions to regulate setting in high volume fly ash mixtures,” *Cement and Concrete Composites*, vol. 34, no. 1, pp. 11–17, 2012.
- [35] M. F. Carrasco, G. Menéndez, V. Bonavetti, and E. F. Irassar, “Strength optimization of “tailor-made cement” with limestone filler and blast furnace slag,” *Cement and Concrete Research*, vol. 35, no. 7, pp. 1324–1331, 2005.
- [36] Y. A. Villagrán-Zaccardi, V. L. Taus, and Á. A. Di Maio, “Time evolution of chloride penetration in blended cement concrete,” *ACI Materials Journal*, vol. 107, no. 6, pp. 593–601, 2010.
- [37] K. Vance, M. Aguayo, T. Oey, G. Sant, and N. Neithalath, “Hydration and strength development in ternary portland cement blends containing limestone and fly ash or metakaolin,” *Cement and Concrete Composites*, vol. 39, pp. 93–103, 2013.
- [38] M. Ghrici, S. Kenai, and M. Said-Mansour, “Mechanical properties and durability of mortar and concrete containing natural pozzolana and limestone blended cements,” *Cement and Concrete Composites*, vol. 29, no. 7, pp. 542–549, 2007.
- [39] A. M. Neville, *Properties of Concrete*, Pearson Education, 5th edition, 2011.
- [40] H. T. Cao, L. Bucea, A. Ray, and S. Yozghatlian, “The effect of cement composition and pH of environment on sulfate resistance of Portland cements and blended cements,” *Cement and Concrete Composites*, vol. 19, no. 2, pp. 161–171, 1997.
- [41] S. Aydin, H. Yazici, H. Yiğiter, and B. Baradan, “Sulfuric acid resistance of high-volume fly ash concrete,” *Building and Environment*, vol. 42, no. 2, pp. 717–721, 2007.
- [42] E. Dan and I. Janotka, “Chemical resistance of Portland cement, blast-furnace slag Portland cement and sulphoaluminate-belite cement in acid, chloride and sulphate solution: Some preliminary results,” *Ceramics - Silikaty*, vol. 47, no. 4, pp. 141–148, 2003.
- [43] Y. Senhadji, G. Escadeillas, M. Mouli, H. Khelafi, and Benosman, “Influence of natural pozzolan, silica fume and limestone fine on strength, acid resistance and microstructure of mortar,” *Powder Technology*, vol. 254, pp. 314–323, 2014.
- [44] M. T. Bassuoni and M. L. Nehdi, “Resistance of self-consolidating concrete to sulfuric acid attack with consecutive pH reduction,” *Cement and Concrete Research*, vol. 37, no. 7, pp. 1070–1084, 2007.
- [45] M. T. Bassuoni, M. Nehdi, and M. Amin, “Self-compacting concrete: using limestone to resist sulfuric acid,” *Proceedings of the Institution of Civil Engineers - Construction Materials*, vol. 160, no. 3, article 700030, pp. 113–123, 2007.
- [46] Z. Makhloufi, E. H. Kadri, M. Bouhicha, and A. Benaissa, “Resistance of limestone mortars with quaternary binders to sulfuric acid solution,” *Construction and Building Materials*, vol. 26, no. 1, pp. 497–504, 2012.
- [47] S. H. Liu and Z. Wang, “Effect of limestone powder on acid attack characteristics of cement pastes,” *Medziagotyra*, vol. 20, no. 4, pp. 503–508, 2014.
- [48] F. Rendell and R. Jauberthie, “Deterioration of mortar in sulphate environments,” *Construction and Building Materials*, vol. 13, no. 6, pp. 321–327, 1999.

- [49] V. Pavlík, "Effect of carbonates on the corrosion rate of cement mortars in nitric acid," *Cement and Concrete Research*, vol. 30, no. 3, pp. 481–489, 2000.
- [50] E. F. Irassar, M. González, and V. Rahhal, "Sulphate resistance of type V cements with limestone filler and natural pozzolana," *Cement and Concrete Composites*, vol. 22, no. 5, pp. 361–368, 2000.
- [51] M. Antoni, J. Rossen, F. Martirena, and K. Scrivener, "Cement substitution by a combination of metakaolin and limestone," *Cement and Concrete Research*, vol. 42, no. 12, pp. 1579–1589, 2012.

Research Article

Flexural Behaviour of Combined FA/GGBFS Geopolymer Concrete Beams after Exposure to Elevated Temperatures

Jun-ru Ren, Hui-guo Chen, Tao Sun, Hao Song, and Miao-shuo Wang

Department of Civil Engineering, Logistical Engineering University, Chongqing 401311, China

Correspondence should be addressed to Hui-guo Chen; chenhg_mail@163.com

Received 11 July 2017; Accepted 8 October 2017; Published 6 November 2017

Academic Editor: Prinya Chindapasirt

Copyright © 2017 Jun-ru Ren et al. This is an open access article distributed under the Creative Commons Attribution License, which permits unrestricted use, distribution, and reproduction in any medium, provided the original work is properly cited.

As a promising alternative to OPC concrete, geopolymer concrete has been investigated and has demonstrated superior mechanical performance. Studying the thermal behaviour on the scale of a structural element is significant for introducing a new material to engineering applications. Four geopolymer concrete beams and four OPC concrete counterparts with the same reinforcement structure and similar concrete strength were subjected to three different heating cases at the rate of ISO834. The experimental results showed that the geopolymer concrete beams underwent a colour change, severe cracking, and no spalling after the exposure. While under load, the geopolymer concrete specimens exhibited a lower crack resistance and flexural stiffness. The residual load capacities were 110%, 107%, and 90% of the ambient specimen for the geopolymer concrete samples and 103%, 97%, and 80% for the OPC concrete samples. To some extent, the geopolymer concrete beams achieved superior fire endurance compared to their OPC concrete counterparts.

1. Introduction

With the increasing awareness of emission reduction in all industries, geopolymer concrete (GC) has been seen as a promising alternative to ordinary Portland cement (OPC) concrete. Due to the use of industrial by-products, such as fly ash (FA), ground granulated blast furnace slag (GGBFS), metakaolin, and mine tailings, the carbon footprint emitted by the production of geopolymer cement is reported to be 80%–90% less than that of OPC [1]. These raw materials, which are abundant in aluminium and silicon, can easily dissolve in alkaline solution, breaking down to covalent O-Si and O-Al and eventually forming a Si-O-Al tetrahedral structure [2]. The reaction is called alkali activation or geopolymerization. Among the abovementioned synthesis precursors, FA and GGBFS wastes from electricity plants and iron works, respectively, have been found to be suitable for geopolymer cement. Both materials, which have huge annual productions, need no more calcinations than metakaolin and require less energy during fabrication. GGBFS was first employed as an additive to FA-based GC, which generally needs thermal curing to catalyse the reaction for better strength. Reports [3–5] showed that the addition of GGBFS with an angular shape

not only enhanced its early-stage strength but also enabled it to attain a strength and workability similar to those of heat-cured GC dominated by FA with a spherical shape at room temperature.

With decades of development, there have been numerous investigations, patents, and applications of GC [6], but the current use of this material in building construction is rare. The distinctive mechanical properties of GC have been extensively investigated in structural components, including beams, columns, panels, and pipes [7]. Sumajouw et al. [8, 9] pioneered and examined six underreinforced GC beams with various reinforcement ratios for flexural failure. The load capacities of another sixteen beams were also evaluated and compared to AS 3600 [10]. The results revealed that the flexural behaviours of GC specimens were similar to those of conventional cement concrete in terms of the effect of the reinforcement ratio on flexural capacity and the ductility index. Other investigations [11–15] also reported analogous performances of both types of beams in bending tests, such as first cracking load, crack width, load-deflection relationship, flexural stiffness, ultimate load, and failure mode. It was also reported that the capacities computed from AS 3600 [10], ACI

TABLE I: Chemical composition of FA and GGBFS (mass%).

Compounds	SiO ₂	Al ₂ O ₃	Fe ₂ O ₃	CaO	MgO	K ₂ O	SO ₃	TiO ₂	P ₂ O ₅	Na ₂ O	MnO
FA	32.31	13.47	12.3	25.95	9.02	0.45	3.94	0.69	0.02	0.54	0.18
GGBFS	30.64	11.62	0.44	42.29	8.46	0.57	2.05	1.46	0.03	0.42	0.5

318 [16], and IS 456 [17] were more conservative than the experimental results [9, 11, 12]. Hence, the existing codes were suitable for designing GC beams with conservative test-to-prediction ratios. The GC beams were also shown to present an equal or higher shear capacity than that of OPC concrete beams [12]. All the articles above laid the foundation for the construction application of GC.

However, before putting any new building materials into practice, they should have a certain degree of fire resistance. Materials that lack fire resistance could lead to the catastrophic loss of life and property, especially if the impaired structure collapses. Due to the ceramic-like properties of geopolymer matrix, GC was widely believed to possess better fire resistance than OPC concrete [18, 19]. Previous studies [20–22] investigated various systems of GC with respect to residual strength, as well as the mechanisms of deterioration on the macroscale and microscale. Though different types of raw materials might lead to contrasting thermal performance [18], an agreement on the three main causes of deterioration was reached: pore pressure, phase transformation [23], and incompatible deformation [21]. It was also proved in other geopolymer systems that the precursor type, specimen size [21], aggregate size [21], and heating regime [24] could affect the residual strength of GC. Limited studies [25, 26] highlighted the effects of high temperature on GGBFS/FA geopolymer materials. Guerrieri and Sanjayan [26] analysed the compressive strength of a combined FA and GGBFS geopolymer paste after exposure to 800°C with variables of mixture proportion, alkaline solution modulus, and sodium dosage. It was shown that the residual strength was influenced by the initial strength and that GC with a low initial strength would be enhanced by further hydration and sintering. Ren et al. [25] investigated the residual behaviour of FA/GGBFS GC subjected to different temperatures and cooling regimes. The weight change, strength loss, and ultrasonic characteristics were studied.

Despite the numerous works on GC in the shape of a cube or cylinder, the results cannot be translated into the thermal performance of larger specimens embedded with reinforcements. Likewise, though GC members behaved similarly to OPC concrete components in ambient conditions, the effects of elevated temperature and raw material type should be considered because of the distinct chemical reactivity and bulk matrix of the geopolymer binder. A study on the behaviour of damaged reinforced GC after elevated temperature exposure was not found. To the authors' knowledge, only Sarker and Mcbeath [27] examined the fire endurance of a FA-based GC panel. The report revealed that GC panels achieved less cracking, no spalling, and a higher residual load capacity than the OPC concrete counterparts. Furthermore, specimens in most works were subjected to a certain temperature, which

did not mimic the actual conditions of a fire with a serious rate of increase in temperature.

In this research, four GC beams and four OPC concrete beams were fabricated and tested under a four-point flexural load after three diverse temperature exposures. The mid-span deflection, crack development, and load capacity were examined and compared to those of OPC concrete beams. Each heating regime was controlled at the rate of ISO834 [28], the most widely adopted temperature curve for fires. The experimental data presented in this paper may assist in the application of GC to the sustainable development of infrastructure construction.

2. Experimental Work

2.1. Materials. Commercially available F class (low calcium) FA and normal GGBFS were prepared for GC specimens. GGBFS had a density of 2.9 g/cm³ and a specific surface area of 470 m²/kg. The chemical proportions of GGBFS and FA determined by XRF are tabulated in Table I. General-purpose Portland cement was procured for OPC specimens. The alkaline activator utilized was a sodium silicate solution developed with an ordinary sodium silicate solution, sodium hydroxide flakes with 98% purity, and tap water. The modulus (SiO₂/Na₂O by mass) of the sodium silicate solution was 3.13 (SiO₂ = 25.72%, Na₂O = 8.48%, and water = 65.8%). Aggregates, including fine aggregates and coarse aggregates, were employed in the SSD condition. The coarse aggregates were crushed limestone from a local quarry with a size of 5–35 mm, and the fine aggregates were river sand with a fineness modulus of 2.58. The reinforcement of every beam was normal ductility deformed bars.

2.2. Mixture Proportions. It was noted that the moisture content and the modulus of the alkaline activator would affect the workability and strength of GC [29, 30]. Based on many trial experiments, the modulus and the water content of the alkaline activator were adjusted to 1.8 and 73%, respectively, by adding extra NaOH and water. The NaOH solution was prepared one day prior to casting. The mixture proportions of GC and OPC concrete are provided in Tables 2 and 3. The initial strength of both concretes and reinforcement is given in Figure 6.

2.3. Specimen Preparation. Four GC beams, four OPC concrete beams, and the corresponding heating cases are listed in Table 4. As shown in Figure 1, the same size, same reinforcement design, and similar concrete strengths were controlled for a credible comparison. The reinforcement ratio of the longitudinal tensile bars was 1.6% ($A_s = 628 \text{ mm}^2$, $h_0 = 257 \text{ mm}$), indicating an underreinforced design. The stirrups were placed along the shear span in case of shear failure.

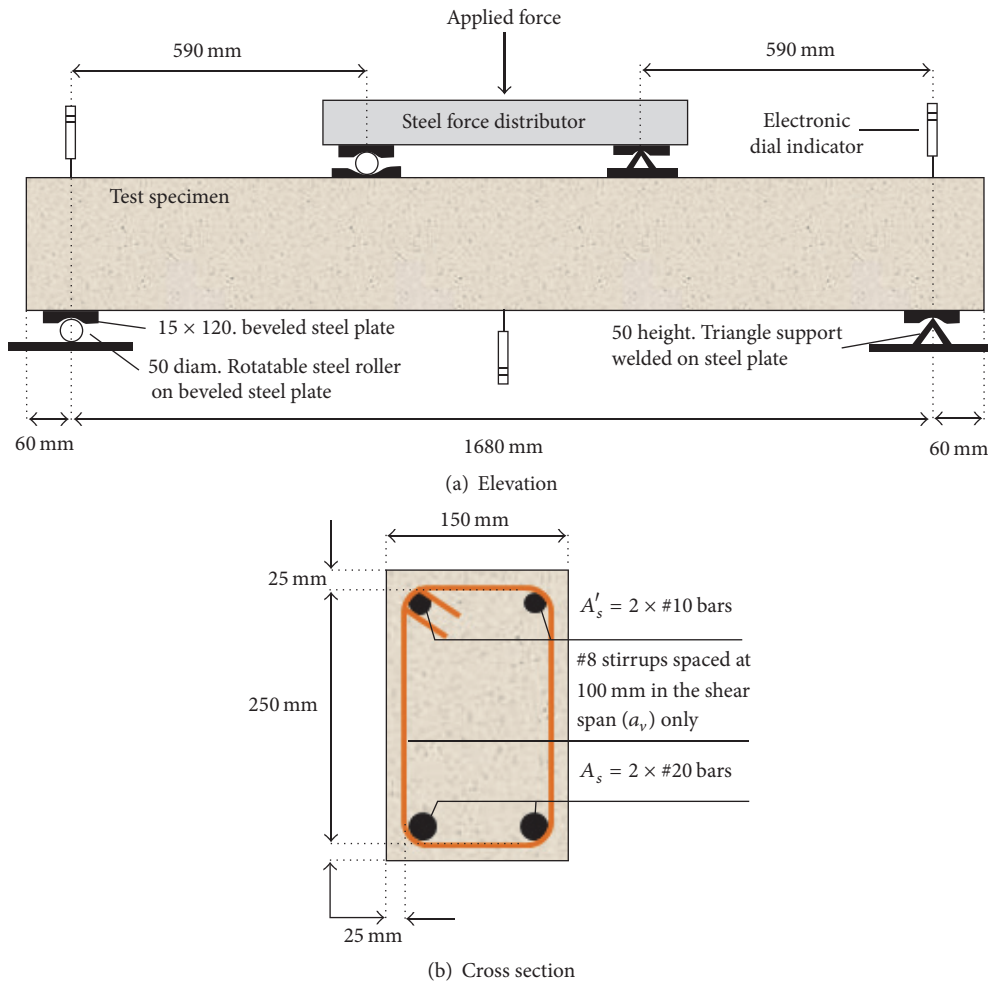


FIGURE 1: Test sample details.

TABLE 2: Geopolymer concrete mixture composition (kg/m³).

GGBFS	FA	Sand	Coarse aggregates	Alkaline activator		Water
				Sodium silicate	Sodium hydroxide	
140	210	644	1196	134	11	65

Reinforcement-structured and wooden moulds were fabricated onsite. GC and OPC concrete were mixed in a span mixer with a power of 4 kW. The manufacturing procedure of geopolymer specimens was as follows: (1) blend the GGBFS, FA, and fine aggregates for 2 min; (2) add coarse aggregates and dry-mix them for another 1 min; (3) add alkaline activator and mix it for a final 1 min; and (4) pour the mixture into the moulds and compact them with an electric vibrator. The specimens were demoulded 1 d after casting, sprayed with water, and covered with plastic film for 30 d for the ambient curing. Before the thermal exposure, the specimens were put in a cool and dry place to reach SSD. Three concrete cubes and two 500 mm samples of tensile rebar were derived from each specimen.

2.4. Heating Regime. Three heating treatments were used in this work: Case (I) 400°C for 1h; Case (II) 600°C for 1h;

TABLE 3: OPC concrete mixture composition (kg/m³).

Cement	Sand	Coarse aggregates	Water	W/C ratio	Sand ratio
488	599	1163	200	0.41	34

and Case (III) 600°C for 2 h. ISO834 [28] was employed to simulate the temperature in an actual fire. A gas furnace was used to calcinate the specimens. It had a two-clamshell structure insulated by high alumina fibre blankets with one thermocouple and four burners equipped on each shell. The specimens were placed upside down onto the insulation to create a three-face burning scenario. The furnace could be automatically operated using stored programmes. When the temperature reached the target, the furnace would automatically hold for the scheduled time and then cut off the gas to let the specimens cool to room temperature inside. The

TABLE 4

Material	Heating case	Temperature	Sample ID
Geopolymer concrete	—	Ambient	GB-A
	(I)	400°C	GB-4
	(II)	600°C-1 h	GB-6
	(III)	600°C-2 h	GB-6-2
OPC concrete	—	Ambient	OB-A
	(I)	400°C	OB-4
	(II)	600°C-1 h	OB-6
	(III)	600°C-2 h	OB-6-2

reserved samples were heated in the corresponding heating case simultaneously (see Figures 2 and 3).

2.5. Loading Regime. As shown in Figure 1, the specimens were under four-point load through a steel force distributor. The force was implemented by an electrohydraulic servo testing system (HONGSHAN China) with a maximum load of 500 kN which can also automatically record the loads. A preload of 5 kN was applied to detect the possible disorder of instruments and ensure contact between every component. After zero setting, step loading was operated. 20 kN and 10 kN load for each step were used before and after the yielding of reinforcement, respectively. The load in each step was held for 5 min and all measurements were recorded before and after the holding duration.

2.6. Measuring Method

2.6.1. Deflection. To measure the actual mid-span deflection, avoiding the influence of the support settlement, three electronic dial indicators were placed to gauge the deflection and the support settlement separately. At the beginning and end of the load holding duration, all data were manually recorded.

2.6.2. Cracks. The temperature cracks were traced on the specimens with a marker pen after thermal exposure. During the load holding, the opening and spacing of stressed cracks were likewise traced. The widths of the main cracks were detected twice at the beginning and end of the hold duration using a reading microscope at the position of the longitudinal steel bar. For safety, the data near the failure of the beam were not measured.

3. Results and Discussion

3.1. Physical Observation. Both specimen types underwent qualitative changes, including a colour change and temperature cracking, after being subjected to an elevated temperature. The colour of the GC specimens turned to dark grey, light grey, and pink in the three heating cases, respectively. However, the colour of each specimen was nonuniform, which might have resulted from the air motion in the furnace and the location of each specimen. Some beams also locally became orange, which was ascribed to the high iron content of FA that induced a kinetic ferrihydrite-hematite phase

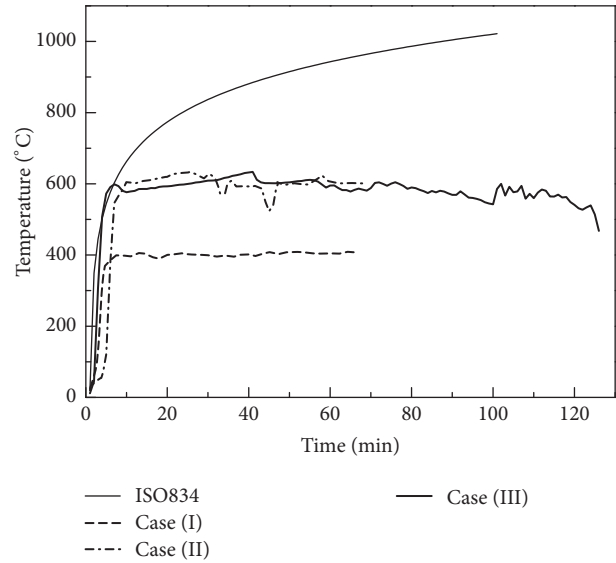


FIGURE 2: Temperature curves.

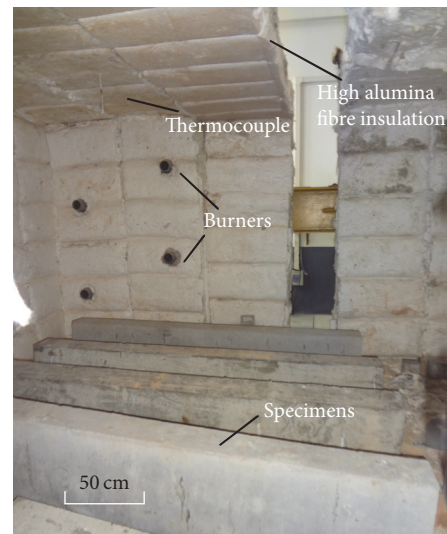


FIGURE 3: Gas furnace.

change [31]. Comparatively, the colour changes of the GC specimens were more obvious, which could reflect the degree of damage to the structures.

The thermal cracking was affected by pore pressure, thermal deformation, and phase change of geopolymer. The steam pressure caused the initial cracks. However, the shrinkage of geopolymer and corresponding incompatible deformation with coarse aggregates were primary causes because when aggregates expanded in high temperature, the geopolymer exhibited evident shrinkage [20, 22, 23]. Meanwhile, the dehydroxylation and dehydration were typical and dominant phase changes of FA geopolymer at around 600°C, which also led to shrinkage.

Temperature-induced crack nets covered each specimen, and their area and width developed progressively with the heating regimes. The distribution of the temperature cracks

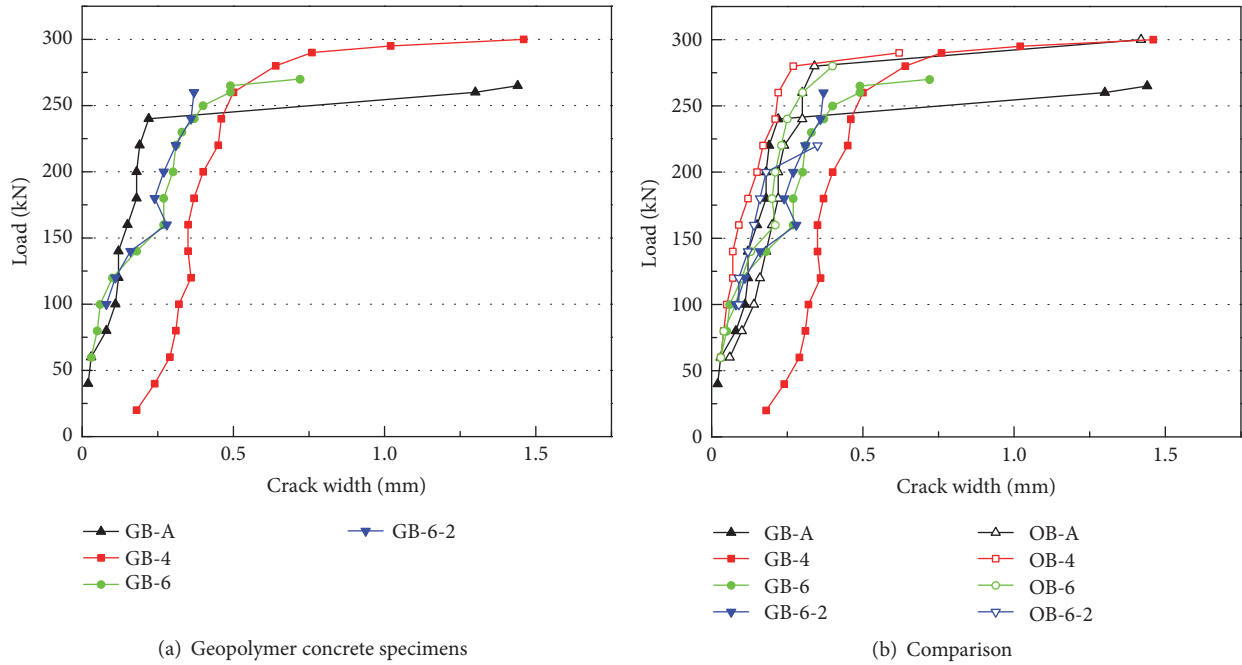


FIGURE 4: Load-crack width curves.

of both types of specimens was also nonuniform along the length and height. Most cracks began at the top of the specimen, which was not directly get burnt, and then spread to the bottom, where fewer cracks opened. This might have been caused by the asymmetric reinforcement structure, where the thicker ribbed steel bars at the bottom provided more powerful constraints.

In comparison, the temperature cracks of the GC specimens were more crucial than those of the OPC concrete specimens, which were more intense and wider. It was reported that the shrinkage of the geopolymer binder was more substantial than that of the OPC paste, especially when Na_2SiO_3 was used as the alkaline activator [32]; the binder also demonstrated sharp shrinkage at high temperatures [22, 33]. On the other hand, the observation contradicted the results in [27] that GC cracked less, which might be attributed to the distinctive type of geopolymer system. It is worth noting that more pores and no spalling phenomena were observed in the GC specimens.

3.2. Cracks. The initiation and propagation of cracks indicate the ability of structural members to serve as such. In addition to the temperature cracks, flexural cracks and shear cracks formed under load. The width of the failure crack of each specimen is provided in Figure 4. The bearing cracks generally developed along the temperature cracks with the load energy dissipated among them. This led to curl cracks, making it difficult to trace the cracks of some specimens, such as GB-6-2, until failure. As the temperature increased, the cracks propagated faster, the height of which decreased, foreboding an overreinforced failure.

The GC beams cracked faster than the OPC concrete beams. The flexural cracks almost emerged in the first load

step, and all appeared in the second or third load step; one or two of these cracks developed to failure cracks. The shear cracks initiated later but became wider and more intense than the flexural cracks, the latter indicating the pronounced deterioration in shear capacity. One GC specimen experienced shear failure, and the phenomenon did not fit the description in [12] that GC beams acquired an equal or higher shear capacity.

As shown in Figure 4(a), there was no distinct regularity in the crack width with varying heating cases. The exposed specimens developed wider cracks than the ambient samples, and GB-4 developed the widest cracks. The curves were concentrated with a similar trend under a lower load (<150 kN) and then dispersed as the load increased. The appearance and extension of the crack span revealed the plasticity of the GC beams. After the yielding of the reinforcements, the width of GB-A and GB-4 rose quickly with a slight increase of load showing an improvement in capacity and a clear portent of failure. However, the spans of GB-6 and GB-6-2 were not detected, and they collapsed abruptly during the load-sustained period.

It is revealed in Figure 4(b) that the cases with a gradual change in temperature equally had little impact on the crack width of the OPC concrete beams. The exposed specimens even developed narrower cracks than the ambient ones. Comparatively, the GC specimens displayed wider cracks than the OPC concrete specimens under the same load. The inferior crack resistance was not in agreement with former research showing that GC had a residual tensile strength higher than that of the OPC concrete. This might be attributed to the compounded effects of multiple factors, such as the bond properties and material type.

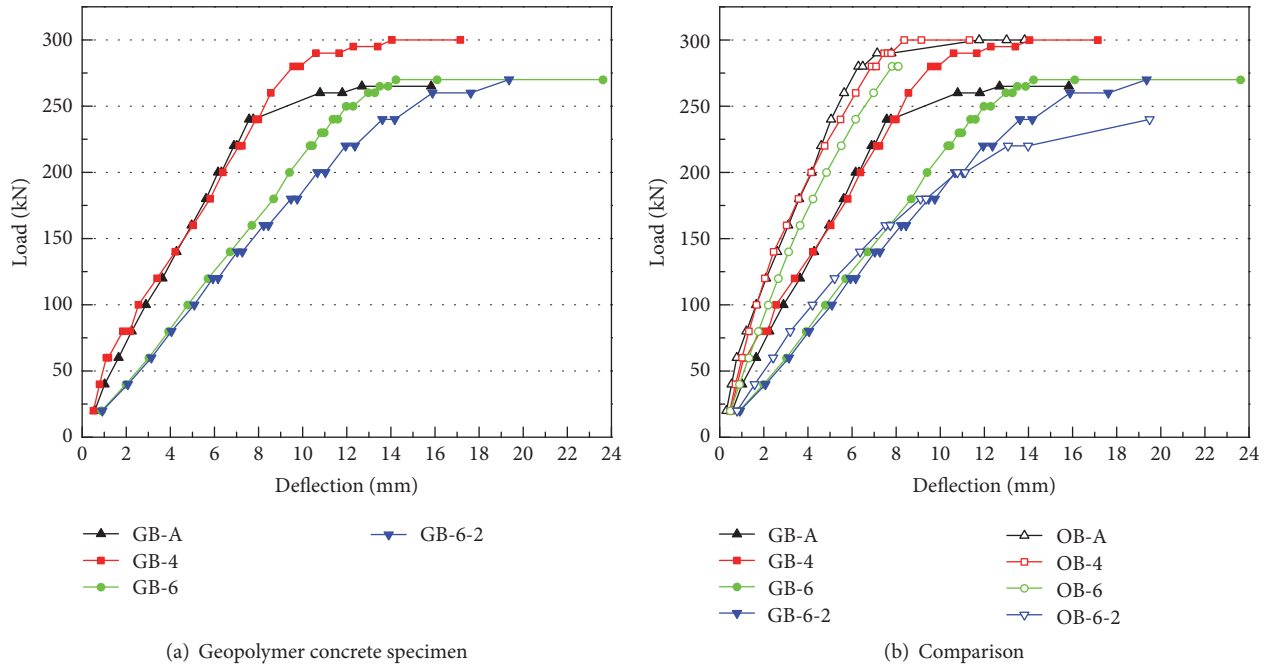


FIGURE 5: Load-deflection curves.

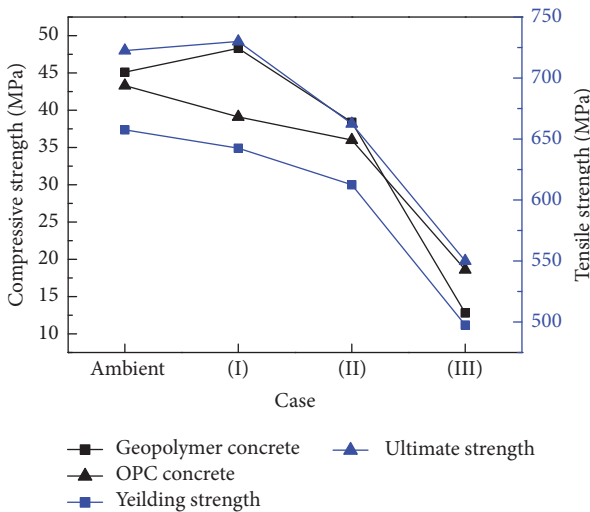


FIGURE 6: Strength of reserved concrete and reinforcement.

3.3. Load-Deflection Results. Deflection could imply some mechanical changes to the beams, such as local buckling, local cracking, and reinforcement slippage. As shown in Figure 5(a), the two-stage curves of the GC specimens included the inelastic stage with cracks, the slope of which reflected the stiffness, and the plastic stage, which presented the ductility and bearing capacity. The GB-4 curve corresponded approximately to that of GB-A and even overtook the latter in the second stage, demonstrating a higher capacity, while the slope noted a slight reduction in stiffness. GB-6 and GB-6-2 displayed similar load capacities. However, the smaller slope and the shorter plateau of GB-6-2 indicated

an evident decrease in stiffness and plastic deformation. As shown in Figure 5(b), the OPC concrete specimens gained a positively gradual reduction in bearing capacity and bending stiffness upon thermal exposure. This was especially true for OB-6-2, which achieved the smallest capacity and stiffness. It should be noted that the plateau stage was not detected for OB-6 and OB-6-2, which suddenly failed in the load-keeping period without conspicuous plastic deformation. Comparatively, the curves of GC specimens were below the curves of the OPC concrete specimens, indicating the smaller flexural stiffness of the GC specimens after being subjected to elevated temperatures.

3.4. Load Capacity and Failure Mode. The failure mode of each specimen was determined through the crack and deflection results, along with field observation. The pronounced increases in crack width and deflection were considered to be the marks of reinforcement yielding, and the yielding load was correspondingly recorded; the ultimate load was recorded automatically by the testing system.

The ambient specimen GB-A presented the typical failure of an underreinforced beam under bending. From the yielding of the steel bar to the crush of compressive concrete, the capacity improved with a sharp increase in deflection, and the width of the cracks clearly indicated the following collapse with proper ductility. Nonetheless, the yielding features of the exposed specimens, such as GB-4 and GB-6, were not prominent, and the increment of capacity also decreased. Some beams broke down without reinforcement yielding, such as GB-6-2, which gained a slight increase in crack width and deflection, along with shorter cracks, before failure. The collapse of GB-6-2 started from the stratiform cracks on the mid-span upper concrete and was followed by the heaving



FIGURE 7: Failure of GC beams.

TABLE 5: Flexural bearing capacity of simply supported beams.

ID	P_y /kN	P_u /kN	Reduction ratio/%
Type	Geopolymer concrete		
GB-A	250	268	—
GB-4	270	300	+11
GB-6	255	270	+0.7
GB-6-2	—	265	-1
Type	OPC concrete		
OB-A	285	301	—
OB-4	295	310	+3
OB-6	285	291	-3
OB-6-2	—	240	-20

and crush of concrete, conspicuous characteristics of an overreinforced failure.

The evolution of the specimens' capacities and damage patterns was closely connected to the residual strength of the concrete and reinforcement after being exposed to elevated temperatures. As shown in Figure 6, the residual strength of GC was higher than that of the OPC concrete, which lost more strength for the same case. Furthermore, GC was characterized by the strength gain behaviour observed in Case (I). For the reinforcements, a sharper reduction in tensile strength occurred after thermal exposure at 600°C. It was reported in [34, 35] that the basic properties of steel bars could recover after being exposed to temperatures lower than 600°C.

Table 5 provides the yielding capacity (P_y), ultimate capacity (P_u), and the reduction ratio to the ambient specimen. GB-4 obtained a remarkable improvement in yielding and ultimate capacity that was mainly attributable to the strengthening behaviour of GC. The enhancement of GC after temperature exposure was commonly reported in [18, 33, 36, 37] that the alkali activation of the remnant precursors induced by ambient curing was catalysed by the high temperature when free water was not liberated. The augmentation of GC predominated over the damage brought about by vapor pressure and thermal incompatibility. Meanwhile, the deterioration of the rebar was relatively slight, and it was concluded that GB-4 achieved the net result of a higher capacity.

In other cases, 600°C was the critical temperature for GC [25]. The geopolymerization terminated because of the loss of moisture, while the geopolymer matrix was still complete [33, 38, 39]. The main reasons for the decrease in cubic strength might be the thermal incompatibility between the binder and aggregates [22], which regularly amounts to between

65% and 80%. It was revealed in some studies [20, 22, 23] that while coarse aggregates progressively expanded at elevated temperatures, geopolymer binders experienced notable shrinkage. Furthermore, dehydration and dehydroxylation could be somewhat responsible for the reduction of strength [37]. However, on a larger scale, GB-6 had a similar capacity to GB-A. Because of the nonuniform temperature field of the specimen, the outer concrete began to lose strength while the inner part was strengthened. In addition, with the sharper decrease of tensile strength for the rebars, GB-6 did not have an improvement in capacity. Contributing to the weakest GC and steel bars, GB-6-2 achieved the lowest capacity without rebar yielding, demonstrating the characteristics of overreinforced failure.

GC beams under a flexural load resembled the mechanical performance and changing behaviour of the OPC concrete beams. The OPC specimens had a relatively obvious decline in capacity. From the angle of the bearing capacity, the GC beams had better fire resistance (see Figure 7).

4. Conclusion

The geopolymer concrete beams after exposure to elevated temperatures experienced clear colour changes and temperature cracks, which evolved with the aggravation of heating conditions. The temperature cracks were more intense and wider than those of the OPC concrete beams. The evident features after fire exposure could be utilized to appraise the extent of the fire damage of geopolymer concrete structures. Under loads, the geopolymer concrete specimens cracked earlier, developed more shear cracks, and exhibited lower flexural stiffness than the OPC concrete counterparts. With a similar failure mode to the OPC concrete beams, the geopolymer concrete beams achieved a higher capacity in Case (I) and retained more load capacity in the other heating cases.

The structural performance of geopolymer concrete after being subjected to elevated temperature was influenced by multiple factors, and the material demonstrated some defects; this was inconsistent to the behaviour of the ambient beams and the behaviour described in former research. Further investigations should be conducted to analyse the temperature field and bond behaviour, as well as to improve the crack resistance and flexural stiffness of GC for possible applications.

Conflicts of Interest

The authors declare that they have no conflicts of interest.

Acknowledgments

This work was supported by the Chongqing Science and Technology Commission, Chongqing, China [cstc2016jcyjA0569].

References

- [1] P. Duxson, J. L. Provis, G. C. Lukey, and J. S. J. V. Deventer, "The role of inorganic polymer technology in the development of green concrete," *Cement & Concrete Research*, vol. 37, no. 12, pp. 1590–1597, 2007.
- [2] J. Davidovits, "Geopolymers: inorganic polymeric new materials," *Journal of Thermal Analysis and Calorimetry*, vol. 37, no. 8, pp. 1633–1656, 1991.
- [3] S. Kumar, R. Kumar, and S. P. Mehrotra, "Influence of granulated blast furnace slag on the reaction, structure and properties of fly ash based geopolymer," *Journal of Materials Science*, vol. 45, no. 3, pp. 607–615, 2010.
- [4] P. S. Deb, P. Nath, and P. K. Sarker, "The effects of ground granulated blast-furnace slag blending with fly ash and activator content on the workability and strength properties of geopolymer concrete cured at ambient temperature," *Materials & Design*, vol. 62, pp. 32–39, 2014.
- [5] Z. Li and S. Liu, "Influence of slag as additive on compressive strength of fly ash-based geopolymer," *Journal of Materials in Civil Engineering*, vol. 19, no. 6, pp. 470–474, 2007.
- [6] P. J. Davidovits, "30 years of Successes and Failures in Geopolymer Applications," *Market Trends and Potential Breakthroughs*, 2002.
- [7] K. H. Mo, U. J. Alengaram, and M. Z. Jumaat, "Structural performance of reinforced geopolymer concrete members: A review," *Construction and Building Materials*, vol. 120, pp. 251–264, 2016.
- [8] M. J. Sumajouw, D. Hardjito, S. E. Wallah et al., "Behavior and strength of reinforced fly ash-based geopolymer concrete beams," *Civil Engineering Dimension*, vol. 6, no. 2, 2005.
- [9] D. M. J. Sumajouw, "Low-calcium fly ash-based geopolymer concrete: reinforced beams and columns," Research Report GC, Curtin University of Technology, Perth, Australia, 2006.
- [10] Australian Standard AS 3600, Concrete Structures, Standards Australia, Sydney, 2004.
- [11] J. K. Dattatreya, N. P. Rajamane, D. Sabitha, P. S. Ambily, and M. C. Nataraja, "Flexural behaviour of reinforced geopolymer concrete beams," *International Journal for Computational Civil & Structural Engineering*, vol. 2, no. 1, pp. 138–159, 2011.
- [12] J. R. Yost, A. Radlińska, S. Ernst, M. Salera, and N. J. Martignetti, "Structural behavior of alkali activated fly ash concrete. Part .Structural testing and experimental findings," *Materials and Structures/Materiaux et Constructions*, vol. 46, no. 3, pp. 449–462, 2013.
- [13] S. Kumaravel and S. Thirugnanasambandam, "Flexural behaviour of reinforced low calcium fly ash based geopolymer concrete beams," *Global Journal of Researches in Engineering*, vol. 13, no. 8, pp. 177–180, 2013.
- [14] S. Kumaravel, S. Thirugnanasambandam, and C. A. Jeyasehar, "Flexural Behaviour of Geopolymer Concrete Beams with GGBS," *IUP Journal of Structuring Engineering*, vol. 7, no. 1, pp. 45–54, 2014.
- [15] W. Yodsudjai, "Application of fly ash-based geopolymer for structural member and repair materials," *Advances in Science & Technology*, vol. 92, pp. 74–83, 2014.
- [16] ACI Committee 318, *Building Code Requirements for Structural Concrete (ACI 318-02)*, American Concrete Institute, Farmington Hills, Mich, USA, 2002.
- [17] IS: 456-2000, Indian Standard. Plain and Reinforced Concrete – Code of Practice, New Delhi, India, 2000.
- [18] D. L. Y. Kong, J. G. Sanjayan, and K. Sagoe-Crentsil, "Comparative performance of geopolymers made with metakaolin and fly ash after exposure to elevated temperatures," *Cement & Concrete Research*, vol. 37, no. 12, pp. 1583–1589, 2007.
- [19] D. L. Y. Kong, J. G. Sanjayan, and K. Sagoe-Crentsil, "Factors affecting the performance of metakaolin geopolymers exposed to elevated temperatures," *Journal of Materials Science*, vol. 43, no. 3, pp. 824–831, 2008.
- [20] D. L. Y. Kong and J. G. Sanjayan, "Damage behavior of geopolymer composites exposed to elevated temperatures," *Cement & Concrete Composites*, vol. 30, no. 10, pp. 986–991, 2008.
- [21] D. L. Y. Kong and J. G. Sanjayan, "Effect of elevated temperatures on geopolymer paste, mortar and concrete," *Cement & Concrete Research*, vol. 40, no. 2, pp. 334–339, 2010.
- [22] Z. Pan, J. G. Sanjayan, and D. L. Y. Kong, "Effect of aggregate size on spalling of geopolymer and Portland cement concretes subjected to elevated temperatures," *Construction & Building Materials*, vol. 36, no. 36, pp. 365–372, 2012.
- [23] A. V. Riessen, W. Rickard, and J. Sanjayan, "15 – Thermal properties of geopolymers," *Geopolymers*, vol. 40, no. 9, pp. 315–342, 2009.
- [24] A. Diouri, M. Talha Junaid, A. Khennane et al., "Investigation into the effect of the duration of exposure on the behaviour of GPC at elevated temperatures," in *Proceedings of the MATEC Web of Conferences II*, vol. 11, article 01003, April 2014, 10.1051/mateconf/01003.
- [25] W. Ren, J. Xu, and E. Bai, "Strength and ultrasonic characteristics of alkali-activated fly ash-slag geopolymer concrete after exposure to elevated temperatures," *Journal of Materials in Civil Engineering*, vol. 28, no. 2, article 04015124, 2016.
- [26] M. Guerrieri and J. G. Sanjayan, "Behavior of combined fly ash/slag-based geopolymers when exposed to high temperatures," *Fire and Materials*, vol. 34, no. 4, pp. 163–175, 2010.
- [27] P. K. Sarker and S. Mcbeath, "Fire endurance of steel reinforced fly ash geopolymer concrete elements," *Construction & Building Materials*, vol. 90, pp. 91–98, 2015.
- [28] International Standards Organisation, Fire Resistance Tests, Elements of Building Construction (ISO 834), Switzerland; 1980.
- [29] P. S. Deb, P. Nath, and P. K. Sarker, "The effects of ground granulated blast-furnace slag blending with fly ash and activator content on the workability and strength properties of geopolymer concrete cured at ambient temperature," *Materials & Design*, vol. 62, pp. 32–39, 1980.
- [30] X.-H. Yuan, Y. Yan, Z.-A. Lu, and L.-M. Yu, "Hydration process study on the alkali-activated slag cementing materials," *Journal of Chemical and Pharmaceutical Research*, vol. 6, no. 4, pp. 1180–1184, 2014.
- [31] W. D. A. Rickard, A. Van Riessen, and P. Walls, "Thermal character of geopolymers synthesized from class F Fly ash containing high concentrations of iron and α -quartz," *International Journal of Applied Ceramic Technology*, vol. 7, no. 1, pp. 81–88, 2010.
- [32] C. Shi, P. V. Krivenko, and D. Roy, *Alkali-Activated Cements and Concretes*, Taylor & Francis, New York, NY, USA, 2006.

- [33] Z. Pan, J. G. Sanjayan, and F. Collins, "Effect of transient creep on compressive strength of geopolymer concrete for elevated temperature exposure," *Cement & Concrete Research*, vol. 56, no. 2, pp. 182–189, 2013.
- [34] W.-Z. Zheng, M.-X. Xu, and Y. Wang, "Fire resistance behavior of reinforced concrete and prestressed concrete materials," *Harbin Jianzhu Daxue Xuebao/Journal of Harbin University of Civil Engineering and Architecture*, vol. 35, no. 4, pp. 6–10, 2002.
- [35] Z. Guo, *Mechanical Properties of Concrete And Structural Elements in Ambient and High Temperature*, Tsinghua University Press, Tsinghua, China, 2006.
- [36] T. W. Cheng and J. P. Chiu, "Fire-resistant geopolymer produce by granulated blast furnace slag," *Minerals Engineering*, vol. 16, no. 3, pp. 205–210, 2003.
- [37] O. A. Abdulkareem, A. M. M. A. Bakri, H. Kamarudin, I. K. Nizar, and A. E. A. Saif, "Effects of elevated temperatures on the thermal behavior and mechanical performance of fly ash geopolymer paste, mortar and lightweight concrete," *Construction & Building Materials*, vol. 50, suppl. 1, pp. 377–387, 2014.
- [38] Z. Wang, J. Xu, and W. Ren, "Damage evolution and dynamic constitutive model of geopolymeric concrete at elevated temperature," *Journal of Vibration & Shock*, vol. 35, no. 2, pp. 110–115, 2016.
- [39] P. Duxson, G. C. Lukey, and J. S. J. van Deventer, "Thermal evolution of metakaolin geopolymers: Part 1 - Physical evolution," *Journal of Non-Crystalline Solids*, vol. 352, no. 52-54, pp. 5541–5555, 2006.

Research Article

Long-Term Properties of Cement-Based Composites Incorporating Natural Zeolite as a Feature of Progressive Building Material

Alena Sičáková, Matej Špak, Mária Kozlovská, and Marek Kováč

Faculty of Civil Engineering, Technical University of Košice, Vysokoškolská 4, 042 00 Košice, Slovakia

Correspondence should be addressed to Matej Špak; matej.spak@tuke.sk

Received 9 June 2017; Revised 14 August 2017; Accepted 7 September 2017; Published 18 October 2017

Academic Editor: Prinya Chindaprasirt

Copyright © 2017 Alena Sičáková et al. This is an open access article distributed under the Creative Commons Attribution License, which permits unrestricted use, distribution, and reproduction in any medium, provided the original work is properly cited.

This study is aimed at the utilization of natural zeolite as a prospective type of Supplementary Cementitious Material in connection with the innovations of construction solutions through the materials. The influence of zeolite on several properties of cement-based composites is studied. Basic characteristics of input powdery materials as well as the technological parameters of zeolite tested on mortar containing 50% of cement replacement are presented. The technical parameters of concrete containing 8, 13, and 25% of cement replacement by zeolite are presented as well. The paper is valuable due to the three-year testing period. The density of the hardened concrete was found to be decreasing with increasing zeolite content. While no significant differences in compressive strength were found after 28 days, differences between individual samples were clear after the long-term period. The presence of zeolite influenced the compressive strength positively in the case of the 8% and 13% replacement, while the higher proportion of natural zeolite (25%) caused lower compressive strength after 28 days but was similar to the reference concrete after three years. A major increase in strength was detected for all samples in the long-term period. It confirms the long-term potential of zeolite for strength improvement.

1. Introduction

The ordinary Portland cement is one of the most utilized binder materials for the production of building materials. However, its production has negative environmental impact due to the requirement of high amount of energy, production of greenhouse gases, and so on. Utilization of supplementary cementitious materials (SCMs) for the production of cement-based composites can help to significantly minimize these adverse influences. Additionally, different SCMs bring several types of improvement to composites properties, for example, better workability or durability. Moreover, the costs of concrete can decrease. The incorporation of SCM is a feature of the current advanced concrete and is connected with the modern approaches to concrete production. Thus, it can be successfully involved in the modern methods of construction. Natural zeolite is one of the best-applicable SCMs, mainly due to its pozzolanic activity.

The quality and durability of concrete are strongly dependent on the kind, properties, and dosage of the basic components (cement, water, and aggregates) and the additives and admixtures. The alternative materials play an important role in current concrete technology such as SCMs. Due to the improvement of mechanical properties and durability of concrete, the trend of utilization of SCMs has increased [1–3]. SCMs improve the microstructure of concrete by minimizing its porosity and improving the resistance against the aggressive attack due to their chemical nature [2, 4–7]. In the standard EN 206 [8], three kinds of Type II additions—fly ash, blast furnace slag, and silica fume—are mentioned, and the conditions of their application to the concrete are specified.

The other kinds of addition can be used in specific cases of concrete structure exposure. Both zeolite and silica fume are recommended if a chemical attack occurs. The standard [8] defines the kind of addition in accordance with both the

nature and intensity of chemical environment, but the recommended dosage is not specified in the standard. Therefore, the practical production of concrete can be uncertain. There are a number of studies investigating zeolite as cement supplement (pozzolanic additions) [9–17]. Some results of these studies are ambiguous, as shown below. There is a lack of information on the influence of specific dosage of additions on the long-term properties of the concrete and information about other relevant properties, such as length deformation and water absorption capacity.

Natural zeolites are hydrated aluminosilicates that have high amounts of reactive SiO_2 and Al_2O_3 . Their reactivity is mainly attributed to their highly porous structure, which is related to the large external surface area giving interaction of zeolite with lime [11, 12], ability of ion exchange, and meta-stability, which supports the dissolution of zeolitic crystals and precipitation of hydrated calcium silicates and aluminates during interaction of OH^- ions available in the saturated lime solution [13, 14].

Researchers have found that the zeolites of different modifications act as pozzolanic additions in concretes; during cement hydration, CSH and CAH gel phases increase, which also increases the resistance of Portland cement compositions to acids and sulphate corrosion and increases its durability as well [11].

Regarding the early-age strength, the references are different. According to Yun-Sheng et al., zeolite added at 15% to the cement mix increases the early-age strength of concrete [15]. Turkish researchers carried out tests on concrete specimens containing 5, 10, 20, and 40% of zeolite. Compressive strength was measured after one, two, seven, and 28 days of curing. The results showed that the concrete specimens with zeolite additive had lower compressive strength compared to the control specimen after 24 hours of curing. The same trend was observed after two and seven days of curing. After 28 days of curing, the compressive strength of specimens containing 5% of zeolite increased by 6.8% compared to the control specimens; the compressive strength of the next specimens increased by 15.9%, 22.3%, and 4.1% for specimens containing 10%, 20%, and 40% of zeolite, respectively [16].

According to Ramezani pour et al. [17], the addition of natural zeolite delays the strength development during the first seven days, after which the concretes containing 10% of natural zeolite provide almost similar compressive strength compared to that of the reference concretes. The strength of concrete mixtures containing 15% of natural zeolite, however, is marginally lower than that of the reference concrete. The pozzolanic activity of natural zeolite is significantly high, as most of the pozzolanic reactions occurred between seven and 28 days. The use of natural zeolite leads to considerable reductions in water permeability and capillary absorption for each of the selected water-to-cementitious material ratios. The highest improvements through the use of natural zeolite were observed in the rapid chloride permeability and electrical resistivity tests. The electrical resistivity of concrete samples containing natural zeolite was two to four times better than those of the reference samples. These improvements were more significant for concretes with higher water-to-cementitious materials ratios (w/cm). The electrical resistivity

and rapid chloride penetrability of mixtures with 10 and 15% natural zeolite and w/cm of 0.50 was better than that of the reference concrete with w/cm of 0.35, indicating that using 10–15% of natural zeolite was more effective in improving permeability than reduction in w/cm from 0.50 to 0.35. The depth of carbonation increases with the use of natural zeolite. While the reduction of chloride penetration enhances the concrete resistivity against corrosion, the increased carbonation results in the opposite performance. Study of the SEM images shows significant improvements in porosity of the studied pastes through the use of natural zeolite. In addition, studying the images taken from transition zone reveals that natural zeolite enhances the structure of the transition zone favourably. The calcium hydroxide content is considerably reduced by the use of natural zeolite as an SCM, which results in the production of secondary C-S-H.

According to Vejmelková et al. [18], both the bulk and the matrix density of cement-based composites decrease with increase in the zeolite supplementary. Poon et al. [19] also state that 15% replacement of zeolite results in lower porosity, while a higher replacement level (25%) increases the porosity at all studied ages.

The drying shrinkage of products made with Portland-pozzolan cements is dependent on the hydration products and water demand of the mixtures. Although tests should be conducted to determine the drying shrinkage of Portland cement and natural pozzolans combinations, there is a scarcity of studies in this field [20]. Jana [21] investigates the effects of using 10, 20, and 30% of zeolite as an SCM. He observes that drying shrinkage of zeolite mixtures at 10 and 20% of Portland cement replacement levels is similar or slightly higher than that of the control mixture, whereas by using 30% of zeolite, the drying shrinkage is about 20% higher than the control mixture. Moreover, Kasai et al. [22] examined drying shrinkage for the mortars blended with clinoptilolite and mordenite. Both clinoptilolite and mordenite blended mortars experienced higher shrinkage than the control one.

It is reported that although natural zeolite reduces the slump of concrete, it can prevent bleeding and segregation. Regarding hardened concrete, natural zeolite increases compressive strength due to its pozzolanic property. Moreover, it enhances the durability of conventional concrete by reducing concrete permeability and, mainly, by improving resistance to alkali-aggregate reaction [23]. According to Najimi et al. [24], natural zeolite can be properly used as an SCM in normally consolidated concrete, considering the environmental protection and sustainable development. Chan and Ji [25] report that the pozzolanic reactivity of natural zeolite is between that of silica fume and fly ash.

This paper is aimed at the utilization of zeolite as a perspective kind of SCM and its influence on the long-term (up to three years) properties of concrete, since there is a lack of information about the long-term properties. Most reports are oriented towards the 28-day properties, or eventually up to one year, because of the challenges of long-term research. However, the pozzolanic additions need a longer time to develop their properties in the construction due to the slower progress of pozzolanic hydration processes. The short-term values of properties could be misleading.

TABLE 1: Chemical composition and particle size characteristics of binders.

Binder	SiO ₂	CaO	Fe ₂ O ₃ [% wt.]	Al ₂ O ₃	MgO	CaO/SiO ₂ [—]	<i>d</i> (0.5) [μm]	<i>d</i> (0.9) [μm]
OPC (CEM I 42.5 N)	20.34	64.1	2.99	2.97	9.03	3.150	26.68	67.87
Natural zeolite	78.75	3.50	1.73	11.6	1.16	0.040	20.68	91.97
Silica fume	97.00	0.70	1.50	1.10	—	0.007	0.226	8.647

Comprehensive results for zeolite, including basic characteristics (chemical composition and particle size distribution), technological parameters (mixing water demand, initial setting time, activity index, and relative linear deformation), and technical parameters of concrete incorporating zeolite (density, compressive strength, and total water absorption) are presented in the paper. For comparison, addition of silica fume is presented as well.

2. Materials and Methods

The main scope of the experiment is to observe the long-time technical parameters (density, compressive strength, and water absorption) of zeolite-based concrete and to assess the possibility of the practical utilization of natural zeolite for the production of progressive building material.

2.1. Materials Characteristics. Three types of mineral binders are used in the experiment. Ordinary Portland cement (OPC) class CEM I 42.5 N came from Turňa nad Bodvou, Slovakia, natural zeolite (NZ) came from Lehôtka pod Brehmi, Slovakia, and silica fume (SF) came from Istebné, Slovakia.

The chemical composition of ordinary Portland cement, natural zeolite, and silica fume was determined through X-ray fluorescence analysis (XRF). SPECTRO iQ II (Ametek, Germany) with silicon drift detector (SDD) with resolution of 145 eV at 10,000 pulses was used for the analysis. The primary beam was polarized using Bragg crystal and Highly Ordered Pyrolytic Graphite (HOPG) target. The samples were measured at 300 and 180 s at voltage of 25 kV and 50 kV and current of 0.5 and 1.0 mA in a helium atmosphere by using the standardized method of fundamental parameters for cements or liquids. The chemical compositions of binder solids are listed in Table 1.

The particle size distribution of binder solids was determined using a laser granulometric analyser (Mastersizer 2000; Malvern Instruments Ltd, UK). The parameters of grain size distribution are characterized by *d*(0.5) and *d*(0.9) medians, which are also listed also in Table 1. The curves of particle size distribution of binders are shown in Figures 1–3, respectively.

The differences in the particle size of binding materials are evident and in accordance with their character. Results also inform indirectly about the specific surface area in terms of mutual comparison: the smaller the particle size, the larger the specific surface area.

2.2. Technological Characterization of Natural Zeolite. Technological characterization (water demand for standard consistency, initial setting time, activity index, and relative linear

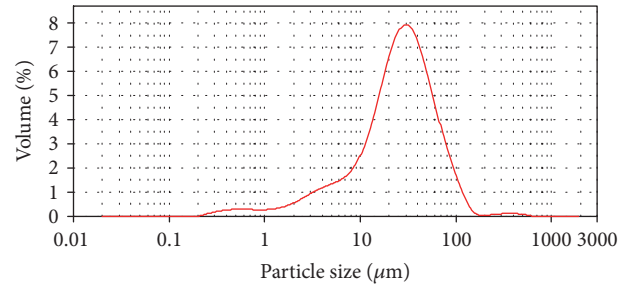


FIGURE 1: Particle size distribution of OPC.

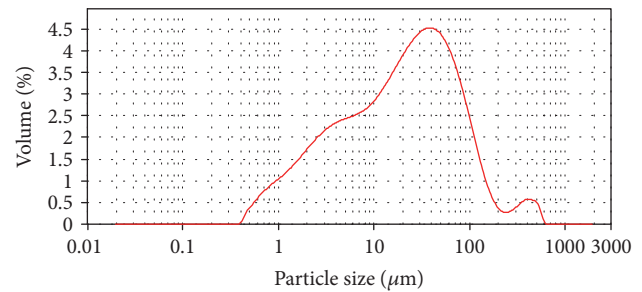


FIGURE 2: Particle size distribution of natural zeolite.

deformation) of natural zeolite was investigated. Both the water demand and initial setting time were tested on pastes composed of 50% of OPC and 50% of NZ and pastes consisting of OPC only, while the water-to-binder ratio was 0.5. Both the strength activity index and relative linear deformation were tested on mortars consisted of 1350 g of normalized silica sand, 500 g of binder, and 225 g of water, while two samples with different binder composition were tested. The control mixture contained 100% of OPC and research mixture contained 50% of OPC and 50% of NZ.

The water demand for standard consistency (the consistency that will permit the distance between plunger of Vicat apparatus and base-plate of 4–8 mm) and the initial setting time (the elapsed time, measured from zero to the time at which the distance between the needle and the base-plate is 3–9 mm) were measured using standard methods for testing cements (according to [26]).

The activity index was found in accordance with [27]. Here, the activity index refers to the ratio of the average compressive strength of SCM-based mortar and the reference cement-based mortar at the designated ages. Compressive strength was tested in accordance with [28].

The deformation changes of tested mortars were measured through active linear deformation [mm], using the

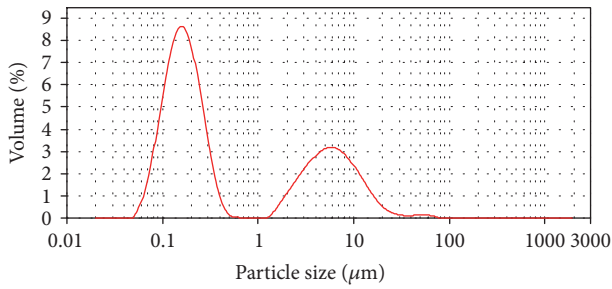


FIGURE 3: Particle size distribution of silica fume.

length comparator, while three samples were measured for each recipe. The relative linear deformation was then calculated as the ratio of the active linear deformation [mm] to the actual length of the sample [mm]. Specimens of dimensions $40 \times 40 \times 160$ mm were measured during 60 days at regular intervals. During this time, samples were kept in standard wet conditions (20°C temperature and water curing).

2.3. Physical-Mechanical Properties of Natural Zeolite-Based Concrete. The mineral binders (OPC, NZ, and SF) were used for concrete preparation. Natural normal-weight fine and coarse aggregates of fractions 0/4, 4/8, and 8/16 (NFA-0/4, NCA-4/8, NCA-8/16) were used. The superplasticizer based on polycarboxyl ether (PCE) was used to obtain optimal consistence together with tap water.

The experiment was focused on testing the concrete mixture designed by the acceptance of the standard recommendations for the composition for aggressive exposure. The recipe of the reference concrete was designed to achieve the compressive strength corresponding to C 35/45 strength class (according to [8]). Water-to-binder ratio (w/b) was 0.45 and cement content was $360 \text{ kg per } 1 \text{ m}^3$ of fresh concrete. Natural zeolite was applied in varying replacement percentages to cement (8%, 13%, and 25% by weight). For directly showing binder modification by well-known silica fume, it was decided to use the combination of 8% of zeolite and 8% of SF. The materials and compositions of the tested concretes are given in Table 2.

The samples of cubes shape with dimensions $150 \times 150 \times 150$ mm were prepared with standard methods. Specimens were released after one day and consequently cured in water under laboratory conditions until the tests execution. The standard tests (density, compressive strength, and water absorption) were executed after 28 days and the compressive strength after 365, 730, and 1095 days (one, two, and three years) according to [29–31].

3. Results and Discussion

3.1. Technological Characterization of Natural Zeolite. The water demand for standard consistency, initial setting time, and activity index of mortars are listed in Table 3. The consistent results comparing [17, 32, 33] have been found, in fact, to determine the expansion of water demand (probably due to a larger specific surface area) and to increase the setting time increasing of zeolite-blended mortars. The presented

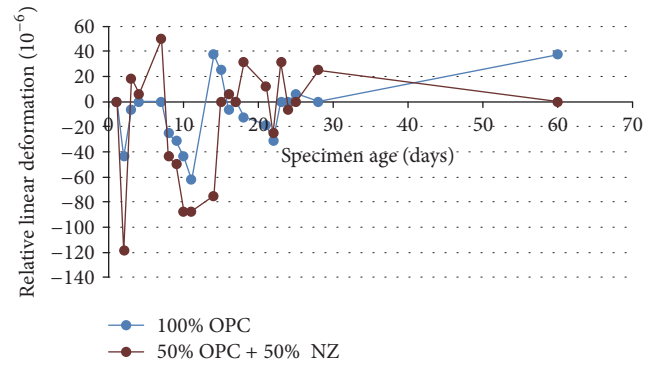


FIGURE 4: Relative linear deformation of the 100% OPC and 50% OPC + 50% NZ mortar.

results for the zeolite paste also refer to the higher need for water to obtain the standard consistency. The initial setting time is practically three times longer than that of cement. Activity index after seven days (20.4) and 28 days (48.5%) shows low increase in strength at an early age and high cement replacement (50%).

Deformation changes in tested mortars are given through 60-day development of relative linear deformation, as shown in Figure 4.

Results of drying shrinkage presented worldwide are often not consistent because of nonuniform methods, apparatus, and curing conditions; these results are discussed in both positive and negative ways [21, 24, 34]. Here, the method of relative linear deformation is given for the direct comparison of two kinds of mortars cured under the same conditions, while the effect of zeolite is clearly visible. The relationship between the linear deformation changes and the risk of cracking is generally known.

The linear deformations of both samples are quite active up to 60 days, while the linear deformation of zeolite samples is somewhat larger than that of the cement-only samples; the values ranges of NZ and OPC based samples are -120 to $+50$ and -62 to $+37$, respectively. Jana [21] reports similar results when using 30% of zeolite as SCM; he obtained about 20% higher drying shrinkage than that of control mixture without zeolite.

3.2. Physical-Mechanical Properties of Natural Zeolite-Based Concrete

3.2.1. Density. The density of hardened concrete is referred as one of the durability-related properties, due to the porosity and permeability context. Concrete porosity is inversely proportional to density. Usually, the concrete permeability increases with an increase in porosity and decreases with an increase in density. The relation between permeability and porosity depends on the pore system properties. Lower concrete porosity leads to reduction in permeability and consequently in better durability. A very highly impermeable concrete reduces or eliminates the ingress of water and other aggressive chemicals and gases. This leads to improved concrete durability due to avoided expansive reactions, which can occur in the presence of these aggressive agents [35].

TABLE 2: The recipes of concrete mixtures. Components proportion was calculated for 1 m³ of fresh concrete.

Mixture	OPC	NZ		SF		NFA-0/4	NCA-4/8	NCA-8/16	PCE	w/b*
	[kg·m ⁻³]	[kg·m ⁻³]	[%]	[kg·m ⁻³]	[%]	[kg·m ⁻³]	[kg·m ⁻³]	[kg·m ⁻³]	[kg·m ⁻³]	[—]
V0	360	—	—	—	—	825	235	740	0.8	0.45
VZ1	330	29	8	—	—	825	235	740	0.8	0.45
VZ2	313	47	13	—	—	825	235	740	0.8	0.45
VZ3	270	90	25	—	—	825	235	740	0.8	0.45
VZ-SF	302	29	8	29	8	825	235	740	0.8	0.45

*Using the k -value = 2 for silica fume in accordance with EN 206.

TABLE 3: Technological parameters of zeolite comparing to cement.

Binder	Water demand	Initial setting time	7-day activity index	28-day activity index
	[%]	[min.]	[%]	[%]
OPC	100.00	110	100	100
50% OPC + 50% NZ	126.62	320	20.4	48.5

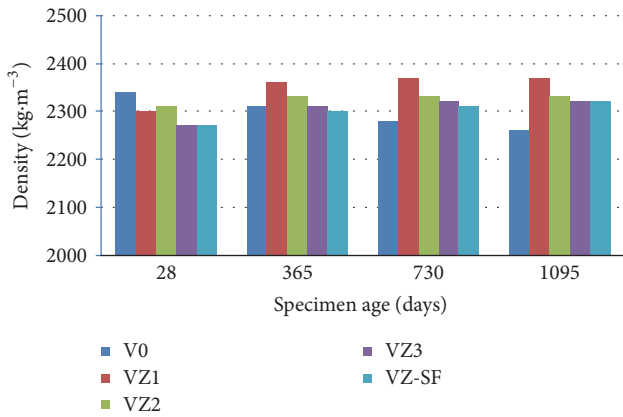


FIGURE 5: Density of hardened concretes after different time of hardening.

The results of density measurement are summarized in Figure 5. Values at 28 days and three years of setting and hardening ranged from 2270 to 2340 kg·m⁻³ and from 2260 to 2370 kg·m⁻³, respectively. The density of all concretes increased during the time, excluding the concrete V0. The highest growth of density was found between measurements after 28 and 365 days—that is, during the first year of hardening. The density increased during the later stage only gradually. Concrete V0 obtained the highest density of all after 28 days but the lowest at the end of the experiment. Concrete VZ1 obtained highest density after one year and also in later stages. The amount of zeolite proportionally affected the density; thus, the higher dosage of zeolite caused the lower concrete density. This is in contrast to some research [36, 37], but, there, the zeolite content was up to 10%. According to Vejmelková et al. [18], both the bulk and matrix densities of the cement-based composites decrease with increase in the zeolite supplementary. Also, Poon et al. [19] observe that 15% replacement of zeolite resulted in lower porosity (affecting density), but a higher replacement amount (25%) increased the porosity at all the studied ages. Based on those comments

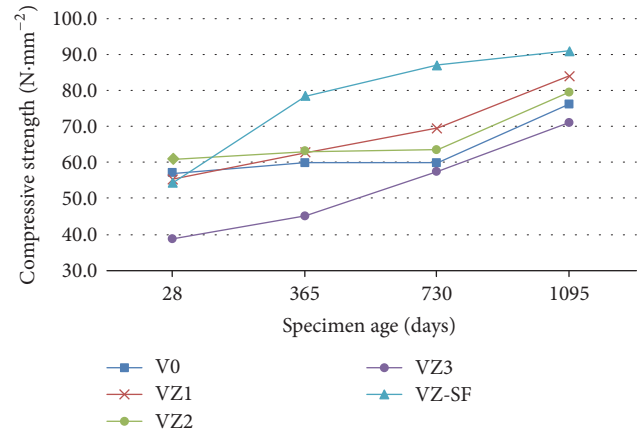


FIGURE 6: Time dependence of compressive strength of hardened concretes.

and our results, the decrease in density can be attributed to the increase in zeolite amount.

The long-term results (one-, two-, and three-year) of all concretes incorporating the natural zeolite are higher than that of the OPC sample (V0), unlike the 28-day values. In this case, the results are lower and do not show the clear dependence on the amount of zeolite. This is clearly visible just after the long-term period. The presence of zeolite manifests itself differently over a longer period of setting and hardening of concrete.

Silica fume in combination with zeolite (concrete VZ-SF) decreased the density significantly compared to the reference concrete (V0) after 28 days. On the other hand, the density of VZ-SF was about 2.6% higher than V0 after three years.

3.2.2. Compressive Strength. The compressive strength was measured on 150 mm cubes after 28, 365, 730, and 1095 days of hardening. The time-development of compressive strength is shown in Figure 6. Generally, compressive strength of all concretes increased during the time, as also reported in previous research [17, 24]. The values after 28 days of

setting and hardening ranged from 40 to 60 MPa, while values after three years ranged from 70 to 90 MPa. The initial reference strength (after 28 days) was almost the same for all concretes except VZ3. In the case of VZ3, the strength development was slower because of the high dosage of zeolite in the binder (25%). The early strength of concrete is commonly supplied by the hydration of CaO and silicates from cement clinker, while the pozzolanic activity of zeolite later influences the strength. The CaO/SiO₂ ratio of the zeolite used was under 0.5 (Table 1), which refers to its pozzolanic nature. It was in accordance with results from Ramezaniyanpour et al. and others [17, 36]. The amount of zeolite in total binder influenced the compressive strength, especially after two and three years of hardening. Concretes VZ1 and VZ2 with 8% and 13% of zeolite supplementary achieved about 16.4% and 6.2% higher compressive strength compared to the reference concrete after two years and 10.4% and 4.5% after three years, respectively. Concrete VZ3 with 25% zeolite supplementary obtained about 3.8% and 6.7% lower compressive strength compared to sample V0 after two and three years, respectively. According to Valipour et al. [38], the optimal content of zeolite to obtain highest compressive strength is 10%.

The significant increase in the compressive strength of all concretes was observed in the long term (three-year period). It confirms the long-term potential of natural zeolite to improve the mechanical properties. The positive change in strength was observed between 28-day and 3-year measurements, following the increase of about 33%, 53%, 30%, 83%, and 67% for concretes V0, VZ1, VZ2, VZ3, and VZ-SF, respectively. The concrete VZ3 achieved the most significant increase in compressive strength during the monitored period.

The silica fume significantly influenced the compressive strength of concrete. While the strength of VZ-SF sample after 28 days was similar to that of the other samples, the long-term strength values after forwarding periods were much higher. It is also evident that the strength development shows convex behaviour for all VZ concretes and concave behaviour for only VZ-SF concrete. Thus, the compressive strength of SF concrete increased faster than zeolite-based ones, but the strength of zeolite samples grew faster at the end of the monitored period.

The activity index was calculated as a relation between compressive strength of the related concrete and the reference concrete (VZ-/V0) after three years of hardening. This value characterizes the improvement or deterioration of zeolite-based concrete compared to the control one. It was 1.1, 1.0, 0.9, and 1.2 for samples VZ1, VZ2, VZ3, and VZ-SF, respectively. As expected, the higher zeolite content in binder caused lower compressive strength against the reference concrete.

With the exception of VZ-3, the long-term results (one-, two-, and three-year) of all concretes incorporating the natural zeolite are higher than that of the OPC sample (V0), except 28-day values. In this case, the results are close to each other and do not show the clear dependence on the amount of zeolite. This is clearly visible just after the long-term period.

3.2.3. Water Absorption. The water absorption of hardened concretes is summarized in Figure 7. Values after 28 days of

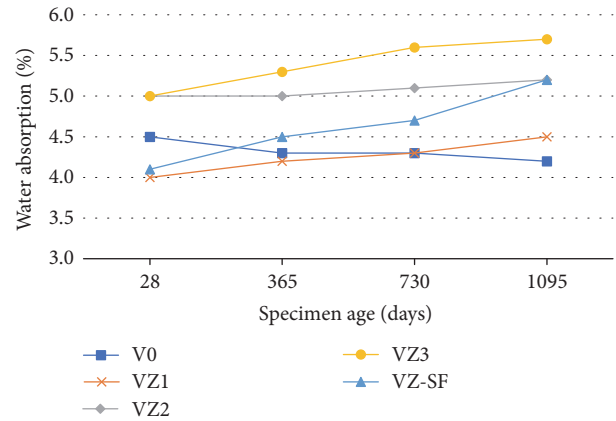


FIGURE 7: Time dependence of water absorption of hardened concretes.

setting and hardening ranged from 4.0 to 5.0%, while values after three years ranged from 4.2 to 5.7%. The long-term changes in water absorption of zeolite-based concretes were not significant. The relative differences in 28-day and three-year values were 12.5, 4.0, and 14.0% for VZ1, VZ2, and VZ3, respectively. The highest increase in water absorption (26.8%) was found for VZ-SF. Contrary to the control OPC sample (V0), values increase during the three-year period while the amount of zeolite in concrete influences the water absorption negatively. The higher content of zeolite leads to increase in water absorption. It is connected with the water absorption of natural zeolite, which is higher than that of cement [34]. Poon et al. [19] report that the porosity increases due to the higher replacement amount (25%) of zeolite at all studied ages; this may also be attributed to the higher absorption ability. It was recognized that the water absorption grew together with density. This result is unexpected, because several research works [17, 24] obtained adverse results.

The long-term results (one-, two-, and three-year) of all concretes including the natural zeolite are higher than that of the OPC sample (V0), unlike 28-day values. In this case, VZ1 and VZ-SF obtained lower values. The presence of zeolite manifests itself differently over a longer period of setting and hardening.

4. Conclusion

In this paper, the technological properties of natural zeolite and the long-term mechanical properties, density, and water absorption of concrete based on natural zeolite as SCM were evaluated. The results can be summarized as follows:

- (i) At high cement replacement (50%) by the zeolite, the zeolite paste led to a higher demand for mixing water to obtain the standard consistency than that of OPC paste. The initial setting time was practically 2.9 times longer. Strength activity index after 28 days was 48.5%; this low increase in strength at an early age reflects the slow hydration process.
- (ii) The long-term density of all zeolite-based concretes was higher than that of OPC concrete, unlike the

28-days values. Although the increase in zeolite amount caused the decrease in density, samples incorporating 25% zeolite achieved higher density than that of OPC in all later ages.

- (iii) A major increase in strength was observed for all samples in the long term (three-year period). An increase in the zeolite amount caused a decrease in compressive strength, but the replacement of 8% and 13% of cement by natural zeolite brought about an improvement in long-term compressive strength compared to the only-OPC-based concrete. A higher replacement (25%) caused a decrease in strength after 28 days of setting and hardening; however, significant positive change (83%) was observed during the three-year period. This confirms the long-term potential of zeolite to improve the strength. Silica fume, in combination with natural zeolite, significantly improved the strength.
- (iv) Long-term changes in water absorption of zeolite-based concretes were not significant, up to 14.0% in relative difference (26.8% for VZ-SF). Except for the V0 sample, values were increasing during the three-year period, while the higher amount of zeolite in concrete negatively influenced the water absorption.
- (v) Generally, the long-term properties of zeolite-based concrete are different from that of 28-day properties, while both the density and compressive strength are influenced positively. The differences in concretes composition are manifested after a longer time, when the results are ordered more clearly and show a better sequence dependence on the sample's composition.

The results demonstrate the long-term potential of SCMs for the improvement of the concrete properties, which are important for the long-term role of concrete in the structure.

Conflicts of Interest

The authors declare that they have no conflicts of interest.

Acknowledgments

This article has been carried out within the project ITMS "Center of Excellent Integrated Research of Progressive Building Constructions, Materials and Technologies" no. 26220120037 and also presents a partial research result of project VEGA-1/0677/14 "Research of Construction Efficiency Improvement through MMC Technologies."

References

- [1] K. Obla, C. Lobo, and L. Lemay, "Specifying Concrete for Durability".
- [2] P. C. Aitcin, *High-Performance Concrete*, Taylor & Francis, Abingdon, UK, 1998.
- [3] P. Tikalsky, B. Mather, and J. Olek, *Concrete Durability*, Transp. New Millennium – State Art Futur. Dir., 2000.
- [4] M. Najimi, J. Sobhani, and A. Pourkhorshidi, "Durability of copper slag contained concrete exposed to sulfate attack," *Construction and Building Materials*, vol. 25, no. 4, pp. 1895–1905, 2011.
- [5] S. Levy and P. Helene, "Durability of concrete mixed with fine recycled aggregates," *Exacta*, vol. 5, no. 1, 2007.
- [6] K. Byfors, "Influence of silica fume and flyash on chloride diffusion and pH values in cement paste," *Cement and Concrete Research*, vol. 17, no. 1, pp. 115–130, 1987.
- [7] V. G. Papadakis, "Effect of supplementary cementing materials on concrete resistance against carbonation and chloride ingress," *Cement and Concrete Research*, vol. 30, no. 2, pp. 291–299, 2000.
- [8] European Committee for Standardization, "(20025). EN 206-1 "Concrete. Part 1:Specification, performance, production and conformity". Brussels".
- [9] D. Caputo, B. Liguori, and C. Colella, "Some advances in understanding the pozzolanic activity of zeolites: The effect of zeolite structure," *Cement and Concrete Composites*, vol. 30, no. 5, pp. 455–462, 2008.
- [10] T. Perraki, E. Kontori, S. Tsvilis, and G. Kakali, "The effect of zeolite on the properties and hydration of blended cements," *Cement and Concrete Composites*, vol. 32, no. 2, pp. 128–133, 2010.
- [11] I. Janotka and L. Krajči, "Utilization of natural zeolite in Portland pozzolan cement of increased sulfate resistance," in *Proceedings of the 5th CANMET/ACI Conf. Durab. Concr.*, pp. 223–238, 2000.
- [12] T. Perraki, G. Kakali, and F. Kontoleon, "The effect of natural zeolites on the early hydration of Portland cement," *Microporous and Mesoporous Materials*, vol. 61, no. 1-3, pp. 205–212, 2003.
- [13] I. Janotka, A. Ray, and S. C. Mojumdar, "Acid and sulfate resistance of Portland cement - natural zeolite mortar," in *Proceedings of 8th CANMET/ACI International Conference on Fly Ash, Silica Fume, Slag and Natural Pozzolans in Concrete, Las Vegas*, pp. 639–652, 2004.
- [14] R. Sersale and G. Frigione, "Natural zeolites as constituents of blended cements," *Studies in Surface Science and Catalysis*, vol. 24, pp. 523–530, 1985.
- [15] T. Yun-Sheng, C. Huang, and K. Hsu, "The pozzolanic activity of a calcined waste FCC catalyst and its effect on the compressive strength of cementitious materials," *Cement and Concrete Research*, vol. 35, no. 4, pp. 782–787, 2005.
- [16] B. Yılmaz, A. Uçar, B. Öteyaka, and V. Uz, "Properties of zeolitic tuff (clinoptilolite) blended portland cement," *Building and Environment*, vol. 42, no. 11, pp. 3808–3815, 2007.
- [17] A. A. Ramezani-pour, R. Mousavi, M. Kalhori, J. Sobhani, and M. Najimi, "Micro and macro level properties of natural zeolite contained concretes," *Construction and Building Materials*, vol. 101, pp. 347–358, 2015.
- [18] E. Vejmelková, D. Koňáková, T. Kulovaná et al., "Engineering properties of concrete containing natural zeolite as supplementary cementitious material: Strength, toughness, durability, and hygrothermal performance," *Cement and Concrete Composites*, vol. 55, pp. 259–267, 2015.
- [19] C. S. Poon, L. Lam, S. C. Kou, and Z. S. Lin, "A study on the hydration rate of natural zeolite blended cement pastes," *Construction and Building Materials*, vol. 13, no. 8, pp. 427–432, 1999.
- [20] V. J. Inglezakis and A. A. Zorpas, *Handbook of Natural Zeolites*, Cyprus Open University, 2012.
- [21] D. Jana, "A new look to an old pozzolan, clinoptilolite A promising pozzolan in concrete," in *Proceedings of the 29th ICMA Conference on Cement Microscopy*, pp. 168–206, Quebec City, West Chester, 2007.

- [22] Y. Kasai, K. Tobinai, E. Asakura, and N. Feng, "Comparative study of natural zeolites and other inorganic admixtures in terms of characterization and properties of mortars," in *Proceedings of the 9th Canmet/ACI Int. Conf. Fly Ash, Silica Fume, Slag Nat. Pozzolans Concr.*, V. D. Malhotra, Ed., pp. 615–634, 1992.
- [23] N. Feng and H. Jia, "Prevention of AAR in cement concrete with natural zeolite," *Concr. Cem. Prod.*, vol. 2, 1995.
- [24] M. Najimi, J. Sobhani, B. Ahmadi, and M. Shekarchi, "An experimental study on durability properties of concrete containing zeolite as a highly reactive natural pozzolan," *Construction and Building Materials*, vol. 35, pp. 1023–1033, 2012.
- [25] S. Y. N. Chan and X. Ji, "Comparative study of the initial surface absorption and chloride diffusion of high performance zeolite, silica fume and PFA concretes," *Cement and Concrete Composites*, vol. 21, no. 4, pp. 293–300, 1999.
- [26] European Committee for Standardization, *EN 196 -3 "Methods of Testing Cement - Part: Determination of Setting Times and Soundness*, 2005, Brussels.
- [27] European Committee for Standardization, *EN 196 - 1, Methods of testing cement - Part 1: Determination of strength*, Brussels, 2005.
- [28] European Committee for Standardization, *EN 15167-1, Ground granulated blast furnace slag for use in concrete, mortar and grout. Part 1: Definitions, specifications and conformity criteria*, Brussels, 2007.
- [29] European Committee for Standardization, *EN 12390-7, Testing Hardened Concrete, part 7: Density of hardened concrete*, Brussels, 2011.
- [30] European Committee for Standardization, *EN 12390-3, Testing Hardened Concrete, part 3: Compressive Strength of Test Specimens*, Brussels, 2010.
- [31] *STN 731316 Determination of moisture, water absorption and capillarity of concrete*, Slovak Office of Standards, Metrology and Testing, Bratislava, 1989.
- [32] S. Özen, *Pozzolanic activity of natural zeolites: mineralogical, chemical and physical characterization and examination of hydration products [Thesis]*, Middle East Technical University, 2013.
- [33] F. Canpolat, K. Yılmaz, M. Köse, M. Sümer, and M. Yurdusev, "Use of zeolite, coal bottom ash and fly ash as replacement materials in cement production," *Cement and Concrete Research*, vol. 34, no. 5, pp. 731–735, 2004.
- [34] T. Markiv, K. Sobol, M. Franus, and W. Franus, "Mechanical and durability properties of concretes incorporating natural zeolite," *Archives of Civil and Mechanical Engineering*, vol. 16, no. 4, pp. 554–562, 2016.
- [35] T. R. Naik, "Concrete durability as influenced by density and/or porosity," Report No. CBU-1997-27, Center for By-Products Utilization, 1997.
- [36] D. Nagrockiene and G. Girskas, "Research into the properties of concrete modified with natural zeolite addition," *Construction and Building Materials*, vol. 113, pp. 964–969, 2016.
- [37] D. Nagrockienė, G. Girskas, and G. Skripkiūnas, "Properties of concrete modified with mineral additives," *Construction and Building Materials*, vol. 135, pp. 37–42, 2017.
- [38] M. Valipour, M. Yekkalar, M. Shekarchi, and S. Panahi, "Environmental assessment of green concrete containing natural zeolite on the global warming index in marine environments," *Journal of Cleaner Production*, vol. 65, pp. 418–423, 2014.

Research Article

The Role of Various Powders during the Hydration Process of Cement-Based Materials

Shuhua Liu, Hongling Wang, and Jianpeng Wei

State Key Laboratory of Water Resources and Hydropower Engineering Science, Wuhan University, Wuhan 430072, China

Correspondence should be addressed to Shuhua Liu; shliu@whu.edu.cn

Received 19 June 2017; Accepted 7 August 2017; Published 11 September 2017

Academic Editor: Prinya Chindaprasirt

Copyright © 2017 Shuhua Liu et al. This is an open access article distributed under the Creative Commons Attribution License, which permits unrestricted use, distribution, and reproduction in any medium, provided the original work is properly cited.

The role of various powders including glass powder (GP), limestone powder (LP), and steel slag powder (SSP) during the hydration process of cement-based materials was investigated by using X-ray diffraction (XRD), thermogravimetric and differential thermal analysis (TG-DTA), scanning electron microscopy (SEM), and strength tests. GP has adverse impact on early strength, but the pozzolanic reaction at later stage enhances the strength development greatly. LP can significantly improve early strength. SSP has a good contribution to the early and later strength of the paste when its content is less than 15%. GP has little effect on the kind of hydration products but relatively large effects on the quantity. Calcium hydroxide (CH) content of GP paste decreases over curing age gradually, which is different from pure cement paste because its pozzolanic activity consumes more CH than that generated from the cement hydration. SSP and LP mainly play a role of filling effect at early stage. Nucleating effect of LP also promotes the early hydration of cement. The hydration of LP occurs at later stage and forms the calcium carboaluminate hydrates. The hydration of SSP is relatively slow, which generates CH at later stage and is effective in the strength development.

1. Introduction

Mineral admixture has become an indispensable component in concrete because it generally has some pozzolanic reactivity during the hydration process. Mineral admixture can replace cement and reduce cost of concrete; moreover, it can improve the workability of fresh concrete or some properties of hardened concrete. Therefore, the use of mineral admixture in concrete brings significant benefits.

Glass powder (GP) is ground waste glass which mainly comes from industrial waste glass (such as flat glass and glass fiber) and household waste glass (such as glass containers and light bulbs) [1]. GP has not been used as a cement replacement until recent years. It is amorphous and contains large quantities of silicon and calcium. Soda-lime glass is pozzolanic or even cementitious in theory when it is ground enough [1]. The use of GP in cementitious materials can effectively enhance the strength and inhibit the ASR reaction of the system [2–4]. GP was used to prepare reactive powder concrete (RPC) by replacing partial Portland cement to reduce the cost [5, 6]. It is found that using Portland cement, glass powder, silica fume, and water reducer can prepare

high performance concrete with compressive strength up to 100 MPa. Concrete with GP has improved properties, that is, higher strength, lower dry shrinkage, and so on than those of the concrete with fly ash [3, 7]. However, the study on the action mechanism of GP in cement-based materials is still at the initial stage.

The main component of limestone powder (LP) is calcite (CaCO_3), which is a cheap and easily available material. At present, LP is mainly used to replace partial fine aggregate or as mineral admixture in the concrete. As a mineral admixture, LP is observed to have hydration reactivity when it is ground to a certain degree of fineness and it needs to have a certain environment and enough hydration time [8]. LP reacts with aluminum phase in cement clinker to form calcium carboaluminate hydrates, which effectively accelerates the hydration and hardening process [9], and thus improves the properties of concrete [10, 11].

Steel slag powder (SSP) is the slag exhausted from converter, electric furnace, and refining furnace, whose main components are silicate and ferrite. In developed countries, the majority of SSP is used as aggregate in concrete [12]. China has studied the application of SSP as mineral admixture in

TABLE 1: Chemical compositions of raw materials/mass, %.

Compositions	SiO ₂	Al ₂ O ₃	CaO	Fe ₂ O ₃	MgO	SO ₃	K ₂ O	Na ₂ O	P ₂ O ₅	loss
Cement	21.25	2.91	63.09	3.24	0.68	3.36	1.12	0.31	0.17	3.52
GP	55.75	10.64	6.60	0.28	1.01	0.27	0.54	9.92	0.03	11.9
LP	1.79	0.56	54.69	0.35	0.40	0.03	—	0.06	—	41.93
SSP	14.11	3.51	42.39	17.45	6.60	0.50	0.13	0.22	1.63	8.72

recent thirty years. The studies have shown that SSP can be used as a kind of active cementitious material, but its activity is much lower than that of cement clinker.

Recently, little existing literatures focused on investigation of the hydration properties and process of the three various powders. As mineral admixtures, the hydration process and strength development of cement-based materials containing the three powders are relatively different. In this paper, GP, LP, and SSP will be used as mineral admixtures to study the role during the hydration process of cement-based materials.

2. Experimental

The ordinary Portland cement PO 42.5 (POC) complied with the Chinese standard GB175-2007 is used in this test. The chemical compositions of GP, LP, SSP, and POC determined by X-ray fluorescence (XRF) are listed in Table 1. The main compositions of GP are SiO₂, Al₂O₃, and Na₂O accounting for 55.75%, 10.64%, and 9.92%, respectively. LP contains high content of CaCO₃, which mainly relied on raw limestone. The content of CaO, Fe₂O₃, and SiO₂ in SSP is around 74%, because the source of steel slag is iron and steel materials, smelting slag material, eroded lining refractory, and the sediment carried by the solid material. SSP contains C₂S, which can also be detected by XRD test.

40 mm × 40 mm × 40 mm paste specimens used in this paper were prepared by the paste mixer with water to binder ratio of 0.4. All the specimens were cured in normal environment with relative humidity (RH) higher than 90% and temperature of 20 ± 2°C till the stipulated age of 3, 7, 28, and 90 days. The mixture ratios are shown in Table 2. The content of mineral mixtures in cementitious system is 15%, 30%, and 45% by mass. The samples containing 30% powders were used for microtest. The compressive strength of the pastes at different ages was tested by WAY-2000, a battery solution type compression testing machine. Specific test procedure is referred to GB/T17671-1999, *Method of Testing Cement-Determination of Strength*. The cores of broken pastes were collected to be soaked in anhydrous ethanol to stop the continued hydration for SEM tests. Before XRD and TG-DTA tests, the specimens were removed from the ethanol and quickly ground into powder in the agate mortar and dried in 60°C for 2 hours to avoid carbonization. The chemical compositions were measured by Axios advanced X-ray fluorescence instrument, in voltage range from 30 to 60 kV, current 50 to 100 mA. Morphology of the specimens was investigated by using a SEM (JSM-5610LV, Japan). The XRD was detected by X'Pert Pro, PANalytical of Netherland, with scanning speed of 6°/min. The TG-DTA experiments

TABLE 2: Mix proportions of the cement pastes/g.

Samples	Cement	GP	LP	SSP	Water
PC	600	0	0	0	240
GP-15	510	90	0	0	240
GP-30	420	180	0	0	240
GP-45	330	270	0	0	240
LP-15	510	0	90	0	240
LP-30	420	0	180	0	240
LP-45	330	0	270	0	240
SSP-15	510	0	0	90	240
SSP-30	420	0	0	180	240
SSP-45	330	0	0	270	240

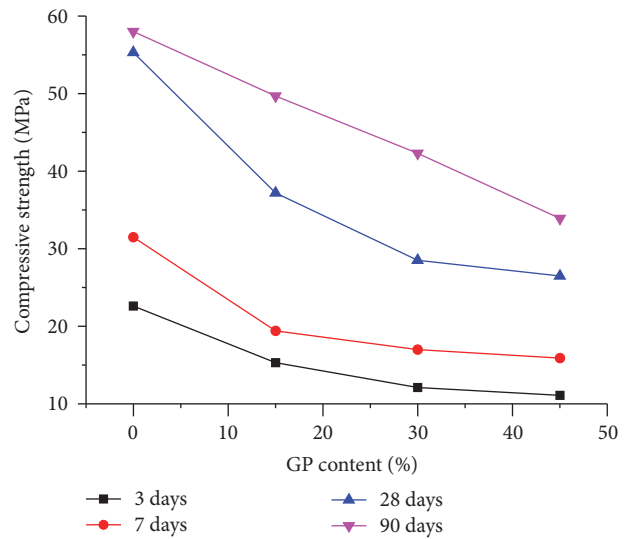


FIGURE 1: Effect of GP content on the compressive strength of the paste.

were measured on the Diamond TG/DTA analyzer, produced by Perkin Elmer Instruments Plant (Shanghai), in the temperature range from 0 to 900°C, using platinum crucibles with approximately 4 mg of sample, under dynamic N₂ atmosphere (50 mL/min).

3. Results and Discussion

3.1. Strength. Figures 1–3 present the compressive strength of the three groups. According to the results, GP reduces the early strength of the paste, and the strength reduction becomes more obvious with the increase of GP content, which indicates that GP has significant adverse effect on the

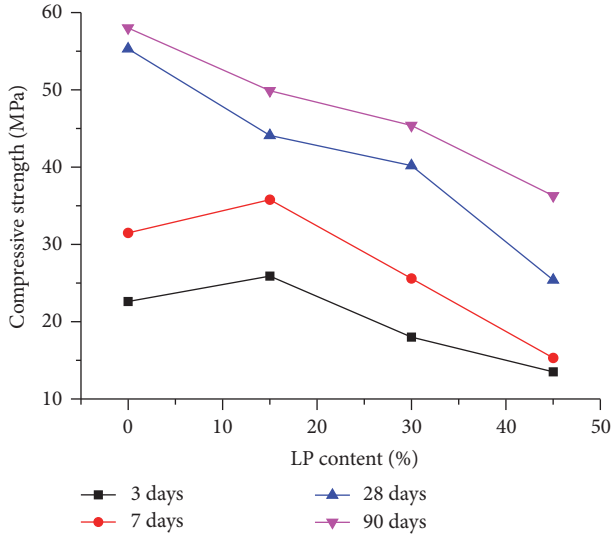


FIGURE 2: Effect of LP content on the compressive strength of the paste.

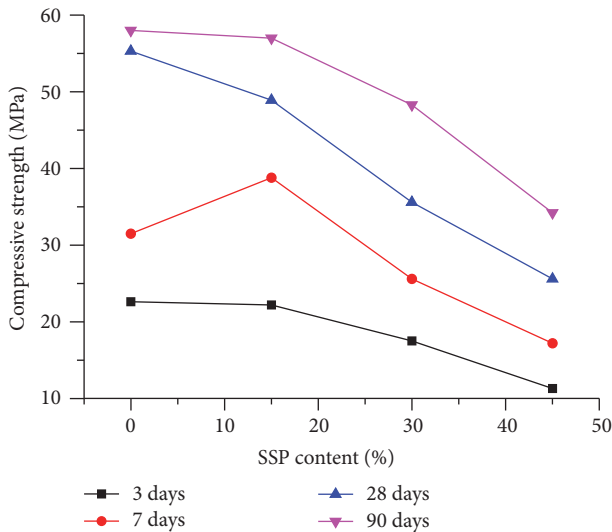


FIGURE 3: Effect of SSP content on the compressive strength of the paste.

strength of the composite cementitious materials. But, the later strength of the GP sample improves faster than that of the pure cement (PC) sample. The strength of PC paste at 90 days increases 4.9% higher than that at 28 days, while GP-15, GP-30, and GP-45, respectively, increase 33.7%, 48.3%, and 17.9%. The characteristics of the multiedges and smooth surface of the glass particles might reduce the early mechanical properties of the cementitious system. Furthermore, GP has no independent hydraulicity but has high pozzolanic activity. At the later stage, GP reacts with $\text{Ca}(\text{OH})_2$, the hydration product of cement, and generates calcium silicate hydrate (C-S-H) which makes the microstructure denser and improves strength.

Different from GP group, the strength of LP group at 3 and 7 days first increases and then decreases along with the

increase of LP content. When the content is 15%, the paste strength increases obviously.

When the content increases to 30%, the paste strength decreases and is lower than that of PC sample. The strength at 28 and 90 days is all less than that of PC sample. Moreover, the more the LP content is, the more the strength decreases. The reason is that a proper content of LP provides the nucleation site [13] for cement hydration at early stage, which promotes early hydration of cement [14] and thus improves the strength; but at the later stage, the hydrates from the cementitious system containing LP are less than that of PC sample, resulting in lower strength [15].

The strength of SSP group increases along with the curing age. 15% SSP content has little reduction effect on the strength and the strength at 7 days even is higher than that of PC sample. When the content is 30% or higher than 30%, the strength decreases rapidly, which suggests that large amount of SSP is disadvantageous to the strength.

In order to analyze the activity of the three powders, the activity index [16] is used to reflect their activity. The calculation progress is as formulas (1) to (3). Here, R_{sa} is the relative strength of cement paste containing powders, R_a is the strength of cement paste containing powders, and q_0 is the mass fraction of the cement. For the reference (PC sample), $q_0 = 100$, its relative strength is R_{sc} . R_c is the reference strength,

$$R_{sa} = \frac{R_a}{q_0}, \quad (1)$$

$$R_{sc} = \frac{R_c}{100}.$$

Although the cement content of the paste containing various powders decreases correspondingly compared to PC group, R_a is higher than R_c and R_{sa} is higher than R_{sc} in general because of the enhancement of hydration activity effect. And the difference between the two is relative strength of the hydration activity effect contribution, which is called relative strength of hydration activity (R_{sp}). The calculation is formula

$$R_{sp} = R_{sa} - R_{sc}. \quad (2)$$

Thus a relative index is obtained, which is the contribution rate of hydration activity (P_a), which can be used to characterize the hydration activity contribution of the powders in the cement paste. The calculation formula is as follows, and the results are shown in Table 3:

$$P_a = \frac{R_{sp}}{R_{sa}} = \frac{R_{sa} - R_{sc}}{R_{sa}} = 1 - \frac{R_{sc}}{R_{sa}} = 1 - \frac{R_c * q_0}{R_a * 100}. \quad (3)$$

The contribution rate of GP increases along with the curing time. The value of contribution rate developing from early negative to the late positive reveals that the pozzolanic reaction degree of GP at the later stage is significantly higher than that at the early stage. LP's early contribution rate is high and decreases along with the curing time in general, which indicates that the early filling effect and accelerating effect obviously improve the strength of the paste, but the later hydration

TABLE 3: The compressive strength contribution rate of the mineral mixtures' hydration activity.

Samples	3 days	7 days	28 days	90 days
GP-15	-0.25	-0.38	-0.26	-0.10
GP-30	-0.31	-0.30	-0.36	0.04
GP-45	-0.12	-0.09	-0.15	0.06
LP-15	0.26	0.25	-0.06	0.01
LP-30	0.13	0.14	0.04	0.11
LP-45	0.08	-0.13	-0.20	0.12
SSP-15	0.14	0.25	0.04	0.14
SSP-30	0.10	0.14	-0.08	0.16
SSP-45	-0.10	-0.01	-0.19	0.07

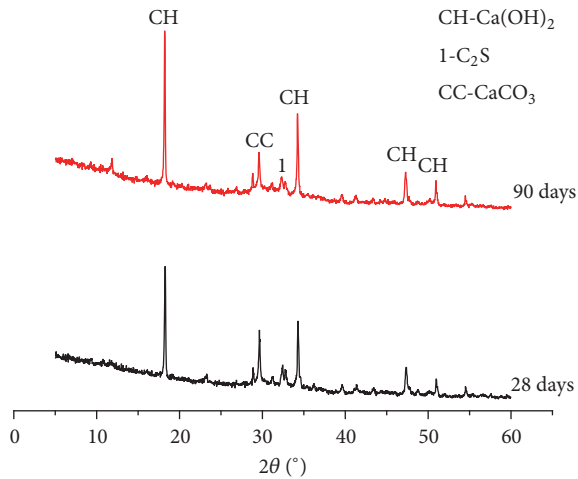


FIGURE 4: XRD patterns of PC paste at different curing ages.

activity is low. SSP has better early filling effect and the later hydration activity works a long time; thus the SSP group has higher early and later contribution rate than GP group.

3.2. Hydration Products

3.2.1. XRD. Figures 4–7 display the hydration products of the pastes with different powders. The main crystal hydrates of GP samples are similar to those of PC paste, that is, $\text{Ca}(\text{OH})_2$ (CH), calcium aluminate hydrate (CAH), and unreacted clinker, because the main chemical compositions of GP and cement are similar. Compared with the PC sample, the CH of GP group decreases gradually along with curing time, because GP consumes some CH by pozzolanic reactivity at the later stage. GP has feeble pozzolanic reactivity at early stage, which mainly occurs at later stage. The pozzolanic reactivity of GP needs to be under certain excitation conditions, such as enough alkali, thermal, and physical conditions [17]. In this experiment, the pozzolanic reactivity of GP is excited by an alkaline environment produced by cement hydration.

Compared with GP group, Figure 6 displays that CH diffraction peak of LP group significantly reduces, while CaCO_3 (CC) diffraction peak is greatly enhanced, which is main composition of LP. A small amount of calcium carboaluminate hydrates $\text{C}_3\text{A}\cdot\text{CaCO}_3\cdot 11\text{H}_2\text{O}$ diffraction peak can

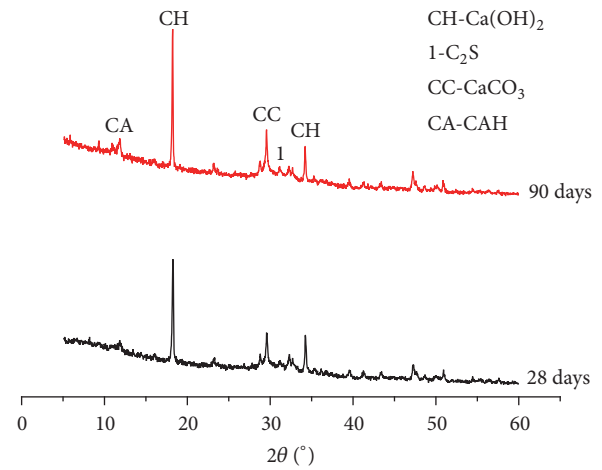


FIGURE 5: XRD patterns of GP-30 cement paste at different curing ages.

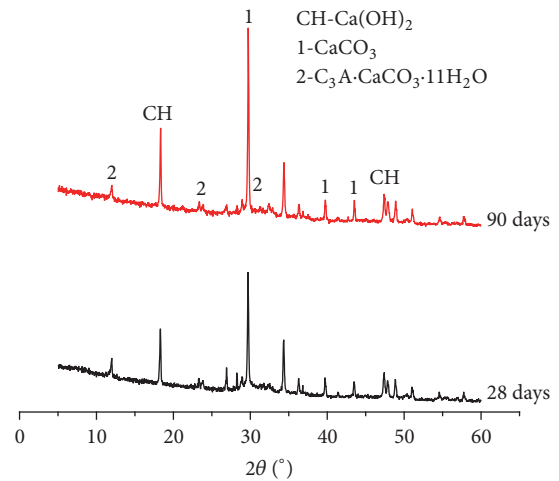


FIGURE 6: XRD patterns of LP-30 cement paste at different curing ages.

be found at 90 days but hardly found at 28 days. It is probably because the cement contains a little C_3A and LP reacts with C_3A in cement to generate carboaluminate hydrates; thus it has a little strength contribution rate at later stage. The formation of calcium carboaluminate hydrates has been found in other researches, the generation time may be at 7 to 127 days, and the time is based on reaction activity of different LP [18].

Figure 7 displays XRD pattern of SSP, which shows that SSP contains C_2S . Figure 8 displays the hydration products of SSP group at 28 days and 90 days. The main crystal hydration products are CH, the unhydrated clinker, and a small amount of CC. The CH content of SSP group gradually increases along with the curing time because SSP consumes no CH but C_2S generates CH, and the cement hydration continues to produce CH, so the CH content will increase overall which proves that the later strength contribution rate of SSP can keep high over a long time.

3.2.2. TG-DTA. The TG-DTA curves of the pastes are shown in Figures 9–12. The characteristics of all TG-DTA curves

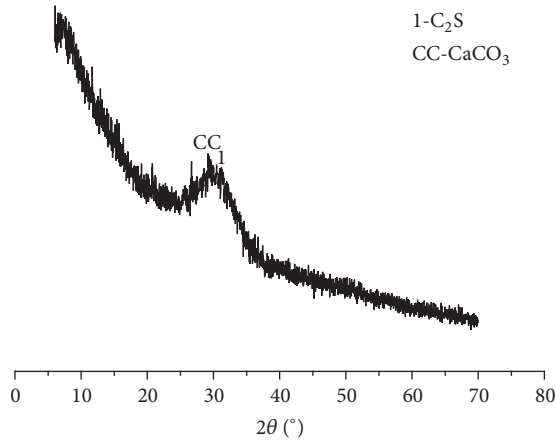


FIGURE 7: XRD pattern of SSP.

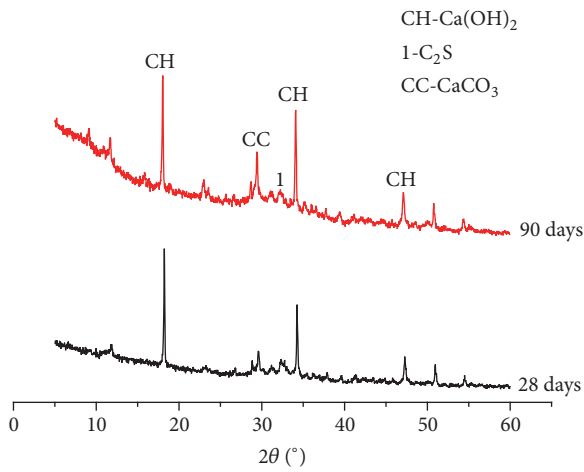


FIGURE 8: XRD patterns of SSP-30 cement paste at different curing ages.

are roughly the same. All the DTA curves have an obvious endothermic peak at 400 to 500°C where the samples mainly take off the coordinated water. The position of highest endothermic peak is about 470°C which is caused by the CH and C-S-H's (mainly CH) dehydrated decomposition where the TG curves have a significant weight loss gradient which relates to the weight loss of CH [19].

Based on the endothermic peak and the weight loss rate of TG-DTA curves, the CH content can be calculated quantitatively. The dehydrated decomposition of CH will occur at 400 to 500°C which will result in a loss in quality and the content of CH can be calculated as formula (4). The CH content is shown in Figure 13.

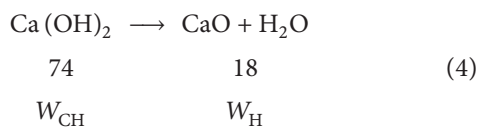


Figure 13 indicates that the CH content of LP sample, in accordance with PC sample, increases gradually over curing time which is consistent with the CH diffraction peaks of

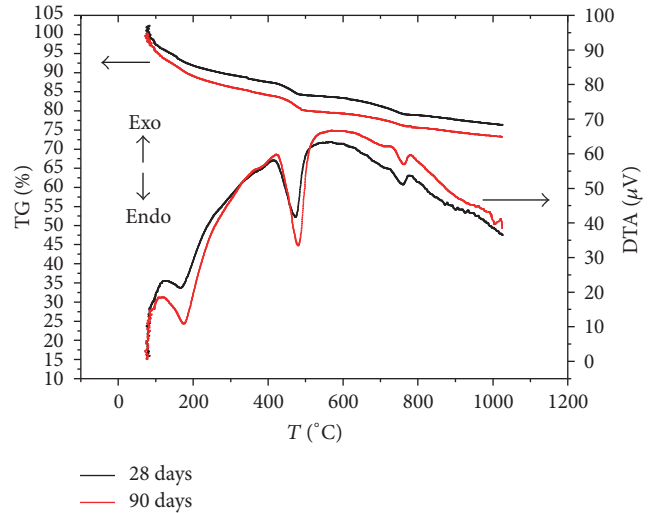


FIGURE 9: TG-DTA curves of PC paste at different curing ages.

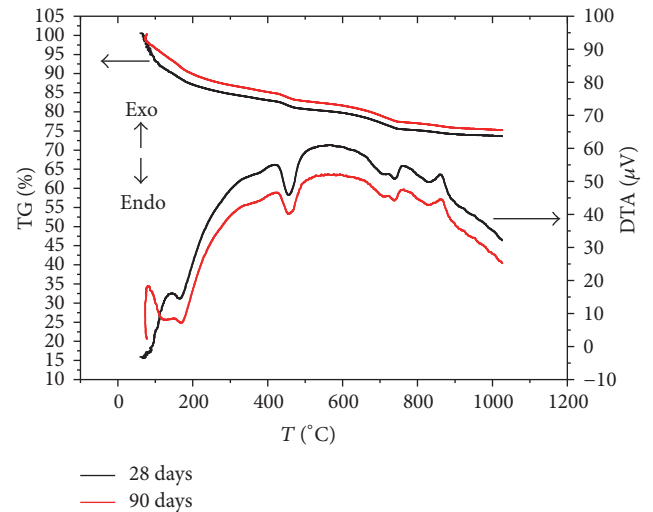


FIGURE 10: TG-DTA curves of GP-30 cement paste at different curing ages.

XRD patterns. And it is the same as SSP sample because both cement and SSP can generate CH instead of the CH consumption resulting from the pozzolanic hydration which has been proven by the XRD patterns. Different from PC, LP, and SSP, the CH content of GP sample declines along with the curing time because GP consumes CH during the pozzolanic reaction, which has also been revealed in the XRD patterns. Along with the curing time, on the one hand, the cement generates CH; on the other hand, GP consumes some CH. In fact, the amount of CH changing along with curing time is determined by the relative content of cement and GP and their reaction speed.

3.2.3. SEM. SEM images of the pastes at 28 and 90 days are shown in Figures 14–17. Figure 14(a) reveals that PC paste at 28 days has a large amount of fibrous C-S-H gel, some needle-shaped ettringite, and hexagonal CH crystals which forms a framework by staggering, overlapping to a network structure

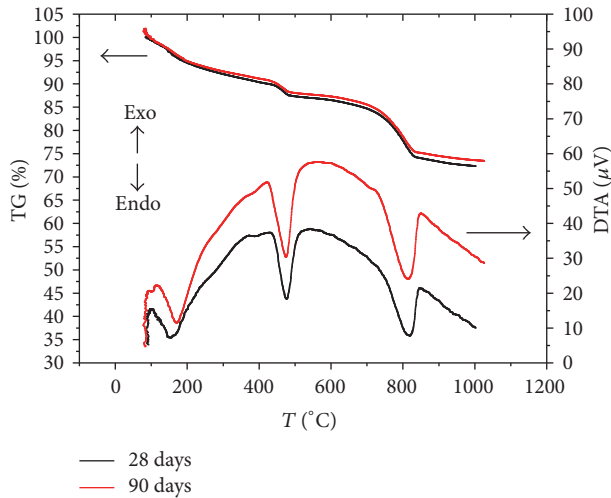


FIGURE 11: TG-DTA curves of LP-30 cement paste at different curing ages.

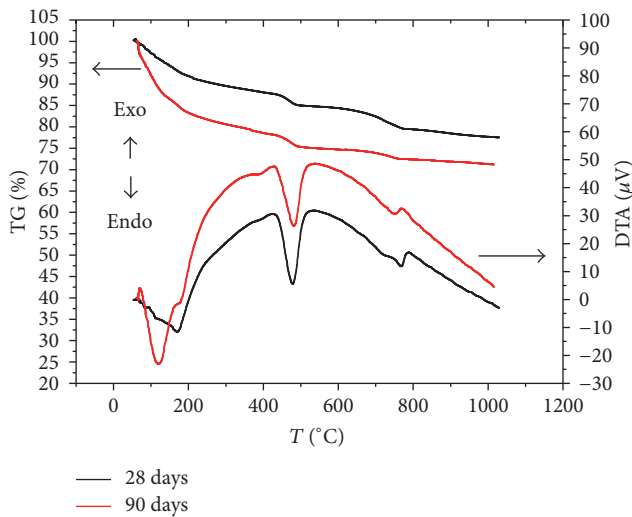


FIGURE 12: TG-DTA curves of SSP-30 cement paste at different curing ages.

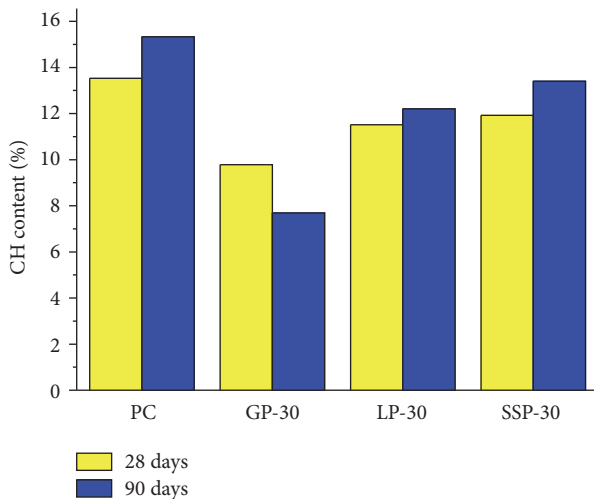


FIGURE 13: CH content of the pastes at different curing ages.

and connecting with the surrounding unhydrated cement particles. But, the microstructure of the paste at 28 days appears loose. Figure 14(b) displays that the cement hydration is more adequate over curing age, and various hydration products fill into the original loose pores and form dense microstructure. The more hydration products are produced over curing age, similar to the TG-DTA and XRD results.

Similar to the PC sample, a large number of fibrous C-S-H gel can also be observed in Figure 15(a), and sometimes it also presented strip or rod-like, tubular, foil-like sheet [20]. The microstructure of the paste containing GP becomes denser than that of PC sample; it is difficult to observe and identify the crystal phases. GP plays the role as the filler at the early stage. It can be found from Figure 15(b) that the paste has formed dense microstructure, and most of the hydration products are unable to identify from the morphology. GP consumes CH generated by cement hydration and forms C-S-H gel, which has been proven by XRD and TG-DTA tests. C-S-H gel connects with other hydrates and forms a denser entirety, which plays an important role in the improvement of strength and microstructure and illustrates why the strength contribution rate of GP becomes positive at the later stage.

Figure 16(a) displays that the hydration products of LP-cement paste at 28 days adhere to the surface of LP particles. The hydration products of C_3S generate free Ca^{2+} which will produce hydration products along the surface of limestone particles; this is the so-called "crystal nucleus effect." This effect can promote the early cement hydration and increase the early strength but hinder the development of later strength, which is consistent with the strength test. Figure 16(b) shows that the C-S-H gel presents II type network at 90 days. At the same time, LP particle surface has been eroded, which confirms that LP takes part in the later hydration reaction again.

Figure 17(a) shows that the microstructure is loose; thus the early hydration degree of SSP is very low at 28 days. It can be seen from Figure 17(b) that C-S-H gel has been basically filled in the pore system at 90 days. The surface of the SSP has been corroded seriously and covered by C-S-H gel which indicates that SSP reacts with cement at the later stage. CH crystals have been gradually surrounded by other hydration products and formed dense microstructure, which better explains why SSP has a relative high strength contribution rate over a long time.

4. Conclusions

(1) GP has negative effect on the early strength but a high strength development due to the pozzolanic reaction at later stage. LP can obviously improve the early strength, especially at 3 and 7 days; it mainly plays a role of filling effect and nucleating effect at the early stage and reactive effect at later stage. SSP has a high contribution to the early and later strength of the paste when its content is under 15%. The early filling effect and the later hydration of SSP improve the strength contribution rate over a long time.

(2) GP has little effect on the kind of hydration products, but relatively large effect on the quantity. CH content of PC sample increases gradually along with the curing age,

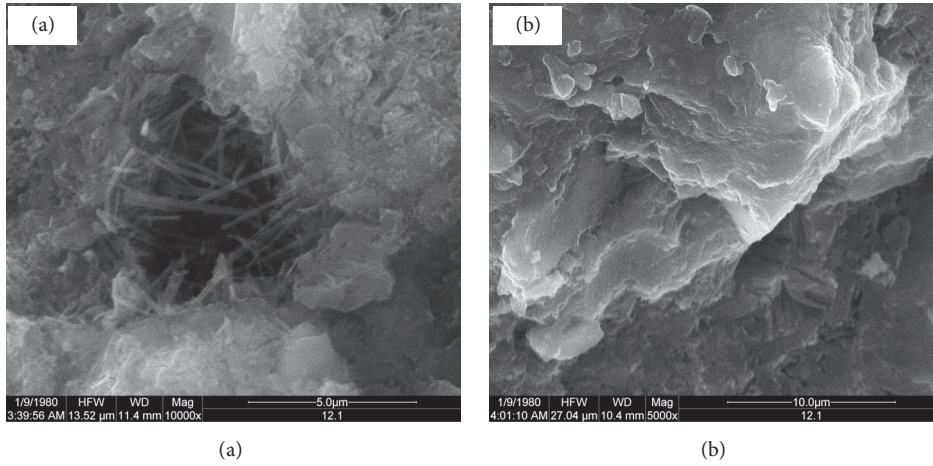


FIGURE 14: SEM images of PC samples at curing age of (a) 28 days and (b) 90 days.

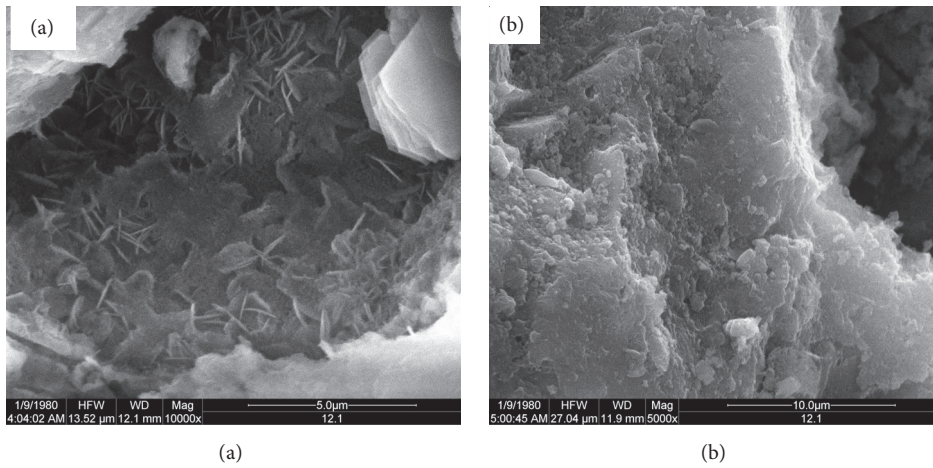


FIGURE 15: SEM images of GP-30 cement samples at curing age of (a) 28 days and (b) 90 days.

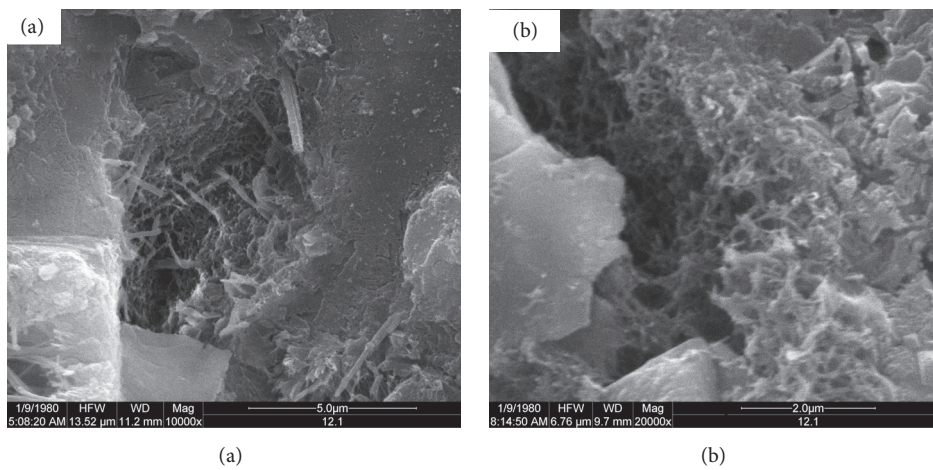


FIGURE 16: SEM images of LP-30 cement samples at curing age of (a) 28 days and (b) 90 days.

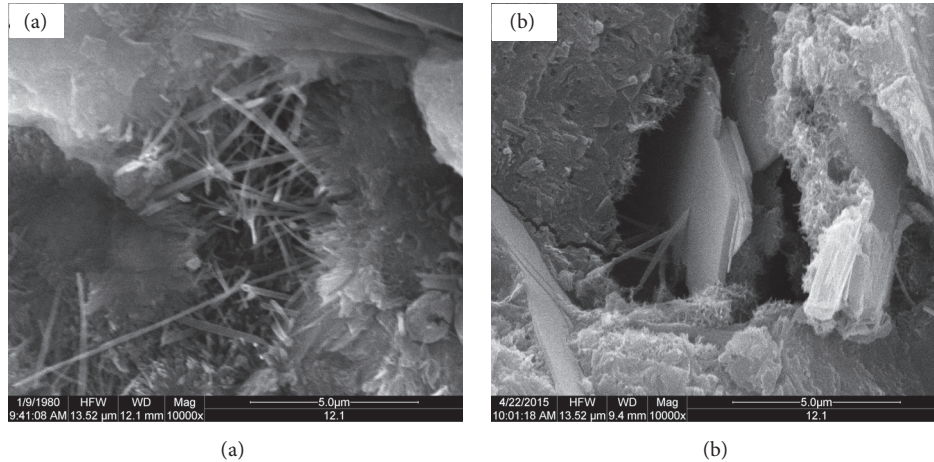


FIGURE 17: SEM images of SSP-30 cement samples at curing age of (a) 28 days and (b) 90 days.

while the GP group is contrary. The CH content produced by cement hydration gradually increases, which stimulates the pozzolanic activity of GP; GP consumes CH more than that cement hydration generates. And CH content of LP and SSP samples are similar to PC group which increases along with curing age. The LP hydration product calcium carboaluminate hydrates can be detected by XRD and also be confirmed by SEM. The active substances C_2S of SSP generate CH at the later stage.

(3) GP, LP, and SSP mainly play the role of filling effects at the early stage, and the nucleating effect of LP promotes the early hydration of cement. The surface of GP, LP, and SSP has been eroded at 90 days indicating that they take part in hydration reaction at later stage, which is also proven by the strength tests.

Conflicts of Interest

The authors declare that they have no conflicts of interest.

Acknowledgments

This project is funded by the National Key R&D Program of China (2016YFC0401907) and Opening Funds of Guangxi Key Laboratory of New Energy and Building Energy Saving (15-J-22-4-001).

References

- [1] Z. Z. Bian, "The recycle and utilization of waste glass in China looked from the practice of developed countries," *Glass*, vol. 60, no. 1, pp. 51–55, 2003.
- [2] G. S. Xie, Y. N. Kong, and S. H. Liu, "Research progress on alkali aggregate reaction of glass concrete," *Advanced Materials Industry*, no. 7, pp. 65–71, 2012.
- [3] A. Shayan and A. Xu, "Value-added utilisation of waste glass in concrete," *Cement and Concrete Research*, vol. 34, no. 1, pp. 81–89, 2004.
- [4] W. Jin, *Alkali-silica reaction in concrete with glass aggregate: a chemo-physico-mechanical approach [Ph.D. thesis]*, Columbia University, New York, NY, USA, 1998.
- [5] S. H. Liu, Z. H. Xu, Y. B. Sun et al., "Study on the application of waste glass powder in ultra-high performance cement-based material," *China Concrete and Cement Products*, no. 11, pp. 77–79, 2012.
- [6] C. Qu, Z. Y. Gao, S. H. Liu et al., "Study on the application of waste glass powder in reactive powder concrete," *Concrete*, no. 8, pp. 82–84, 2011.
- [7] N. Schwarz and N. Neithalath, "Influence of a fine glass powder on cement hydration: comparison to fly ash and modeling the degree of hydration," *Cement and Concrete Research*, vol. 38, no. 4, pp. 429–436, 2008.
- [8] L. D. Zhang and J. M. Mou, *Nanostructures and Nanomaterials: Synthesis, Properties, and Applications*, The Science Publishing Company, 2001.
- [9] G. Kakali, S. Tsivilis, E. Aggeli, and M. Bati, "Hydration products of C_3A , C_3S and Portland cement in the presence of $CaCO_3$," *Cement and Concrete Research*, vol. 30, no. 7, pp. 1073–1077, 2000.
- [10] P. Poitevin, "Limestone aggregate concrete, usefulness and durability," *Cement and Concrete Composites*, vol. 21, no. 2, pp. 89–97, 1999.
- [11] P. Lu and S. B. Lu, "Effect of $CaCO_3$ on hydration of C_3S ," *Journal of the Chinese Ceramic Society*, vol. 15, no. 4, pp. 28–32, 1987.
- [12] J. N. Murphy and T. R. Meadow, "Enhancement of the cementitious properties of steelmaking slag," *Canadian Metallurgical Quarterly*, vol. 36, no. 5, pp. 331–335, 1997.
- [13] S. H. Liu, "Influence of limestone powder on the hydration characteristic of complex binder," *Journal of Building Materials*, vol. 13, no. 2, pp. 218–221, 2010.
- [14] R. J. Detwiler and P. D. Tennis, *The Use of Limestone in Portland Cement: A State of the Art Review*, Portland Cement Association, Skokie, Ill, USA, 1996.
- [15] H. Yuan, "The influence of limestone powder on concrete performance," *Central South University*, vol. 21, no. 2, pp. 13–15, 2009.
- [16] X. C. Pu, *Ultra-High Strength High Performance Concrete*, Chongqing University Press, 2004.
- [17] Q. B. Yang, S. Zhang, S. Huang, and Y. He, "Effect of ground quartz sand on properties of high-strength concrete in the steam-autoclaved curing," *Cement and Concrete Research*, vol. 30, no. 12, pp. 1993–1998, 2000.

- [18] W. A. Klemm and L. D. Adama, *Carbonate Additions to Cement*, American Society for Testing and Materials, Philadelphia, Pa, USA, 1990.
- [19] Z. F. Xu, M. X. Zhang, and J. H. Li, "Study on properties of low grade compressive strength cement-based composite materials modified by superfine silica fume," *Bulletin of the Chinese Ceramic Society*, vol. 31, no. 2, pp. 401–405, 2012.
- [20] R. Z. Yuan, *Cementitious Materials Science*, Wuhan University of Technology Press, 1996.

Research Article

Development and Characterization of Norite-Based Cementitious Binder from an Ilmenite Mine Waste Stream

Mahmoud Khalifeh,¹ Arild Saasen,¹ Helge B. Larsen,² and Helge Hodne¹

¹Department of Petroleum Engineering, University of Stavanger, 4036 Stavanger, Norway

²Department of Mathematics and Natural Sciences, University of Stavanger, 4036 Stavanger, Norway

Correspondence should be addressed to Mahmoud Khalifeh; mahmoud.khalifeh@uis.no

Received 6 May 2017; Revised 5 July 2017; Accepted 20 July 2017; Published 23 August 2017

Academic Editor: Kedsarin Pimraksa

Copyright © 2017 Mahmoud Khalifeh et al. This is an open access article distributed under the Creative Commons Attribution License, which permits unrestricted use, distribution, and reproduction in any medium, provided the original work is properly cited.

Norite is a major type of solid waste generated during the production of ilmenite. This study focuses on the usability of norite as a solid precursor of alkali-activated cement. Sensitivity analysis was performed to find the influence of different alkali types and particle sizes of the source material on polycondensation. Norite was ground and mixed with sodium hydroxide and potassium hydroxide solutions to produce a binder. Potassium-containing systems were more effective compared to sodium-containing systems with respect to strength development. The X-ray diffraction patterns indicated formation of zeolites, albite, and oligoclase based on the type of activator and used additives. The patterns also revealed formation of an amorphous phase in the matrices of the binder that was cured at 87°C. Microstructure analysis revealed some degree of crystallization with different Si : Al ratios, which indicated heterogeneity of the binder matrices.

1. Introduction

Alkali-activated binders are a class of inorganic alkaline polymers, which are produced during the alkaline activation of silica-rich and alumina-rich materials. The reaction shows a complex process. Generally, in an alkaline medium, the bonds of Si-O-Si are broken and aluminum (Al) atoms penetrate into the original Si-O-Si structure. Consequently, aluminosilicate gels (oligomers) are formed and finally polycondensation takes place. Cations (e.g., Na⁺, K⁺, and Ca⁺) must be present in the framework cavities to balance the negative charges of ions [1, 2]. The result is a cementitious phase with high mechanical strength and high fire and acid resistance. Polycondensation depends on parameters such as chemical and mineralogical composition, particle size, and surface area of the source materials. In addition, curing pressure and temperature, Si : Al ratio of the used substances (the active silica content), alkali type (e.g., NaOH, KOH), alkali concentration, liquid-to-solid ratio, and types of additives significantly influence the binder synthesis [3–8].

Based on the source used, different types of binders can be produced such as fly ash-based and blast furnace slag-based

binders. Utilization of fly ashes in the production of binders has been extensively studied [9, 10]. However, few studies have been carried out on the usability of natural rocks to make binders in alkaline media.

One of the world's largest ilmenite producers has its quarry on the southwest coast of Norway. The mine is operated by Titania AS and the facility uses different methods to separate ilmenite from ore. The facility produces 850,000 metric tons of ilmenite concentrate per year. Ilmenite is a mineral chemically described as FeTiO₃. When the iron is removed, the final product becomes TiO₂ which is known as "titanium white," a widely used white pigment. Normally, ilmenite is found in large quantities in the anorthosite or norite rocks. Thus, norite or anorthosite must be separated from the valuable ilmenite. This can be done by conventional separation techniques that leave large amounts of ground norite and anorthosite particles as a waste stream. Norite is one of the main waste tailings during the production of ilmenite at Titania AS. The norite used in this study was supplied by Titania AS.

Norite is an intrusive igneous rock and is predominantly composed of orthopyroxene and plagioclase. Orthopyroxene

TABLE 1: Chemical composition of norite (wt.%).

SiO ₂	TiO ₂	Al ₂ O ₃	Fe ₂ O ₃	MgO	CaO	Na ₂ O	MnO	K ₂ O	P ₂ O ₅	Cr ₂ O ₃	SO ₃	LOI
43	8.2	15.5	12.5	6.8	6.6	3.4	0.1	0.9	0.3	0.03	0.1	2.57

TABLE 2: Traced minerals in the norite.

Minerals	Mass%
Plagioclase [(Na, Ca, Al)-silicates]	64
Hyperstone [(Ca, Mg, Fe, Al)-silicates]	10
Biotite [(K, Mg, Al)-silicates]	7
Other silicates	5
Ilmenite [FeOTiO ₂]	13
Sulfides	0.5
Apatite [Ca(PO ₄) ₃ (F, Cl, OH)]	0.5

TABLE 3: Chemical composition of GGBFS (wt.%).

SiO ₂	Al ₂ O ₃	CaO	MgO	TiO ₂	Mn ₂ O ₃	S ²⁻	Na ₂ O
34	13	31	17	2.4	0.6	1.1	0.9

is an inosilicate and therefore has interlocking chains of silicate tetrahedra. Plagioclase is a common series of aluminosilicate (tectosilicate) minerals within the feldspar family. In the Streckisen classification system, norite is in the group with gabbro and anorthosite. Similar to gabbro and anorthosite, norite is very rich in plagioclase compared to K-feldspar, feldspathoids, and quartz [11, 12]. Therefore, norite has the potential to be utilized as a solid precursor in the development of a new cementitious binder. The current study presents a fundamental procedure for developing a norite-based binder in alkali media.

2. Experimental Program

2.1. Materials. Titania AS provided the norite; its chemical analysis and the traced minerals are presented in Tables 1 and 2. The laboratory at Titania AS reported a pH value of 6.5 for the norite [13]. Sodium hydroxide (NaOH) and potassium hydroxide (KOH) pellets used for the preparation of alkali solutions were caustic soda and caustic potash with 99% purity. Sodium silicate solution (Na₂SiO₃) and potassium silicate solution (K₂SiO₃) were used in some mix designs. The Na₂SiO₃ (supplied by Merck KGaA in Germany) was reported to contain 28.5% SiO₂, 8.5% Na₂O, and 63% H₂O; the K₂SiO₃ (supplied by Univar AS, Norway) was reported to contain 38% potassium silicate and 62% H₂O. An aluminum- and calcium-rich blast furnace slag (product name “Merit 5000” from Merit 5000, Sweden) was used as an additive (Table 3). Distilled water was used throughout the experiments.

2.2. Test and Analysis Methods. As the norite particle size was high, 0.4–2 mm, the specific surface area of the norite was increased to enhance its reactivity by milling. Therefore, every 100 g of the norite was ground by using a Retsch PM100 ball mill at 356 rpm for 10 minutes. Particle size distribution

(PSD) of the ground norite, Figure 1, was measured using a Sympatec HELOS laser diffraction particle size analyzer. The analysis was done at Tel-Tek National Research Institute, Norway. Sauter mean diameter (SMD) and volume mean diameter (VMD) were reported to be 6.43 and 47.16 μm, respectively. The particle density of norite was estimated to be 2.00 g/cc.

A Zeiss Supra 35VP model scanning electron microscopy-energy dispersive X-ray spectroscopy (SEM-EDXS) analyzer was used. The analysis was performed at ambient temperature and under high vacuum conditions.

An Agilent Cary 630 FTIR (Fourier transform infrared) spectrometer was used to investigate the structure of the norite and the investigation was carried out in the 1200–400 cm⁻¹ region. The KBr (potassium bromide) wafer technique was used for the spectra determination [2].

X-ray powder diffraction (XRD) analysis of the norite and the binder was performed using X-ray synchrotron radiation with the wavelength of 0.6888 Å. The XRD measurements were performed with a PILATUS2M pixel detector-based diffractometer at the Swiss-Norwegian beamline (SNBL-BM01A), at the European Synchrotron Radiation Facility, ESRF, Grenoble, France. The two-dimensional diffraction patterns spanned a maximal diffraction angle, 2θ, of 46 degrees. One-dimensional diffraction patterns were obtained by azimuth integration using the program Fit2D [14]. The mineral analysis program, Match!, and Crystallography Open Database (COD) were used for phase identification [15].

To measure the compressive strength of the binder, two different uniaxial compressive strength (UCS) mechanical testers were utilized: a Zwick/Z020 for specimens with compressive strength lower than 10 MPa and a Toni Technik-H for specimens with compressive strength higher than 10 MPa. The Zwick/Z020 and Toni Technik-H testers applied TestXpert II v3.2 and TestXpert v7.11 testing software, respectively, to calculate UCS of the specimens.

2.3. Specimen Preparation. In order to produce a pure norite-based binder, the ground norite was mixed with an alkali solution for 2 minutes. To investigate the influences of ground granulated blast furnace slag (GGBFS) and type of alkali silicate solution, the GGBFS and alkali silicate solution were introduced into some of the mixes as presented in Tables 4 and 5. When an alkali silicate solution was required, the alkali solution and the alkali silicate solution were mixed prior to adding the solid phase. Whenever the GGBFS was necessary, it was entered into the blend during the final part of the mixing. A Hamilton Beach blender was used for the mixing.

The slurries were poured in cylindrical plastic molds with 52 mm diameter and 100 mm length. The specimens were cured at ambient pressure and different temperatures: ambient temperature and 87°C. Tables 4 and 5 present the mix designs.

TABLE 4: Compressive strength of the binders without any additives. The specimens were cured at 87°C and ambient pressure.

Norite (g)	Alkali sol.	Wt. of alkali sol. (g)	Specimen 1		Estimated compressive strength (± 2 MPa)
			L/S ratio	Curing time (days)	
300	8 M NaOH	125	0.42	5	2.5
300	8 M NaOH	125	0.42	7	3
300	8 M NaOH	125	0.42	14	23
300	8 M NaOH	125	0.42	28	24

TABLE 5: Influence of GGBFS on the compressive strength of the binder. The specimens were cured at ambient pressure.

Specimen	Norite (g)	GGBFS (g)	Alkali sol.	Wt. of alkali sol. (g)	K ₂ SiO ₃ (g)	Na ₂ SiO ₃ (g)	L/S ratio	Curing temp. (°C)	Curing time (days)	Estimated compressive strength (± 2 MPa)
2	183	91	8 M NaOH	52	0	72	0.45	23	7	20
3	183	91	4 M KOH	53	72	0	0.46	23	7	26
4	248	40	10 M NaOH	61	61	0	0.42	87	1	5.0
4	248	40	10 M NaOH	61	61	0	0.42	87	5	9.0
4	248	40	10 M NaOH	61	61	0	0.42	87	7	9.0

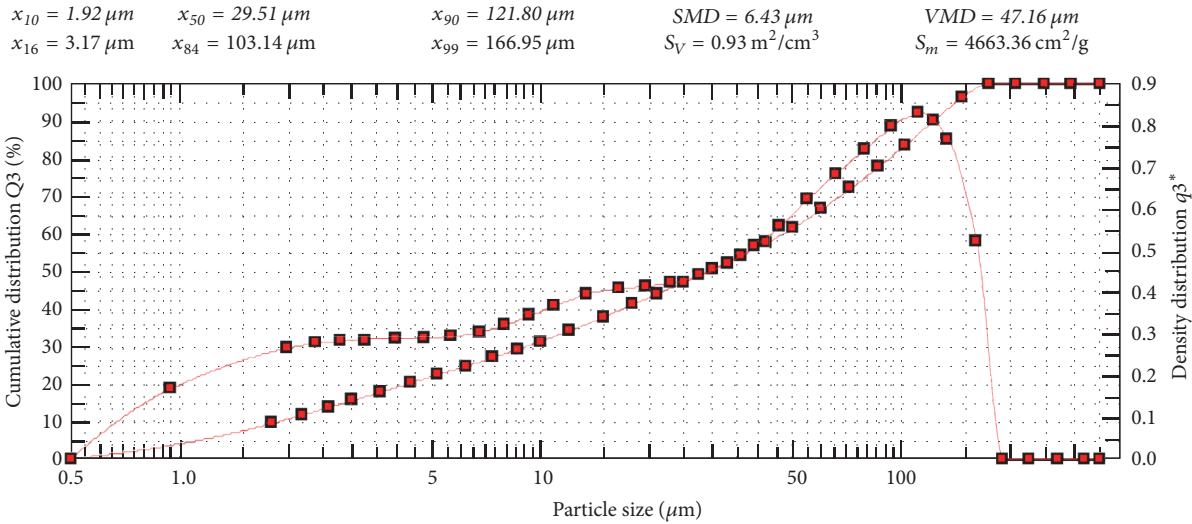


FIGURE 1: Graphical representation of particle size distribution analysis of the analyzed norite.

3. Results and Discussion

For a better understanding of the binder synthesis, sets of analytical experiments were conducted. For each test, only one parameter was changed while the others were kept constant. The compressive strength of the different specimens was measured, besides the XRD and microstructure analyses.

3.1. Effect of Particle Size. The norite particle size could be important for understanding its physical and chemical properties. So, two specimens were prepared to evaluate the influence of the norite particle size on its reactivity. The specimens were prepared by using the nonground and the ground norite. The maximum particle size of the nonground

norite was reported to be 2 mm. Both specimens were mixed by using 8 M NaOH and cured at ambient pressure and temperature for 7 days. A liquid-to-solid mass ratio of 0.42 was selected to maintain fluidity of the slurries; however, generally, a liquid-to-solid mass ratio of 0.35 is recommended [16]. The prepared slurry with the nonground norite never solidified while the ground norite solidified (Figure 2). Although the larger precursor particles have lower surface-to-volume ratio and the slurry requires a lower activator content, the formation of gels was not observed. The smaller the particle sizes, the higher the reactivity of the norite. Likely, the large particles do not participate in the reaction to form the binder but they act as an aggregate (Figure 4(a)). It could be said that milling activates the material mechanically.



FIGURE 2: Effect of particle size on the reactivity at 87°C and ambient pressure: (a) nonground norite and (b) ground norite.

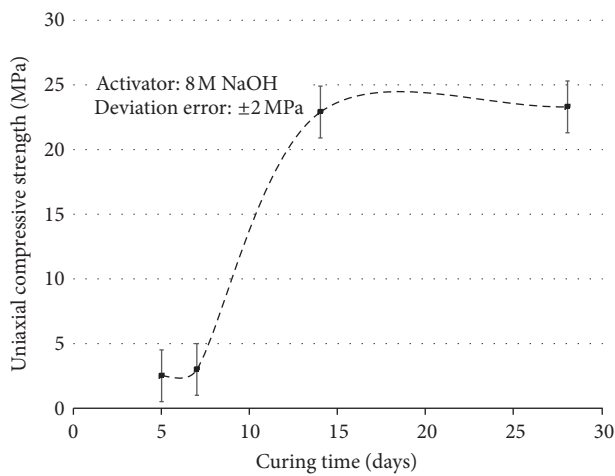


FIGURE 3: Strength development of specimen 1 at 87°C and ambient pressure.

Figure 3 presents the compressive strength development of the norite-based binder, which was cured at 87°C and ambient pressure. A radical strength development was observed after 7 days of curing. The specimens were prepared by mixing the norite with 8 M solution of sodium hydroxide (Table 4).

3.2. Microstructure Analysis of the Binder

3.2.1. Scanning Electron Microscopy (SEM). Figure 4 presents the SEM images of specimen 1, which was cured at 87°C and ambient pressure for 7 days. The crystallization is shown through Figures 4(a)–4(c). Two crystals were selected for element analysis to confirm the polycondensation. The crystals are marked with a green cross (Figures 4(b)–4(c)). The resulting crystals mainly contain Si, Al, O, and Na. The element analysis of the marked crystals resembled erionite and oligoclase. From microstructural observations, it could be said that the selected matrices are not homogeneous (Figures 4(b)–4(c)). One crystal has a Si:Al ratio of 1.5 (Figure 4(b)), while the other crystal has a Si:Al ratio of 2 (Figure 4(c)). Higher magnifications on the crystals showed existence of some fissures as shown in Figure 4(b).

As shown in Figure 4(b), some rod-like species have been identified in some parts of the binder. The influence of these rod-like species on the compressive strength could not be figured out and, in this regard, further studies should be carried out in the future.

3.2.2. X-Ray Diffraction Analysis. Figure 5 shows the XRD patterns of the binder cured for 7 days at 87°C and ambient pressure. The XRD analysis shows that the starting material mainly consists of anorthite sodian ($\text{Al}_{1.52}\text{Ca}_{0.52}\text{Na}_{0.48}\text{O}_8\text{Si}_{2.48}$). But erionite, albite, and stilbite-Na seem to be synthesized as a result of polycondensation. In addition, the formation of an amorphous phase was noticed as a broad diffuse halo, or a “hump,” in the 2θ range between 5 and 15°. Nonetheless, it has been shown that amorphous inorganic polymers are formed in the 2θ range between 20 and 39 degrees. The identification of the amorphous phases requires further study.

The XRD patterns show that when the norite was mixed with pure 8 M NaOH solution, the content of the amorphous phase increased (Figure 5(a)). He et al. [17] reported that curing alkali-activated based slurries at elevated temperatures leads to a higher degree of crystallization. It should be mentioned that, for the K-containing system, the pattern showed lower content of the amorphous phase compared to the Na-containing system. However, the GGBFS used as an additive was almost amorphous.

The oligoclase determined by the XRD patterns ($\text{Al}_{1.277}\text{Ca}_{0.277}\text{Na}_{0.723}\text{Si}_{2.723}$) with low content of erionite-Ca ($\text{Al}_{3.954}\text{Ca}_{1.22}\text{H}_{72.096}\text{K}_6\text{Mg}_{0.26}\text{O}_{49.2}\text{Si}_{14.046}$) was the reaction product of a Na-containing system (Figure 5(a)). Oligoclase is a high sodium content feldspar which could be reasonable due to the use of Na-containing solution [12]. Erionite-Ca is a member of the zeolite minerals. Gougazeh and Buhl [18] studied the synthesis of zeolite A by treating the activated metakaolin from natural kaolin with various concentrations of NaOH at 100°C. Their result shows that zeolite A was the major constituent phase, while quartz and hydroxysodalite were the minor constituents of the final product.

Further, the patterns show that albite ($\text{AlNaO}_8\text{Si}_3$) and stilbite-Na ($\text{Al}_{2.42}\text{Ca}_{0.84}\text{H}_{18}\text{Na}_{0.75}\text{O}_{24.12}\text{Si}_{6.64}$) are the reaction products for the K-containing system (Figure 5(b)). Albite is a plagioclase feldspar mineral and stilbite is a series of

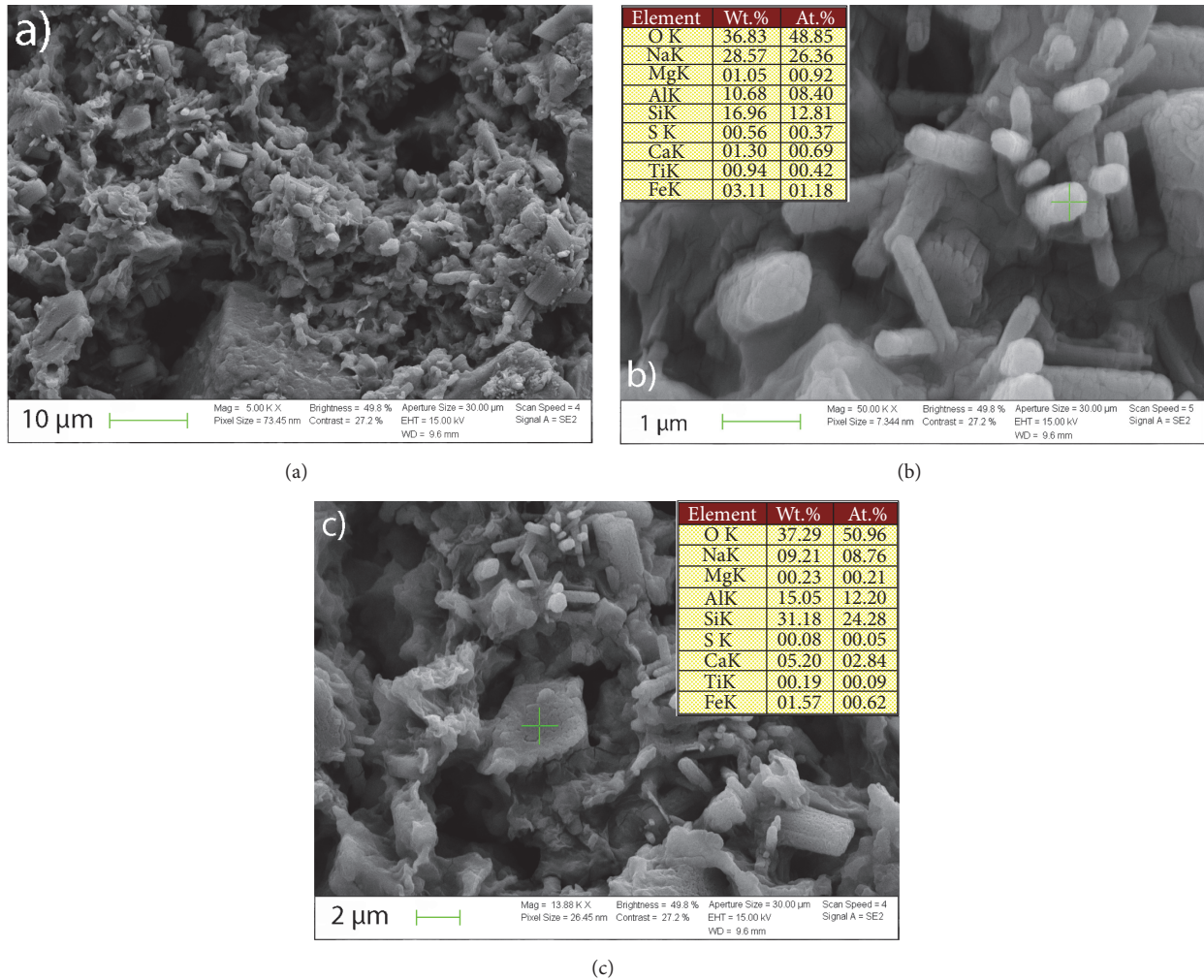


FIGURE 4: SEM images of specimen 1 cured for 7 days at 87°C and ambient pressure; (a) pores are visible; (b) needle structures; (c) elemental analysis of a selected point.

tectosilicate minerals of the zeolite group. Kawano and Tomita [19] reported the synthesis of zeolites from obsidian in various concentrations of NaOH and KOH solutions at 150 and 200°C. They showed that smectite, phillipsite, and rhodsite formed in an NaOH solution as pH increased and smectite, merlinoite, and sanidine were produced in KOH solutions as pH increased. The pH and Si : Al and Na : K ratios of the reacting solutions were important parameters determining the nature of the products formed from obsidian. Formation of the zeolite could be due to the quantity of silica and grain size as investigated by Prudhomme et al. [20].

3.2.3. *Infrared Analysis (IR)*. The infrared spectra of the norite and the norite-based binder are given in Figure 6. The binder was cured for 7 days at 87°C and ambient pressure. As shown in Figure 6, the chemical shifts of main IR characteristic bands and appearance of new peaks were observed. The IR for the solid precursors (norite) and the binder consists of the strongest vibrations at 980–1020 cm⁻¹ and 420–560 cm⁻¹. Comparing the IR spectra of the norite and

norite-based binder shows that, during polycondensation, the outstanding band at 1008 cm⁻¹ shifted towards a lower wavenumber (1000 cm⁻¹). It seems that 1008 cm⁻¹ band is caused by asymmetrical vibration of Si(Al)-O bonds and 540 cm⁻¹ band by bending vibration of Si-O-Al bonds [2, 21]. The appearance of new peaks at 881 and 577 cm⁻¹ is due to reaction. Muksi et al. [22] studied the formation of fly ash-based geopolymer by using Fourier transformed infrared (FTIR) spectroscopy and suggested that the appearance of a new peak at 881 cm⁻¹ is related to Si-O stretching and the bending of O-H in the Si-OH bond.

3.3. *Influence of the GGBFS on the Compressive Strengths*. Inclusion and influence of GGBFS on fly-ash have been studied on the setting time and strength development of fly ash-based binder. It is believed that addition of an amorphous silica phase leads to a shorter setting time and higher compressive strength. It has also been reported that the addition of GGBFS to concrete enhances setting time of concrete at ambient temperature. However, it may affect the

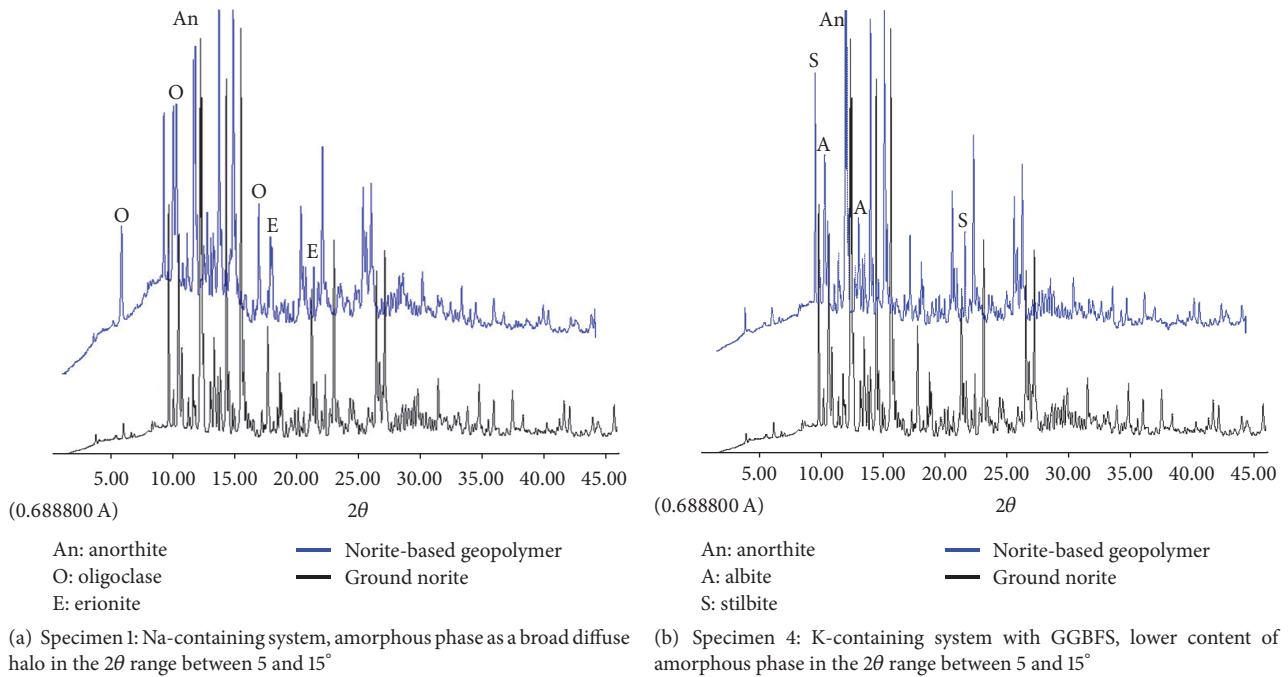


FIGURE 5: X-ray patterns of the norite-based binders cured for 7 days at 87°C and ambient pressure.

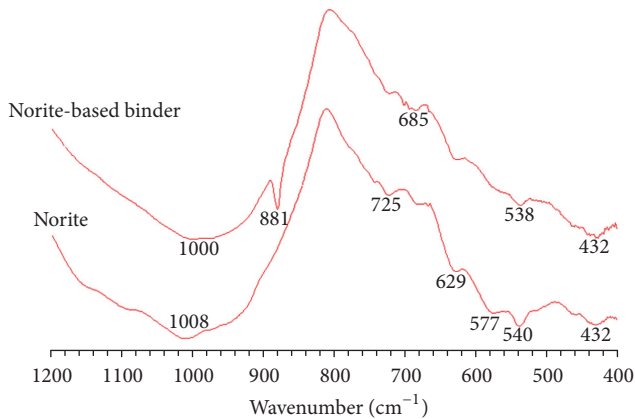


FIGURE 6: FTIR of aluminosilicates of the solid precursor and the norite-based binder, which was cured for 7 days at 87°C and ambient pressure.

final compressive strength of the slurry due to incomplete reaction [16, 23].

As the measured 7-day compressive strength of the binder was low, the influence of GGBFS was studied. As shown in Table 5, addition of the GGBFS to the slurries strongly influenced the compressive strength of the specimens, which were cured at ambient pressure and temperature. However, there was no supplementary information about the hydraulic reactivity relation for the used GGBFS.

3.4. Effect of Alkali Solution. The influence of alkali type was studied in this work. The obtained results show higher compressive strength for the specimens prepared using

K-containing systems than with sodium (Table 5). It has been reported that dissolution of aluminosilicate in a sodium solution is more effective than in a potassium solution. However, the compressive strength of the binder is higher for the K-containing systems than for the Na-containing systems [2, 24, 25]. This phenomenon is explained by the size of K^+ cations and the formation of zeolite in the geopolymer structure [26]. Therefore, to get the same strength as the K-containing system, the amount of sodium solution may be increased. The used concentrations are classified as corrosive in the criteria for classification of substances; therefore, the K-containing system may have a lower risk of hazard, which makes it user-friendly. Hence, it could be said that K-containing systems are more user-friendly in comparison to Na-containing systems. However, a combination of potassium and sodium solutions substantially reduces the compressive strength (Table 5).

4. Conclusion

A norite-based binder has been successfully produced from the waste tailing of an ilmenite mine consisting mainly of anorthosite. The particle size of the source material significantly affected the reactivity. The IR spectra of norite-based binder showed a shift towards a lower wavenumber. The maximum compressive strength was obtained for the fully potassium-containing system while a combination of sodium and potassium reduced the strength development. The XRD patterns showed formation of oligoclase, albite, and zeolites. Furthermore, the patterns indicated amorphous phases for the Na-containing systems at 87°C of curing; however, crystallization was expected at elevated temperatures. The SEM images showed some degree of crystallization and heterogeneity in the binder matrices.

Conflicts of Interest

The authors declare that there are no conflicts of interest regarding the publication of this paper.

Acknowledgments

The authors acknowledge the Research Council of Norway, ConocoPhillips, AkerBP, Statoil, and Wintershall for financing the work through the research center DrillWell (Drilling and Well Centre for Improved Recovery), research cooperation between IRIS, NTNU, SINTEF, and UiS. The authors are also grateful to the management of Titania AS, Norway, for their support. Special thanks are due to the Swiss-Norwegian beamlines (SNBL) at the European Synchrotron Radiation Facility (ESRF) for providing beamtime and technical support during the experiment.

References

- [1] F. Pacheco-Torgal, J. A. Labrincha, C. Leonelli et al., *Handbook of Alkali-activated Cements, Mortars and Concretes*, Oxford: Woodhead Publishing, Oxford, UK, 5th edition, 2014.
- [2] J. Davidovits, *Geopolymer Chemistry and Application*, Saint-Quentin: Institut Geopolymere, Saint-Quentin, France, 3rd edition, 2011.
- [3] I. Garcia-Lodeiro, A. Fernández-Jimenez, P. Pena, and A. Palomo, "Alkaline activation of synthetic aluminosilicate glass," *Ceramics International*, vol. 40, no. 4, pp. 5547–5558, 2014.
- [4] D. L. Y. Kong, J. G. Sanjayan, and K. Sagoe-Crentsil, "Factors affecting the performance of metakaolin geopolymers exposed to elevated temperatures," *Journal of Materials Science*, vol. 43, no. 3, pp. 824–831, 2008.
- [5] E. I. Diaz, E. N. Allouche, and S. Eklund, "Factors affecting the suitability of fly ash as source material for geopolymers," *Fuel*, vol. 89, no. 5, pp. 992–996, 2010.
- [6] J. Nemecek, V. Smilauer, and L. Kopecky, "Nanoindentation characteristics of alkali-activated aluminosilicate materials," *Cement and Concrete Composites*, vol. 33, pp. 163–170, 2011.
- [7] J. Stark, "Recent advances in the field of cement hydration and microstructure analysis," *Cement and Concrete Research*, vol. 41, pp. 666–678, 2011.
- [8] D. Ravikumar, S. Peethamparan, and N. Neithalath, "Structure and strength of NaOH activated concretes containing fly ash or GGBFS as the sole binder," *Cement and Concrete Composites*, vol. 32, no. 6, pp. 399–410, 2010.
- [9] M. Khalifeh, A. Saasen, T. Vralstad, and H. Hodne, "Potential utilization of class C fly ash-based geopolymer in oil well cementing operations," *Cement and Concrete Composites*, vol. 53, pp. 10–17, 2014.
- [10] M. C. M. Nasvi, P. G. Ranjith, and J. Sanjayan, "The permeability of geopolymer at down-hole stress conditions: application for carbon dioxide sequestration wells," *Applied Energy*, vol. 102, pp. 1391–1398, 2013.
- [11] H. Pichler and C. Schmitt-Riegraf, *Rock-Forming Minerals in Thin Section*, Chapman and Hall, London, UK, 2nd edition, 1993.
- [12] W. D. Nesse, *Introduction to Mineralogy*, Oxford University Press, Inc, Oxford, UK, 1st edition, 2000.
- [13] P. I. Norkyn, *Laboratory Analysis of Norite*, Kronos Titania AS, 2004.
- [14] A. P. Hammersley, S. O. Svensson, M. Hanfland, A. N. Fitch, and D. Häusermann, "Two-dimensional detector software: from real detector to idealised image or two-theta scan," *High Pressure Research*, vol. 14, no. 4-5, pp. 235–248, 1996.
- [15] Match!, Phase Identification from Powder Diffraction, Version 2, Crystal Impact, Dr. H. Putz and Dr. K. Brandenburg GbR, Kreuzherrenstr, 102, 53227 Bonn, Germany, <http://www.crystal-impact.com/match>.
- [16] P. S. Deb, P. Nath, and P. K. Sarker, "The effects of ground granulated blast-furnace slag blending with fly ash and activator content on the workability and strength properties of geopolymer concrete cured at ambient temperature," *Materials & Design*, vol. 62, pp. 32–39, 2014.
- [17] P. He, D. Jia, M. Wang, and Y. Zhou, "Thermal evolution and crystallization kinetics of potassium-based geopolymer," *Ceramics International*, vol. 37, no. 1, pp. 59–63, 2011.
- [18] M. Gougazeh and J.-C. Buhl, "Synthesis and characterization of zeolite A by hydrothermal transformation of natural Jordanian kaolin," *Journal of the Association of Arab Universities for Basic and Applied Sciences*, vol. 15, no. 1, pp. 35–42, 2014.
- [19] M. Kawano and K. Tomita, "Experimental study on the formation of clay minerals from obsidian by interaction with acid solution at 150° and 200°C," *Clays and Clay Minerals*, vol. 43, no. 2, pp. 212–222, 1995.
- [20] E. Prudhomme, P. Michaud, E. Joussein, and S. Rossignol, "Influence of raw materials and potassium and silicon concentrations on the formation of a zeolite phase in a geopolymer network during thermal treatment," *Journal of Non-Crystalline Solids*, vol. 358, no. 16, pp. 1908–1916, 2012.
- [21] Z. Yunsheng, S. Wei, C. Qianli, and C. Lin, "Synthesis and heavy metal immobilization behaviors of slag based geopolymer," *Journal of Hazardous Materials*, vol. 143, no. 1-2, pp. 206–213, 2007.
- [22] G. Mucsi, S. Kumar, B. Csoke et al., "Control of geopolymer properties by grinding of land filled fly ash," *International Journal of Mineral Processing*, vol. 143, pp. 50–58, 2015.
- [23] H. Xu, W. Gong, L. Syltebo, K. Izzo, W. Lutze, and I. L. Pegg, "Effect of blast furnace slag grades on fly ash based geopolymer waste forms," *Fuel*, vol. 133, pp. 332–340, 2014.
- [24] L. Xin, J.-Y. Xu, W. Li, and E. Bai, "Effect of alkali-activator types on the dynamic compressive deformation behavior of geopolymer concrete," *Materials Letters*, vol. 124, pp. 310–312, 2014.
- [25] G. S. Ryu, Y. B. Lee, K. T. Koh, and Y. S. Chung, "The mechanical properties of fly ash-based geopolymer concrete with alkaline activators," *Construction and Building Materials*, vol. 47, pp. 409–418, 2013.
- [26] M. Khalifeh, A. Saasen, T. Vralstad, H. B. Larsen, and H. Hodne, "Experimental study on the synthesis and characterization of aptite rock-based geopolymers," *Journal of Sustainable Cement-Based Materials*, vol. 5, no. 4, pp. 233–246, 2016.

Research Article

Properties and Internal Curing of Concrete Containing Recycled Autoclaved Aerated Lightweight Concrete as Aggregate

Teewara Suwan^{1,2} and Pitiwat Wattanachai¹

¹Department of Civil Engineering, Faculty of Engineering, Chiang Mai University, 239 Huay Kaew Road, Muang District, Chiang Mai 50200, Thailand

²Center of Excellence for Natural Disaster Management (CENDIM), Chiang Mai University, 239 Huay Kaew Road, Muang District, Chiang Mai 50200, Thailand

Correspondence should be addressed to Pitiwat Wattanachai; pitiwat@eng.cmu.ac.th

Received 1 June 2017; Accepted 10 July 2017; Published 20 August 2017

Academic Editor: Tung-Chai Ling

Copyright © 2017 Teewara Suwan and Pitiwat Wattanachai. This is an open access article distributed under the Creative Commons Attribution License, which permits unrestricted use, distribution, and reproduction in any medium, provided the original work is properly cited.

Global warming is a vital issue addressed to every sector worldwide, including the construction industry. To achieve the concept of green technology, many attempts have been carried out to develop low-carbon footprint products. In the construction sector, Autoclaved Aerated Concrete (AAC) has become more popular and been manufactured to meet the construction demand. However, errors from manufacturing process accounted for approximately 3 to 5% of the AAC production. The development of AAC waste as lightweight aggregate in concrete is one of the potential approaches which was extendedly studied in this paper. The results showed that the compressive strength of AAC-LWA concrete was decreased with an increase in volume and coarse size. The optimum mix proportion was the AAC aggregate size of 1/2" to 3/8" with 20 to 40% replacement to normal weight aggregate. Internal curing by AAC-LWA was also observed and found to provide sufficient water inside the specimens, leading to an achievement in higher compressive strength. The main goal of this study is not only utilising unwanted wastes from industry (recycling of waste materials) but also building up a new knowledge of using AAC-LWA as an internal curing agent as well as the production of value-added lightweight concrete products.

1. Introduction

To achieve the concept of green construction technology, many attempts have been carried out to develop low-carbon footprint products or techniques. An approach of transforming wastes from any industrial sectors to become a new raw starting material for other industries has received much more attention as a zero-waste society. Commonly, the simplest eliminating of industrial wastes is to utilise them as cement or concrete replacement, for example, cement additives or concrete aggregates. In Thailand, although a conventional masonry wall is made from local clay-bricks, with launching of Lightweight Autoclaved Aerated Concrete (AAC) blocks they turn into a new choice for engineers and builders, therefore becoming more and more popular in the construction industry. However, it was reported that scraps and wastes from overall AAC block production accounted

for approximately 3 to 5% (58 tonnes monthly), resulting in a huge number of AAC residues heading directly to a land-filled site (Figure 1). Developing AAC wastes as a lightweight aggregate in concrete production is one of the potential approaches that not only is beneficial for utilising industrial by-products and the reduction of energy consumption but also is beneficial for a strength improvement by internal curing and a reduction of final concrete weight [1, 2].

External curing is a common method to acquire sufficient Portland cement hydration, which can be achieved by preventing moisture loss on surfaces, wrapping with any wet-covers, or even submerging the concrete samples in the water bath. However, in some cases, the effectiveness of external curing may be limited due to an unsatisfied penetration of curing-water into the samples by physical barrier or geometry of the concrete components [3]. Internal curing is an alternative approach introducing internal water reservoir



FIGURE 1: Scrap of AAC block production.

for curing purpose inside the concrete mixtures. It has already been proved that internal curing can significantly enhance the strength and reduce an autogenous shrinkage of the final concrete products [4, 5]. Any porous lightweight material can be used as an internal curing aggregate (e.g., vermiculite, perlite, pumice, scoria, expanded shale, expanded clay, and crushed-AAC wastes) [6, 7] as they could absorb water during preparation and mixing and then gradually release reserved water inside the mixtures during hardening process [8]. Moreover, the rough surface and coarse pore structure of those lightweight aggregates can also contribute to an interlocking manner on transition zones between cement paste and aggregate (interconnected surfaces), leading to an improvement in mechanical properties [9].

The main aim of this paper is to utilise available local AAC waste as a lightweight aggregate in concrete production which could allow converting industrial wastes into value-added products. Lightweight and highly uniformly distributed porosity are key characteristics of AAC that could serve as an internal curing material to provide sufficient curing condition for concrete construction. The suitable sizes and optimum replacement percentage of AAC aggregate were investigated as well as the final properties of fresh and hardened concrete during the internal curing approach.

2. Materials and Preparations

Portland cement was a commercial grade type I with a specific gravity of 3.15. Local river sand was used as a fine aggregate with specific gravity and fineness modulus of 2.39 and 2.90, respectively. The moisture content of sand was 0.80% with a bulk density of $1,645 \text{ kg/m}^3$. Coarse aggregate was commercial grade gravel from local suppliers. The specific gravity, moisture content, and bulk density were 2.70, 0.50%, and $1,540 \text{ kg/m}^3$, respectively. AAC wastes were collected from PCC Autoclave Concrete Company Limited, Chiang Mai, Thailand. Its specific gravity was 1.06 with a dry-unit weight of 360 kg/m^3 . As-received AAC, with a water absorption value of 28 to 30%, was crushed into a smaller size by a standard Jaw crusher (Figure 2).

The gradation of AAC coarse aggregates was then analysed by the US standard sieve analysis. The effective coarse size used in this study was between $3/8''$ (9.5 mm.) and $3/4''$

TABLE 1: Grading of crushed-AAC aggregates.

Sieve size (mm.)	Percent retained on the sieve
2'' (50.80)	1.31
1'' (25.40)	9.18
3/4'' (19.05)	18.22
1/2'' (12.70)	20.12
3/8'' (9.53)	11.35
#4 (4.75)	11.14
Pan	28.67

TABLE 2: Mixture labels and descriptions.

Label	Description
NC	Normal weight aggregate concrete
LWA	Lightweight aggregate
LWA20	Concrete with 20% lightweight aggregate replacement
LWA40	Concrete with 40% lightweight aggregate replacement
LWA60	Concrete with 60% lightweight aggregate replacement
S1	Lightweight aggregate with class size of $1''-3/4''$
S2	Lightweight aggregate with class size of $3/4''-1/2''$
S3	Lightweight aggregate with class size of $1/2''-3/8''$
S4	Lightweight aggregate with mixed class size of $1''-3/4''$ to $3/4''-1/2''$ to $1/2''-3/8''$ by 20 : 40 : 40

(19.0 mm.), which accounted for around 50% of the overall amount of AAC aggregates and has an average fineness modulus of 7.20 (Table 1). It is noted that the majority of effective AAC-LWA size values were $3/4''$, $1/2''$, and $3/8''$, and the size classes (as indicated with S1 to S4) of coarse aggregates replacement were therefore employed in the experiment. Mixture labels and descriptions of concrete mixtures, including size classes of AAC-LWA, are illustrated in Table 2.

The coarse aggregate, commercial grade, and size distributions are in the comparison of ASTM C33 with size number



FIGURE 2: Crushed-AAC scraps into AAC aggregates.

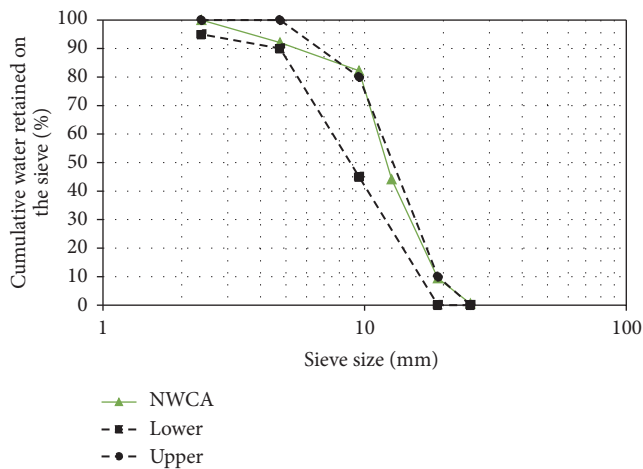


FIGURE 3: Size distribution of normal weight coarse aggregates (NWCA) used in accordance with ASTM C33 Size Number 67.

67. Figure 3 shows the size distribution of normal weight coarse aggregates (NWCA) used in NC mixture. It was found that the size distributions of normal weight aggregate are between 1/2" and 3/8" and mostly filled in the upper and lower boundaries of ASTM C33 size number 67 standard. In addition, as varied in class size of S1–S4, the size distributions of AAC-LWA replacement to normal weight aggregate by 20, 40, and 60% (LWA20, LWA40, and LWA60) are also plotted against upper and lower boundaries of ASTM C33 number 67 criteria.

As specific AAC-LWA class sizes (S1–S4) were replaced to a normal gradation of commercial grade gravel, the graphs of size distribution therefore started to shift to the upper limit of the ASTM C33 boundaries (Figure 4). It can be seen that a bundle of all LWA20 class sizes are aligned closely inside the upper boundary (Figure 4(a)). Moreover, the lines of size distribution were apparently shifted to the right beyond the upper limit, when the amount of AAC-LWA replacement increased from LWA40 (Figure 4(b)) to LWA60 (Figure 4(c)) in all class sizes. Thus, the presence of AAC-LWA aggregates does not only affect the overall gradation of concrete coarse aggregate but could also affect the mechanical properties of the final result of hardened concrete.

3. Experimental Details

3.1. Mixture Designations. Mixture designation was carried out following ACI 211.1 standard for concrete mixing. In controlled mixture (Normal Concrete, NC) with water-to-cement (w/c) ratio of 0.35, normal weight aggregates were added with the largest particle size of 3/4". The required concrete slump was set to 5 to 10 cm. Apart from that, in the mixtures with AAC wastes as lightweight aggregates (AAC-LWA), the volume of normal weight aggregates was substituted by the saturated surface-dry (SSD) AAC-LWA, namely, 20, 40, and 60%, respectively. It is noted that the total weight of AAC-LWA replacement was calculated from the same volume of normal aggregate in a cubic meter of concrete. For example of 20% AAC-LWA replacement (LWA20), as bulk density of normal weight aggregates and AAC-LWA were 1,540 and 360 kg/m³, respectively, 188 kg of normal weight aggregates was replaced by 46 kg of AAC-LWA. All concrete mixtures were mixed in a tilting drum mixer until reaching suitable conditions. The fresh concrete was then carried out for workability testing and placed in the prepared moulds. After 24 hours, all concrete samples were demoulded and kept in specific designed-curing conditions, water and air curing. Mixture proportions are as presented in Table 3.

3.2. Analytical Methods. Properties of fresh concrete were carried out by slump test and flow test. Concrete slump test was done with ASTM C143. The slump value of 10 cm. was set in accordance with ACI 213R-87, which is recommended for the construction of slab, column, and bearing wall structures. Flow ability of concrete was measured by using flow table along with ASTM C124 standard. Properties of hardened concrete were carried out with both standard and minute compressive strength tests. After demoulding (in the next 24 hours), all samples were cured in water or in the air until reaching their testing ages of 1, 3, 7, and 28 days. Weight and dimension of all samples were measured before further handling for the apparent density calculation. Standard compressive strength test of all cylindrical specimens (15 cm dia. and 30 cm height) was obtained by using Universal Testing Machine (UTM) in accordance with ASTM C39. An optical microscope was used to observe interfacial transition zone (ITZ) of AAC-LWA and cement paste.

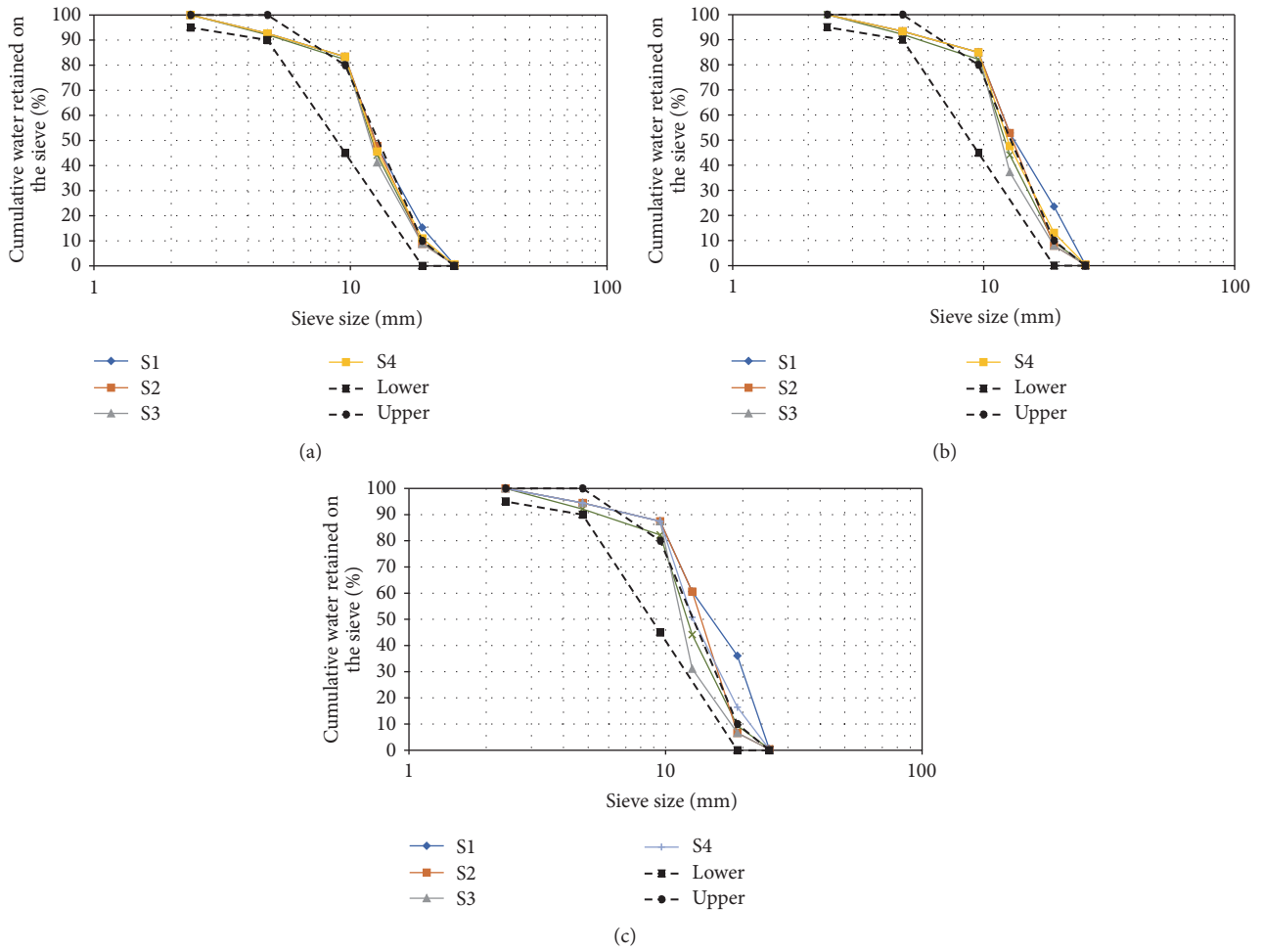


FIGURE 4: Size distribution of AAC-LWA of (a) LWA20, (b) LWA40, and (c) LWA60 in accordance with ASTM C33 Size Number 67. The green curve refers to the normal weight coarse aggregates (NWCA) (as shown in Figure 3), for comparison to S1-S4.

TABLE 3: Details of mixture designation (kg/m³).

Mixture	ACC-LWA replacement (%)	Class size	Portland cement	Water	Fine aggregate	Coarse aggregate	ACC aggregate
NC	—	—	571	200	588	938	—
LWA20	20	S1	571	200	588	750	46
	20	S2	571	200	588	750	46
	20	S3	571	200	588	750	46
	20	S4	571	200	588	750	46
LWA40	40	S1	571	200	588	563	93
	40	S2	571	200	588	563	93
	40	S3	571	200	588	563	93
	40	S4	571	200	588	563	93
LWA60	60	S1	571	200	588	375	139
	60	S2	571	200	588	375	139
	60	S3	571	200	588	375	139
	60	S4	571	200	588	375	139

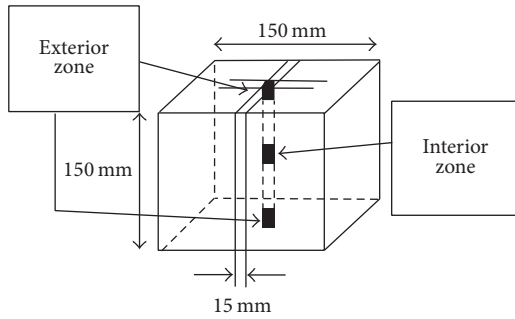


FIGURE 5: Cutting layout of $15 \times 15 \times 150$ mm. prisms.

Minute compressive strength ($3 \times 3 \times 3$ mm. cubic specimen) was introduced and carried out in this test to identify the effect of AAC-LWA on internal curing [10]. To prepare minute strength test samples, the $150 \times 150 \times 150$ mm. concrete cube was mixed and cured in designed-conditions. Three locations of the concrete cube (exterior zone and interior zones) were cut into $15 \times 15 \times 150$ mm. prisms (Figure 5). Each prism was then sliced into 3 mm thick layers with the dimensional length of $3 \times 15 \times 15$ mm., namely, L1, L2, and L3. It is noted that L1 was a layer right next to the AAC-LWA, while L2 and L3 were further aligned over (Figure 6). Those layers (L1, L2, and L3) were finally cut into $3 \times 3 \times 3$ mm. cubes (Figure 7) and then tested with a standard proving ring attached to the UTM.

4. Results and Discussions

4.1. Slump Test. The results of concrete slump test are illustrated in Figure 8. The AAC-LWA size classes, as indicated by S1, S2, S3, and S4 (see Table 2), had no significant difference in the test. The slump of controlled concrete (NC) was 5.80 cm., while slump values of AAC-LWA concrete tended to increase with a higher percentage of AAC aggregate replacement, for example, from around 7.50 cm. (LWA20) to around 10.60 cm. (LWA60). In fact, sharp shape and rough surface of AAC-LWA could decrease the slump value due to interlocking and internal friction among materials [11]. However, in this case, the slump value was mainly dominated by water retainability, extra water on the surface of AAC particles. Water-to-cement ratio was therefore raised, leading to an increase of concrete slump value. A similar result was also reported by Singh and Siddique (2016) that highly absorption materials (e.g., coal-bottom ash) can act as a water reservoir and could raise the final w/c ratio of concrete mixtures [12].

4.2. Flow Test. There was no significant difference in flow ability between controlled mixture (NC) and AAC-LWA mixtures. An average flow of AAC-LWA concrete seemed to be slightly decreased when the AAC aggregate replacement increased. The average flow value of NC was 53.3% while average flow values of LWA20, LWA40, and LWA60 mixtures were 55%, 56%, and 53%, respectively (Figure 9). However, as the flow values were in the range of 50 to 100%, the AAC-LWA concrete mixtures were classified in medium consistency

which could easily be placed and compacted into the moulds during a casting process.

4.3. Apparent Density of Concrete Mixtures. As presented in Figure 10, the apparent density of controlled mixture (NC) was around $2,380 \text{ kg/m}^3$ at 28 days of age. Apart from that, the overall apparent density of LWA20 concrete was slightly decreased approximately 3 to 4% to around $2,290$ to $2,310 \text{ kg/m}^3$ when compared with NC mixture. With LWA40 and LWA60 mixtures, the apparent density was continuously decreased by 8 to 9% ($2,160$ to $2,180 \text{ kg/m}^3$) and 13 to 15% ($2,030$ to $2,070 \text{ kg/m}^3$), respectively. The similar results were reported by Hossain et al. (2011) and Topçu and Işıkdağ (2008) whose substituted normal weight aggregates by pumice and perlite as concrete coarse aggregates [13]. It can be concluded that the overall density of AAC-LWA concrete was significantly decreased because of LWA replacement as its density was just 360 kg/m^3 . In contrast, the compressive strength is the next issue which needs to be considered as the most crucial properties of hardened concrete.

4.4. Standard Compressive Strength Test. The standard compressive strength test by using cylindrical specimens was carried out at 1, 3, 7, and 28 days of age. The comparative strength measurement between water and dry-air curing, including its size classes, was studied and is presented in Figures 11(a)–11(c).

It can be clearly seen that all mixtures cured in water achieved higher strength than that of mixtures cured in the dry-air as more degree of hydration was obtained [14]. The size class of S4-AAC aggregate (see Table 2) received the highest strength among S1, S2, and S3 classes due to a well gradation of the coarse aggregates in concrete mixtures according to ASTM C33 number 67. More compact structure was also achieved as well as an appropriated interlocking of well-graded coarse aggregate. Comparable strength improvement was obviously obtained from the higher density of hardened cement paste in the interfacial transition zone (ITZ) by internal curing [15]. The examples of normal-bonding (NWCA) and well-bonding (AAC-LWA) are as presented in Figure 12. It can be seen that the failure of normal-bonded NWCA occurred at cement paste, while well-bonded AAC-LWA was at AAC aggregate. Apart from the strength property of each aggregate, AAC-LWA clearly exhibited a terrific bonding performance at ITZ. Nevertheless, the final strength of AAC as aggregate concrete was decreased when the amount of AAC-LWA increased because AAC has extremely low load bearing capacity when compared with normal weight aggregate.

4.5. Minute Compressive Strength Test. Minute compressive strength is a technique used to verify an effect of internal curing by porous aggregate in the concrete mixtures. The compressive strength of $3 \times 3 \times 3$ mm. cube specimens of LWA20, LWA40, and LWA60 mixtures (all with S4 class size, cured in the air) were tested and presented in Figure 13. It can be apparently seen that the strength of samples collected from the exterior zone obtained lower strength than that

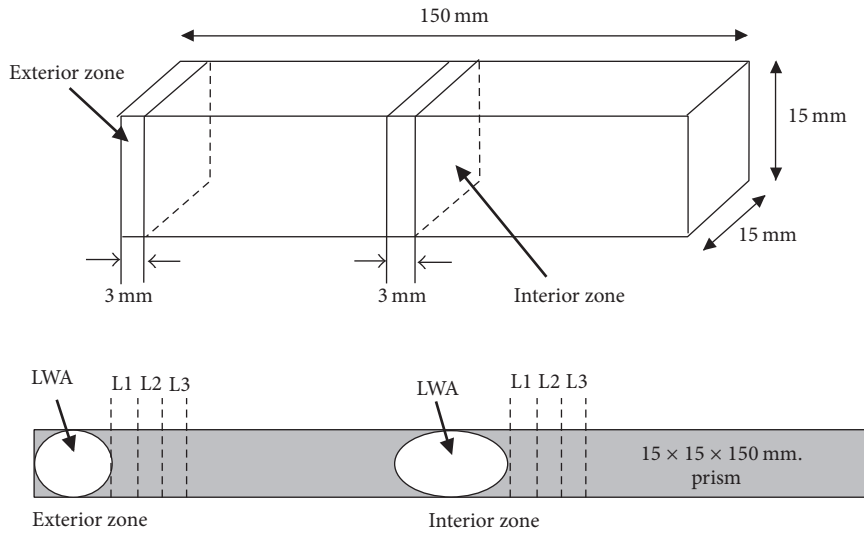


FIGURE 6: Cutting layout of 3 × 15 × 15 mm. layers (L1, L2, and L3).

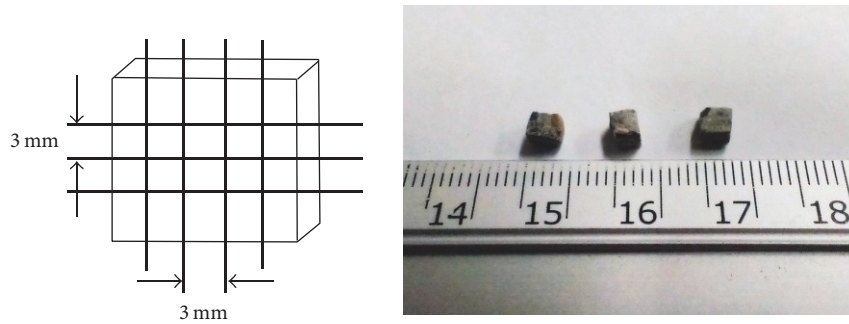


FIGURE 7: Cubic specimens in 3 × 3 × 3 mm. size.

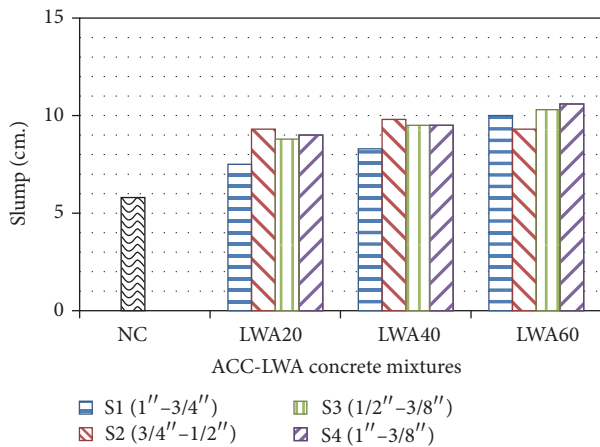


FIGURE 8: Slump values of NC and LWA mixtures.

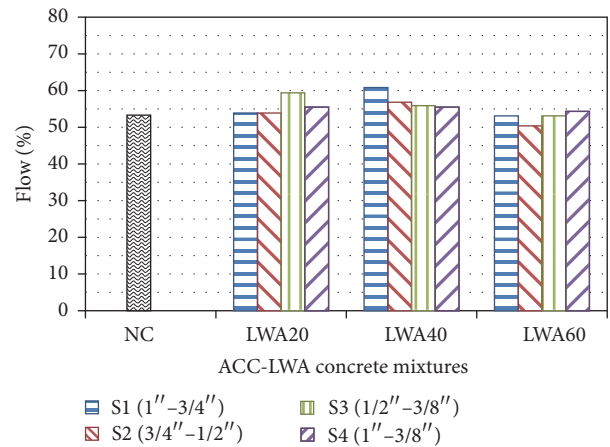


FIGURE 9: Flow values of NC and LWA concrete mixtures.

of the interior zone. Moreover, the strength of L1 sample (L1; the layer next to AAC aggregate) obviously achieved higher mechanical strength than those of the faraway layers, L2 and L3 (see Figure 6). In general, more completion of internal hydration process of AAC-LWA could be achieved

by water retainability in the concrete mixture. Especially for porous aggregates, extra water for internal curing purpose was not only obtained from water absorption but also from water adsorption, which directly affects the curing-water of concrete in later stage [16]. Moreover, the internal curing

TABLE 4: Differential percentage of minute compressive strength in layer 1 (L1) between 7 and 28 days of age.

Mixtures	Air curing (AC)						Water curing (WC)					
	L1 Ext. (MPa)			L1 Int. (MPa)			L1 Ext. (MPa)			L1 Int. (MPa)		
	7 d	28 d	% Δ	7 d	28 d	% Δ	7 d	28 d	% Δ	7 d	28 d	% Δ
NC	0.64	0.84	31.75	0.95	1.30	36.78	0.77	1.21	57.22	1.03	1.54	49.48
LWA20	0.83	1.12	34.00	1.12	1.69	51.10	1.11	1.48	33.33	1.41	2.01	42.08
LWA40	0.93	1.00	7.24	1.30	1.55	19.55	1.26	1.32	4.73	1.57	1.73	10.59
LWA60	0.93	1.13	21.37	1.23	1.62	31.42	1.15	1.43	25.06	1.39	1.80	29.04

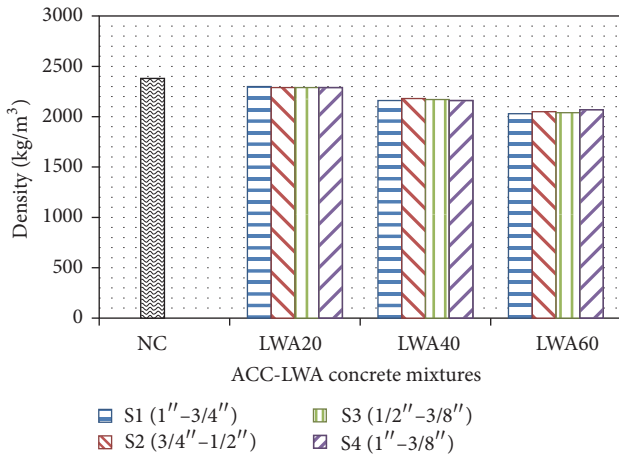


FIGURE 10: Apparent density of NC and LWA concrete mixtures.

process would also occur with “capillary suction” of which the transferring of water occurs from larger pores to the smaller ones. In this study, the capillary pores of AAC aggregates (50 to 100 microns, μm) were larger than that of average cement paste pores (1 to 100 nanometers, nm).

By this condition, some reserved water in AAC aggregates would, therefore, be transferred to cement paste across ITZ, increasing hydration level to the cement binders. The strength improvement in later age was mainly influenced by more C-S-H formation and denser microstructures [9]. The usage of AAC-LWA in saturated surface-dry (SSD) condition in this study would provide higher strength in all cases than the as-received/dry AAC-LWA [15]. The reasons are that as-received AAC-LWA could actively absorb the water in the system during its initial stage of mixing. Micropores and incomplete microstructures would appear on ITZ, leading to an adverse effect on the final properties of concrete [15]. The same trends and results were obtained by the minute compressive strength of S4-class size of LWA20, LWA40, and LWA60 cured in water. As far as sufficient curing water was served from both external and internal sides, the average strength of 3×3 mm. cube was thus slightly higher than the others cured in the dry-open air condition (Figure 14).

4.6. The Strength Development and a Relationship between Standard and Minute Compressive Strength. The strength development of layer 1 (L1) minute compression test over 7 and 28 days is presented in Table 4. While keeping NC

as a reference mixture, the LWA20 achieved the greatest difference of strength development in all conditions at 34.00% (AC L1 Ext.), 51.10% (AC L1 Int.), 33.33% (WC L1 Ext.), and 42.80% (WC L1 Int.). A huge differentiation of the L1 minute compressive strength can be observed between exterior and interior zones of LWA20 (26.98% and 35.32%) and LWA40 (39.03% and 54.99%) mixtures as illustrated in Table 5. It is obviously seen that the minute compressive strength of the air curing (AC) condition can be improved with internal curing regimes, especially for the interior zone. The optimum AAC-LWA proportions, which would receive the most benefit from internal curing, are in the range of LWA20 to LWA40 mixtures.

In contrast, the highest minute compressive strength of layer 1 (L1) was also plotted against standard cylindrical compressive strength with S4 class size at 7 and 28 days of age. Figure 15 presents the relationship of that minute and standard compressive strength of specimens cured in the dry-air curing condition (AC) in both their exterior zone (Figure 15(a)) and interior zone (Figure 15(b)). As mentioned earlier in Section 4.4, the average standard compressive strength of AAC-LWA concrete decreased when the amount of AAC-LWA replacement increased from 35.1 MPa (7 d) and 41.2 MPa (28 d) in LWA20 mixtures to around 26.2 MPa (7 d) and 28.1 MPa (28 d) in LWA60 mixtures. However, it is clearly seen that LWA20 and LWA40 mixtures seem to achieve higher strength than that of normal weight aggregate concrete (NC).

Minute compressive strength (as presented in Section 4.5) of the interior zone is clearly higher than the exterior one due to the internal curing of AAC-LWA with the highest value of LWA20 mixture. The investigation suggested that the 20% to 40% AAC-LWA replacement (LWA20 and LWA40) could be an optimum proportion for AAC-LWA concrete.

By this, it can be explained that those proportions mainly achieved the superior strength from normal weight aggregate while the suitable amount AAC aggregate replacement served the extra amount of water for internal curing to the cement paste. An increase of C-S-H formation not only strengthens the concrete matrices but also provides a well-bonding between AAC aggregate and cement paste at their ITZ. The similar trend of strength development was found in the specimens cured in water curing condition (WC) as shown in Figure 16. Additionally, as mentioned before, overall compressive strength of both minute and standard specimens was significantly higher than that of dry-air curing as sufficient water for curing purpose was obtained. Despite

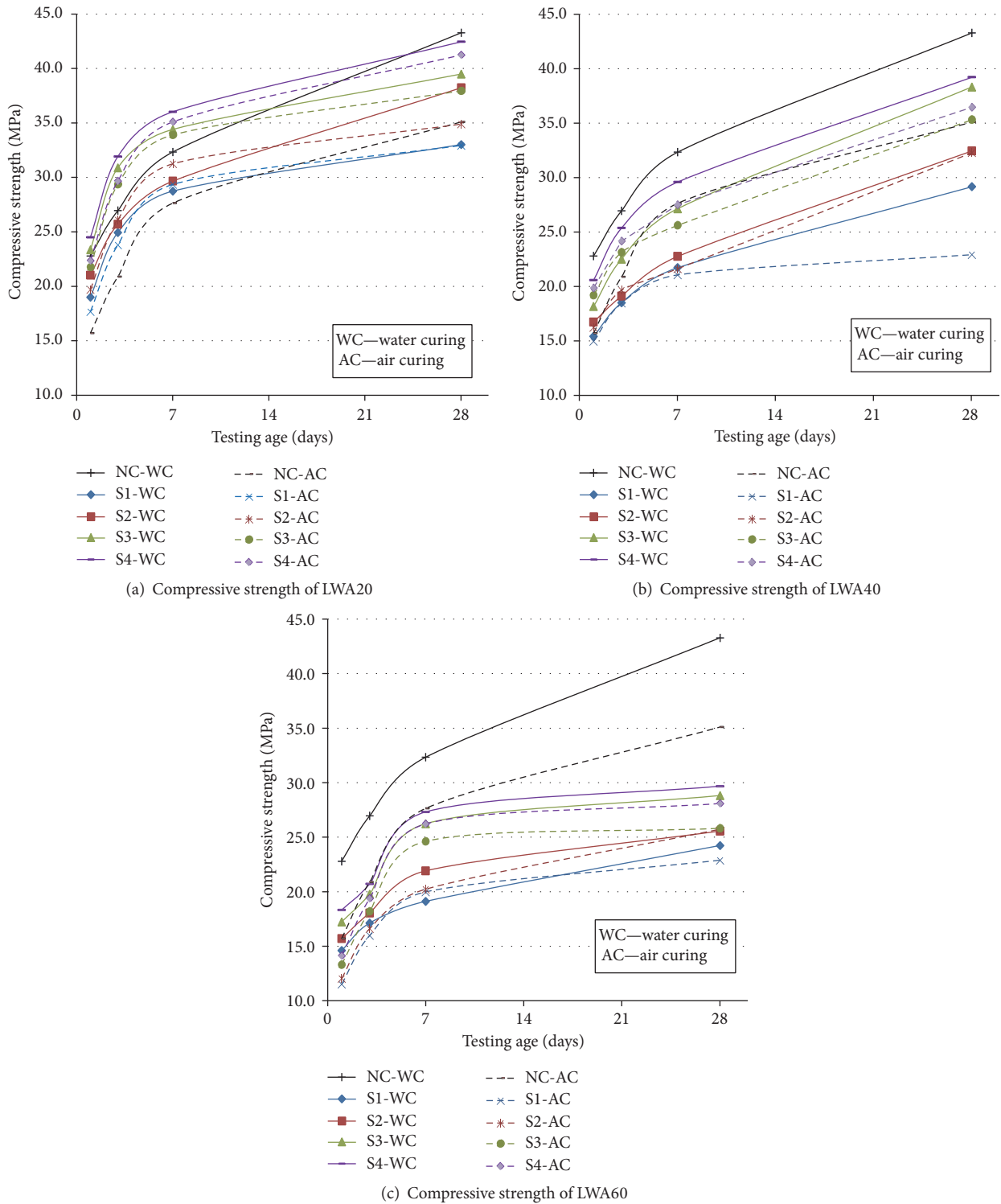


FIGURE 11: Standard compressive strength test of NC and AAC-LWA concrete in different size classes (S1 to S4) at the age of 1, 3, 7, and 28 days.

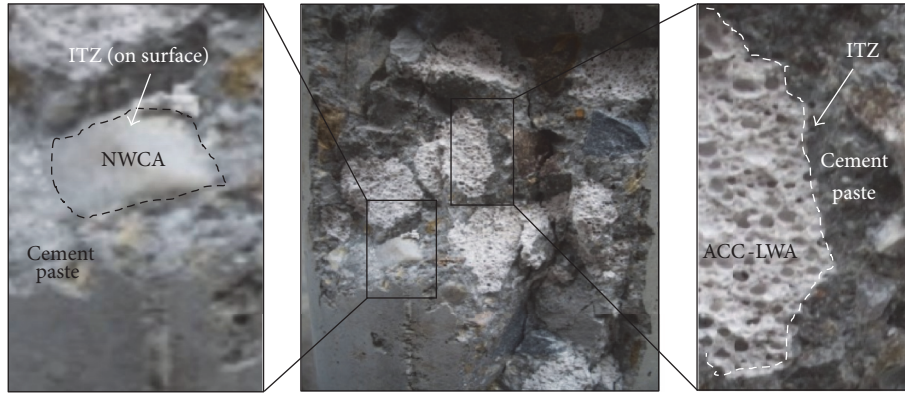


FIGURE 12: Normal-bonded NWCA (left) and well-bonded AAC-LWA (right) with cement paste on interfacial transition zone (ITZ).

TABLE 5: Differential percentage of minute compressive strength in layer 1 (L1) between exterior and interior zone.

Mixtures	Air curing (AC)						Water curing (WC)					
	L1 7 d (MPa)			L1 28 d (MPa)			L1 7 d (MPa)			L1 28 d (MPa)		
	Ext.	Int.	%Δ	Ext.	Int.	%Δ	Ext.	Int.	%Δ	Ext.	Int.	%Δ
NC	0.64	0.95	48.47	0.84	1.30	54.13	0.77	1.03	34.48	1.21	1.54	27.86
LWA20	0.83	1.12	34.00	1.12	1.69	51.10	1.11	1.41	26.98	1.48	2.01	35.32
LWA40	0.93	1.30	39.03	1.00	1.55	54.99	1.26	1.57	23.82	1.32	1.73	30.74
LWA60	0.93	1.23	32.00	1.13	1.62	42.93	1.15	1.39	21.64	1.43	1.80	25.51

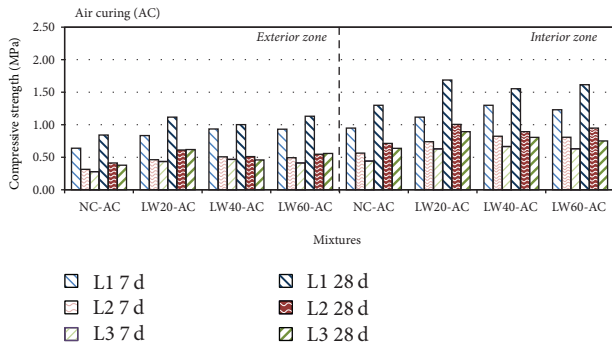


FIGURE 13: Minute compressive strength of NC and LWA mixtures at L1, L2, and L3 cured in the air (7 and 28 days of age).

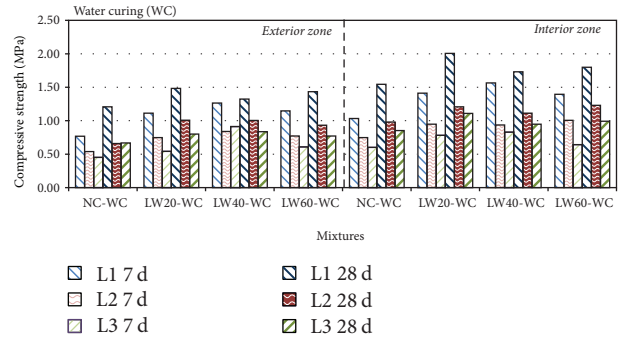


FIGURE 14: Minute compressive strength of NC and LWA mixtures at L1, L2, and L3 cured in the water (7 and 28 days of age).

a slight difference in compressive strength between water curing and air curing which water reserve of recycled AAC aggregate seems not necessary to provide moisture for further cement hydration process, the effectiveness of external curing may be limited due to an unsatisfied penetration of curing water into the samples, and the internal curing will then enlarge the positive curing regime from inside the concrete structure in the real use applications (e.g., huge structure or concrete component).

5. Conclusions

From the study, conclusion can be summarised as follows.

(1) The slump values were affected by the amount of water content. The slump value tended to rise with an increase

of AAC-LWA replacement as extra water on aggregate's surface was obtained. However, flow values of all mixtures were similar to normal weight aggregate concrete (NC) and classified as medium consistency category with the flow of 50 to 60%.

(2) The apparent density was decreased when the amount of AAC-LWA replacement increased from 2,380 kg/m³ (NC) to around 2,050 kg/m³ (LWA60). Although the minimum density in this test (2,030 kg/m³ in LWA60 mixture) did not meet the criteria of lightweight concrete advised by ACI 213R-87 at 1,850 kg/m³, the lower value in density can alternatively be achieved by increasing AAC-LWA proportion or even using lightweight fine aggregates (e.g., lightweight sand or bottom ash).

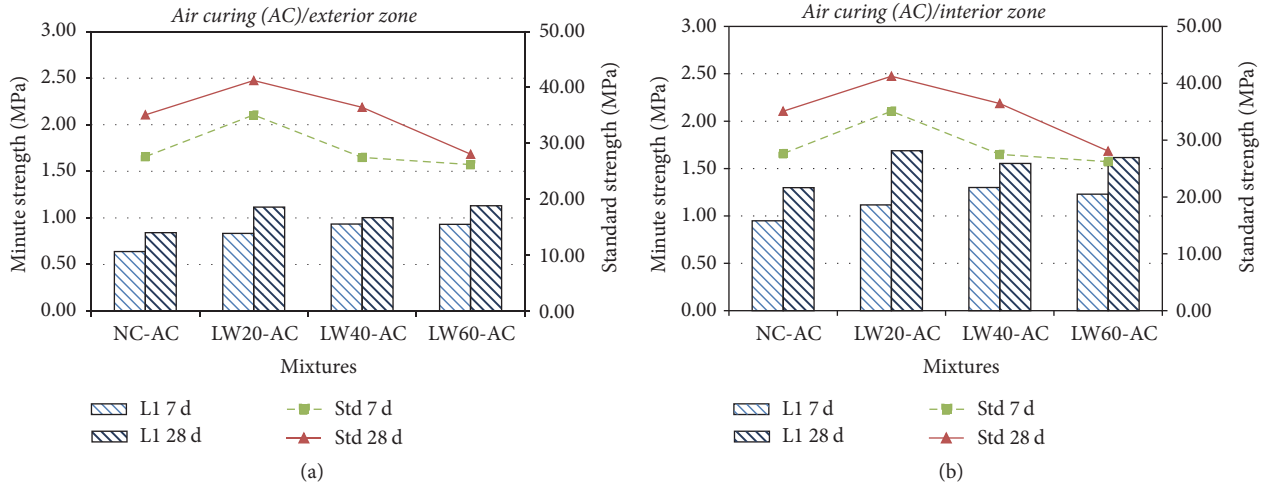


FIGURE 15: Relationship between standard and minute compressive strength of dry-air curing regime at (a) exterior zone and (b) interior zone.

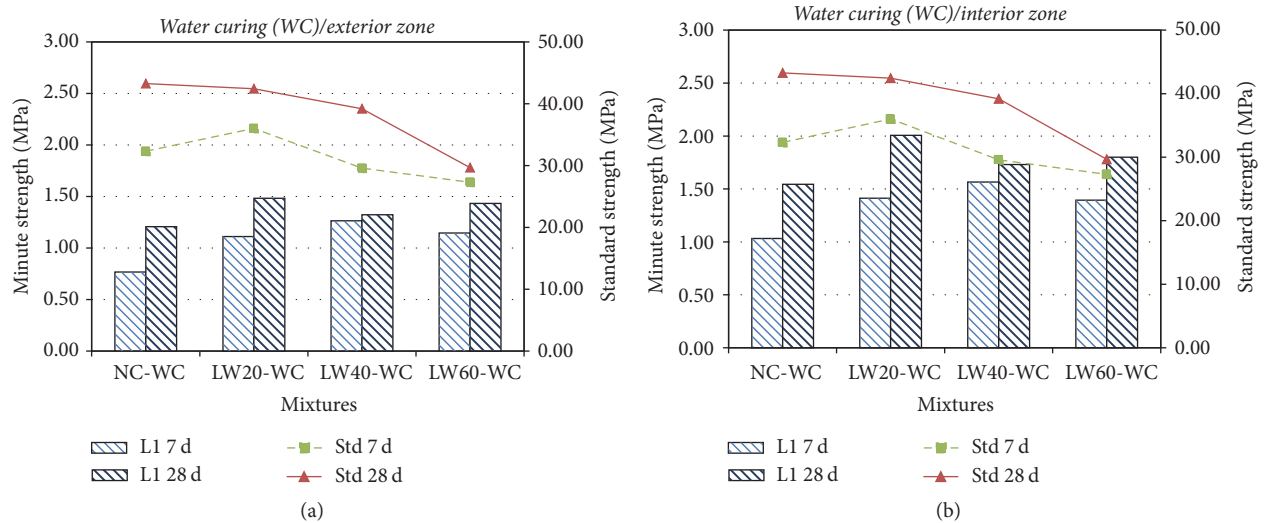


FIGURE 16: Relationship between standard and minute compressive strength of water curing regime at (a) exterior zone and (b) interior zone.

(3) The standard compressive strength by cylindrical specimens was decreased with higher AAC-LWA proportion in both dry-air and water curing, even though the water curing achieved slightly higher compressive strength. The mixed size of AAC-LWA (S4 class size) provided satisfactory gradation and superior strength than the single graded-aggregates (S1, S2, and S3).

(4) The highest strength of minute compressive test was achieved by 3 × 3 × 3 mm. cube located in layer 1 (L1), followed by layer 2 (L2) and layer 3 (L3), respectively. It can be concluded that internal curing by AAC-LWA obviously improves the strength of concrete by providing extra internal water resource for more possible C-S-H formation. In conjunction with minute and standard compressive strength, the optimum proportions of AAC-LWA replacement were in

the range of LWA20 to LWA40. Those mixture proportions mainly achieved the superior strength from normal weight aggregate while the suitable amount AAC aggregate replacement provided extra amount of water for internal curing to the cement paste.

(5) The development of AAC as a coarse aggregate replacement in concrete is not only utilising unwanted wastes from industry (recycling of waste materials) but also building up a new knowledge of using LWA as an internal curing agent as well as the production of value-added lightweight concrete products.

Conflicts of Interest

The authors declare that they have no conflicts of interest.

References

- [1] I.-J. Chiou, K.-S. Wang, C.-H. Chen, and Y.-T. Lin, "Lightweight aggregate made from sewage sludge and incinerated ash," *Waste Management*, vol. 26, no. 12, pp. 1453–1461, 2006.
- [2] S. Zhao, C. Li, M. Zhao, and X. Zhang, "Experimental study on autogenous and drying shrinkage of steel fiber reinforced lightweight-aggregate concrete," *Advances in Materials Science and Engineering*, vol. 2016, Article ID 2589383, 9 pages, 2016.
- [3] P. Lura, M. Wyrzykowski, C. Tang, and E. Lehmann, "Internal curing with lightweight aggregate produced from biomass-derived waste," *Cement and Concrete Research*, vol. 59, pp. 24–33, 2014.
- [4] B. Akcay and M. A. Tasdemir, "Optimisation of using lightweight aggregates in mitigating autogenous deformation of concrete," *Construction and Building Materials*, vol. 23, no. 1, pp. 353–363, 2009.
- [5] ACI Committee 213, *Guild for Structural Lightweight Aggregate Concrete*, American Concrete Institute, Detroit, Michigan, Mich, USA, 1999.
- [6] K. M. A. Hossain, S. Ahmed, and M. Lachemi, "Lightweight concrete incorporating pumice based blended cement and aggregate: Mechanical and durability characteristics," *Construction and Building Materials*, vol. 25, no. 3, pp. 1186–1195, 2011.
- [7] D. Sari and A. G. Pasamehmetoglu, "The effects of gradation and admixture on the pumice lightweight aggregate concrete," *Cement and Concrete Research*, vol. 35, no. 5, pp. 936–942, 2005.
- [8] S. Weber and H. W. Reinhardt, "New generation of high performance concrete: concrete with autogeneous curing," *Advanced Cement Based Materials*, vol. 6, no. 2, pp. 59–68, 1997.
- [9] T. Y. Lo, H. Z. Cui, and Z. G. Li, "Influence of aggregate pre-wetting and fly ash on mechanical properties of lightweight concrete," *Waste Management*, vol. 24, no. 4, pp. 333–338, 2004.
- [10] W. Yodsudjai, *Evaluation of strengths and choride ion diffusivity of minute regions in concrete using newly developed methods [Ph.D. thesis]*, Tokyo Institute of Technology, Japan, 2003.
- [11] W. C. Tang, P. C. Ryan, H. Z. Cui, and W. Liao, "Properties of self-compacting concrete with recycled coarse aggregate," *Advances in Materials Science and Engineering*, vol. 2016, Article ID 2761294, 2016.
- [12] M. Singh and R. Siddique, "Effect of coal bottom ash as partial replacement of sand on workability and strength properties of concrete," *Journal of Cleaner Production*, vol. 112, pp. 620–630, 2016.
- [13] I. B. Topçu and B. Işıkdağ, "Effect of expanded perlite aggregate on the properties of lightweight concrete," *Journal of Materials Processing Technology*, vol. 204, no. 1-3, pp. 34–38, 2008.
- [14] P. Wattanachai, N. Otsuki, T. Saito, and R. Wongjeeraphat, "Influence of curing condition on the properties of mae moh fly ash mortar at surface and interior," in *Proceedings of the Proceeding of the 6th Regional Symposium on Infrastructure Development*, Bangkok, Thailand, January 2009.
- [15] M. Suzuki, M. Seddik Meddah, and R. Sato, "Use of porous ceramic waste aggregates for internal curing of high-performance concrete," *Cement and Concrete Research*, vol. 39, no. 5, pp. 373–381, 2009.
- [16] R. Kasemchaisiri and S. Tangtermsirikul, "A method to determine water retainability of porous fine aggregate for design and quality control of fresh concrete," *Construction and Building Materials*, vol. 21, no. 6, pp. 1322–1334, 2007.

Research Article

Optimising the Performance of Cement-Based Batteries

Aimee Byrne,¹ Shane Barry,¹ Niall Holmes,¹ and Brian Norton²

¹*School of Civil & Structural Engineering, Dublin Institute of Technology, Bolton St., Dublin 1, Ireland*

²*Dublin Energy Lab, Dublin Institute of Technology, Grangegorman, Dublin 7, Ireland*

Correspondence should be addressed to Aimee Byrne; aimee.byrne@dit.ie

Received 10 November 2016; Revised 8 June 2017; Accepted 14 June 2017; Published 20 August 2017

Academic Editor: Kedsarin Pimraksa

Copyright © 2017 Aimee Byrne et al. This is an open access article distributed under the Creative Commons Attribution License, which permits unrestricted use, distribution, and reproduction in any medium, provided the original work is properly cited.

The development of a battery using different cement-based electrolytes to provide a low but potentially sustainable source of electricity is described. The current, voltage, and lifespan of batteries produced using different electrolyte additives, copper plate cathodes, and (usually) aluminium plate anodes were compared to identify the optimum design, components, and proportions to increase power output and longevity. Parameters examined include water/cement ratio, anode to cathode surface area ratio, electrode material, electrode spacing, and the effect of sand, aggregate, salts, carbon black, silica fume, and sodium silicate on the electrolyte. The results indicate that the greatest and longest lasting power can be achieved using high proportions of water, carbon black, plasticiser, salts, and silica fume in the electrolyte and using a magnesium anode and copper cathode. This cell produced an open-circuit voltage of 1.55 V, a resistor-loaded peak current over 4 mA, maintaining over 1 mA for 4 days, and a quasi steady current of 0.59 mA with a lifespan of over 21 days.

1. Introduction

For autonomous applications both wind and solar energy systems require batteries or other energy storage mechanisms to merit continuous loads due to the intermittency of their supply. Novel battery design can thus help ease society's dependence on oil, coal, and gas. Research into new forms of battery focuses on creating higher power storage and greater recharge capacity and extending the life of traditional batteries by adapting their components and materials.

Electricity is the flow of electrons through a conductive material initiated by an imbalance of electric charge [1]. Voltage is the amount of potential energy available or work to be done, per unit charge to move electrons through a conductor. In a battery, electrons move from one electrode to another via ionic reactions between the electrode molecules and the electrolyte molecules [1]. These reactions are enabled when there is an external path for electric current (via an electric circuit) and cease when it is broken. During discharge, electrons are transferred from the anode to the cathode via the external wire. Figure 1 displays the basic battery concept with a zinc anode, copper cathode, and sodium chloride (NaCl) solution as the electrolyte. In water,

NaCl salt splits into sodium (Na^+) and chloride (Cl^-) ions. Zinc atoms dissolve in the electrolyte as ions missing two electrons (Zn^{2+}) and combine with two negative chloride ions in the electrolyte to form ZnCl_2 . Two negatively charged electrons from the dissolved zinc atom are left in the zinc metal ($2e^-$). The water molecules (H_2O) in the electrolyte reduce to form molecular hydrogen (H_2) on the surface of the copper and bubbles out of the solution. The electrons lost in the reaction are replenished by moving two electrons from the zinc through the external wire as shown in Figure 1.

The electrolyte is an ionic conductor [2]. Liquid electrolytes are favoured in batteries as there is a high mobility of ions and continuity of interface between electrode and electrolyte. The main issue with liquid-electrolyte batteries is the use of toxic materials and their tendency to leak during use or after disposal. Solid electrolytes are not prone to leakage but their ionic conductivity tends to be less than their liquid counterparts and are more costly. Some examples of solid electrolytes are polymers doped with ions [3–5] or ceramics with ions arranged to allow substantial movement of same [6–8]. Cement is an ionic conductor due to its pore solution which can be stored in, and travel through, its pores and microcracks as shown in Figure 2. This facilitates

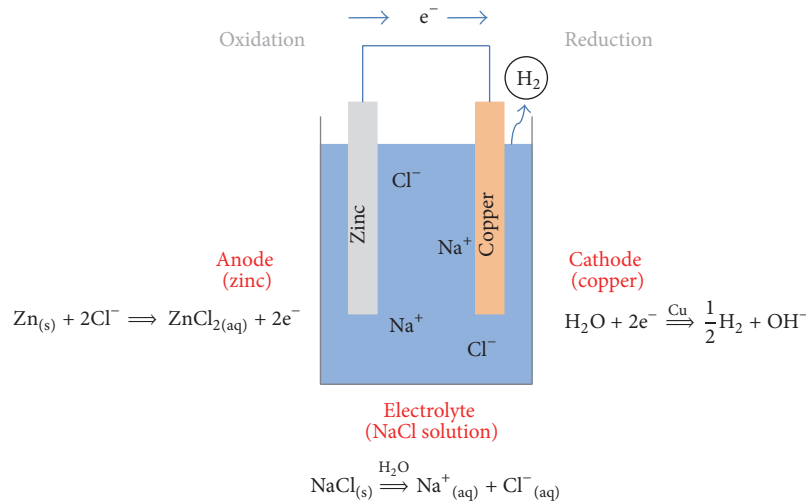


FIGURE 1: Example of basic battery chemical behaviour.

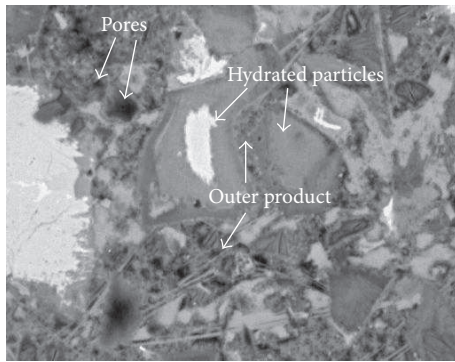


FIGURE 2: Backscattered SEM image of a mature cement paste showing the main microstructural features [9].

its potential as a good electrolyte for novel cement battery designs.

Meng and Chung [2] provided the initial proof of concept that cement-based batteries could indeed be designed to provide a voltage and current output. In their design, cement and water are the common constituents of all layers as shown in Figure 3 with the cathode also containing manganese dioxide particles and the anode layer zinc particles. Carbon black and a water reducing agent were added to both electrode layers. The proposed advantage of this design over the noncement-based electrode probes (Figure 1) is that the active phase is present in all layers (pore solution in the cement paste) and not just at the electrode/electrolyte interface. Manganese dioxide (MnO_2) is one of the most common cathodic battery materials as it is inexpensive and readily available. Zinc has a wide variety of applications as a negative electrode material in batteries, for example, in alkaline zinc-manganese dioxide, silver-zinc, nickel-zinc, and zinc-air batteries [10]. The carbon was added to increase the conductivity of interface between zinc and cement and to increase its overall electronic conductivity. The output from this battery design was very low with open-circuit voltages of

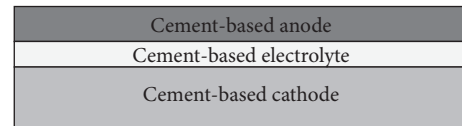


FIGURE 3: Proof of concept layered battery using cement as the continuous constituent throughout the layers [2].

0.72 V, with peak currents of $120 \mu\text{A}$ and only operated when completely saturated.

Examples of the successful development of cement batteries tend to follow the Meng and Chung [2] design of electrode cement layers with active additives separated by a basic cement electrolyte. Rampradheep et al. [11] used a similar design adding a self-curing agent to produce a maximum voltage of 0.6 V and an undisclosed current value. Qiao et al. [12] produced batteries based on the Meng and Chung design [2] and adding carbon fibres and nanotubes in the electrolyte layers which achieved maximum voltages and current densities of approximately 0.7 V and $35.21 \mu\text{A}/\text{cm}^2$. Holmes et al. [13] compared batteries similar to Meng and Chung [2] which were cured in either a deionised water solution or a 0.5 M Epsom salt solution and found that the latter caused a decrease in output with faster drying time and a shorter lifespan. Maintaining a high water content is essential to the life of the layered cement battery.

Examples of electrode-probe type batteries similar to the design of Figure 1 but using cement in the electrolyte tend to focus on corrosion energy harvesting. Burstein and Speckert [14] developed a battery with a steel cathode and an aluminium anode set into a concrete electrolyte that could provide a small current density. Ouellette and Todd [10] developed a seawater battery energy harvester with magnesium and carbon probe electrodes where cement was included in the electrolyte to passively limit the amount of consumable oxygen in deeper water. Holmes et al. [13] showed that limiting cement to the electrolyte greatly

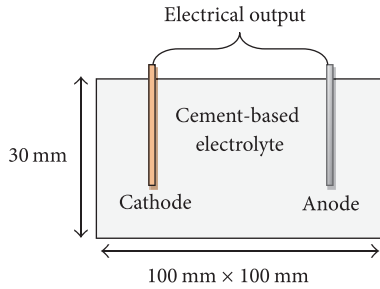


FIGURE 4: Basic schematic of the battery with cement-based electrolyte.

enhanced both the lifespan and output from cement batteries when compared to the layered design of Figure 3.

This paper presents a parametric experimental study to develop a cement-based battery to provide a reliable and sustainable source of electrical energy. Cement-based battery advancement has not been fully academically investigated up to now although there are many examples of small scale experimentation available on video sharing websites and online energy forums. Because the area is so lightly researched there have not been many advances in making these batteries more efficient, powerful, long lasting, and rechargeable. Here, different cement mix designs are compared with regard to their power output and longevity in order to identify which additives enhance battery output and/or increase its lifespan.

The intended use of the cement batteries presented here is for Impressed Current Cathodic Protection (ICCP) of steel reinforcement in concrete structures. ICCP is a method of protecting reinforcing steel in concrete from corrosion by connecting it to an inert, less noble metal than the steel and running a low level of current through it using an external power source [17]. The recommended design current density is 20 mA/m^2 of the circumferential area of the bars [18] or lower values for fully submerged concrete exposed on both sides of 1 mA/m^2 [19]. Cathodic prevention, which is the provision of protective current before any corrosion has taken place, requires a lower current density of $2\text{--}5 \text{ mA/m}^2$ [20]. Therefore the battery testing and development regime presented in this paper focused on enhancing resistor-loaded current and lifespan.

2. Concept

2.1. Basic Design. Following on from the findings of Holmes et al. [13] a battery with solid metal electrodes and cement only present in electrolyte was considered most efficient for the application. The standard form of battery chosen is shown in Figure 4 and used to compare different electrolyte and electrode designs while limiting other characteristics such as size and shape. The base battery consisted of a cement and water paste to form the electrolyte, a copper plate cathode, and an aluminium plate anode. The size of the cell is irrelevant to its voltage; however, it does affect its internal resistance, which in turn affects the maximum current that a cell can

provide [1]. Therefore, all batteries except for the electrode ratio examinations were designed to the same size. Spacing between electrodes was maintained at 100 mm, except for the electrode spacing tests.

2.2. Cement Electrolyte. As discussed in Section 1 a good electrolyte is an ionic conductor which facilitates the movement of charge across it. There are a number of examples of ionic solution migration through hardened concrete. Chloride ions are considered to be the most dominant cause for corrosion of embedded reinforced steel in concrete [21, 22] and can ingress through absorption, diffusion, wicking, and capillary action through an interconnected pore network. The process of corrosion of embedded steel in concrete is another example of ionic flow through set concrete. During corrosion, iron atoms are removed from the steel surface by electrochemical reaction and then dissolve into the surrounding electrolyte solution, which in concrete can only occur where pores meet the reinforcing steel surface at the anode. As it is a redox reaction, electrons must transfer from the anode to a cathodic site which gains in electrons. The transfer of electrons occurs along the metal and creates a current between areas of differing potential. The ions from the reactions such as the ferrous ion (Fe^{2+}) pass into the solution trapped in the concrete pores and react with hydroxyl ions (OH^-) to form ferric hydroxide which further reacts to form rust as shown in Figure 5.

Ionic flow through concrete pores can also be encouraged or forced using ionic extraction techniques. These techniques are used to protect concrete steel reinforcement from corrosion by drawing the ions away. Cathodic protection is essentially the reversal of the corrosion process, acting as an electrochemical cell by introducing an external anode and applying a small current onto the reinforcement, forcing it to act as the cathode (as opposed to the dissolving anode) in an electrochemical cell [23]. Chloride extraction is similar to cathodic protection but it involves a much higher current density and is a once-off application. The ionic conductivity of cement can be increased by increasing the proportion of solution in the paste, thereby increasing the pore volume and the amount of solution in the pores. It can also be increased by enhancing the ionic conductivity of the solution itself by adding constituents whose chemicals dissociate readily to form free ions, for example, salts.

2.3. Electrodes. The amount of voltage (electromotive force) generated by any battery is specific to the particular chemical reaction for that cell type. Chemical interactions where electrons are transferred directly between molecules and atoms are called oxidation-reduction or (redox) reactions. In a battery the anode and the cathode undergo oxidation and reduction, respectively. The galvanic series of metals displayed in Table 1 is in the presence of seawater. Aluminium and copper were chosen due to being highly anodic and cathodic, respectively, resulting in an expected electromotive potential of 2 V ($0.34 \text{ V} + 1.66 \text{ V}$) for the base battery design.

Theoretically the proportion of cathode to anode should be determined using their oxidation and reduction reactions (see (1) and (2)) and their molar mass resulting in a design

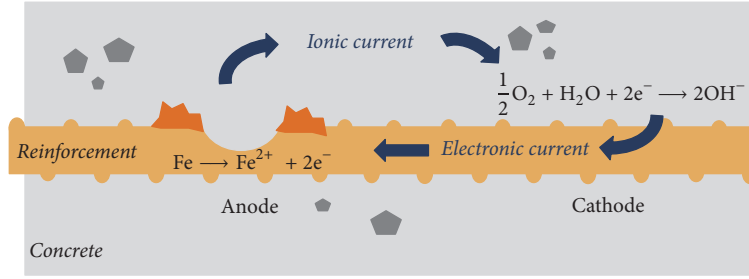
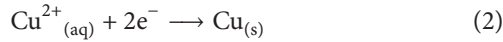
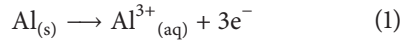


FIGURE 5: Process of embedded steel reinforcement providing an example of ionic flow in concrete [13].

TABLE 1: Partial standard electromotive force series as measured against a hydrogen reference electrode [15].

Material		Standard electrode potential (V)
Magnesium	Anodic ↑	-2.363
Aluminium		-1.662
Zinc		-0.763
Iron		-0.440
Nickel	Cathodic ↓	-0.250
Copper		+0.345
Platinum		+1.200
Gold		+1.498

of 2.5 parts copper (Cu) to 1 part aluminium (Al). However a proportion of 1:1 was taken in the base designs before this theory was tested.



A common issue with metals, particularly highly anodic materials, is the formation of oxide layers (a thin layer of reaction product). Aluminium reacts with oxygen very rapidly and forms aluminium oxide (Al_2O_3) in the atmosphere. Copper also forms an oxide layer when exposed to air, but these reactions are slower and mainly consist of Cu_2O and CuO [23]. These oxide layers can impede the output of the battery as it reduces the interface between the electrodes and electrolyte. Such layers can be removed by scraping using sand paper or washing with acetic acid and rinsing with a volatile liquid such as ethanol [2] prior to addition to the mix.

3. Methodology

3.1. Preparation. Materials of the highest purity were chosen so that their specific impact could be distinguished from the potential impact of their impurities. Materials were also chosen to be nontoxic if leaked so that these batteries could offer an advantage over many conventional liquid-electrolyte types. Details on the material used in the batteries are summarised in Table 2.

A water/cement ratio of 0.4 was used as the basic electrolyte design. The electrolyte materials were weighed and passed through a 200 μm sieve to remove any nonconforming

lumps or bulk to achieve the desired powder format. The dry constituents were mixed well with deionised water and placed into 100 × 100 × 30 mm plastic moulds (300 × 120 × 50 mm for electrode ratio testing) to create the electrolyte block.

The 60 × 30 × 0.5 mm electrode plates were sanded and washed in a borax solution to remove any impurities and inserted into the wet electrolyte block protruding 5 mm from the surface to facilitate connection to the resistor circuit. Batteries were then placed on a vibration table for 30 seconds to remove any remaining air and allowed to cure for 24 hours under a polythene sheet after which testing began.

3.2. Data Acquisition. Open-circuit voltage and continuous voltage (V) readings during current discharge (I) through a 10 Ω resistor (R) were recorded over the life of the batteries. Current discharge through the resistor was calculated from the voltage readings using Ohm's law ($I = V/R$).

A 10 Ω resistor was connected between the anode and cathode of the battery to act as a resistor load as per Figure 6. A LabVIEW National Instruments differential data acquisition (DAQ) unit NI 9205 was used to record voltage either side of the resistor as shown in the same schematic. Pilot testing using a multimeter refined the frequency of readings and provided likely ranges of measured current and voltages. These values allowed for a suitable LabVIEW programme to be finalised (Figure 6). The setup was calibrated against a DC power unit and volt meter. Logged files from the LabVIEW programme were written into CSV (comma separated values) format and imported directly into MS Excel after testing was complete.

3.3. Battery Design and Reasoning. Seven different components were examined for their effect on resistor-loaded-current, open-circuit voltage, and lifespan. These were the water/cement ratio (WC 1-4), the anode to cathode ratio (Al 4:1 Cu-Al 4:4 Cu), basic additives (Add 1-6), 0.5 M salt solutions to replace water (Soln 1-Soln 3), salt added as solid crystals (Crys 1-2), sodium silicate as full and partial water replacement and as a coating to the plates (SS 1-3), electrode spacing (Sp 1-5), carbon black proportion (CB 1-4), and the effect of using different electrode materials (El 1-4). The proportions of the mix designs, materials, and electrode spacing are presented in Table 3. Add 1 and Add 5, shown in bold, were often used as base mixes from which to compare other batteries. The average dry weight of each cell was 335 g.

TABLE 2: Details of cement battery materials.

Element	Material	Details
Electrolyte	Carbon black	Porous carbon agglomerates; average size 30 nm
	Cement	CEM I complying with BS EN 197-1, 2000 [16]
	Water reducer	Sika VistoCrete 30HE
	Salts (NaCl, Alum & Epsom salt)	Over 99% purity for all
	Sand and lightweight aggregate	Sand 0.4 mm, expanded clay aggregate 15 mm
	Sodium silicate	Density of 1.38 g/cm ³ (40 Be) and a pH of 11.3
Anode	Zinc plates	>99% purity
	Aluminium plates	>99% purity
	Magnesium alloy plates	96% purity (3% aluminium & 1% zinc)
Cathode	Copper plate	99.5% purity, 0.4 mm thick
	Carbon	Graphite rod

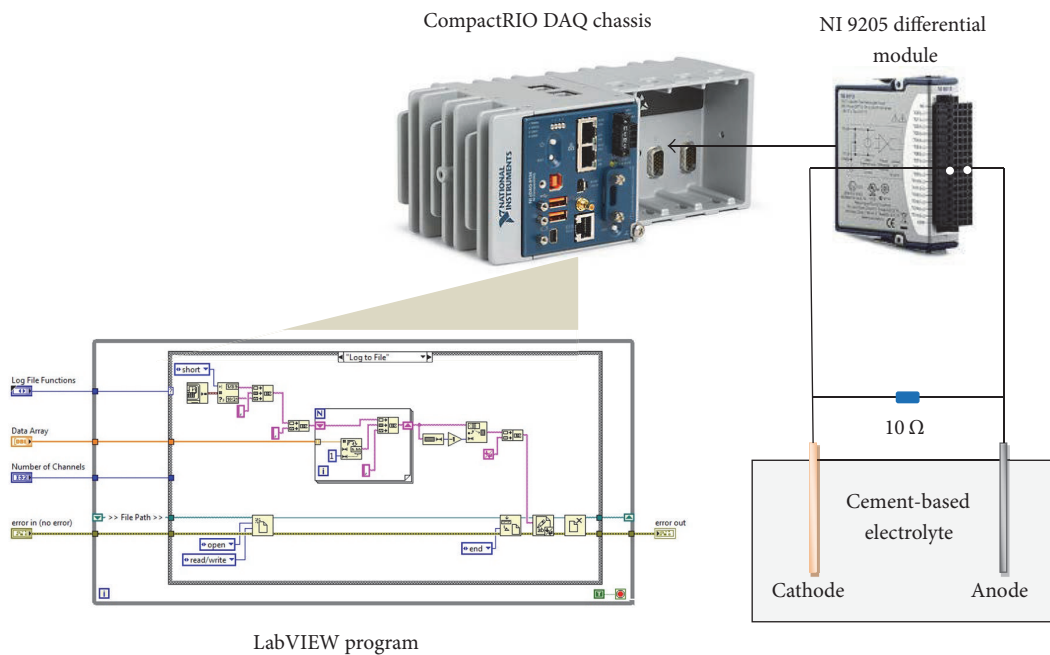


FIGURE 6: LabVIEW voltage recording across the battery's 10 Ω resistor load.

3.3.1. *Water/Cement Ratio.* The pore water solution in set cement mixes provides the network for ions to travel allowing the transfer of charge and the production of current. Therefore, the relationship between water/cement ratio (and therefore the volume of water in the cement pores) and the performance of the battery was compared by adjusting the w/c ratio between 0.3 and 0.6 and recording the output.

3.3.2. *Anode/Cathode Ratio.* Theoretically when designing a battery the ratio of anode to cathode can be calculated as discussed in Section 2.3 using their molar mass. For aluminium and copper this should be approximately Al 2.5 : 1 Cu. Therefore the ratio of anode to cathode was examined here by altering the ratios in favour of the anode or the cathode.

As discussed in Section 2.3, the greater the surface area of contact between the electrodes and electrolyte is, the greater

the current should be and there should be no effect on voltage. Therefore, an increase in both anode and cathode material was also examined.

3.3.3. *Additives.* The rigidity of the battery was enhanced by adding sand (Add 2) or lightweight expanded clay aggregate (Add 3) to the base mix design (Add 1). Plasticiser is generally added to allow for a reduction in the amount of water needed while maintaining workability. However, as a reduction in water would lead to a reduction in pores and pore solution, the volume of water added to the mix was not reduced for Add 4. Add 5 included carbon black as an admixture as it is known to increase electronic conductivity and formed the base carbon black mix for comparison with batteries that included carbon black along with other developments. Silica fume has been shown to improve the mechanical properties and durability of cement [20]. Silica fume was introduced as

TABLE 3: Cement battery designs.

Ref.	CEM I (g)	Water (g)	Anode	Cathode	Pl (g)	CB (g)	Additive (g) or space between electrodes (mm)	Photo	
WC 1	300	90	Al	Cu					
WC 2	300	120	Al	Cu					
WC 3	300	150	Al	Cu					
WC 4	300	180	Al	Cu					
Al 4:1 Cu	900	360	Al	Cu	15	5			
Al 3:1 Cu	900	360	Al	Cu	15	5			
Al 2:1 Cu	900	360	Al	Cu	15	5			
Al 1:1 Cu	900	360	Al	Cu	15	5			
Al 1:2 Cu	900	360	Al	Cu	15	5			
Al 1:3 Cu	900	360	Al	Cu	15	5			
Al 1:4 Cu	900	360	Al	Cu	15	5			
Al 4:4 Cu	900	360	Al	Cu	15	5			
Add 1	300	120	Al	Cu					
Add 2	300	120	Al	Cu					100 g sand
Add 3	300	120	Al	Cu					100 g agg
Add 4	300	120	Al	Cu	5				
Add 5	300	120	Al	Cu	5	5			
Add 6	300	120	Al	Cu	5	5			100 g silica fume
Soln 1	300	—	Al	Cu	5	5	120 g 0.5 M NaCl		
Soln 2	300	—	Al	Cu	5	5	120 g 0.5 M Epsom		
Soln 3	300	—	Al	Cu	5	5	120 g 0.5 M Alum		
Crys 1	300	120	Al	Cu	5	5	100 g Epsom salt		
Crys 2	300	120	Al	Cu	5	5	100 g Alum salt		
SS 1	300	—	Al	Cu	5	5	120 g sodium silicate		
SS 2	300	100	Al	Cu	5	5	20 g sodium silicate		
SS 3	300	120	Al	Cu	5	5	Sodium silicate coating		
Sp 1	300	120	Al	Cu	5	5	5 mm		
Sp 2	300	120	Al	Cu	5	5	10 mm		
Sp 3	300	120	Al	Cu	5	5	30 mm		
Sp 4	300	120	Al	Cu	5	5	60 mm		
Sp 5	300	120	Al	Cu	5	5	80 mm		
CB 1	300	120	Al	Cu	5	3			
CB 2	300	120	Al	Cu	5	4.5			
CB 3	300	120	Al	Cu	5	6			
CB 4	300	120	Al	Cu	5	7.5			
El 1	300	120	Mg	Cu	5	5			
El 2	300	120	Al	Cu	5	5			
El 3	300	120	Zn	Cu	5	5			
El 4	600	230	Al	C	12	12			

an additive to the base mix alongside conductive carbon black and plasticiser as Add 6.

3.3.4. Salts. Pure water is not very conductive; however, when salt is dissolved in it, salt molecules readily split and provide additional ions in the fluid as discussed in Section 1. Add 5, which contained carbon black and plasticiser, was used as the base mix for the salt batteries. 0.5 Molar solutions of sodium chloride (NaCl), Alum salt ($\text{AlK}_2\text{O}_8\text{S}_2 \cdot 12\text{H}_2\text{O}$), and Epsom salt ($\text{MgSO}_4 \cdot 7\text{H}_2\text{O}$) were made up using deionised water. These solutions were used as total water replacements when compared to the base mix as Soln 1, Soln 2, and Soln 3. Alum (Crys 1) and Epsom salts (Crys 2) were also added to the base Add 5 mix as solid crystals and the water content was maintained as per the base mix.

3.3.5. Sodium Silicate. Sodium silicate is typically added to concrete to reduce its porosity by forming calcium silicates which fill the pores reducing water permeability [21]. Sodium silicate was added to the base mix design as full replacement (SS 1) and partial replacement (SS 2) of water content. The solution was further used to coat the electrodes (SS 3) in an attempt to reduce the gas which had been observed surfacing in the electrolyte at the aluminium anode plate thereby increasing the smoothness of the electrode/electrolyte interface.

3.3.6. Electrode Proximity. The cement electrolyte layer is kept as thin as possible to reduce resistance in layered batteries [2]. The base paste mix (Add 5) was used to compare electrode spacing of 5, 10, 30, 60, and 80 mm. This is examined in order to determine whether the volume of electrolyte between the electrodes had any significant influence on performance.

3.3.7. Carbon Black. Carbon black (CB) particles are very small, have high porosity, and can form long branched chains which result in improving the electrical conductivity of the compound such as conductive plastic composites [24]. It was used in previous battery designs [2, 11, 13] to enhance the connectivity between electrode particles or in cement batteries to create a more intimate interface between the active electrode material and the cement [2, 25]. However, in the arrangement under investigation here, carbon black cannot be added to the electrodes as they are solid plates and is instead added as an admixture to the cement electrolyte.

The addition of carbon black makes the hardened cement brittle [13]. It was therefore decided to determine the effects of increasing the proportion of carbon black in the design on output while not impinging on the rigidity of the block. Carbon black was added to the base mix design by 3, 4.5, 6, and 7.5 g alongside 5 g of plasticiser (PI) so that no additional water was required (which would increase the brittleness).

3.3.8. Electrode Material. As discussed in Section 2.3 the electrode material and the respective electromotive force potentials control the voltage of any battery cell. The designs so far (Sections 3.3.1–3.3.8) used copper and aluminium electrodes. The base design (Add 5) was used to compare different

electrode materials Al : Cu (El 1), Mg : Cu (El 2), Zn : Cu (El 3), and Al : C (El 4). The plate sizes were maintained the same to allow for direct comparison with the exception of El 4 as carbon could only be sourced in probe form with a greater surface area in which case the aluminium anode volume had to be increased to match it. These materials each possess different electromotive potentials as presented in Table 1 where different combinations should present the different voltages.

4. Results and Discussion

4.1. Parameters of Interest. The following sections present the current discharge curves on a logarithmic scale to show the effect of the different parameters discussed in Sections 3.3.1–3.3.8 in terms of current discharge through a 10 Ω resistor and lifespan.

4.2. Water/Cement Ratio. The open-circuit voltage and lifespan were unaffected by the increasing water content. However, a direct correlation exists between the water content and the current under resistor load as shown in Figure 7. A pattern of increased current of 3.5–5% was observed for every 0.1 increases in water/cement ratio. Any higher water content resulted in the water settling out of the mix during curing.

The pore structure, shape, size, distribution, and connectivity affect the movement of ions in a cement battery electrolyte [21]. Lower w/c ratios have been shown to result in smaller porosity and constrictivity (depends on the ratio of the diameter of the diffusing particle to the pore diameter) as well as a higher tortuosity factor (property of pathway being tortuous) [26]. The work presented here reflects the findings of these simulations as low w/c ratios resulted in lower current outputs from the battery cells due to the reduced connectivity and volume of pores.

4.3. Anode/Cathode Ratio. A ratio of anode to cathode as per molar mass calculation which would lead to a balancing of reactions in the electrode materials did not lead to a greater output from the cells. Instead the more general trend of more electrode material resulting in higher current was observed (Figure 8). Open-circuit voltage was not impacted as the electromotive force of the electrode materials remained the same (around 1.2 V), but more current was produced with the higher anode and cathode volumes as more chemical reactions were facilitated.

4.4. Additives. As may be seen in Figure 9, the addition of sand, lightweight aggregate, or plasticiser showed no significant impact on current, voltage, or lifespan. Carbon black was found to slightly increase the voltage (by approximately 0.15 V) and improved the flow of electric charge (current) with a better discharge life to over 7 hours. The addition of silica fume on top of carbon black further increased both the current and lifespan but had no further impact on open-circuit voltage. Silica fumes relationship with ionic conductivity in cement is complex. It has been shown to reduce the overall electrical conductivity of cement paste and reduce porosity [27, 28]; however, at higher proportions it

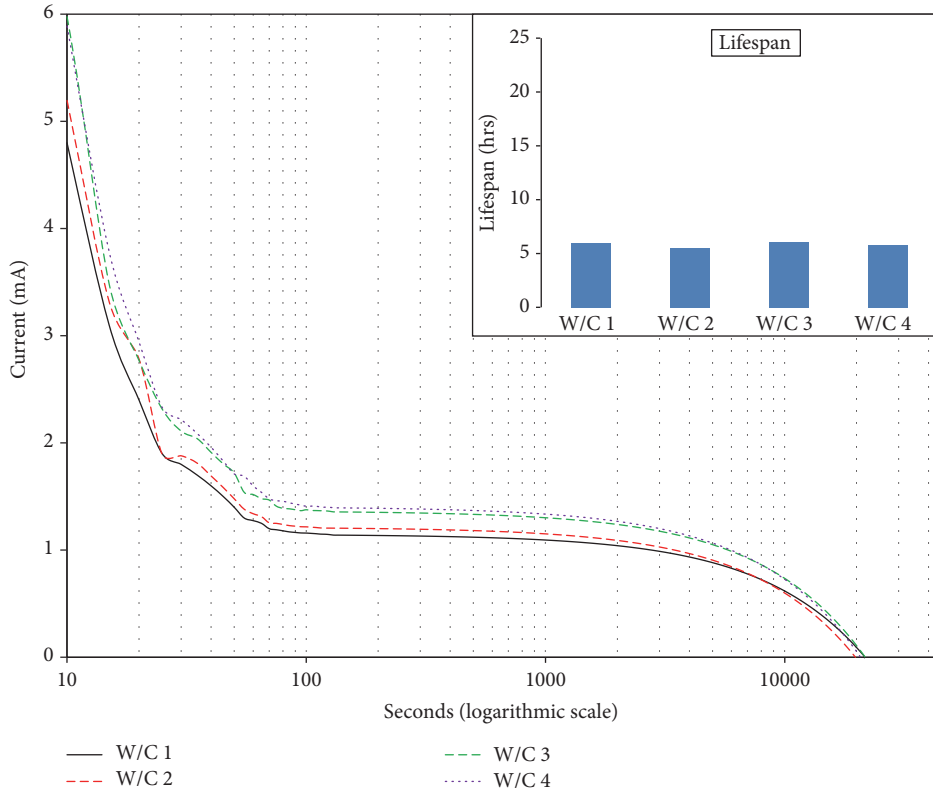


FIGURE 7: Current discharge curves across a 10 Ω resistor for increasing w/c ratio.

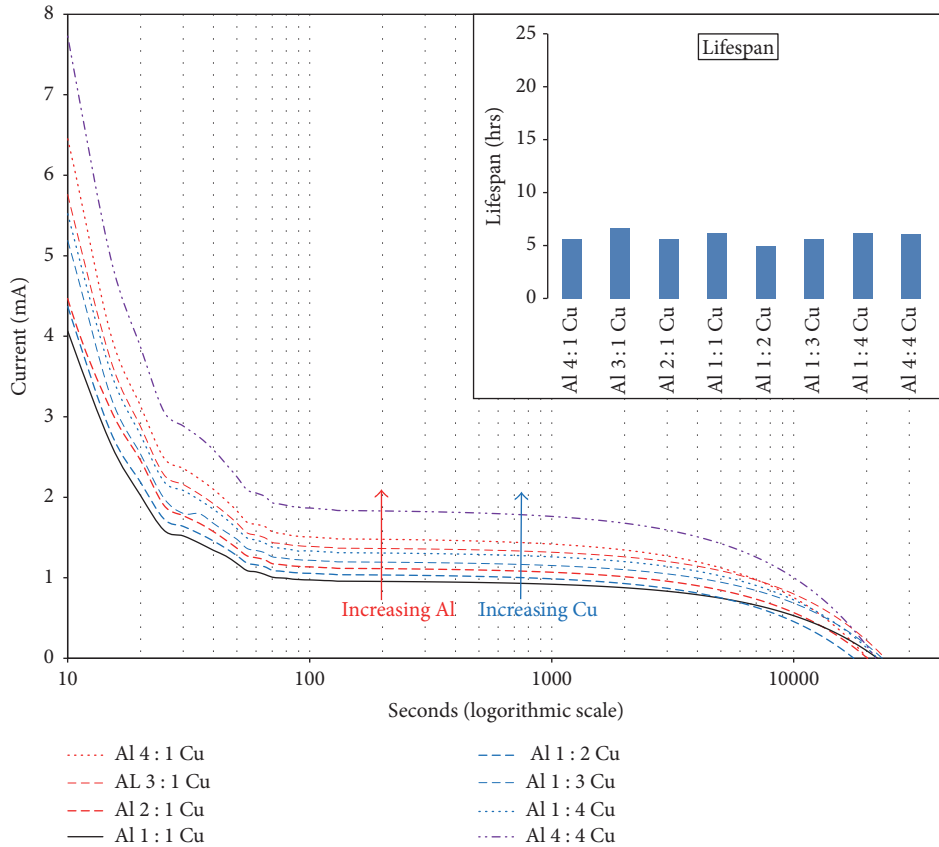


FIGURE 8: Current discharge curves across a 10 Ω resistor for different anode to cathode ratios.

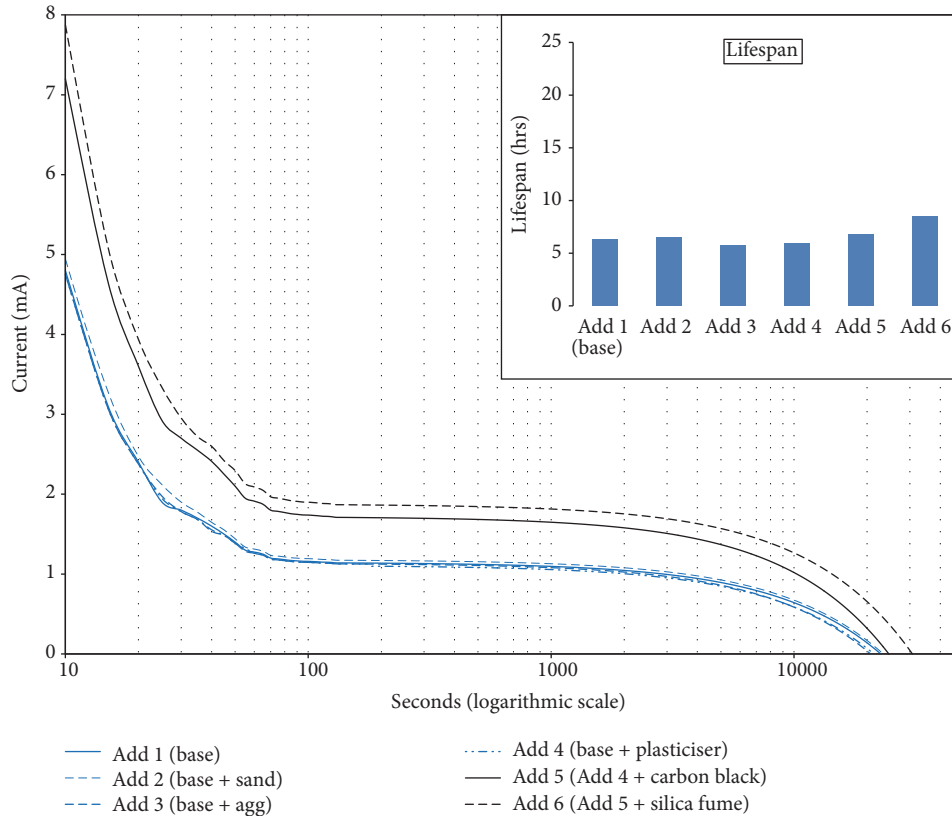


FIGURE 9: Current discharge curves across a $10\ \Omega$ resistor for different additives.

can increase the porosity of the paste [28] which is associated with increasing ionic conductivity. However, similar to these findings, silica fume has previously been shown to increase the electrical conductivity of cement pastes containing conductive additives such as carbon fibres by improving their dispersion in the mix [29, 30].

4.5. Salts. The addition of salt, whether in solution or raw crystal form, to the electrolyte significantly increased the battery lifespan and improved the flow of electric charge as shown in Figure 10. The base mix contained only deionised water in the solution. In the other three battery designs different 0.5 Molar salt solutions were used. Compared to the base mix, the use of salt solutions led to an increase in current output by approximately 20% from 1.69 mA to 2.02 mA. The lifespan of the batteries was greatly increased by approximately 50% from 6.82 hrs to 9.77–12.17 hrs. Although salt solution increased current and longevity, adding it in solid granule form was also beneficial increasing current by 15% from 1.69 mA to 1.90 mA and lifespan by 62.5% from 6.82 hrs to 12.54–12.57 hrs.

4.6. Sodium Silicate. Sodium silicate is typically added to concrete to reduce porosity and water penetration which would inhibit ionic flow. However, it has a high conductive ion concentration in the pore solution and therefore has shown a higher passing of charge than other activation materials in alkali-activated slag mortars [31]. The electrical

conductivity of most ordinary silicate glasses is due to the motion of alkali ions, especially sodium [32]. The total replacement of water with sodium silicate (SS 1) reduced both current and lifespan of the battery to almost nothing as seen in Figure 11. Its addition as a partial water replacement (SS 2) showed no significant impact when compared to the base design with currents within 0.02 mA of each other and lifespan within half an hour.

In Burstein and Speckert's work [14] a swelling of the electrolyte system was observed during setting of the concrete due to hydrogen evolution at the aluminium anode. This was also observed in the batteries presented here as bubbles observed between the anode and the concrete electrolyte. Coating the anode with sodium silicate (SS 3) was an attempt to provide ions for the hydrogen to react with forming harmless water; however, this did not result in any improvement in output.

4.7. Electrode Proximity. Figure 12 shows no discernible correlation in between electrode spacing and current, lifespan, or open-circuit voltage. Current was within 0.05 mA of the base mix, lifespan within 43 minutes, and open-circuit voltage within 0.08 V.

4.8. Carbon Black. Carbon black has been shown to increase output, particularly current and longevity as found in Section 4.4. As may be observed in Figure 13, there is a clear correlation between carbon black content and both current

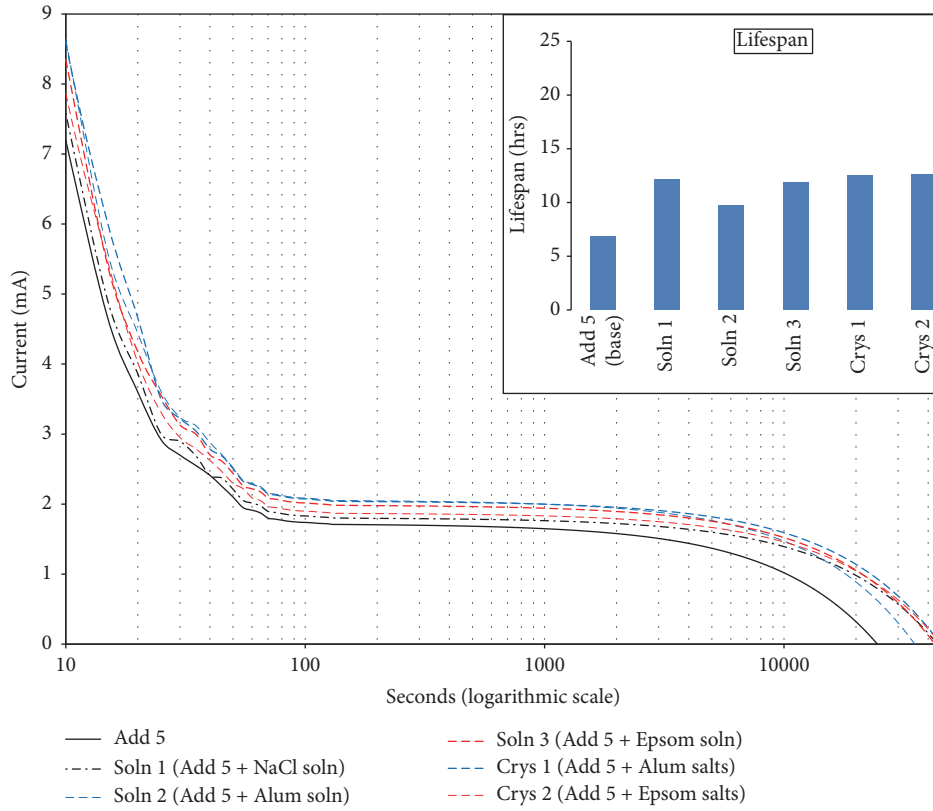


FIGURE 10: Current discharge curves across a 10 Ω resistor for different salts.

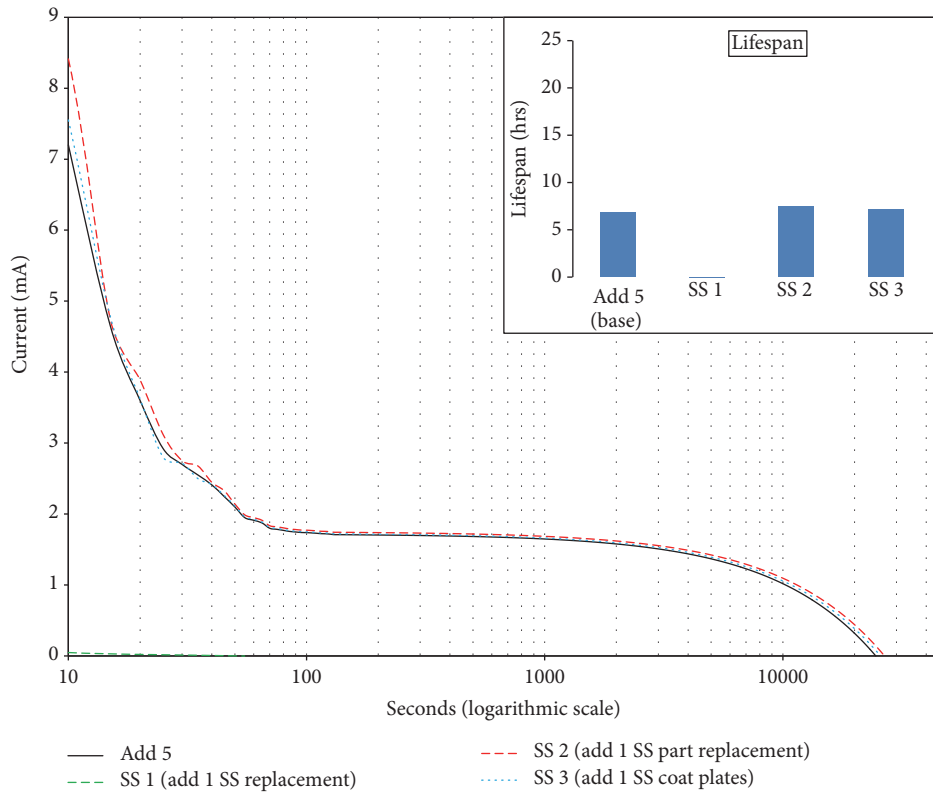


FIGURE 11: Current discharge curves across a 10 Ω resistor for sodium silicate additive.

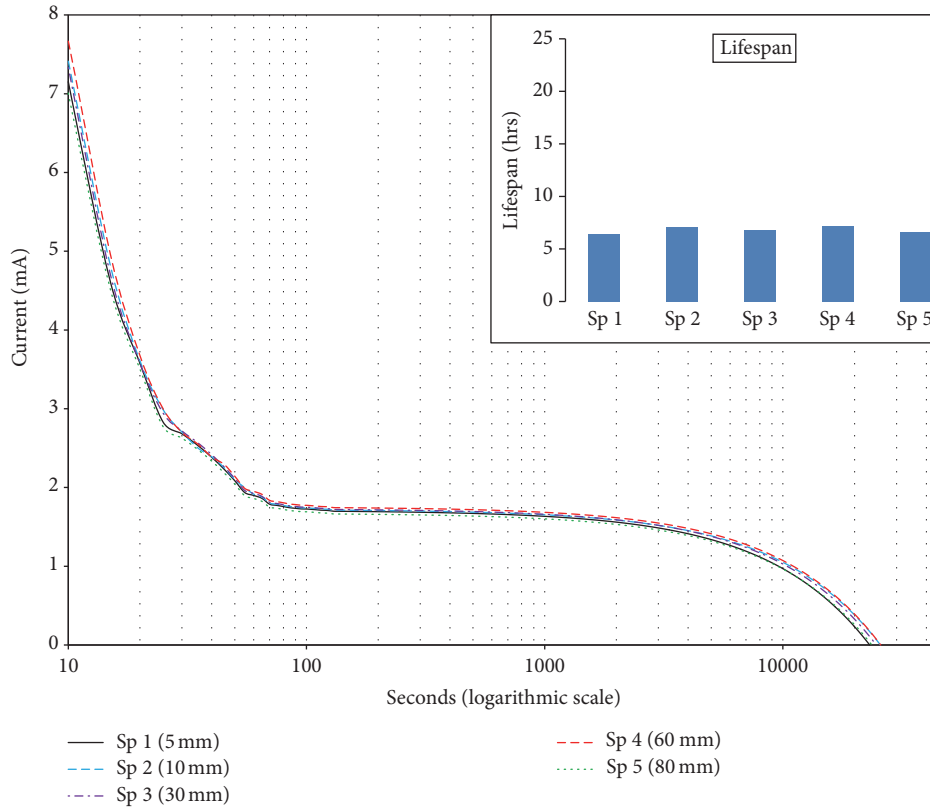


FIGURE 12: Current discharge curves across a 10Ω resistor for increasing electrode spacing.

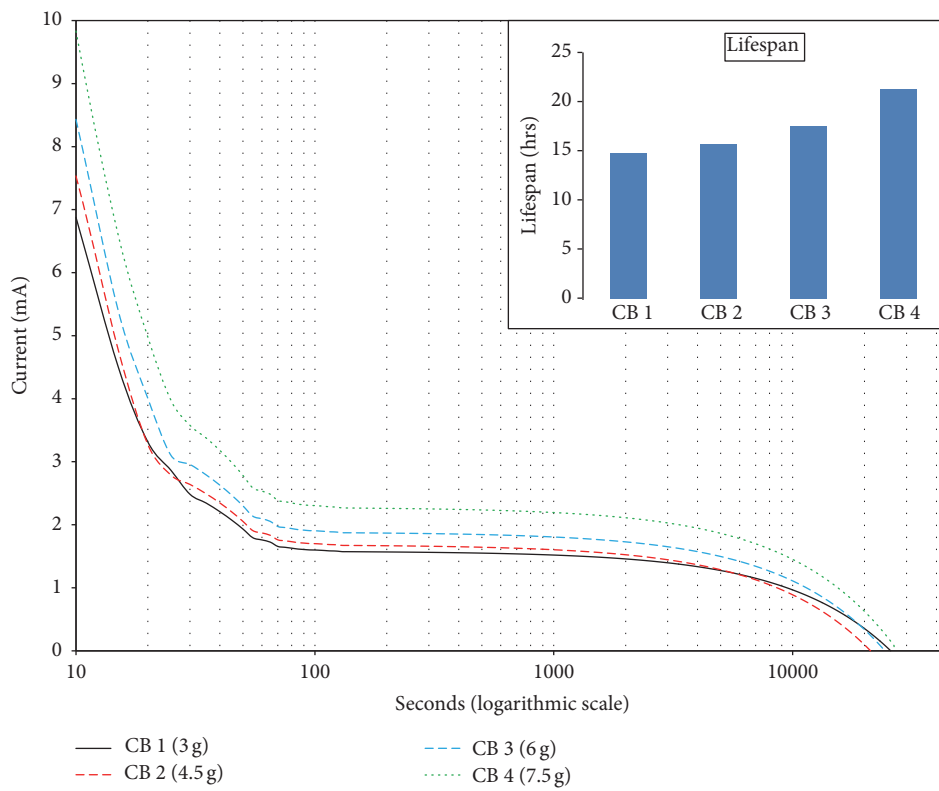


FIGURE 13: Current discharge curves across a 10Ω resistor with increasing carbon black content.

TABLE 4: Overview of findings.

Variable	Current (under 10 Ω load)	Voltage (initial open-circuit)	Lifespan
Increase w/c ratio	↑	=	=
Sand	=	=	=
Aggregate	=	=	=
Silica fume	↑	=	↑
Carbon black (+plasticiser)	↑	↑	↑
Increase electrode material	↑	=	=
Salt solution	↑	=	↑
Salt crystals	↑	=	↑
Sodium silicate	=	=	=
Closer electrodes	=	=	=
Magnesium anode	↑	↑	↑

output and lifespan. As its proportion by weight increases from 0.7% to 1.7%, the resting current increases from 1.5 mA to 2.2 mA (44%), open-circuit voltage increases from 1.3 to 1.4 V (13%), and lifespan increased from under 15 hours to over 21 hours (33%), respectively. Due to the fineness of carbon black particles its addition makes cells considerably more brittle [13] and inclusion of a plasticiser proved to be essential when using carbon black in the cement paste in these proportions.

Carbon black particles have a graphite-type crystalline structure, which improves electrical conductivity and is, therefore, more typically used in electrode materials [33, 34]. It is therefore likely that the increase in voltage is due to the carbon black particles in contact with the electrode. In the electrolyte, the movement of charge in the cell involves the generation and consumption of both ions and electrons. High reaction activity is achieved when transport rates are high for both ions and electrons. Furthermore, similar increases in ionic conductivity have been found in previous studies using carbon black in polymer mixes where it was speculated that the carbon black may contain a small number of mobile ions that are able to contribute to ionic conductivity upon exposure to moisture [35]. Modified carbon materials including carbon black have also previously been added to enhance the ionically conductive pathways of polymer-ionic liquid electrolytes [36]. For these tests the wealth of electrons in the carbon and the affinity with the ions in the polymer facilitated ion dissociation and transportation through the electrolyte.

4.9. Electrode Material. Replacing the aluminium anode with magnesium greatly increased the current, voltage, and lifespan of the cell as shown in Figure 14. Replacing the copper cathode with carbon also showed a benefit; however, the total size of the El 4 cell was double that of the other cells due to the available carbon cathode size meaning that a direct comparison cannot be made.

Copper was consistently used as the cathode material as it is highly noble. Comparing aluminium, zinc, and magnesium anodes, it can be seen that magnesium produced a substantial improvement in all areas, particularly current and longevity. Magnesium is one of the most active materials (Table 1)

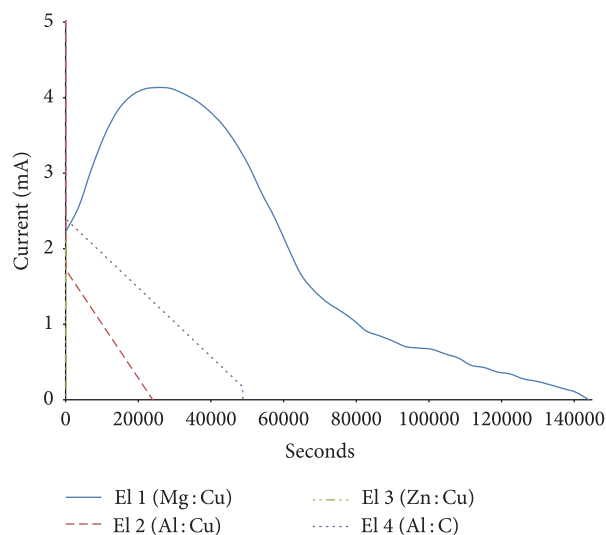


FIGURE 14: Current discharge curves across a 10 Ω resistor for different electrode combinations (note: this is not a logarithmic scale).

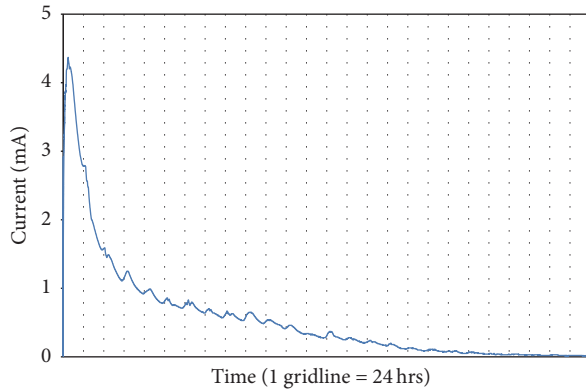
followed by zinc and then aluminium [37]. The measured open-circuit voltages for El 1 and El 2 reflect this at 1.553 V for Mg:Cu and 1.311 V Al:Cu. However, the value for zinc measured to be 0.059 V. It can therefore be presumed that an error occurred during the zinc test, by short circuiting the battery, or that the zinc plates were sealed or had an oxide layer that was not removed adequately, thus creating a barrier between the anode and the electrolyte. This is an area where further investigation is required.

4.10. Results Summary. Table 4 presents a summary of the impact of each individual change in battery constituent or proportion on loaded current, open-circuit voltage, and lifespan. Cases listed as equal include minor changes (below 0.1 mA, 0.2 V, or 1 hour) or where no discernible pattern was identified.

Initial battery testing, with prioritised current and lifespan, indicates that optimal output could be achieved by designing high w/c ratios, using magnesium as the anode

TABLE 5: Final battery design.

CEM I (g)	Water (g)	Carbon black (g)	Plasticiser (g)	Silica fume (g)	Epsom salt (g)	Alum salt (g)	Magnesium anode (mm)	Copper cathode (mm)
300	176	6	5	20	50	50	60 × 30 × 0.5	60 × 30 × 0.5

FIGURE 15: Final battery current discharge curve across $10\ \Omega$ resistor (note: this is not a logarithmic scale).

and adding high proportions of carbon black, plasticiser, salt granules, and silica fume. Changes to the electrolyte constituents or the electrode proximity and ratio showed no significant influence on the time taken for the current output to plateau. However, changing the electrode material had a significant influence, particularly in the Mg : Cu cell. A final battery was designed as per Table 5 which has a high water/cement ratio of 0.6. Although carbon black is inert, it is similar in density to silica fume and its inclusion has been shown to increase the strength of cement mixes [27]; therefore, if both carbon black and silica fume are considered as pozzolanic materials, the presented mix water/cement + pozzolan ratio is 0.54.

As shown in Figure 15 the lifespan of the battery was considerably higher than the previous designs lasting 21 days. The quasi steady $10\ \Omega$ resistor-loaded current taken from three days after the initial peak (4.37 mA) over a 12-day period was 0.59 mA.

The discharge curve has a similar shape to the previous battery design that used magnesium as the anode (El 1 in Figure 14) with a curved peak and slow decline. The peak current achieved (4.37 mA) was also similar to El 1 (4.13 mA). However, there was a considerable increase in lifespan when comparing these batteries, from 40 hrs to 505 hrs. Furthermore, the average quasi steady discharge current of 0.59 mA lasted only 19 hrs for El 1 (Figure 14) increasing to 288 hrs for the final battery (Figure 15). As the anode and cathode materials and sizes were the same for both batteries, this enhancement in both current and longevity can be attributed to the design of the electrolyte which provided more carbon black, higher water content, and the introduction of silica fume and Epsom and Alum salts. This battery type can provide over 1 mA through the $10\ \Omega$ resistor for 4 days and a quasi steady current of 0.59 mA with a lifespan of over 21 days.

Further development of cement batteries found that sealing the electrolyte can increase the current output by 50% and that the capacity can be successfully increased by connecting cells in parallel [38].

5. Conclusion

This paper presented the findings from a study into the design of cement-based battery blocks. The study investigated the influence of water content, anode to cathode surface area, various additives, electrode type, electrode spacing, and the addition of carbon black. Previous work in this area developed a layered cement-based battery which produced small electrical outputs with a very short discharge life. The results here present much improved battery designs with higher electrical outputs and lifespan. In the cement electrolyte the use of higher w/c ratios, carbon black addition with plasticiser, Alum and Epsom salts, and silica fume all increased the voltage, current, and lifespan. A magnesium anode and a copper cathode proved to be the most effective electrode combination of those studied producing an adequate cathodic protection current for $1\ \text{m}^2$ of submerged concrete for 4 days. Testing is ongoing to increase the lifespan and current output through constituent design and sealing methods. Initial tests into recharging the batteries using photovoltaics have been promising.

Conflicts of Interest

The authors declare that they have no conflicts of interest.

Acknowledgments

This research was funded by Science Foundation Ireland's Technology Innovation Development Award (SFI TIDA).

References

- [1] T. R. Kuphaldt, *Lessons in electric circuits*, 1, 2006.
- [2] Q. Meng and D. D. L. Chung, "Battery in the form of a cement-matrix composite," *Cement and Concrete Composites*, vol. 32, no. 10, pp. 829–839, 2010.
- [3] R. Ashrafi, D. K. Sahu, P. Kesharwani, M. Ganjir, and R. C. Agrawal, "Ag⁺-ion conducting Nano-Composite Polymer Electrolytes (NCPEs): synthesis, characterization and all-solid-battery studies," *Journal of Non-Crystalline Solids*, vol. 391, pp. 91–95, 2014.
- [4] B. Sun, J. Mindemark, K. Edström, and D. Brandell, "Polycarbonate-based solid polymer electrolytes for Li-ion batteries," *Solid State Ionics*, vol. 262, pp. 738–742, 2014.
- [5] N. U. Taib and N. H. Idris, "Plastic crystal-solid biopolymer electrolytes for rechargeable lithium batteries," *Journal of Membrane Science*, vol. 468, pp. 149–154, 2014.

- [6] B. R. Shin, Y. J. Nam, D. Y. Oh, D. H. Kim, J. W. Kim, and Y. S. Jung, "Comparative study of $\text{TiS}_2/\text{Li-In}$ all-solid-state lithium batteries using glass-ceramic Li_3PS_4 and $\text{Li}_{10}\text{GeP}_2\text{S}_{12}$ solid electrolytes," *Electrochimica Acta*, vol. 146, pp. 395–402, 2014.
- [7] M. Tatsumisago, R. Takano, K. Tadanaga, and A. Hayashi, "Preparation of $\text{Li}_3\text{BO}_3\text{-Li}_2\text{SO}_4$ glass-ceramic electrolytes for all-oxide lithium batteries," *Journal of Power Sources*, vol. 270, pp. 603–607, 2014.
- [8] M. Tatsumisago and A. Hayashi, "Superionic glasses and glass-ceramics in the $\text{Li}_2\text{S-P}_2\text{S}_5$ system for all-solid-state lithium secondary batteries," *Solid State Ionics*, vol. 225, pp. 342–345, 2012.
- [9] P. Stutzmann, Hydration and microstructure of portland cement paste, 2014 <http://iti.northwestern.edu/cement/monograph/Monograph5.5.1.html>.
- [10] S. A. Ouellette and M. D. Todd, "Cement seawater battery energy harvester for marine infrastructure monitoring," *IEEE Sensors Journal*, vol. 14, no. 3, pp. 865–872, 2014.
- [11] G. S. Rampradheep, M. Sivaraja, and K. Nivedha, "Electricity generation from cement matrix incorporated with self-curing agent," in *Proceedings of the 1st International Conference on Advances in Engineering, Science and Management, ICAESM-2012*, pp. 377–382, India, March 2012.
- [12] G. Qiao, G. Sun, H. Li, and J. Ou, "Heterogeneous tiny energy: an appealing opportunity to power wireless sensor motes in a corrosive environment," *Applied Energy*, vol. 131, pp. 87–96, 2014.
- [13] N. Holmes, A. Byrne, and B. Norton, "First steps in developing cement-based batteries to power cathodic protection of embedded steel in concrete," *Sustainable Des and Res (SDAR)*, 2015.
- [14] G. T. Burstein and E. I. P. Speckert, "Developing a battery using set concrete as electrolyte," in *Proceedings of the Metal/Air and Metal/Water Batteries - 210th ECS Meeting*, pp. 13–20, Mexico, November 2006.
- [15] M. Orazem, *Underground Pipeline Corrosion*, Elsevier Science, 2014.
- [16] British Standards Institution. BS EN 197-1: Cement: composition, specifications and conformity criteria for common cements. London, 2000.
- [17] R. B. Polder, "Cathodic protection of reinforced concrete structures in the Netherlands - experience and developments: Cathodic protection of concrete - 10 years experience," *Heron*, vol. 43, no. 1, pp. 3–14, 1998.
- [18] R. Polder, J. Leggedoor, G. Schuten, S. Sajna, and A. Kranjc, Guideline for smart cathodic protection of steel in concrete, Assessment and Rehabilitation of Central European Highway Structures 2009.
- [19] NORSOK Standardisation Work Group, "Common Requirements for Cathodic Protection", 1994.
- [20] P. M. Chess and J. P. Broomfield, *Cathodic Protection of Steel in Concrete*, Taylor and Francis, 2003.
- [21] A. M. Neville, *Properties of concrete*, Prentice Hall, 2011.
- [22] W. J. McCarter, T. M. Chrisp, G. Starrs et al., "Developments in performance monitoring of concrete exposed to extreme environments," *Journal of Infrastructure Systems*, vol. 18, no. 3, pp. 167–175, 2012.
- [23] P. Keil, D. Lützenkirchen-Hecht, and R. Frahm, "Investigation of room temperature oxidation of Cu in air by Yoneda-XAFS," in *Proceedings of the X-Ray Absorption Fine Structure - XAFS13: 13th International Conference*, pp. 490–492, USA, July 2006.
- [24] Presearch Department. Carbon black magic turning electrically conductive plastics into products. P. Group, 2013.
- [25] Q. Meng, Y. Kenayeti, and D. D. L. Chung, "Battery in the form of a soil-matrix composite," *Journal of Energy Engineering*, vol. 141, no. 3, Article ID 04014013, 2015.
- [26] Z. Liu, Y. Zhang, and Q. Jiang, "Continuous tracking of the relationship between resistivity and pore structure of cement pastes," *Construction and Building Materials*, vol. 53, pp. 26–31, 2014.
- [27] J. C. Maso, *Interfaces in Cementitious Composites*, Taylor and Francis, 2004.
- [28] S. A. A. El-Enein, M. F. Kotkata, G. B. Hanna, M. Saad, and M. M. A. El Razeq, "Electrical conductivity of concrete containing silica fume," *Cement and Concrete Research*, vol. 25, no. 8, pp. 1615–1620, 1995.
- [29] D. D. L. Chung, "Electrical conduction behavior of cement-matrix composites," *Journal of Materials Engineering and Performance*, vol. 11, no. 2, pp. 194–204, 2002.
- [30] S. Wen and D. D. L. Chung, "Seebeck effect in carbon fiber-reinforced cement," *Cement and Concrete Research*, vol. 29, no. 12, pp. 1989–1993, 1999.
- [31] C. Shi, "Strength, pore structure and permeability of alkali-activated slag mortars," *Cement and Concrete Research*, vol. 26, no. 12, pp. 1789–1799, 1996.
- [32] W. E. Martinsen, "Selected properties of sodium silicate glasses and their structural significance. Digital Repository at Iowa State University, 1969".
- [33] D. Pantea, H. Darmstadt, S. Kaliaguine, and C. Roy, "Electrical conductivity of conductive carbon blacks: influence of surface chemistry and topology," *Applied Surface Science*, vol. 217, no. 1–4, pp. 181–193, 2003.
- [34] R. Alcántara, J. M. Jiménez-Mateos, P. Lavela, and J. L. Tirado, "Carbon black: A promising electrode material for sodium-ion batteries," *Electrochemistry Communications*, vol. 3, no. 11, pp. 639–642, 2001.
- [35] J. A. Shetzline and S. E. Creager, "Quantifying electronic and ionic conductivity contributions in carbon/polyelectrolyte composite thin films," *Journal of the Electrochemical Society*, vol. 161, no. 14, pp. H917–H923, 2014.
- [36] Y. S. Ye, H. Wang, S. G. Bi et al., "Enhanced ion transport in polymer-ionic liquid electrolytes containing ionic liquid-functionalized nanostructured carbon materials," *Carbon*, vol. 86, article no. 9640, pp. 86–97, 2015.
- [37] CM. Forman and EA. Verchot, "Practical galvanic series," *US Army Missile Command*, pp. 67-11, 1997.
- [38] A. Byrne, N. Holmes, and B. Norton, "Cement based batteries and their potential for use in low power operations," in *Proceedings of the 2nd International Conference on Innovative Materials, Structures and Technologies, IMST 2015*, Iva, October 2015.

Research Article

Effect of Calcined Hard Kaolin Dosage on the Strength Development of CPB of Fine Tailings with Sulphide

Juanrong Zheng,¹ Lijie Guo,^{2,3} and Zhenbo Zhao¹

¹College of Civil Engineering, Zhengzhou University, Zhengzhou, Henan 450002, China

²Beijing General Research Institute of Mining and Metallurgy, Beijing 102600, China

³University of Science and Technology Beijing, Beijing 100083, China

Correspondence should be addressed to Lijie Guo; guolijie@bgrimm.com

Received 18 March 2017; Accepted 4 June 2017; Published 17 August 2017

Academic Editor: Kedsarin Pimraksa

Copyright © 2017 Juanrong Zheng et al. This is an open access article distributed under the Creative Commons Attribution License, which permits unrestricted use, distribution, and reproduction in any medium, provided the original work is properly cited.

This study presents the effect of calcined hard kaolin (CHK) as replacement (15–50 wt.%) to Portland cement (PC) on the strength development of cemented paste backfill (CPB) of fine tailings containing sulphide. PC is used as binder at 20 wt.% dosage. The results show that CPB sample containing 30 wt.% CHK replacements produces the desired strength and durability (i.e., 26.1% increase in strength over the curing period between 28 d and 360 d). CPB without CHK does not produce the desired strength and durability (i.e., 32.8% losses in strength over the curing period between 90 d and 360 d). The quantity of expansive gypsum of CPB containing 30 wt.% CHK is obviously less than that of CPB without CHK. The porosity of the fine pore for pore diameter $< 0.3 \mu\text{m}$ is obviously higher in CPB containing 30 wt.% CHK than in CPB without CHK, regardless of curing time. It can be concluded that CHK can be suitably exploited for CPB of fine tailings with sulphide to improve the strength and stability in short and long terms.

1. Introduction

The tailings are usually separated to fine tailings (average particle size less than 0.037 mm) and coarse tailings by hydrocyclones in China. The fine parts are generally stored in a surface impoundment [1], whereas the coarse tailings mixed water and a hydraulic binder are transported by gravity into underground voids [2, 3]. The lead-zinc tailings are often rich in pyrite and contain toxic metals such as arsenic (As), cadmium (Cd), lead (Pb), zinc (Zn), and copper (Cu). The oxidation of pyrite in presence of water and oxygen generates acidity and facilitates the release of toxic metals contained in the tailings [4, 5]. The finer the granularity of tailings is, the lower the water permeability is, the harder the drainage consolidation is, and the easier the spill of the storage tailings dam is [6]. The spill of the storage tailings dam will lead to increasing the heavy metal content in the downstream soil, acidizing the soil, reducing organic matter content in the soil, and hardening the soil [7, 8]. In recent years, cemented paste backfill (CPB) of potentially hazardous mill tailings into underground and surface disposal practices has gained importance for the environmental management

of such wastes [9, 10]. Environmental problems associated with the storage of sulphide-rich wastes under atmospheric conditions (i.e., the formation of acid mine waters and the release of heavy and toxic metals with the concomitant risk of contamination of soils and underground/drinking waters) can be considerably reduced by the placement of such wastes safely in underground.

CPB is essentially an engineered mixture of wet fine mill tailings (75–85% solids by weight), a hydraulic binder (3–7% by dry total paste weight), and mixing water. However, some potentially long-term durability problems of CPB may be encountered when mill tailings with high sulphide (especially pyrite) content are used. Oxidation products (i.e., acid and sulphate) of sulphide minerals present in the tailings could lead to chemical reactions with hydration products and binder phases, such as calcium hydroxide (CH) and calcium aluminate (C_3A) and, concomitantly, to the formation of expansive phases such as ettringite and gypsum [11–15]. These could then culminate in the reduced backfill strength and potential collapse of the backfill. The incorporation of pozzolanic wastes such as granulated blast furnace slag (GBFS) and silica fume (SF) into the binder phase appeared

TABLE 1: Chemical properties of tailings, PC, and CHK used.

Composition	SiO ₂	Al ₂ O ₃	Fe ₂ O ₃	CaO	MgO	Pb	Na ₂ O	K ₂ O	S	Loss
Tailings	25.37	5.88	21.28	14.47	0.15	0.84	0.009	1.58	19.07	19.97
PC	25.26	6.38	4.05	54.67	2.68	—	—	—	0.06	—
CHK	43.13	45.17	1.25	1.75	0.10	—	—	—	—	7.70

TABLE 2: Physical properties of tailings, PC, and CHK used.

Physical properties	SSA (m ² /kg)	G _s (—)	>90 μm (%)	>45 μm (%)	D ₁₀ (μm)	D ₃₀ (μm)	D ₆₀ (μm)	C _u (—)	C _c (—)	<20 μm (%)
Tailings	633.8	3.0	1.07	7.28	1.50	4.55	14.68	9.8	0.94	73.67
PC	461.9	3.1	—	5.67	5.12	9.19	18.28	3.6	0.90	65.65
CHK	588.1	2.6	1.44	13.11	1.31	4.8	17.97	13.72	0.98	68.69

to mitigate the strength losses in the long term although the initial rate of development of strength of CPB samples tended to slow down with increasing the dosage of these pozzolanic wastes in the binder phase [13, 14]. Therefore, binder properties, that is, its sulphate resistance, are of practical importance for CPB of sulphide-rich tailings. Metakaolin (MK) replacement of cement was found to be effective in improving the resistance of concrete to sulphate attack [16]. “Lower Ca/Si ratios indicate the improvement of compressive strength [17].” The MK used in this study shows lower Ca/Si ratio. However, reports about the effect of calcined hard kaolin (CHK) with metakaolin on the short- and long-term strength and stability of CPB of fine tailings with sulphide (mainly pyrite) (19.07 wt.% S) are scarce.

Given the problems mentioned above, the main objectives of this study are as follows:

- (1) To investigate the effect of CHK replacement to PC on the properties of CPB mixtures.
- (2) To investigate the effect of CHK replacement to PC on unconfined compressive strength (UCS) development of CPB.
- (3) To investigate the mechanism of the short- and long-term strength and stability of CPB of fine tailings with sulphide.

2. Materials and Methods

2.1. Tailings and Binder. The fine tailings sample used in this study is obtained from an underground lead-zinc mine located in the south of China. The fine tailings are a highly hydrous tailings slurry with 63 wt.% solid concentration, which is produced by thickening the overflow tailings with 12 wt.% solid concentration derived from the top of vertical sand storehouse. Chemical compositions of the tailings are showed in Table 1. Particle size analysis of the tailings indicates that the tailings can be classified as a fine size tailings material since 73.67 wt.% of the sample is finer than 20 μm in size (Table 2). The tailings sample is determined to be medium-grade sulphide (19.07 wt.% S) (Table 1). A mineralogical analysis is performed on the tailings via X-ray diffraction (XRD). The main minerals in

the tailings are quartz, pyrite, calcium carbonate, dolomite, and muscovite, in which pyrite is the major sulphide mineral (Figure 1(a)).

The binder used in this study is Portland cement (PC). The PC consisted of silicate cement that satisfied the Chinese standards for “Universal Portland Cement” (GB 175-2007). The chemical compositions and physical properties of the PC are shown in Tables 1 and 2. The main materials in the PC are cement clinker (i.e., tricalcium silicate, dicalcium silicate, tricalcium aluminate, and tetracalcium aluminoferrite) and gypsum (Figure 1(b)).

2.2. Admixtures. One type of calcined hard kaolin (CHK) is used as mineral admixture in this study. Pozzolanic activity index can be reflected by the absorption ability of calcium hydroxide. The CHK used in this study is commercially available and with the absorption ability of 1050 mg Ca(OH)₂/g CHK. The CHK is obtained by calcining coal-measure hard kaolinite and grinding. China is rich in coal hard kaolinite reserves, which belong to sedimentary kaolinite and occur in the coal seam roof and floor and mezzanine. The chemical and physical properties of the CHK are shown in Tables 1 and 2. The main crystal minerals in the CHK are kaolinite and quartz, while the amorphous form mineral (i.e., metakaolin, MK) in the CHK is also obvious (Figure 1(c)).

2.3. Mixing Water. Tap water is used in this study. The effect of the sulphate ions in tap water can be neglected.

2.4. Slump and Wet Density Tests. The workability of CPB mixtures is measured by the slump of CPB mixtures. The high slump and low bleeding rate value of CPB mixtures indicate that the CPB mixture has good workability. The bleeding rate value of all CPB mixtures in this study is all ≤2 wt.%.

The slumps of the samples are tested according to the Chinese standard (GB/T 50080-2002). The desired slump value in this study is 180 mm.

2.5. Preparation and Testing of CPB Samples. The UCS criteria to be achieved in this study are to produce the desired 28-day strength of ≥2.0 MPa and the maintenance of the stability (i.e., ≥2.0 MPa UCS at curing 360 d) according to requirement of mining technology.

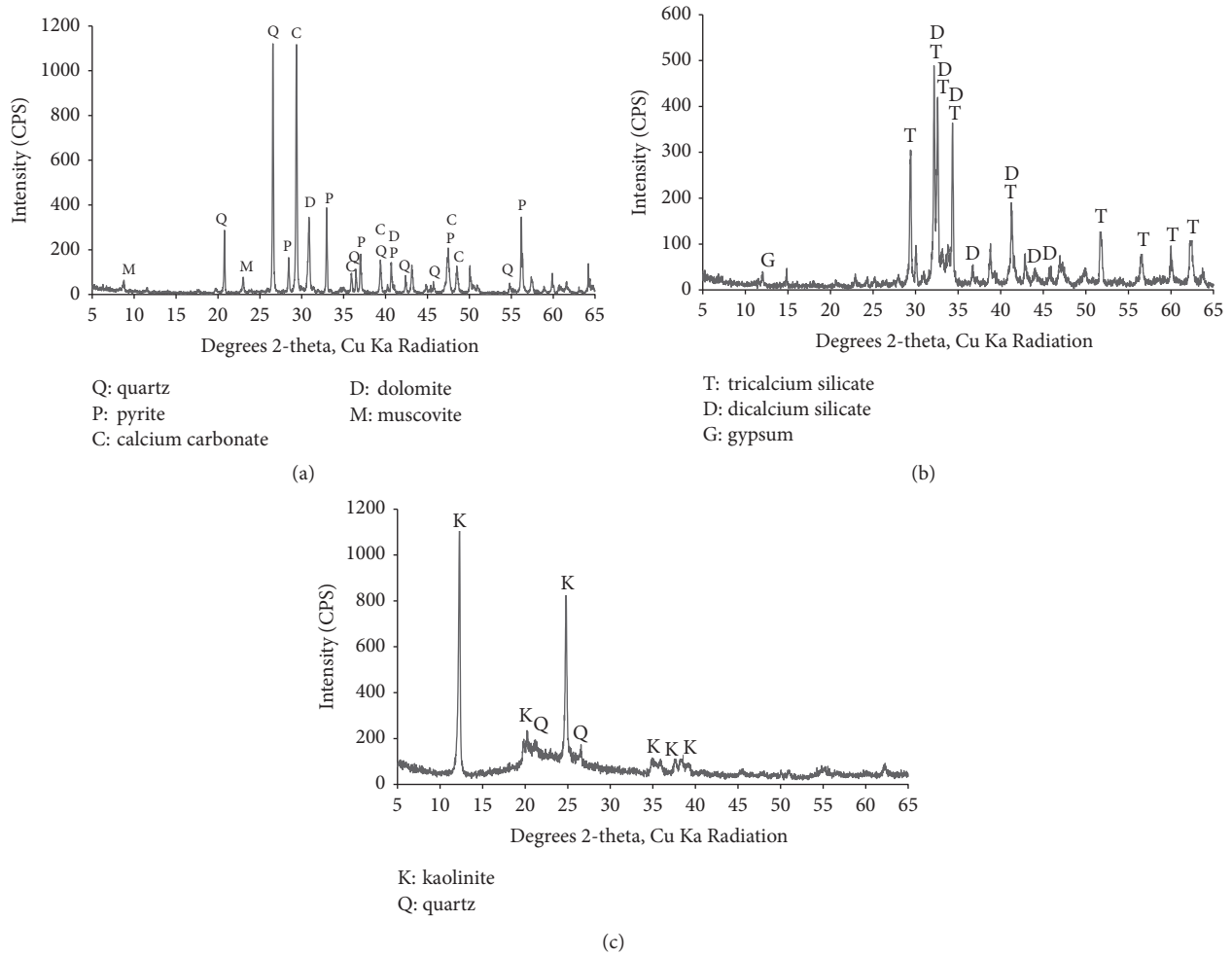


FIGURE 1: XRD profiles of tailings (a), PC (b), and CHK (c).

TABLE 3: Mix proportions and partial properties of CPB mixture.

Number	Mix proportions					Partial properties of CPB mixture			
	Tailings slurry ⁽¹⁾ /g	water /g	PC /g	CHK /g	RL ⁽²⁾ /%	Solids content /wt.%	Water to cement ratio/%	Wet density /(kg/m ³)	Slump /mm
1	1000	92.5	157.5	0	0	63	58.7	1785	185
2	1000	92.5	133.9	23.6	15	63	69.1	1785	180
3	1000	92.5	110.25	47.25	30	63	83.9	1795	180
4	1000	92.5	78.75	78.75	50	63	78.8	1815	175

⁽¹⁾Tailings slurry has 63 wt.% solid concentration; ⁽²⁾RL is CHK replacement to PC. Binder (including PC and CHK) dosage is kept constant at 20 wt.% of total solids.

Binder (including PC and CHK) dosage in this study is kept constant at 20 wt.% of total solids. The required amounts (see Table 3) of CPB ingredients (tailings slurry, PC, CHK, and mix water) are thoroughly mixed in a double spiral mortar mixer for about 5 min to ensure paste homogeneity. Immediately after mixing, samples are poured into 70.7 mm × 70.7 mm × 70.7 mm iron molds. Excess water (i.e., drain away water) in the samples could separate out from the

seam between the broadsides and the baseboard of the iron molds. Then, the open-top samples are placed in a humidity chamber set at 20 ± 1 °C and 90% RH for curing. In total, 84 samples were made and cured for 7, 28, 56, 90, 150, 210, 270, and 360 days. Then the CPB samples are tested for unconfined compressive strength (UCS) according to the Chinese standard (JGJ/T 70-2009), in which the loading rate is 0.25~1.5 KN/s. Prior to a UCS test, the sizes of a sample are

rectified to get valid press surfaces. UCS tests are performed using a computer-controlled mechanical press, which had a load capacity of 100 KN.

2.6. XRD and MIP Studies. After compression testing, representative samples are taken from locations as far as possible from the shear plane to avoid stress concentration effects. The representative samples are treated with acetone and then dried in an oven maintained at 60°C to halt further hydration prior to X-ray diffraction (XRD) and mercury intrusion porosimeter (MIP) studies.

The XRD analysis is performed using a D/max-2500PC X-ray diffractometer from Japan with a copper target with a 2θ range of 4°–60° and a scanning speed of 2°/min to examine the mineralogical compositions of CPB samples after the curing process.

The MIP used in this study is an AutoPore IV 9500 V1.05. Applying pressures ranged from 0 to 414 MPa (60,000 psi), allowing throat pore diameter measurements down to 0.003 μm . MIP is analyzed according to the ISO 15901-1: 2005 standard. In this study, mercury surface tension σ and mercury contact angle θ are taken as 485 dynes/cm and 130°C, respectively.

3. Results and Discussion

3.1. Effect of CHK on the Workability of CPB Mixtures. The influence of CHK replacement level to PC on the workability of CPB mixtures is illustrated in Table 3. Table 3 shows that the slump of CPB mixture tends to decrease with increasing CHK replacement level to PC at the same solids content. However, the wet density of CPB mixture tends to increase with increasing CHK replacement level to PC at the same solids content. Fineness and surface characteristic of CHK can be main influence factors.

3.2. Effect of CHK on the Strength Development of CPB Mixtures. The effect of CHK replacement level to PC on the strength development of CPB samples over a curing period of 360 days is illustrated in Figure 2. Mix proportions and partial properties of CPB mixtures in Figure 2 are shown in Table 3.

Figure 2 shows that the UCS of the control sample (i.e., no CHK in binder) and the samples of 15 wt.% CHK and 50 wt.% CHK in binder tend to increase over a curing period of 90 d, 28 d, and 28 d, respectively; thereafter, the UCSs tend to decrease. The control sample has 32.8% losses in strength over the curing period between 90 days and 360 days. The samples of 15 wt.% CHK and 50 wt.% CHK in binder have 38.6% and 57.2% losses in strength over the curing period between 28 days and 360 days, respectively. The 28 d UCS of CPB sample containing 30 wt.% CHK in binder achieves the desired 28-day strength of ≥ 2.0 MPa. In addition, the CPB samples containing 30 wt.% CHK in binder are observed to develop consistently over a curing period of 360 days and have 26.1% increase in strength over the curing period between 28 days and 360 days. These findings suggest that 20 wt.% binder in total solids and 30 wt.% CHK in binder are extremely effective for increasing the strength and stability

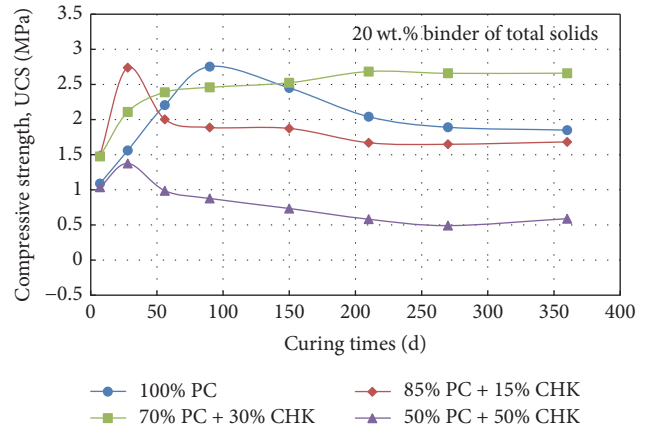


FIGURE 2: The influence of CHK replacement level on the strength development of CPB samples.

in short and long terms of CPB of fine tailings with sulphide (19.07 wt.% S).

When the fine tailings with pyrite (FeS_2) mix with binder and water, a series of complex chemical reactions happen. First of all, the hydration reaction between PC and water produces hydrated calcium silicate gel (C–S–H), portlandite ($\text{Ca}(\text{OH})_2$), and so forth. Secondly, the sulphide phases such as pyrite present in CPB could undergo oxidation under the curing conditions in the presence of air and moisture. The oxidation of pyrite yields acid and sulphate (1). The former can attack and destruct C–S–H bonds while the latter can react with portlandite ($\text{Ca}(\text{OH})_2$) and tricalcium aluminate (C_3A) to form secondary gypsum (2) and ettringite (3) with these leading to the expansion and development of microcracks in cured CPB. The formation of secondary gypsum and ettringite with expansive properties was claimed to be responsible for the reduction of strength of CPB samples after 56 and 90 days. However, the formation of secondary ettringite is not observed by XRD analyses in the CPB samples in this study (see Figures 3(a) and 3(b)).

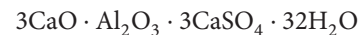
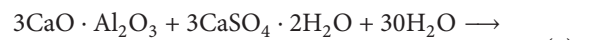
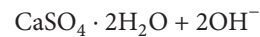
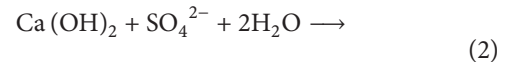
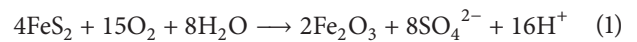


Figure 3 shows that the quantity of expansive gypsum of CPB with 100% PC (a) is obviously higher than that of CPB with 70% PC + 30% CHK (b) at 360 days. The results can be explained by the following mechanisms. First, the replacement of a portion of PC with CHK reduces the total amount of PC clinker in binder of CPB samples. The second mechanism is through the pozzolanic reaction between the MK in CHK and calcium hydroxide released during the hydration of PC, which consumes part of the calcium hydroxides leading to decreasing the quantity of expansive gypsum [15].

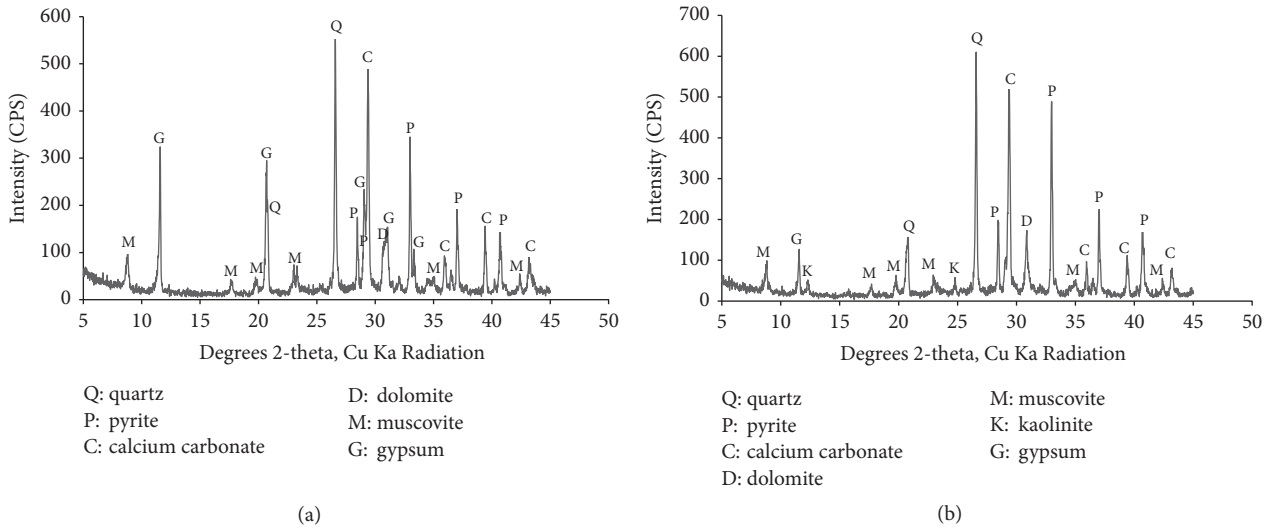


FIGURE 3: XRD profile of CPB with 100% PC (a) and 70% PC + 30% CHK (b) at 360 days.

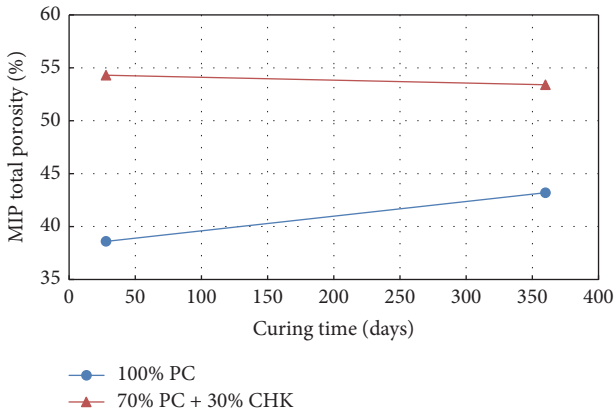


FIGURE 4: Relationships between MIP total porosity and curing time of CPB samples.

It is well known that pore structure can cause significant effects on the strength of CPB. Figure 4 shows that relationships between MIP total porosity and curing time of CPB samples. For CPB samples with the same mixing proportion, the lower the MIP total porosity, the greater the UCS. For CPB samples with different mixing proportion, UCS is not strictly correlated with the MIP total porosity.

Figure 5 shows the changes in incremental pore size distribution (PSD) curves for 28 and 360 cured CPB samples. According to the definition of the capillary pore, pores $\geq 0.3 \mu\text{m}$ correspond to the main interconnected capillary porosity network. The porosity of the fine pore for pore diameter $< 0.3 \mu\text{m}$ is obviously higher in CPB sample with CHK than in CPB without CHK, regardless of curing time. The reason of gaining the result is that the formation of secondary hydrated calcium silicate gel (C-S-H) by the pozzolanic reaction is effective in filling and segmenting large capillary pores into small, discontinuous capillary pores through pore size refinement, which increases the UCS of

CPB samples. An additional potential reason of more finer pores in CHK is the filler effect role of the admixture.

Figure 6 shows visual appearance of CPB samples. In visual appearance of CPB samples, the surface cracks of CPB sample with 100% PC at 360 days can be clearly identified while no surface cracks can be detected in CPB sample with 70% PC + 30% CHK at 360 days.

Figure 7 shows schematic diagram of bonding strength and expansion stress development in CPB samples. The bonding strength of CPB sample increases with increasing curing times due to the increase of hydration products and the porosity of the fine pore for pore diameter $< 0.3 \mu\text{m}$. The expansion stress of CPB sample increases with increasing the quantity of secondary gypsum and ettringite within CPB sample. When the expansion stress (ES1 in Figure 7) produced by forming secondary gypsum and ettringite in CPB sample exceeds the bonding strength (BS in Figure 7) of CPB sample, the sample cracks and MIP total porosity increase, which lead to the decrease of the UCS of the samples such as number 1, number 2, and number 4 in Table 3. However, the secondary gypsum in certain quantity could also fill the voids within CPB. The expansion stress (ES2 in Figure 7) is always less than the bonding strength (BS in Figure 7) within CPB. This in turn leads to a decreased porosity and higher short- and long-term strength of CPB sample such as number 3 in Table 3. This is a conclusion in this study that CPB sample containing 30% CHK replacement level to PC shows excellent short- and long-term mechanical performances.

4. Conclusions

This study presents the results for effect of calcined hard kaolin with metakaolin on the short- and long-term strength and stability of CPB of fine tailings with sulphide. Based on the results obtained from this study, the following conclusions may be warranted:

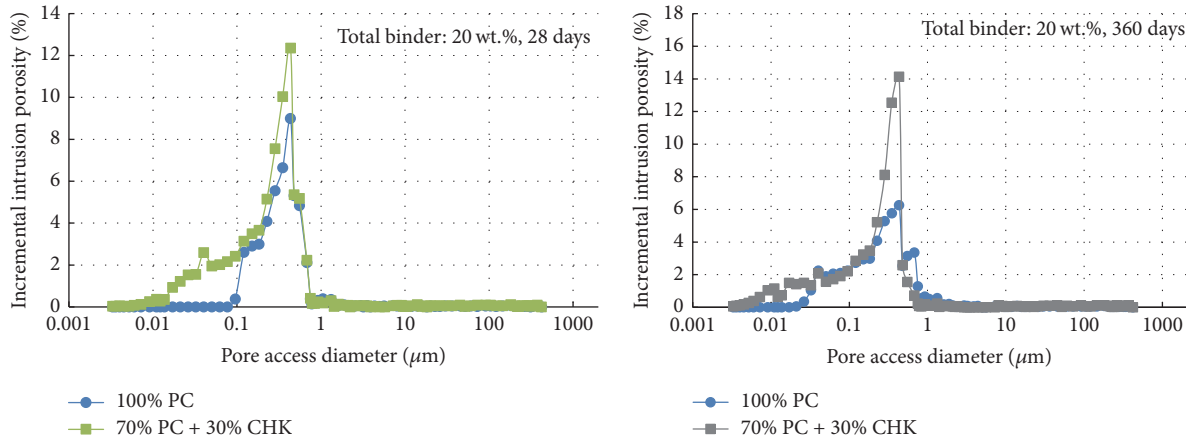


FIGURE 5: Relationships between incremental Hg intrusion porosity and pore access diameter.

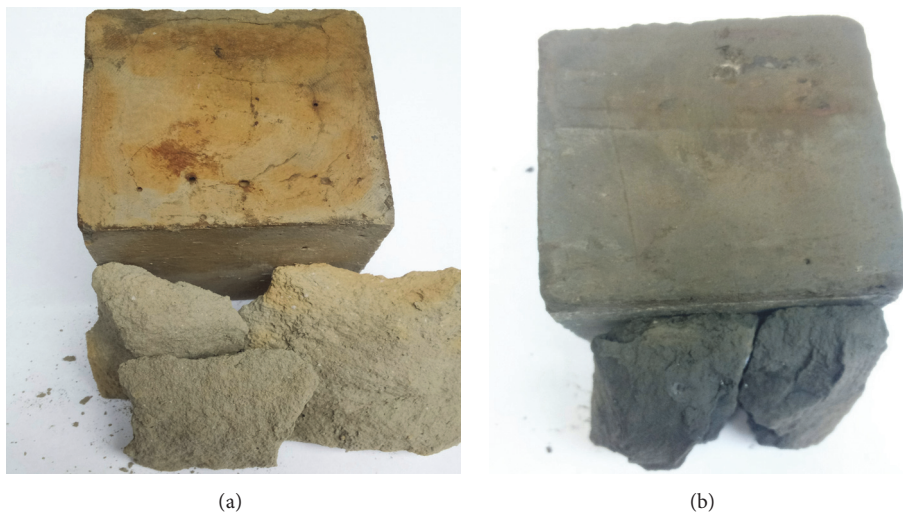


FIGURE 6: Visual appearance of CPB with 100% PC (a) and 70% PC + 30% CHK (b) at 360 days.

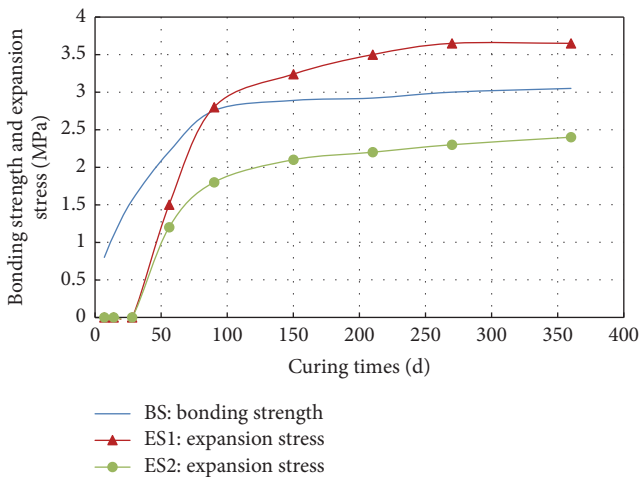


FIGURE 7: Schematic diagram of bonding strength and expansion stress development in CPB samples.

- (1) CPB containing 30 wt.% CHK replacement to PC achieves the desired strength value (i.e., ≥ 2.0 MPa UCS at curing 360 d).
- (2) CPB without CHK has 32.8% losses in strength over the curing period between 90 days and 360 days. CPB containing 30 wt.% CHK replacement level to PC has 26.1% increase in strength over the curing period between 28 days and 360 days.
- (3) The quantity of expansive gypsum of CPB containing 30 wt.% CHK replacement to PC is obviously less than that of CPB without CHK. The porosity of the fine pore for pore diameter $< 0.3 \mu\text{m}$ is obviously higher in CPB containing 30 wt.% CHK replacement to PC than in CPB without CHK, regardless of curing time.
- (4) When the expansion stress produced by forming secondary gypsum and ettringite in CPB samples exceeds the bonding strength of CPB samples, the

sample cracks and MIP total porosity increase, which lead to the decrease of the UCS of the sample, and vice versa.

Conflicts of Interest

The authors declare that they have no conflicts of interest.

Acknowledgments

This study is funded by the National Natural Science Foundation of China (Project no. 51274174) and National Key Research and Development Program (Project no. 2016YFC0600709). The authors would like to thank Professor Dongwu Chang of Zhengzhou University for his assistance with the MIP analysis.

References

- [1] Z. Wei, G. Yin, G. Li, J. G. Wang, L. Wan, and L. Shen, "Reinforced terraced fields method for fine tailings disposal," *Minerals Engineering*, vol. 22, no. 12, pp. 1053–1059, 2009.
- [2] R. Zhou, "Application of cemented filling with classified tailings in Wushan copper mine," *Non-Ferrous Metal (Part of Mine)*, vol. 63, no. 3, pp. 1–5, 2010 (Chinese).
- [3] D. Chen and W. D. Song, "Experimental study on performance of cemented filling with classified tailings in Laixi gold mine," *Non-Ferrous Metal (Part of Mine)*, vol. 67, no. 4, pp. 54–57, 2015 (Chinese).
- [4] M. Pokharel and M. Fall, "Combined influence of sulphate and temperature on the saturated hydraulic conductivity of hardened cemented paste backfill," *Cement and Concrete Composites*, vol. 38, pp. 21–28, 2013.
- [5] M. Benzaazoua, J. Quellet, S. Servant, P. Newman, and R. Verburg, "Cementitious backfill with high sulfur content: physical, chemical and mineralogical characterization," *Cement and Concrete Research*, vol. 29, no. 5, pp. 719–725, 1999.
- [6] Z. D. Liu, Q. Li, and Z. H. Fu, "Investigation on the resources development and utilization of the storage tailings of Fankou lead-zinc mine," *Mining Technology*, vol. 18, no. 5, pp. 101–103, 2008 (Chinese).
- [7] J. Aguilar, C. Dorronsoro, E. Fernández et al., "Soil pollution by a pyrite mine spill in Spain: evolution in time," *Environmental Pollution*, vol. 132, no. 3, pp. 395–401, 2004.
- [8] L. M. Zhai, T. B. Chen, X. Y. Liao, X. L. Yan, L. X. Wang, and H. Xie, "Pollution of agricultural soils resulting from a tailing spill at a pb-zn mine: a case study in huanjiang, guangxi province," *Acta Scientiae Circumstantia*, vol. 28, no. 6, pp. 1206–1211, 2008.
- [9] A. Tariq and E. K. Yanful, "A review of binders used in cemented paste tailings for underground and surface disposal practices," *Journal of Environmental Management*, vol. 131, pp. 138–149, 2013.
- [10] M. Benzaazoua, B. Bussière, I. Demers, M. Aubertin, É. Fried, and A. Blier, "Integrated mine tailings management by combining environmental desulphurization and cemented paste backfill: Application to mine Doyon, Quebec, Canada," *Minerals Engineering*, vol. 21, no. 4, pp. 330–340, 2008.
- [11] A. Kesimal, E. Yilmaz, B. Ercikdi, I. Alp, and H. Deveci, "Effect of properties of tailings and binder on the short-and long-term strength and stability of cemented paste backfill," *Materials Letters*, vol. 59, no. 28, pp. 3703–3709, 2005.
- [12] B. Ercikdi, A. Kesimal, F. Cihangir, H. Deveci, and İ. Alp, "Cemented paste backfill of sulphide-rich tailings: importance of binder type and dosage," *Cement and Concrete Composites*, vol. 31, no. 4, pp. 268–274, 2009.
- [13] B. Ercikdi, F. Cihangir, A. Kesimal, H. Deveci, and I. Alp, "Utilization of industrial waste products as pozzolanic material in cemented paste backfill of high sulphide mill tailings," *Journal of Hazardous Materials*, vol. 168, no. 2-3, pp. 848–856, 2009.
- [14] M. Fall and M. Pokharel, "Coupled effects of sulphate and temperature on the strength development of cemented tailings backfills: portland cement-paste backfill," *Cement and Concrete Composites*, vol. 32, no. 10, pp. 819–828, 2010.
- [15] S. Ouellet, B. Bussière, M. Aubertin, and M. Benzaazoua, "Microstructural evolution of cemented paste backfill: mercury intrusion porosimetry test results," *Cement and Concrete Research*, vol. 37, no. 12, pp. 1654–1665, 2007.
- [16] N. M. Al-Akhras, "Durability of metakaolin concrete to sulfate attack," *Cement and Concrete Research*, vol. 36, no. 9, pp. 1727–1734, 2006.
- [17] S. Dadsetan and J. Bai, "Mechanical and microstructural properties of self-compacting concrete blended with metakaolin, ground granulated blast-furnace slag and fly ash," *Construction and Building Materials*, vol. 146, pp. 658–667, 2017.

Research Article

Strengths and Failure Characteristics of Self-Compacting Concrete Containing Recycled Waste Glass Aggregate

Rahman Khaleel AL-Bawi,^{1,2} Ihsan Taha Kadhim,^{1,3} and Osamah AL-Kerttani^{1,4}

¹Department of Civil Engineering, Gaziantep University, 27310 Gaziantep, Turkey

²Civil Engineering Department, Diyala University, Diyala, Iraq

³Building and Construction Department, University of Technology, Baghdad, Iraq

⁴Civil Engineering Department, Al-Mustansiriyah University, Baghdad, Iraq

Correspondence should be addressed to Ihsan Taha Kadhim; ihsantahak@yahoo.com

Received 18 May 2017; Revised 8 July 2017; Accepted 18 July 2017; Published 17 August 2017

Academic Editor: Tung-Chai Ling

Copyright © 2017 Rahman Khaleel AL-Bawi et al. This is an open access article distributed under the Creative Commons Attribution License, which permits unrestricted use, distribution, and reproduction in any medium, provided the original work is properly cited.

The effects of different proportions of green-colored waste glass (WG) cullet on the mechanical and fracture properties of self-compacting concrete (SCC) were experimentally investigated. Waste bottles were collected, washed, crushed, and sieved to prepare the cullet used in this study. Cullet was incorporated at different percentages (0%, 20%, 40%, 60%, 80%, and 100% by weight) instead of natural fine aggregate (NFA) and/or natural coarse aggregate (NCA). Three SCC series were designed with a constant slump flow of 700 ± 30 mm, total binder content of 570 kg/m^3 and at water-to-binder (w/b) ratio of 0.35. Moreover, fly ash (FA) was used in concrete mixtures at 20% of total binder content. Mechanical aspects such as compressive, splitting tensile, and net flexural strengths and modulus of elasticity of SCC were investigated and experimentally computed at 28 days of age. Moreover, failure characteristics of the concretes were also monitored via three-point bending test on the notched beams. The findings revealed that the mechanical properties as well as fracture parameters were adversely influenced by incorporating of WG cullet. However, highest reduction of compressive strength did not exceed 43% recorded at 100% WG replacement level. Concretes containing WG showed less brittle behavior than reference concrete at any content.

1. Introduction

Turkey as one of the economically promising and developing countries has well operated waste management applications with over 2,000 scattered open dump areas. At the end of 2014, the manufacturers were responsible for collecting and recycling at least 60% of solid waste [1]. However, every year the amount of waste and its consequent disposal problems increased due to the increase in the standards of living, industrialization, and thus population. Moreover, among 25 million tonnes, about 17.5 million tonnes was disposed without any control [2]. Hence, waste recycling is deemed as the most suitable solution because it decreases the pollution of the nature and also helps to reuse energy production procedure. Glass waste is undesirable to disposal because it is non-biodegradable which makes it environmentally less friendly; besides that the landfill capacity is being exhausted [3].

Thus, discarded waste glass (WG) has become a substantial burden on the landfills throughout the world. The challenge of disposal of waste glass continues to increase whenever the amount of waste glass increases and decreasing the capacity of landfill space [4]. In general, not all the waste glasses are suitable to be remelted and used to make new products because of the color mixed glass and contamination by papers and other substances [5]. Therefore, it is essential to find a sustainable alternative to reuse and recycle this material. Glass is a unique inert and ideal material which could be reused too many times without any change in its chemical properties [6]. Concrete construction provides a significant market potential for waste glass recycling via decreasing the cost of concrete [3]. In the past decade, the increase of disposal costs and legislating environmental regulations encouraged several researchers to investigate again the use of glass as concrete aggregates. Hence, Kou and Poon [5] prepared SCC

with recycled glass aggregate. The authors investigated the fresh and mechanical properties and found that it was feasible to produce SCC with WG cullet until 30% replacement level. Afshoon and Sharifi [7] also concluded that WG cullet could be successfully used for producing SCC. In similar way, Sharifi et al., 2013 [8], claimed that WG cullet as fine aggregate can be used to produce SCC in a standard manner. The author's results showed that there was no remarkable reduction in the strengths at 30% replacement ratios of WG and less. Likewise, Meyer et al. [9] emphasized that it was practically feasible to produce SCC by using full replacement level of WG cullet as aggregates beside a suitable amount of fly ash (FA) and superplasticizer (SP). Asokan et al. [10] added 5–50% glass fiber reinforced plastic waste to concrete and tested the compressive strength. The results indicated that the compressive strength varied from 19 to 37 MPa for concrete containing 50 to 5%, respectively. Furthermore, Özkan and Yüksel [11] utilized different percentages of WG to investigate the mechanical and durability properties of cement-based mortars. The results revealed that the decrease in strength at 30% replacement level was tolerable and the durability properties were also valid.

As for mechanical and strength aspects, WG cullet concrete was expected to be inferior to conventional concrete. Indeed, these parameters were essentially controlled by the interlocking bond between cement and aggregate as well as the strength of interfacial transition zone (ITZ). Hence, replacing the rough surface of NA by a smooth one for crushed glass particles necessarily led to drop in strength; also, further reduction of an already low ductility is expected for this concrete [9]. In this regard, several previous literatures [3, 5, 7, 12] emphasized that the compressive strength as well as other mechanical properties were adversely effected by the addition of WG cullet. Conversely, Sangha et al. [13] reported that WG concrete showed higher compressive strength value as compared with conventional concrete. The authors noticed an increase in the value of compressive strength at 10%, 40%, and 60% of green glass replacement levels.

The main problem in glass concrete is related to alkali-silica reaction (ASR), which was the major concern that thwarted the use of WG cullet in construction sectors [4, 14–16]. The chemical reaction occurring between abundant silica in glass particles and the alkali in pore solution of concrete was not well understood decades ago [9]. Although it is believed that ASR process causes volume expansion which leads to cracks, however, this reaction is not restricted for glass aggregates only. Indeed, natural aggregate (NA) such as strained quartz and opaline chert contains certain amount of silica which can cause the same problem. Furthermore, reliable test methods are needed to predict the potential reactivity of NA because this reaction takes years to manifest itself. Hence, glass is deemed as an ideal aggregate to investigate ASR phenomenon in order to mitigate its detrimental results [17]. In this regard, studies are carried out to suppress the ASR expansion in concrete and to find methods for minimizing its effects. Lam et al. [18] and others [3, 6, 14] reported that the incorporating of suitable pozzolanic materials such as FA, ground blast furnace slag (GBFS), or metakaolin

(MK) in concrete mixtures can prevent and suppress this chemical action. Furthermore, Shi, 2009 [16] indicated that the expansion of concrete caused by traditional alkali-silica reaction was different from that of concrete containing glass aggregates. The author emphasized that WG concrete expanded when the moisture was present and when pH of the pore solution was greater than 12.

In spite the fact that several previous literatures investigated the effect of WG cullet (as fine and/or coarse grade) on the properties of concrete, but the fracture parameters of WG concrete have not been examined yet. Moreover, most of conducted studies not only avoid using extreme replacement levels of WG cullet but also tested only one grade of WG aggregate (fine or coarse) [5, 7, 8, 19]. In the present study, fracture properties of SCC as well as strength properties were inquired for multiple replacement levels of WG aggregate (as fine and/or coarse grade). Aside from control mix (CTR), three SCC series were designed with WG replacement levels of 0%, 20%, 40%, 60%, 80%, and 100% by weight of NA. Constant w/b ratio of 0.35 and total binder content of 570 kg/m³ were applied to produce 16 SCC mixtures. Moreover, FA was utilized in these concretes at 20% of total binder content to suppress the ASR reaction. In this study, the strength characteristics of concrete were conducted in the term of compressive, splitting tensile, net flexural strengths, and static modulus of elasticity. Moreover, fracture parameters tested in this study were fracture energy (G_F) and characteristic length (l_{ch}). All aforementioned tests had been performed at 28 days and the results were evaluated and compared statistically.

2. Experimental Program

2.1. Materials. In this study, Portland cement used in all SCC mixtures was ordinary cement named CEM I 42.5 R and identical to the Turkish specifications TS EN 197 [20] which are fundamentally derived from the European EN 197-1. Moreover, FA was utilized in concrete as replacement material by weight of cement at 20% level. The chemical and physical characteristics of cement, FA, and glass are listed in Table 1. The physical properties of WG cullet and NA were determined according to ASTM C127 [21]. In this regard, with specific gravity of 1.07, SP was employed to obtain the desired workability.

WG cullet was used at different replacement levels by weight of NA. In this regard, fine grade waste glass aggregate (WGFA) had a particle size of 0–4 mm and specific gravity of 2.53, while coarse waste glass aggregate (WGCA) was utilized with a particle size of 4–11.2 mm and specific gravity of 2.55 (Figure 1). In effect, 24-hour absorption capacity of WG was too little and it could be neglected. Moreover, river sand type natural coarse aggregate (NCA) and natural fine aggregate (NFA) conforming to the TS 706 EN 12620-A1 [22] were used. The maximum sizes of NCA and NFA were 16 and 4 mm while 24-hour absorption capacities were 0.77% and 1.09% respectively. Moreover, the physical observation of WG had exhibited smooth surfaces, angular shape, and sharp edge. The physical characteristics and sieve analysis of the aggregates used in this study are demonstrated in Table 2.

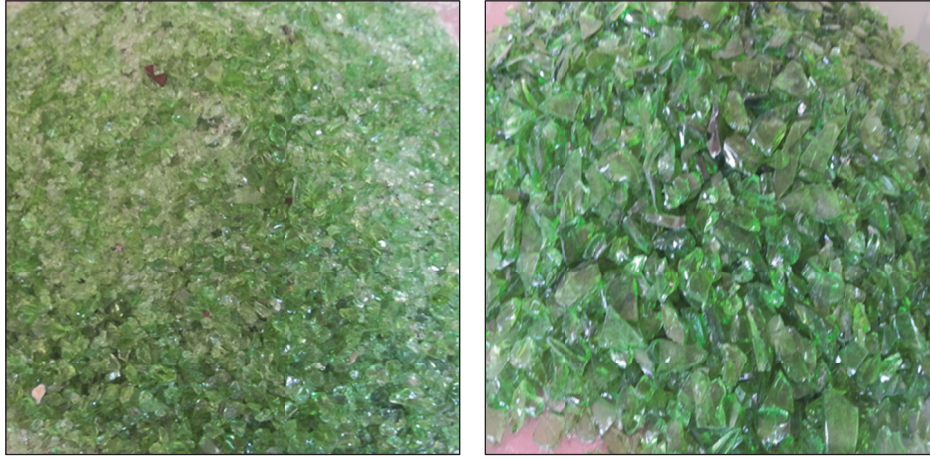


FIGURE 1: Fine and coarse grade of WG cullet.

TABLE 1: Properties of cement and fly ash.

Chemical analysis (%)	Cement	Fly ash	Green glass
CaO+ MgO	67.06	4.64	15.60
SiO ₂	19.79	57.2	71.91
Al ₂ O ₃	3.85	24.4	—
Fe ₂ O ₃	4.15	7.1	0.01
Cr ₂ O ₃	—	—	0.30
SO ₃	2.75	0.29	0.22
K ₂ O	—	3.37	0.53
Na ₂ O	—	0.38	9.58
TiO ₂	—	—	0.06
SrO	—	—	0.01
P ₂ O ₅	—	—	0.06
Other oxides	2.40	2.62	1.72
Loss on ignition	0.87	1.52	—
Specific gravity	3.15	2.04	2.55
Specific surface area (m ² /kg)	326	379	—

TABLE 2: Physical properties of natural and glass aggregates.

Sieve size (mm)	Natural aggregate		Glass aggregate	
	NFA	NCA	WGFA	WGCA
16	100	100	100	100
8	100	30.40	100	24.10
4	100	0	100	0
2	58.13	0	51.57	0
1	37.20	0	30.89	0
0.5	24.24	0	10.63	0
0.25	8.70	0	3.43	0
0.125	0	0	0	0
Fineness modulus	3.72	6.70	4.03	6.76
Specific gravity	2.39	2.69	2.53	2.55

2.2. Mixture Proportioning and Sample Preparation. In addition to control mix (CTR) where NA were used as fine and

coarse grade; 16 other concrete mixtures were designed and produced in a pan-type mixer with a 30 L capacity according to ASTM C192 [23]. SCC mixtures were subdivided into three series. In these mixtures, NA were replaced with WG cullet at replacement levels of 0%, 20%, 40%, 60, 80, and 100% by total volume of aggregate. In series I, NFA were replaced by fine grade WG cullet, while the mixtures in series II were made by replacing NCA with WGCA. Similarly in series III, concretes were incorporated with WG cullet for both coarse and fine grade. Thus, each series consisted of 5 mixtures according to replacement levels mentioned above. All concretes were prepared with a 570 kg/m³ binder content and w/b ratio of 0.35. In this regard and to suppress the potential alkali-silica reaction, FA was used in these concretes at 20% of total binder content. Moreover, to achieve the desired workability, different percentage of SP was utilized. As shown in Table 3, the concrete mixture codes were named basing on the mixture composition. For example, FWG0CWG0 indicated that SCC contained 0% WGFA and 0% WGCA.

Concrete casting sequence started with mixing aggregate and/or WG cullet with the binder for one minute until it homogenized. Then, water containing SP was added in two parts to avoid segregation and the concretes were mixed for 3 minutes. Later, concrete was left for 2 minutes to rest and it was mixed again for an additional 2 minutes to complete the mixing sequence. For all concretes produced in this study, slump flow with diameter of 700 ± 30 mm was assigned to meet the limitation of EFNARC [24]. For this, trial batches were conducted for each mixture until the target slump flow diameter was obtained.

2.3. Test Procedure

2.3.1. Strength and Modulus of Elasticity. In the current study, the compressive strength test was conducted according to the limitation of BS 1881-116 [25]. The results were computed by average of three cube specimens (150 × 150 × 150 mm) for each mix at 28 days. Similar to compressive test, splitting tensile strength also considered the average of three cylinder specimens (100 × 200) according to ASTM C496 [26], while

TABLE 3: Concrete mix proportions.

Mix series	Mix code	Volume fraction%				Fine aggregate Kg/m ³		Coarse aggregates		Fine aggregate Kg/m ³		Coarse aggregate Kg/m ³		SP Kg/m ³
		NFA*	WGFA*	NCA*	WGCA*	NFA	WGFA	NCA*	WGCA*	NFA	WGFA	NCA	WGCA	
CTR	FWG0CWG0	100	0	100	0	762.4	0	762.4	0	762.4	0	762.4	0	4.45
	FWG20CWG0	80	20	100	0	609.9	161.4	762.4	0	609.9	161.4	762.4	0	4.39
	FWG40CWG0	60	40	100	0	457.4	322.8	762.4	0	457.4	322.8	762.4	0	4.28
	FWG60CWG0	40	60	100	0	305	484.2	762.4	0	305	484.2	762.4	0	3.90
	FWG80CWG0	20	80	100	0	152.5	645.6	762.4	0	152.5	645.6	762.4	0	3.82
	FWG100CWG0	0	100	100	0	0	807	762.4	0	0	807	762.4	0	3.76
Series I	FWG0CWG20	100	0	80	20	762.4	0	20	762.4	609.9	144.5	609.9	144.5	4.39
	FWG0CWG40	100	0	60	40	762.4	0	40	762.4	457.4	289.1	457.4	289.1	4.33
	FWG0CWG60	100	0	40	60	762.4	0	60	762.4	305	433.6	305	433.6	4.33
	FWG0CWG80	100	0	20	80	762.4	0	80	762.4	152.5	578.2	152.5	578.2	4.29
	FWG0CWG100	100	0	0	100	762.4	0	100	762.4	0	722.7	0	722.7	4.28
Series II	FWG20CWG20	80	20	80	20	609.9	161.4	20	609.9	609.9	144.5	609.9	144.5	4.28
	FWG40CWG40	60	40	60	40	457.4	322.8	40	457.4	457.4	289.1	457.4	289.1	4.10
	FWG60CWG60	40	60	40	60	305	484.2	60	305	305	433.6	305	433.6	3.93
	FWG80CWG80	20	80	20	80	152.5	645.6	80	152.5	152.5	578.2	152.5	578.2	3.88
	FWG100CWG100	100	0	100	0	807	0	0	807	807	0	722.7	0	3.76

NCA* : natural coarse aggregates; NFA* : natural fine aggregates; WGCA* : waste glass coarse aggregates; WGFA* : waste glass fine aggregates.

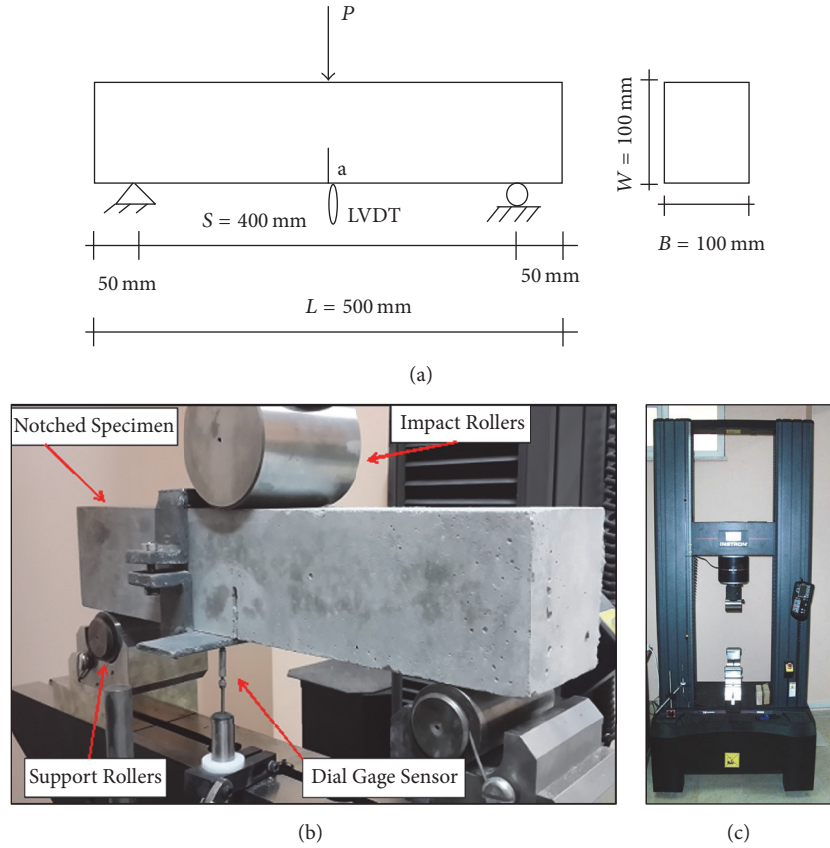


FIGURE 2: (a) Geometry of the three-point bending specimens used, (b) three-point testing schematic for flexural strength and fracture tests, and (c) test setup and specimen.

static modulus of elasticity was carried out with respect to BSI 1881-121 [27]. In this test, $(150 \times 150 \times 150)$ mm cube specimens were employed to evaluate the elasticity of concrete. The specimen was subjected three times to 40% of maximum load, which was already specified through the results of compressive strength test. The values of modulus were measured by the average of the second two sets of readings whereas the first set was ignored for each cube. However, the average of at least three specimens was considered for each of abovementioned tests.

2.3.2. Fracture Parameters. According to RILEM 50-FMC [28], the work required to create one unit area of a crack is expressed as the fracture energy of materials. In cementitious materials, the fracture energy represents the indirect surface energy and it terms to the work of fracture [29]. Linear variable displacement transducer (LVDT) at mid-span of samples was employed to measure the displacement simultaneously. As shown in Figure 2(a), a 500 mm in length with a cross section of (100×100) prism was employed to evaluate the fracture parameters. For this, closed-loop testing machine, Instron 5500R, was used to apply load with a maximum capacity of 250 kN (Figure 2(b)). In the same regard, the overview of testing machine was depicted in Figure 2(c). In effect, 40 mm high notch was done via sawing the samples before testing. Thus, the ratio of notch to depth (a/W) was considered at 0.4. The fracture energy, in a single

edge notched beams, was calculated via measuring the initial ligament area as well as the total dissipated energy. According to work of fracture (WFM) or Hillerborg's method, fracture energy, G_F , can be expressed as [30]

$$G_F = \frac{W_F}{B(W - a)}, \quad (1)$$

where W_F represents the total amount of WFM in the test, while the width and the initial notch depth of the beam are represented by W and a , respectively. In the same regard, RILEM [28] proposed a similar relationship to describe the fracture energy of three-point bending test taking into consideration the effect of single edge notched beam. The equation can be written as

$$G_F = \frac{W_F + mg\delta_s(S/U)}{B(W - a)}, \quad (2)$$

where the terms m , g , δ_s , S , and U denote mass, the acceleration due to gravity, the specified deflection, span, and length of the beam, respectively. Moreover, the net flexural strength, f_{flex} , can be theoretically calculated as follows using $(500 \times 100 \times 100)$ mm prism specimens used in fracture test:

$$f_{\text{flex}} = \frac{3P_{\text{max}}S}{2B(W - a)^2}, \quad (3)$$

in which P_{max} is the ultimate load.

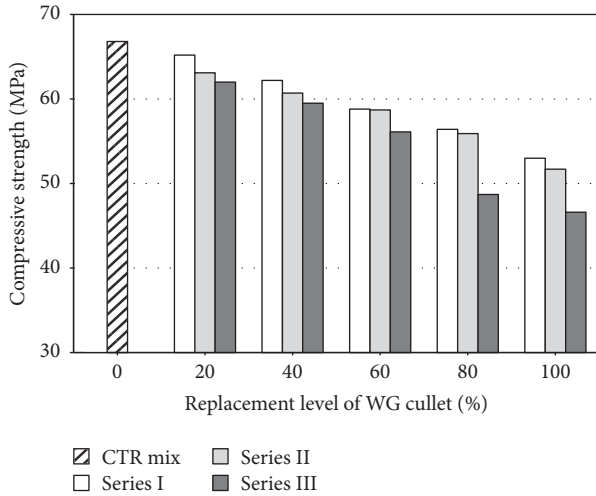


FIGURE 3: Compressive strength of SCC mixtures at 28 days with respect to WG cullet content.

In this regard, Hillerborg [29] described the brittleness of a material in WFM method through employing the fracture process zone length, which is related to the characteristic length parameter, as

$$l_{ch} = \frac{EG_F}{f_{st}^2}, \quad (4)$$

where E , G_F , and f_{st} are the static modulus of elasticity, the fracture energy, and splitting tensile strength of the beam, respectively.

3. Results and Discussion

3.1. Strength Properties. The 28-day compressive test results of concretes are demonstrated in Figure 3 in accordance with the replacement levels of WG cullet. It could be argued that the presence of WG as a full or partial replacement for NA inversely affected on the values of compressive strength. As shown in Figure 4, the concretes with 100% WG replacement level revealed the highest reduction in strength. The corresponding reduction in the strength was in the range of 26%, 29%, and 43% for series I, II, and III, respectively, as compared with CTR mixture; also, the values of compressive strength were in the range of 53.0–65.2, 51.7–63.1, and 46.6–62.0 MPa, respectively. In series III, where mixtures were made of WGFA and WGCA, the lowest values of compressive strength were observed. However, the reduction in compressive strength was deemed as consistent with previous literatures [3, 5, 8, 9, 12, 14], except at high replacement level of series III where the reduction trend was more pronounced. Hence, the range of compressive strength was acceptable for various uses of structural concrete (between 46.6 and 65.2 MPa).

In effect, the declining crushing strength of WG cullet is the main factor affecting on the strength of the produced SCC. This behavior attributes to the properties of glass which make it fragile when it is subjected to stress. Likewise, the

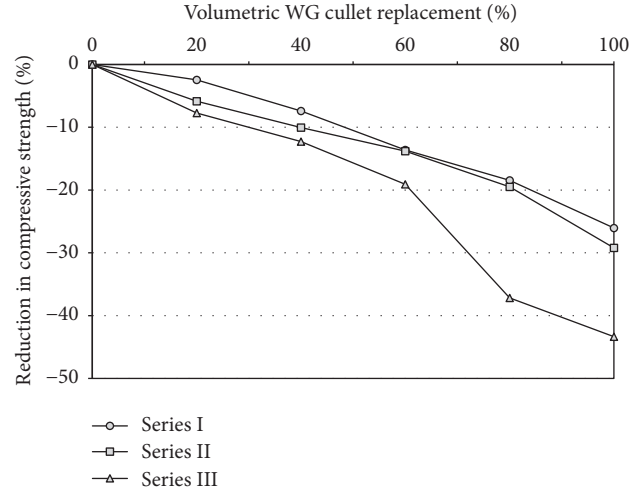


FIGURE 4: The reduction in compressive strength according to the content of WG cullet content.

high brittleness and poor geometry of glass aggregates lead to cracks which affect the adhesion between the glass particles and the cement paste. Indeed, the smooth surfaces and irregular particles shape weaken the mechanical interlocking [17]. Thus, WG cullet creates weak areas inside concrete matrix as well as weak ITZ strength leading to lower concrete strengths. Moreover, the microstructure of glass concrete contains more voids than conventional concrete due to the insufficient cement paste available inside the matrix which in turn adversely affects the bonding between concrete components [31].

Beside the smooth surface of the WG particles, the free water which is not absorbed by glass particles could accumulate at the surface of glass granules; leading to decrease in the strength of ITZ due to forming weak bond between them and cement paste. In the study of Tan and Du [30], it was emphasized that the weak bond strength between glass particles and cement paste dominated the strength of ITZ. According to author's point of view, sharp edges and smooth surface of WG particles were responsible for the weakness of ITZ strength. In this regard, Lam [32] believed that the reduction in the compressive strength of the WG cullet masonry was related to the fineness modulus of aggregates where the most suitable particle size ranged from 3.5 to 4.5.

The results of 28-day splitting tensile and net flexural strengths of SCC are depicted in Figures 5 and 6, respectively. The WG concretes manifested splitting tensile strengths ranging between 3.33 and 4.59, 2.78 and 4.41, and 2.23 and 4.07 MPa for the first, second, and third series, respectively, as compared with 5.03 MPa recorded for CTR mixture. Obviously, the utilizing of WG cullet led to a decrease in tensile strength values depending on the level of replacement. Indeed, the reduction trend was more pronounced at high levels of glass replacement and in series III where glass was used as fine and coarse grade. For instant, the reduction in tensile strength was 33.8, 44.7, and 55.6% for series I, II, and III, respectively, compared with CTR mix. Similarly, flexural strength value followed the same decreasing trend observed

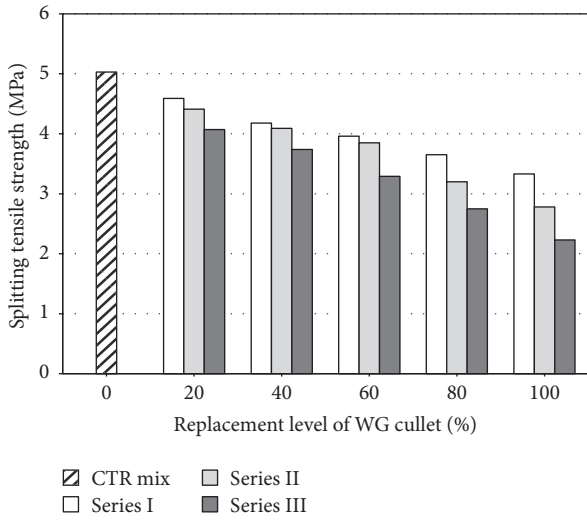


FIGURE 5: Splitting tensile strength of SCC mixtures at 28 days with respect to WG cullet content.

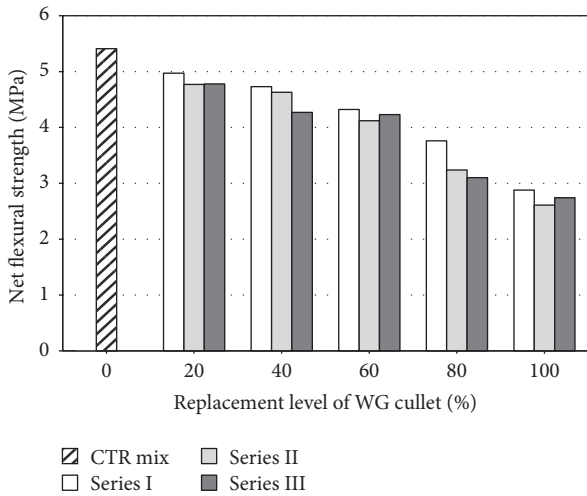


FIGURE 6: Net Flexural strength of SCC mixtures at 28 days with respect to WG cullet content.

for tensile strength. Indeed, as the WG cullet replacement level increased, the flexural as well as tensile strength of concretes decreased, compatible with previous authors results [3, 5, 8]. However, Sharifi et al., 2013 [8], reported that, at low replacement levels, fine grade of NA and WG cullet results in more adhesion between the glass particles and cement paste, producing more flexural and tensile strength values. In this study, flexural strength of SCC was in the range of 2.88–4.97, 2.61–4.77, and 2.74–4.78 MPa for the first, second, and third series, respectively, compared with 5.41 MPa recorded for CTR mixture. In other words, full replacement level of WG resulted in a decrease in strength by 46.7%, 51.7%, and 49.3% for series I, II, and III, respectively.

In effect, the low tensile strength of WG concrete induces rapid spread of microcracks under the applied load; then the concrete fails under lower load than conventional. Moreover, the factors and reasons responsible for decreasing the value

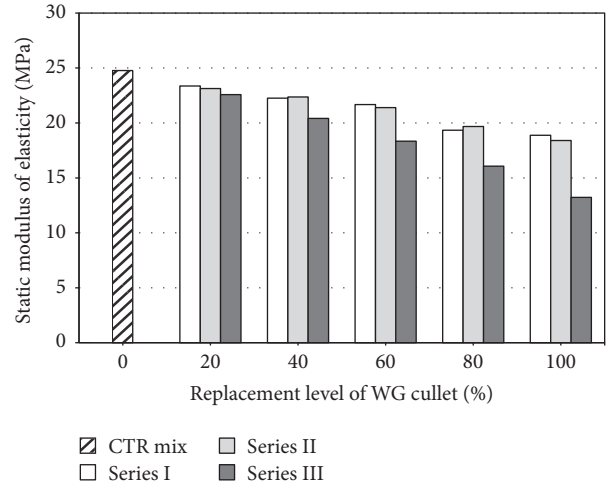


FIGURE 7: Modulus of elasticity of SCC mixtures at 28 days with respect to WG cullet content.

of compressive strength are the same in tensile and flexural strength. The fragile, smooth surface, sharp edges, and other physical properties again reduce the adhesion between the concrete components and thus negatively affect the strength of WG concretes. Moreover, the decrease in strengths might be due to the increase of porosity resulted by utilizing WG cullet as well as abundant mixing water. The tiny absorption capacity increases the availability of such water inside the concrete matrix contributing to the increase of porosity after it evaporates. Kou et al. [33] mentioned that free water would accumulate at the surface of particles due to smooth surface and insufficient water absorption of glass. Roberts [34] and others [3, 5, 12, 17, 30, 31] agreed with abovementioned point of view and reported similar trends.

The 28-day static modulus of elasticity for WG concretes is shown in Figure 7. The static moduli of SCC varied from 23.37 to 18.88, 23.14 to 18.4, and 22.58 to 13.22 GPa for series I, II, and III, respectively. These values could be compared with the corresponding value of 24.77 GPa for CTR mix. The type of aggregate significantly affected on the elasticity of concrete via the elastic deformation of such aggregate which partially impacted the deformation of concrete. Hence, replacing NA by WG cullet decreased the modulus results particularly at high levels. For example, using 100% WG cullet caused a drop in the value of modulus by 23.7%, 25.7%, and 46.6% for the first, second, and third series of SCC. Although the elastic modulus of WG cullet is higher than NA, the cellular microstructure at ITZ region and the weak interlocking in WG concrete cause microcracking inside the concrete structure, leading to lower modulus value than equivalent reference concrete. However, the effect of glass on modulus property of concrete is deemed as the least affected attribute compared with other mechanical aspects [30]. Consistent with the previously reported, the generation of higher porosity due to availability of mixing water might also contribute to the lower elastic behavior.

In the current study, the variation of splitting tensile strength and modulus of elasticity with compressive strength

TABLE 4: Fracture properties of PW concrete at 28 days.

Mix series	Mix code	P_{\max} (N)	Final disp. at mid-span (δ_s) (mm)	Fracture energy (N/m)	Characteristic length (mm)
Series I	CTR	3244	1.43	160.18	156.82
	FWG20CWG0	2985	1.50	155.67	172.68
	FWG40CWG0	2836	1.50	142.85	181.91
	FWG60CWG0	2591	1.50	135.12	186.72
	FWG80CWG0	2256	1.50	129.82	188.46
	FWG100CWG0	1729	1.11	116.06	197.6
Series II	FWG0RCG20	2863	1.50	145.69	173.35
	FWG0CWG40	2780	1.50	133.68	178.69
	FWG0CWG60	2473	1.50	128.9	186.01
	FWG0CWG80	1945	1.21	100.52	193.09
	FWG0CWG100	1563	1.14	85.12	202.66
Series III	FWG20CWG20	2871	1.39	132.27	180.3
	FWG40CWG40	2563	1.50	128.37	187.4
	FWG60CWG60	2540	1.11	117.55	199.17
	FWG80CWG80	1862	1.15	95.84	203.53
	FWG100CWG100	1646	0.77	79.26	210.71

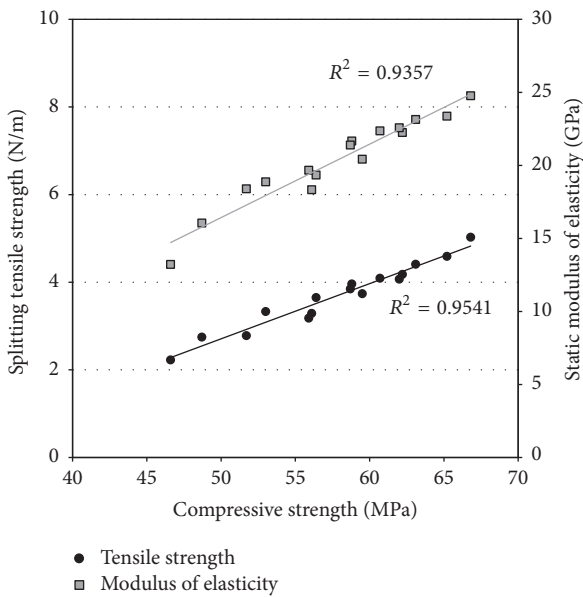


FIGURE 8: Splitting tensile strength and modulus of elasticity of SCC versus compressive strength.

are depicted in Figure 8. In this figure, an excellent correlation could be drawn between these parameters particularly with compressive strength of WG concretes. In this regard, Kou et al. [33] also found similar linear relationship for these parameters with the compressive strength, while Choi et al. [35] preferred to express this relationship via power equation with $(1/3)$ exponent coefficient. Kou and Poon [5] observed good correlation between these parameters and drew a power relationship between compressive strength and modulus of elasticity for SCC mixtures. Hence, linear relationship between tensile and compressive strength by means of regression analysis could be employed via the

results of this study. Moreover, the linear equation below with correlation coefficient (R^2) of 0.95 can describe this relationship:

$$f_{st} = 0.12f_c - 3.58. \quad (5)$$

Furthermore, the below equation expresses the relationship between static modulus of elasticity and compressive strength with R^2 of 0.93:

$$E_c = 0.5f_c - 8.7, \quad (6)$$

where f_{st} , E_c , and f_c represent tensile strength, the modulus of elasticity, and the compressive strength of SCC, respectively. Indeed, the correlation factor, R^2 , of equation above revealed that compressive strength of concretes was well correlated with the other mechanical parameters despite the different replacement levels of WG.

3.2. Fracture Characteristics. The fracture parameter results of glass SCC tested in this study are summarized in Table 4 and graphically depicted in Figure 9, in which mix FWG0CWG0 represents the control mix of the present study. In effect, the presence of WG cullet at any percentage causes a discrete reduction in maximum load value (P_{\max}) recorded for concretes. In the load-displacement curve, the prepeak stiffness was considerably affected by incorporating WG in concrete. Hence, the highest value of peak load was recorded in CTR mixture at 3244 N; then it continuously decreased depending on the replacement levels and the grade of WG used in the concretes. The lowest values were observed for 100% replacement level of WG cullet. They were recorded as 1726, 1563, and 1646 N, for first, second, and third series. As shown in Figure 9, as WG cullet was incorporated in concretes, a trend of decreasing could be noted. For instance, in series I, the reduction in recorded P_{\max} was 8%, 12.6%, 20.1%, 30.5%, and 46.7% for 20%, 40%, 60%, 80%, and

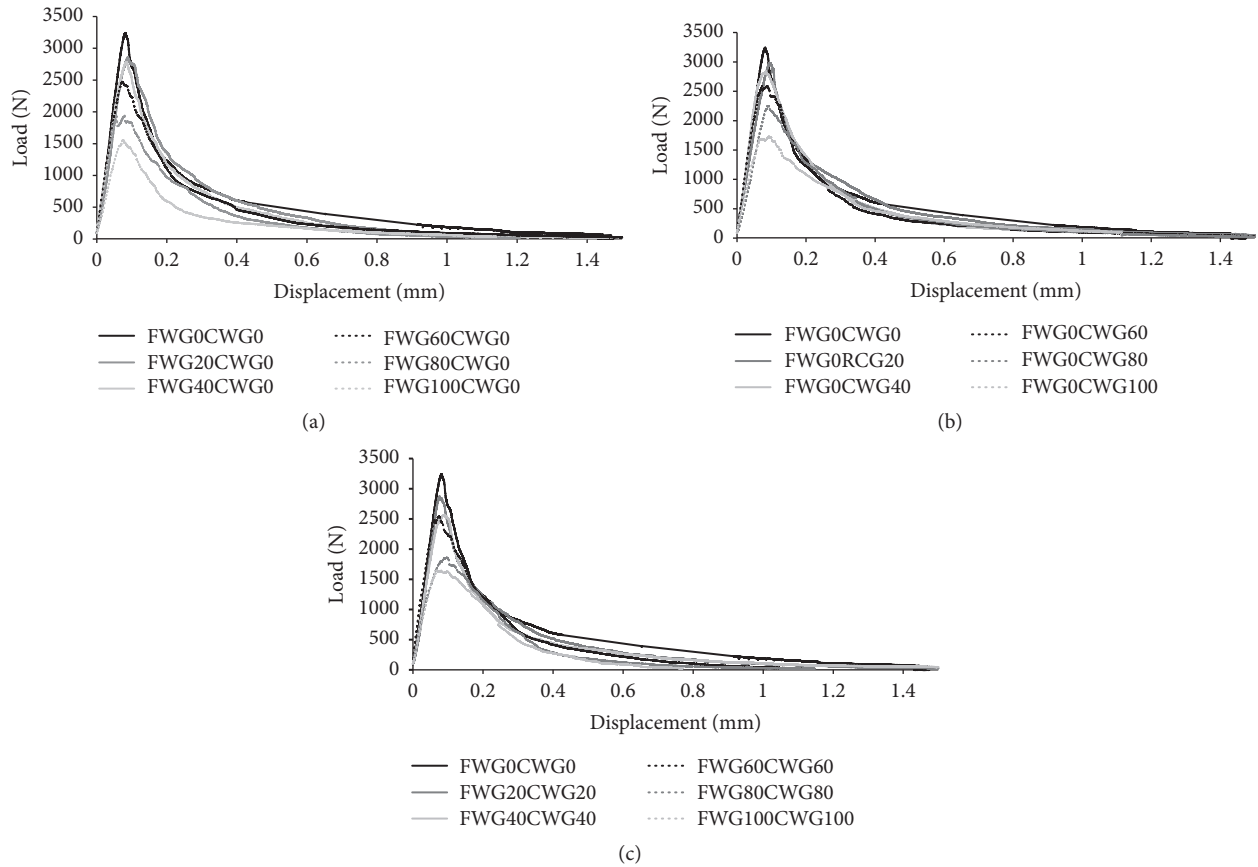


FIGURE 9: Load versus displacement curve of (a) WGFAs (series I), (b) WGCAs (series II), and (c) WGFAs + WGCAs (series III).

100% replacement levels, respectively. Hence, it could be estimated that the peak load noticeably depended on the glass content inside the mixture. However, P_{max} values represent the highest bearing load which the samples can carry before the cracks appear which in turn are controlled by the strength properties of concrete. In effect, the prepeak and max-peak performances in load-displacement curve are affected by the microcracks and their extension in concrete. In WG concrete, cracks can more easily penetrate through the matrix than conventional concrete due to few amounts of stiffer NA [36, 37]. The physical properties as well as inferior strength of glass aggregate compared with NA contribute to the decrease in peak load. In the present study, most mixtures revealed extended final displacement even for WG concrete. Indeed, the variation in the tail of the softening branch referred to higher elastic behavior of concrete except at highest levels of series II and III, in which it showed higher brittle performance than other mixtures.

The variations of fracture energy (G_F), the energy required to create a crack, are illustrated in Figure 10 and tabulated in Table 4. The value of fracture energy for CTR mix recorded 160.2 N/m and gradually reduced until it reached to the range of 116.1–155.7, 85.1–145.7, and 79.3–132.3 N/m for series I, II, and III, respectively. In effect, the extreme reduction could be observed at 100% replacement level in each series. It recorded 27.5%, 46.8%, and 50.5% for the first, second, and third series, respectively, compared with

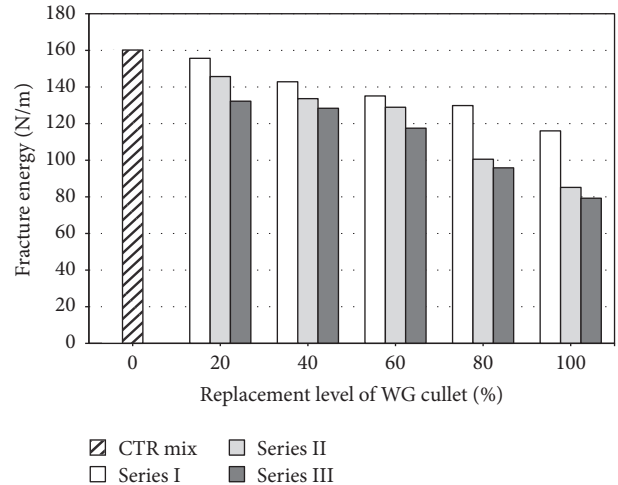


FIGURE 10: Fracture energy of SCC mixtures at 28 days with respect to WG cullet content.

CTR mixture. Previous publications emphasized that G_F of concrete was related to the cement paste-aggregate interfacial bond and the microstructural heterogeneity in the concrete [37, 38]. The utilization of WG in concrete resulted in high porosity, easy crack penetration, and weaker ITZ region than reference concrete. These factors adversely affected and

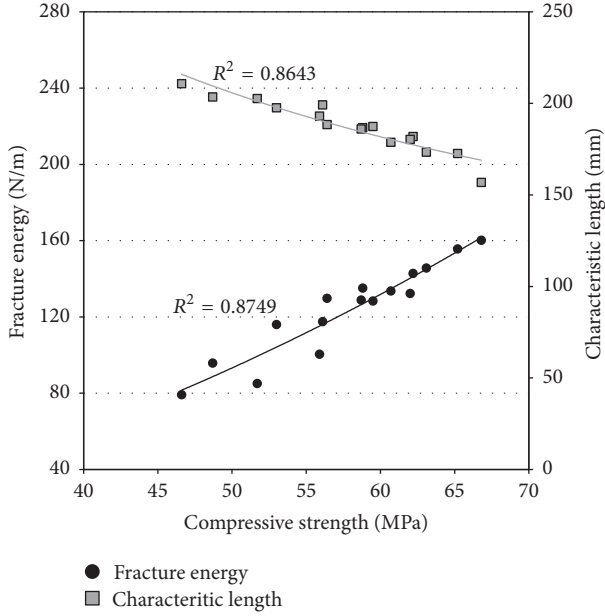


FIGURE 11: Fracture energy and characteristic length of SCCs versus compressive strength.

decreased the value of G_F and hence denoted less brittle behavior.

Fracture parameters such as G_F can be expressed as a function of compressive strength. According to CEB-FIB [39], fracture energy can be related with compressive strength in the form of power function. Moreover, various investigators have suggested a direct relationship between these parameters [40, 41]. As shown in Figure 11, fracture energy was directly proportional with compressive strength and the relationship could be expressed via the power equation below, with correlation coefficient (R^2) of 0.87:

$$G_F = 0.055 f_c^{1.9} \quad (7)$$

in which G_F is the total fracture energy (N/m) and f_c is the mean cube compressive strength at 28 days (MPa).

The brittleness of SCC can be measured via employing (4) proposed by Hillerborg [29]. In the present study, the results revealed that characteristic length (l_{ch}) computed from equation above gradually increased whenever WG replacing level increased. As depicted in Figure 12, the highest value of l_{ch} was recorded for 100% replacement level mixtures regardless of WG cullet grade. Indeed, the value of l_{ch} increased by 20.6%, 22.6%, and 25.5% for mixtures FWG100CWG0, FWG0CWG100, and FWG100CWG100, respectively, which represented the highest value for each series (Table 4). These findings emphasized that WG cullet concrete was less brittle than reference mixture due to the fact that the glass had an adverse effect on the strength of concrete. The inferior bond strength between glass particles and cement paste, which degrades the ITZ of such concrete, produces an increase in stress concentration around aggregates. Thus, cracks may develop through aggregates leading to contraction in fracture process zone and the concrete could have a more ductile

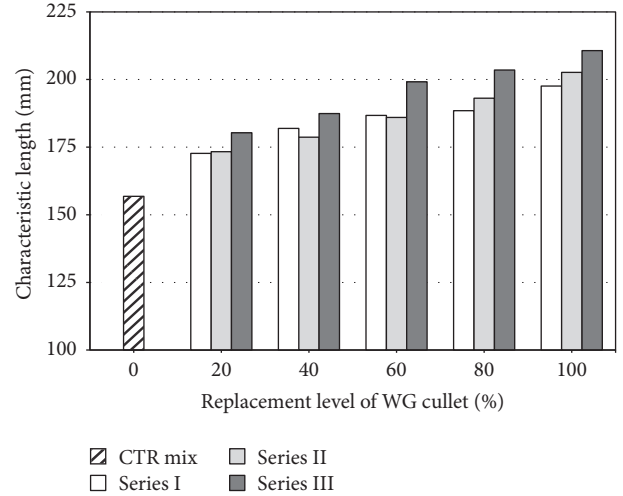


FIGURE 12: Characteristic length of SCC mixtures at 28 days with respect to WG cullet content.

behavior [42]. The weak paste-aggregate interface and non-homogeneous microstructure in WG concrete are responsible for the reduction in the brittleness of such concrete. Hence, the crack pattern is different than reference concrete.

In effect, few publications that dealt with the effect of WG cullet on the fracture parameters were available. Due to the brittleness being strongly related to the strength properties of concrete, WG cullet concretes revealed high brittle behavior. Compared with reference, WG concrete had a higher brittle behavior. This behavior attributed to the presence of cracks in aggregate phase causing changes in concrete fractal dimensions. Indeed, the fragile nature of WG cullet (which made it easy to rupture under stress) also reinforced this performance. Moreover, the lowest fractal dimension and smoother fracture surface are observed when the failure path passes directly through the aggregates [42, 43].

In effect, the ductility index is controlled by the interlocking bond between cement aggregates which is deemed as weak in glass concrete. Hence, in this study l_{ch} revealed lower values whenever the strength increased in agreement with brittle behavior. Characteristic length could also be expressed as a function of compressive strength as shown in Figure 11. In spite of the difference in the mix proportions of concretes, a good correlation could be written below to describe the relationship between characteristic length and compressive strength with R^2 of 0.86:

$$l_{ch} = 2951 f_c^{-0.68}, \quad (8)$$

where l_{ch} is characteristic length (mm) and f_c is the mean cube compressive strength at 28 days (MPa).

4. Conclusions

- (i) As WG cullet was incorporated and its content increased, the compressive strength values were negatively affected. However, among the three series of concretes, the reduction in strength did not exceed

26% and 29% for the first and second series, respectively, as compared to the corresponding reference mixtures. Except in series III, the decrease in strength became more pronounced with a maximum reduction of 43%. However, the lowest compressive strength was 46.6 MPa which was deemed acceptable for various uses of structural concrete.

- (ii) Splitting tensile strength, net flexural strength, and modulus of elasticity findings followed the similar trend observed in compressive strength results, while the reduction in these parameters was more pronounced at high levels of WG replacement and in series III where the glass was used as fine and coarse grade.
- (iii) Regardless of the replacement level of WG cullet, P_{max} , area under the load-displacement curve and fracture energy values revealed minimal values whenever glass aggregate was present and its content increased. Conversely, characteristic length recorded higher values for WG concrete indicating less brittle behavior than reference concrete.
- (iv) An excellent correlation between splitting tensile strength, modulus of elasticity, fracture energy, and characteristic length could be expressed as a function of the compressive strength. These relationships followed linear and power equations for mechanical and fracture parameters, respectively.

Additional Points

Highlights. Waste glass (WG) cullet was prepared through crushing green-colored glass bottles. WG cullet was used at different percentages. Self-compacting concretes (SCCs) were made with and/or without WG cullet. Strength properties of SCCs were adversely affected by the use of WG cullet. The uses of WG cullet resulted in lower fracture energy and higher values of characteristic length.

Conflicts of Interest

The authors declare that they have no conflicts of interest.

References

- [1] Turkish Court of Accounts, *Waste Management in Turkey, National Regulations and Evaluation of Implementation Results, Performance Audit Report*, vol. 81, 2007.
- [2] M. Berkun, E. Aras, and T. Anilan, "Solid waste management practices in Turkey," *Journal of Material Cycles and Waste Management*, vol. 13, no. 4, pp. 305–313, 2011.
- [3] I. B. Topcu and M. Canbaz, "Properties of concrete containing waste glass," *Cement and Concrete Research*, vol. 34, no. 2, pp. 267–274, 2004.
- [4] A. M. Rashad, "Recycled waste glass as fine aggregate replacement in cementitious materials based on Portland cement," *Construction and Building Materials*, vol. 72, pp. 340–357, 2014.
- [5] S. C. Kou and C. S. Poon, "Properties of self-compacting concrete prepared with recycled glass aggregate," *Cement and Concrete Composites*, vol. 31, no. 2, pp. 107–113, 2009.
- [6] A. Shayan, "Value-added utilisation of waste glass in concrete," in *Proceedings of the IABSE Symposium*, p. 11, ARRB Transport Research, Melbourne, Victoria, Australia, 2002.
- [7] I. Afshoon and Y. Sharifi, "Ground copper slag as a supplementary cementing material and its influence on the fresh properties of self-consolidating concrete," *IES Journal Part A: Civil and Structural Engineering*, vol. 7, no. 4, pp. 229–242, 2014.
- [8] Y. Sharifi, M. Houshiar, and B. Aghebati, "Recycled glass replacement as fine aggregate in self-compacting concrete," *Frontiers of Structural and Civil Engineering*, vol. 7, no. 4, pp. 419–428, 2013.
- [9] C. Meyer, S. Baxter, and W. Jin, "Alkali-aggregate reaction in concrete with waste glass as aggregate," in *Proceedings of 4th materials engineering*, pp. 1388–1397, Reston, VA., ASCE, 1996.
- [10] P. Asokan, M. Osmani, and A. D. F. Price, "Assessing the recycling potential of glass fibre reinforced plastic waste in concrete and cement composites," *Journal of Cleaner Production*, vol. 17, no. 9, pp. 821–829, 2009.
- [11] Ö. Özkan and I. Yüksel, "Studies on mortars containing waste bottle glass and industrial by-products," *Construction and Building Materials*, vol. 22, no. 6, pp. 1288–1298, 2008.
- [12] S. B. Park, B. C. Lee, and J. H. Kim, "Studies on mechanical properties of concrete containing waste glass aggregate," *Cement and Concrete Research*, vol. 34, no. 12, pp. 2181–2189, 2004.
- [13] C. M. Sangha, A. M. Alani, and P. J. Walden, "Relative strength of green glass cullet concrete," *Magazine of Concrete Research*, vol. 56, no. 5, pp. 293–297, 2004.
- [14] P. Turgut and E. Yahlizade, "Research into Concrete Blocks with Waste Glass," *International Journal Civil, Environmental, Structural, Construction and Architectural Engineering*, vol. 3, no. 3, 2009.
- [15] Environmental Protection Department, *Monitoring of solid waste in 2005*, Environmental Protection Department, Hong Kong, 2006.
- [16] C. Shi, "Corrosion of glasses and expansion mechanism of concrete containing waste glasses as aggregates," *Journal of Materials in Civil Engineering*, vol. 21, no. 10, pp. 529–534, 2009.
- [17] C. Meyer, N. Egesi, and C. Andela, "Concrete with waste glass as aggregate," in *Proceedings of the International Symposium Concrete Technology Unit of ASCE*, 2001.
- [18] C. S. Lam, C. S. Poon, and D. Chan, "Enhancing the performance of pre-cast concrete blocks by incorporating waste glass—ASR consideration," *Cement and Concrete Composites*, vol. 29, no. 8, pp. 616–625, 2007.
- [19] E. E. Ali and S. H. Al-Tersawy, "Recycled glass as a partial replacement for fine aggregate in self compacting concrete," *Construction and Building Materials*, vol. 35, pp. 785–791, 2012.
- [20] TS EN 197-1, *Cement- Part 1: Composition, Specifications and Conformity Criteria for Common Cements*, Turkish Standards, 2012.
- [21] ASTM C 127, "Standard test method for specific gravity and absorption of coarse aggregate," in *Annual Book of ASTM Standards*, 2015.
- [22] TS 706 EN 12620-A1, *Aggregates for Concrete*, Institute of Turkish Standards, Turkish Standards, 2012.
- [23] ASTM C 192, "Standard practice for making and curing concrete test specimens in the laboratory," in *Annual Book of ASTM Standards*, 2015, Standard practice for making and curing concrete test specimens in the laboratory in.
- [24] EFNARC, *European Guidelines for Self-Compacting Concrete, Specification and Production and Use*, Association House, 2005.

- [25] British Standard Institution, *Part 116. BS 1881-116:1983, Testing Concrete Method for Determination of Compressive Strength of Concrete Cubes, BS 1881*, BSI, London, 2004.
- [26] ASTM C496, "Standard test method for splitting tensile strength of cylindrical concrete specimens. International standards worldwide," in *Proceedings of the Annual book of ASTM standards*, 2015.
- [27] *Part 121. Recommendations for the measurement of static modulus of elasticity. BS 1881*, BSI, 2014.
- [28] RILEM 50-FMC, "Committee of fracture mechanics of concrete. Determination of fracture energy of mortar and concrete by means of three-point bend tests on notched beams," *Mater Struct*, vol. 18, no. 106, pp. 285–290, 1985.
- [29] A. Hillerborg, "Concrete fracture energy tests performed by 9 different laboratories according to a draft RILEM recommendation," Report to RILEM TC50- FMC. Report TVMB-3015, Lund Sweden, 1983.
- [30] K. H. Tan and H. Du, "Use of waste glass as sand in mortar: part I - Fresh, mechanical and durability properties," *Cement and Concrete Composites*, vol. 35, no. 1, pp. 118–126, 2013.
- [31] M. Adaway and Y. Wang, "Recycled glass as a partial replacement for fine aggregate in structural concrete -Effects on compressive strength," *Electronic Journal of Structural Engineering*, vol. 14, no. 1, pp. 116–122, 2015.
- [32] C. Lam, *Use of recycled construction and demolition wastes as aggregates in pre-cast block works [Msc. thesis]*, The Hong Kong Polytechnic University, Hong Kong, 2006.
- [33] S. C. Kou, G. Lee, C. S. Poon, and W. L. Lai, "Properties of lightweight aggregate concrete prepared with PVC granules derived from scraped PVC pipes," *Waste Management*, vol. 29, no. 2, pp. 621–628, 2009.
- [34] L. R. Roberts, *Microsilica in concrete, materials science of concrete*, American Ceramic Society, Westerville, Ohio, OH, USA, 1989.
- [35] Y. W. Choi, D. J. Moon, Y. J. Kim, and M. Lachemi, "Characteristics of mortar and concrete containing fine aggregate manufactured from recycled waste polyethylene terephthalate bottles," *Construction and Building Materials*, vol. 23, no. 8, pp. 2829–2835, 2009.
- [36] A. Bordelon, V. Cervantes, and J. R. Roesler, "Fracture properties of concrete containing recycled concrete aggregates," *Magazine of Concrete Research*, vol. 61, no. 9, pp. 665–670, 2009.
- [37] M. Arezoumandi, J. Drury, J. S. Volz, and K. H. Khayat, "Effect of recycled concrete aggregate replacement level on shear strength of reinforced concrete beams," *ACI Materials Journal*, vol. 112, no. 4, pp. 559–568, 2015.
- [38] C. Taşdemir, M. Taşdemir, F. Lydon, N. Mills, and B. Barr, "Combined effects of silica fume, aggregate type, and size on post-peak response of concrete in bending," *ACI Materials Journal*, vol. 96, no. 1, 1999.
- [39] *CEB-FIP Model Code 2010-Design Code*, Thomas Telford House, London, 2010.
- [40] C. Albano, N. Camacho, M. Hernández, A. Matheus, and A. Gutiérrez, "Influence of content and particle size of waste pet bottles on concrete behavior at different w/c ratios," *Waste Management*, vol. 29, no. 10, pp. 2707–2716, 2009.
- [41] H. Eskandari, S. Muralidhara, B. K. Raghun Prasad, and B. V. Venkatarama Reddy, "Size effect in self consolidating concrete beams with and without notches," *Sadhana - Academy Proceedings in Engineering Sciences*, vol. 35, no. 3, pp. 303–317, 2010.
- [42] M. H. A. Beygi, M. T. Kazemi, I. M. Nikbin, and J. V. Amiri, "The effect of water to cement ratio on fracture parameters and brittleness of self-compacting concrete," *Materials & Design*, vol. 50, pp. 267–276, 2013.
- [43] A. Yan, K.-R. Wu, D. Zhang, and W. Yao, "Effect of fracture path on the fracture energy of high-strength concrete," *Cement and Concrete Research*, vol. 31, no. 11, pp. 1601–1606, 2001.

Research Article

Experimental Study and Application of Inorganic Solidified Foam Filling Material for Coal Mines

Hu Wen,^{1,2,3} Duo Zhang,^{1,2,3} Zhijin Yu,^{1,2,3} Xuezhao Zheng,^{1,2,3}
Shixing Fan,^{1,2,3} and Bin Laiwang⁴

¹School of Safety Science and Engineering, Xi'an University of Science and Technology, Xi'an, Shaanxi 710054, China

²Key Laboratory of Mine and Disaster Prevention and Control of Ministry of Education, Xi'an University of Science and Technology, Xi'an, Shaanxi 710054, China

³Xi'an Research Center National Mine Rescue, Xi'an, Shaanxi 710054, China

⁴Doctoral Program, Graduate School of Engineering Science and Technology, National Yunlin University of Science and Technology, 123 University Rd., Sec. 3, Douliou, Yunlin 64002, Taiwan

Correspondence should be addressed to Duo Zhang; b201512041@stu.xust.edu.cn

Received 25 April 2017; Revised 23 June 2017; Accepted 10 July 2017; Published 10 August 2017

Academic Editor: Prinya Chindaprasirt

Copyright © 2017 Hu Wen et al. This is an open access article distributed under the Creative Commons Attribution License, which permits unrestricted use, distribution, and reproduction in any medium, provided the original work is properly cited.

Spontaneous combustion of residual coal in a gob due to air leakage poses a major risk to mining safety. Building an airtight wall is an effective measure for controlling air leakage. A new type of inorganic solidified foam-filled material was developed and its physical and chemical properties were analyzed experimentally. The compressive strength of this material increased with the amount of sulphoaluminate cement. With an increasing water-cement ratio, the initial setting time was gradually extended while the final setting time firstly shortened and then extended. The change in compressive strength had the opposite tendency. Additionally, as the foam expansion ratio increased, the solidification time tended to decrease but the compressive strength remained approximately constant. With an increase in foam production, the solidification time increased and the compressive strength decreased exponentially. The results can be used to determine the optimal material ratios of inorganic solidified foam-filled material for coal mines, and filling technology for an airtight wall was designed. A field application of the new material demonstrated that it seals crossheadings tightly, leaves no fissures, suppresses air leakage to the gob, and narrows the width of the spontaneous combustion and heat accumulation zone.

1. Introduction

As a major source of energy, coal accounts for 76% of primary energy consumption in China and its dominant position in the energy structure cannot be replaced over the long term [1, 2]. The safety of coal mines is thus of critical importance to China's socioeconomic development [3, 4].

In many modern coal mines in China, the mining roadway is excavated by double tunneling with a continuous miner, resulting in a dense distribution of crossheadings between the two tunnels (with adjacent crossheadings being separated by about 50 m). During mining, the crossheadings should be sealed to reduce air leakage to the gob and further to prevent the spontaneous combustion of coal and gas explosions [5]. In 2012, a gas explosion accident occurred at

the Number 53 crossheading in the gob of working face 22113 in the Cuner colliery, Shenfu-Dongsheng coalfield, Shaanxi Province, China. A detailed investigation concluded that this accident was caused by a loose airtight wall in the crossheading. Because air entered the gob through the fissures of the airtight wall, the residual coal oxidized spontaneously and there was eventually a gas explosion.

In the 1990s, the United States, Germany, Australia, and other countries with advanced coal mining techniques began to study and apply various airtight filling materials [6–10]. In contrast, China is a late comer to research on filling and plugging materials. Chinese workers still use materials like wood, loess, cement grouting [11], and fly ash grouting in coal mines. Recent years have witnessed the development and application of new filling materials, including gel materials,

fly ash composite colloid [12, 13], paste backfilling [14], thickened mortar [15], rigid polyurethane foam [16], Marithan, and Igloneige [17]. However, all these filling materials have disadvantages. Loess and cement slurry, for example, cannot be directly connected to the roof and have relatively low compressive strength. As a new type of excellent cooling and inerting material, gel materials readily crack after dehydration, resulting in poor compressive strength. Organic filling materials like Marithan are expensive and release toxic gases at high temperatures although they are effective in stopping leaks.

Foam has received much attention because of its low density, low thermal conductivity, low permeability, high expansibility, and high strength [18]. The former Soviet Union, United States, northern European countries, and Japan have developed foam cement and successfully applied the cement in construction and oil development [19–22]. Kearsley and Wainwright explored the relationship between the compressive strength and thermal conductivity of foamed concrete and analyzed the effect of the fly ash content on compressive strength [23–26]. Jambor and Luping probed the effect of the pore structure on the strength of foam concrete [27, 28]. Nambiar and Ramamurthy [29] and Kearsley and Wainwright [25] studied the gas pore characteristics of foamed concrete and the effect of porosity on the strength of foamed concrete, respectively. Although many researchers have gone to great effort to investigate foam cement, they have seldom researched filling materials to be used in an underground coal mine in an effort to improve the performance and reduce the cost of the materials. China University of Mining and Technology (Beijing) developed a foamed cement and used the filling to stop leaks [30, 31]. However, the product is not suitable for extensive use because it relies on a special type of cement, which is difficult to prepare and costly.

The aims of the present paper are to develop a high-quality, low-cost inorganic solidified foam-filled material adopting raw materials, such as ordinary Portland cement, fly ash, gelling agent, water, foaming agent, and water reducer, employing a physical mixing method for foaming.

2. Experimental Materials and Methods

2.1. Experimental Materials. The following samples were used in experiments:

- (1) Ordinary Portland cement (Yulin Shanshui Cement Plant, Shaanxi Province, China)
- (2) Sulphoaluminate cement (SC) with apparent density of 3.21 kg/m^3
- (3) Fly ash (Daliuta Thermal Power Plant, Shenfu-Dongsheng Coal Mining Area, Shaanxi Province, China)
- (4) Lignosulfonate water reducer (Shaanxi QinFen Building Material Co., Ltd., Shaanxi Province, China).

Lauryl amidopropyl betaine ($\text{C}_{20}\text{H}_{40}\text{N}_2\text{O}_3$) and potassium monoalkyl phosphate ($\text{C}_{12}\text{H}_{25}\text{OPO}_3\text{K}_2$) were used as activators of the foaming agent and were mixed at a

ratio of 7:3. Triethanolamine ($\text{C}_6\text{H}_{15}\text{NO}_3$) and oleic acid ($\text{C}_{18}\text{H}_{34}\text{O}_2$) were used as foam stabilizers and were mixed at a ratio of 1:1. The foaming agent and foam stabilizers were mixed at a ratio of 1:1. The foam was prepared following steps described in the literature [32].

2.2. Experimental Instruments. The experimental instruments included a compressed-air foam generator [32], LQ-A30001 electronic balance (Ruian Ante Weighing Equipment Co., Ltd., Zhejiang Province, China), NJ-160 cement mixer (Shangyu Zheyi Machinery Manufacturing Co., Ltd., Zhejiang Province, China), Vicat Apparatus (Shandong Taoyin E-commerce Co., Ltd., Shandong Province, China), and YA-2000 microcontrolled pressure testing machine (Shenyang Baote Instrument Co., Ltd., Liaoning Province, China).

2.3. Experimental Methods

2.3.1. Determination of the Gel Time. The following procedure was used in experiments.

- (1) The slurry of inorganic gelled foam was poured into a circular die (having an upper inner diameter of 65 mm, lower inner diameter of 75 mm, and height of 40 mm), and the time was recorded.
- (2) The initial setting test needle was replaced with the final setting test needle. The test needle was released when the material was about to enter the phase of initial setting.
- (3) The time when the test needle reached a level $4 \pm 1 \text{ mm}$ above the bottom plate was recorded; this was the initial setting time of the material.
- (4) The die was turned through 180° and the height of the test needle was adjusted so that the lower surface of the needle was at the same level as the surface of the material inside the circular die. The test needle was released when the material was about to enter the phase of final setting. The time when the test needle submerged into the test piece by 0.5 mm was recorded; this was the final setting time of the material.

2.3.2. Determination of Compressive Strength. Cubic specimens of inorganic foam material having dimensions of $100 \text{ mm} \times 100 \text{ mm} \times 100 \text{ mm}$ were made and dried in an oven (at 105°C for 4 hours). A microcontrolled pressure testing machine was used to apply continuous and uniform pressure to the cubic specimens until the blocks were damaged. The load at that moment was the maximum failure load F . The compressive strength can be calculated as [33]

$$f = \frac{F}{A}, \quad (1)$$

where f is the compressive strength of the test piece (MPa) accurate to 0.01 MPa, F is the maximum failure load (N), and A is the compression area of the test piece (mm^2).

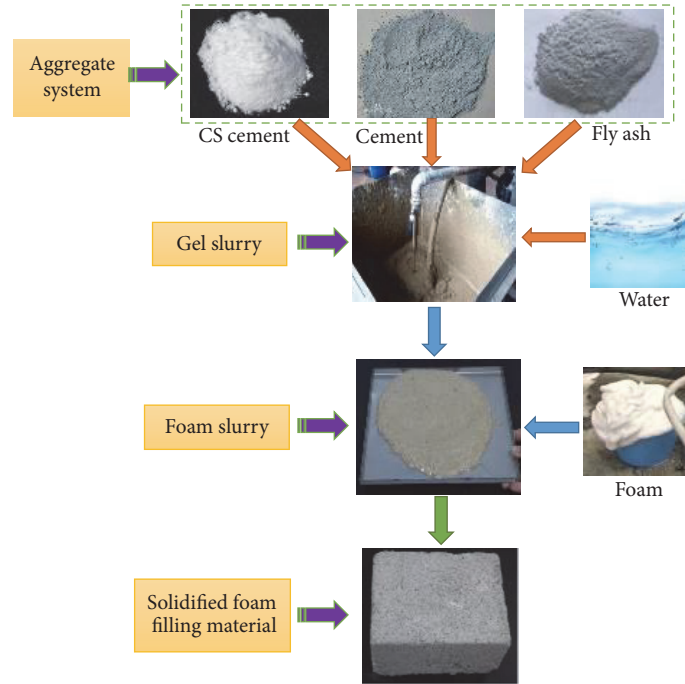


FIGURE 1: Preparation of the filling material.

TABLE 1: Chemical composition of ordinary Portland cement (%).

CaO	SiO ₂	Al ₂ O ₃	Fe ₂ O ₃	SO ₃	MgO	TiO ₂	K ₂ O	Na ₂ O
64.28	20.47	6.57	2.79	1.17	2.31	0.91	0.84	0.66

TABLE 2: Physical parameters of ordinary Portland cement.

Fineness (0.08 mm, residue on square hole sieve)	Apparent density (kg/m ³)	Initial setting time (min)	Final setting time (min)	Compressive strength (MPa) 1 d	Compressive strength (MPa) 28 d
8%	3.06	139	375	12.8	46.7

TABLE 3: Chemical composition of sulphoaluminate cement (%).

CaO	SiO ₂	Al ₂ O ₃	Fe ₂ O ₃	SO ₃	MgO	TiO ₂
42.44	12.46	30.58	2.54	9.52	0.64	1.82

2.3.3. *Material Preparation.* The test procedure was as follows.

- (1) SC, ordinary Portland cement, and fly ash were mixed in certain proportions, to produce an aggregate system.
- (2) The aggregate system and water were mixed in certain proportions, to produce a gel slurry.
- (3) The gel slurry and foam were evenly mixed in certain proportions, to produce a foam slurry.
- (4) The foam slurry was poured into a mold, and the solidified material was the foam filling material.

The process of preparing inorganic solidified foam filling material is shown in Figure 1.

3. Experimental Results and Analysis

3.1. *Material Analysis.* Physical properties and chemical compositions of the ordinary Portland cement, SC, and fly ash are listed in Tables 1–6.

3.2. *Effect of SC Cement on Material Properties.* To explore how the dosage of SC cement affects the inorganic solidified foam, experiments were designed as shown in Table 7. We adjusted the dosage of SC cement and measured the material gel time and compressive strength, as presented in Figure 2.

Figure 2 reveals that, as the dosage of SC cement increased, both the initial and final setting times shortened and the compressive strengths for different ages gradually increased. After the dosage exceeded 30%, the solidification time decreased at a much slower pace. The compressive strength of the filling material was much higher on the 28th

TABLE 4: Physical parameters of sulphoaluminate cement.

Apparent density (kg/m ³)	Initial setting time (min)	Final setting time (min)	Compressive strength (MPa)	
			1 d	28 d
3.21	10	30	37.5	51

TABLE 5: Chemical composition of fly ash (%).

CaO	SiO ₂	Al ₂ O ₃	Fe ₂ O ₃	SO ₃	MgO	TiO ₂	K ₂ O	Na ₂ O
12.24	49.02	22.81	6.79	1.67	2.49	0.97	2.59	1.42

TABLE 6: Physical parameters of fly ash.

Soundness (<1 mm, this was defined as the increased distance after boiling by Le-Chatelier method)	Fineness (<0.045 mm, %)	Loss on ignition (%)	Water content ratio (%)	Water content (%)
4.5	33.4	8.3	102	0.8

TABLE 7: Experimental design of the sulphoaluminate cement content.

Sequence	Aggregate system			Water-cement ratio (%)	Foam		Gel slurry-foam ratio
	Cement (%)	SC (%)	Fly ash (%)		Foaming multiple	Dosage (mL)	
1	100	0	0	50	10	200	1
2	95	5	0	50	10	200	1
3	90	10	0	50	10	200	1
4	85	15	0	50	10	200	1
5	80	20	0	50	10	200	1
6	75	25	0	50	10	200	1
7	70	30	0	50	10	200	1
8	65	35	0	50	10	200	1
9	60	40	0	50	10	200	1
10	55	45	0	50	10	200	1
11	50	50	0	50	10	200	1

Note. The gelling agent contained 0.1% water reducer; the water-cement ratio is the mass ratio of water to aggregate system; the gel-foam ratio is the ratio of the volume of the gel slurry to the volume of the foam.

day than on the first day. After the dosage exceeded 40%, the compressive strength on the 28th day slightly fell. The above phenomena are explained as follows. In the early stage, as the dosage increased, the solidification time shortened but the compressive strength gradually increased because the gas pores in the solidified foam cement were intact. After the dosage exceeded 30%, the solidification time reduced at a much slower place. As the dosage continued to rise, the SC cement would encase the ordinary Portland cement, which hindered the hydration of the ordinary Portland cement and thereby lessened the compressive strength of the material. As a result, the optimal dosage of SC cement was between 30% and 40%.

3.3. Effect of Fly Ash on Material Properties. Previous research has found that fly ash has little effect on the strength of a material, except when the dosage is excessive [22, 34]. To study how the dosage of fly ash affects the inorganic solidified foam, an experiment was designed as shown in Table 8.

The solidification time and compressive strength of the material at different dosages of fly ash are illustrated in Figure 3. When the dosage of fly ash fell between 0% and 20%, both the initial and final setting times lengthened slightly while the compressive strengths on the 1st and 28th days decreased slightly. When the fly ash content was between 20% and 30%, the initial setting time increased appreciably and the final setting time first shortened and then lengthened. The compressive strengths on the 1st and 28th days gradually decreased while the compressive strength on the 90th day increased with the dosage of fly ash. The above results are explained as follows. The glassy fly ash served as a framework among the cement particles and increased the density of the material. Fly ash reacted with cement to form strong covalent bonds. The secondary hydration reaction among SiO₂, Al₂O₃, and Fe₂O₃ in the fly ash and Ca(OH)₂, a product of cement hydration, produced C-S-H and C-A-H. The products filled up the cementitious material, refined the preliminary size, and altered the interface structure, thereby improving the

TABLE 8: Experimental design of the fly ash content.

Sequence	Aggregate system			Water–cement ratio (%)	Foam Foaming multiple	Dosage (mL)	Gel slurry-foam ratio
	Cement (%)	SC (%)	Fly ash (%)				
1	60	40	0	50	10	200	1
2	57	38	5	50	10	200	1
3	54	36	10	50	10	200	1
4	51	34	15	50	10	200	1
5	48	32	20	50	10	200	1
6	45	30	25	50	10	200	1
7	42	28	30	50	10	200	1

Note. The gelling agent contained 0.1% water reducer.

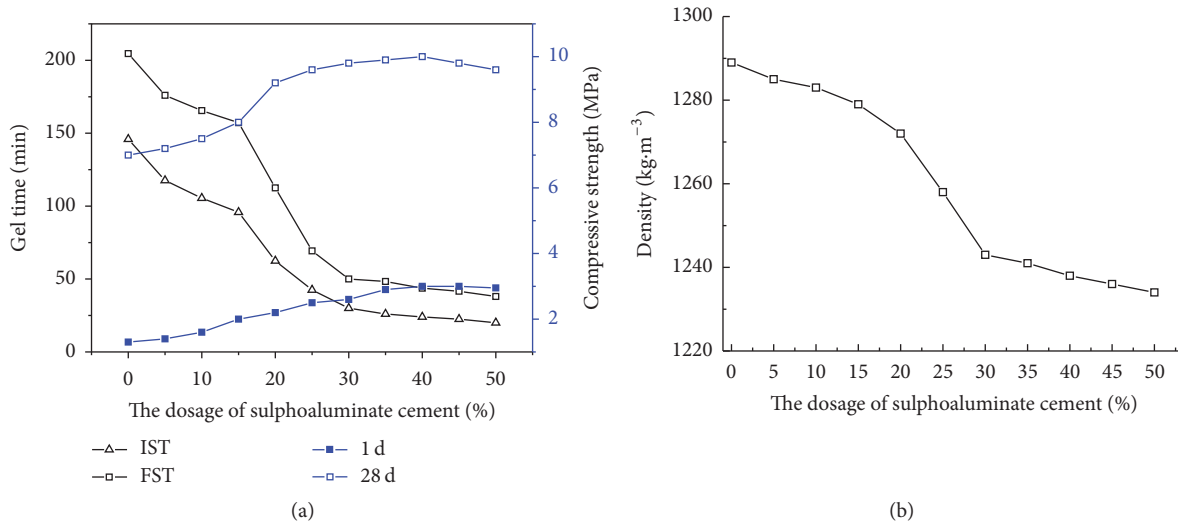


FIGURE 2: Effect of the dosage of sulphoaluminate cement on the filling material. Note. IST: initial setting time; FST: final setting time.

compressive strength [35, 36]. Because of the low activity of fly ash, the secondary hydration reaction did not occur unless the cement was hydrated to release enough $\text{Ca}(\text{OH})_2$ to increase the environmental alkalinity and turn the fly ash from inert to active. The compressive strength on the 28th day therefore lagged the actual status and does not accurately reflect the pozzolanic activity of fly ash [37].

3.4. Effect of the Water–Cement Ratio on Material Properties. To study how the water–cement ratio affects the inorganic solidified foam, an experiment was designed as shown in Table 9.

The material properties were tested at different water–cement ratios. Because the water reducer affected the water consumption of the material, we carried out three groups of comparative tests at water reducer contents of 0%, 0.1%, and 0.2%.

Figure 4 illustrates the effects of the water–cement ratio and water reducer on the solidification time. As the water–cement ratio rose, the initial setting times of all materials gradually lengthened. The final setting times of all materials firstly shortened and then lengthened. The material with no water reducer had a longer initial setting time than the materials for which the water reducer was added. After the

water–cement ratio exceeded 0.4, the material with no water reducer had a longer final setting time than the materials with the water reducer. The above results are explained as follows. When the water–cement ratio was relatively low, the material slurry was highly viscous and readily reached its initial setting state. There was thus insufficient water for the hydration reaction, which lengthened the final setting time. When the water–cement ratio was excessively high, the water in the material slurry diluted the SiO_2 , Al_2O_3 , and $\text{Ca}(\text{OH})_2$ necessary for the secondary hydration reaction, which also lengthened the final setting time.

Figure 5 presents results for the materials with different amounts of water reducer. As the water–cement ratio rose, the compressive strengths on the 1st and 28th days both firstly increased and then decreased. After the water–cement ratio surpassed 0.45, the material with no water reducer had a lower compressive strength than materials of the same age with water reducer. When the dosage of water reducer was 0.1% or 0.2%, there was no appreciable difference in the compressive strengths of materials of the same age. The above results are explained as follows. In the mixing process, both the cement and foam absorbed water. Owing to the better hydrophilicity and water absorbability of cement, the foam had to adhere to the surface of cement particles to absorb the little

TABLE 9: Experimental design of water–cement ratio.

Sequence	Aggregate system			Water–cement ratio (%)	Foam		Gel slurry-foam ratio
	Cement (%)	SC (%)	Fly ash (%)		Foaming multiple	Dosage (mL)	
1	48	32	20	25	10	200	1
2	48	32	20	35	10	200	1
3	48	32	20	45	10	200	1
4	48	32	20	55	10	200	1
5	48	32	20	65	10	200	1
6	48	32	20	75	10	200	1
7	48	32	20	85	10	200	1

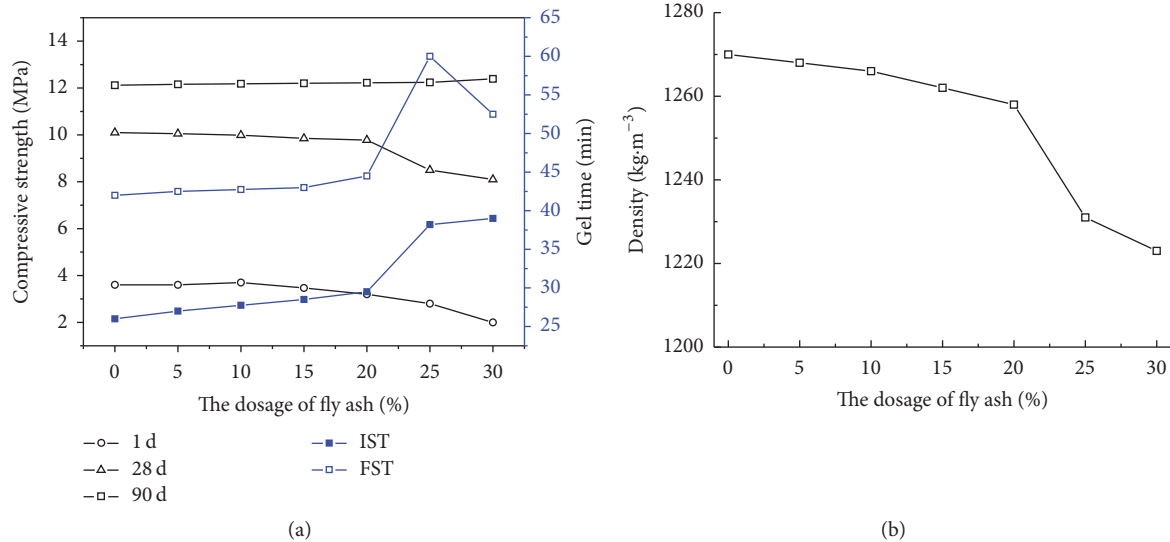


FIGURE 3: Effect of the dosage of fly ash on the filling material.

amount of water. In this process, bubbles burst under surface tension as the convex outer surfaces of bubbles were in contact with concave cement particles. The cement particles had a layer of hydrophobic groups on their surfaces. When other bubbles came into contact with cement particles, they burst as hydrophilic groups encountered hydrophobic groups. As a result, the low water–cement ratio affected the hydration and solidification time of cement and reduced the compressive strength of the material. When the water–cement ratio was greater than 0.55, the foam mixed into the slurry because of the superior fluidity of the latter. Meanwhile, excessive water reduced the stability of the foam, undermined the pore structure of the material, and lowered the material strength. The optimal water–cement ratio thus fell between 0.4 and 0.5, and the optimal dosage of water reducer was 0.1%.

3.5. Effect of Foam on a Material. To study the effect of the foam on an inorganic solidified foam material, an experiment was designed as shown in Tables 10 and 11.

3.5.1. Effect of the Foam Expansion Ratio on the Material. Figure 6 illustrates the effect of the foam expansion ratio on the solidification time and compressive strength. It is seen that both the initial and final setting times decreased as the

expansion ratio rose. The expansion ratio had little effect on the compressive strength of materials on the 1st and 28th days. When the expansion ratio was 15, the material surpassed all others in terms of compressive strengths on the 1st and 28th days, which were 3.15 and 10.34 MPa. Both values were above 1 MPa, the threshold strength required to support overlying rock [38, 39].

3.5.2. Effect of the Foam Dosage on the Material. Figure 7 presents the effect of the foam dosage on the solidification time and compressive strength. It is seen that the solidification time gradually lengthened as the dosage of foam gradually increased, and the compressive strengths on the 1st and 28th days both dropped dramatically with an increase in the foam dosage. The above results are explained as follows. As the dosage of foam increased, the dry density of the material gradually fell and the porosity grew [25]. The increasing number of closed pores in the material then reduced the compressive strength. The material therefore performed best when the foam had the same volume as the gel slurry.

3.6. Scanning Electron Microscopy. We mixed raw materials in the following proportions. The ratio of ordinary Portland

TABLE 10: Effect of expansion ratio on the material.

Sequence	Aggregate system			Water-cement ratio (%)	Foam		Gel slurry-foam ratio
	Cement (%)	SC (%)	Fly ash (%)		Foaming multiple	Dosage (mL)	
1	48	32	20	45	5.2	200	1
2	48	32	20	45	8.1	200	1
3	48	32	20	45	11.7	200	1
4	48	32	20	45	15.1	200	1
5	48	32	20	45	18.1	200	1

TABLE 11: Effect of the dosage of foam on the material.

Sequence	Aggregate system			Water-cement ratio (%)	Foam		Gel slurry-foam ratio
	Cement (%)	SC (%)	Fly ash (%)		Foaming multiple	Dosage (mL)	
1	48	32	20	45	15	200	1
2	48	32	20	45	15	400	0.5
3	48	32	20	45	15	800	0.25
4	48	32	20	45	15	1000	0.2
5	48	32	20	45	15	2000	0.1

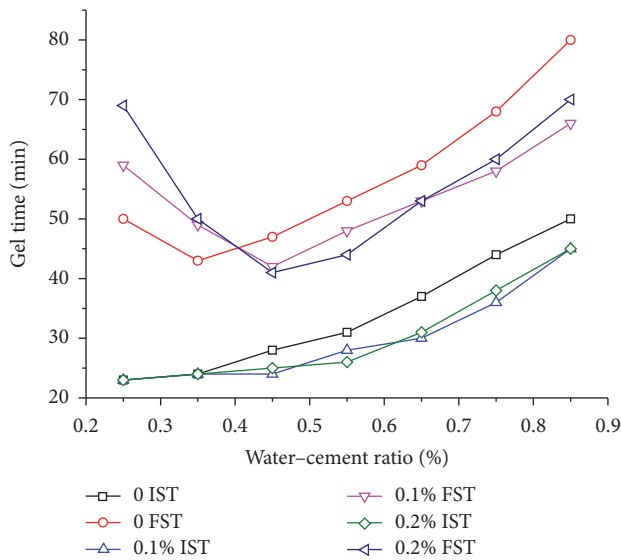


FIGURE 4: Effect of water-cement ratio and water reducer on gelling time.

cement to SC to fly ash in the aggregate system was 0.48:0.32:0.2; the water-cement ratio was 0.45; the water reducer content was 0.1%; the expansion ratio was 15; and there were equal volumes of foam and gelling slurry. We conducted scanning electron microscopy (SEM) after mixing the raw materials. Figures 8 and 9 show SEM images of the inorganic solidified foam filling material at different ages (1st and 28th days).

Figure 8 shows that the fly ash and spherical cement particles were wrapped up by reticular hydration structures on the first day. However, the shapes of fly ash and cement particles were still distinguishable, and the pores were filled with reticular structures. Meanwhile, the reticular structure on the 28th day was bonded with fly ash and cement particles

such that only a small amount of fly ash and few spherical cement particles were still visible.

Figure 9 shows the pore structure of the filling material at 60-fold magnification on the 28th day. The pores produced by the foaming agent were evenly distributed in the material, indicating that the strength of the foam filling material mainly depended on the pore structure and the bonding interface. The pore features were well suited to stopping leaks as most were smaller than 1 mm.

4. Engineering Applications

In 2014, the CO content on working face 31403 of the Halagou coal mine, Shengfu Dongsheng Coalfield, reached 1273 ppm. Examination and analysis revealed that the airtight wall of the Number 56 crossheading on the inlet side was not tightly closed and the surrounding coal body had cracked, resulting in spontaneous combustion of residual coal in the gob. We therefore performed an industrial test at the Halagou coal mine by sealing 20 crossheadings on the inlet side on working face 31405. The best way of detecting the effect of the airtight wall was to record the oxygen concentration in the gob. Using an XK-VI coal spontaneous combustion experiment bench, we obtained the minimum oxygen concentration for the spontaneous combustion of coal on working face 31405, which stands at 7.82%.

4.1. *Dimensions of the Crossheading.* Figure 10 is a sketch map of the crossheading, with a height of 4 m and width of 5.6 m. The crossheading was packed with 2 m of loess in the lower part and filled with 56.0 m³ of inorganic gelled foam cement in the upper part.

4.2. *Material Ratios.* The material ratios of the inorganic gelling material are as follows. The ratio of ordinary Portland cement to SC cement to fly ash in the aggregate system was

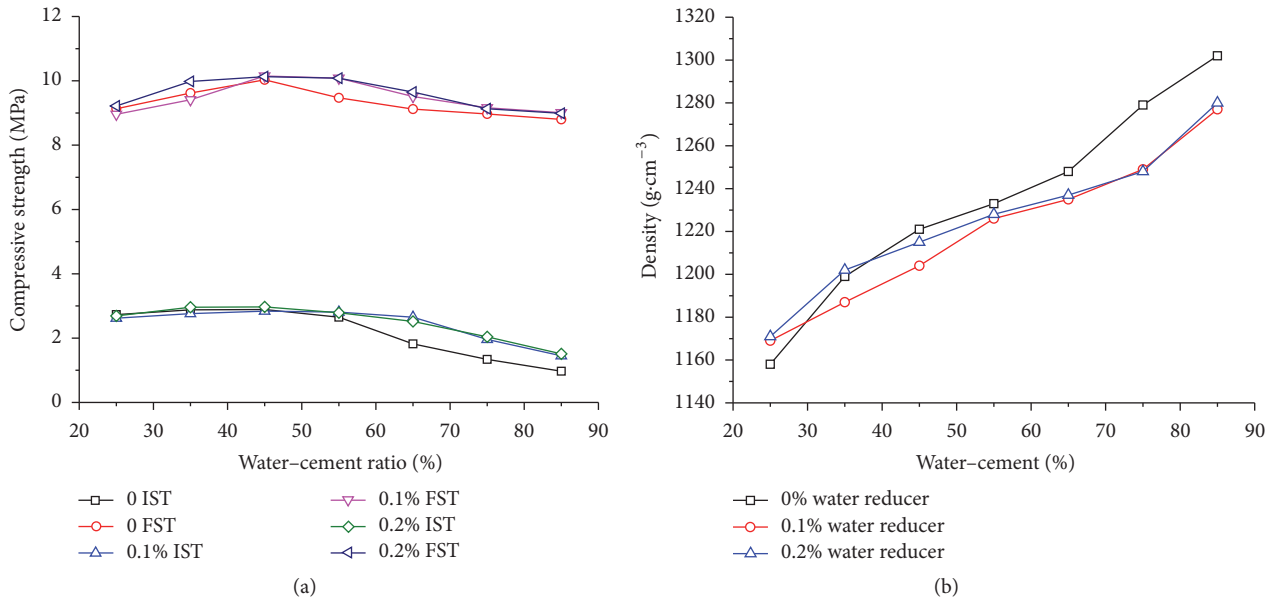


FIGURE 5: Effect of water-cement ratio and water reducer on compressive strength.

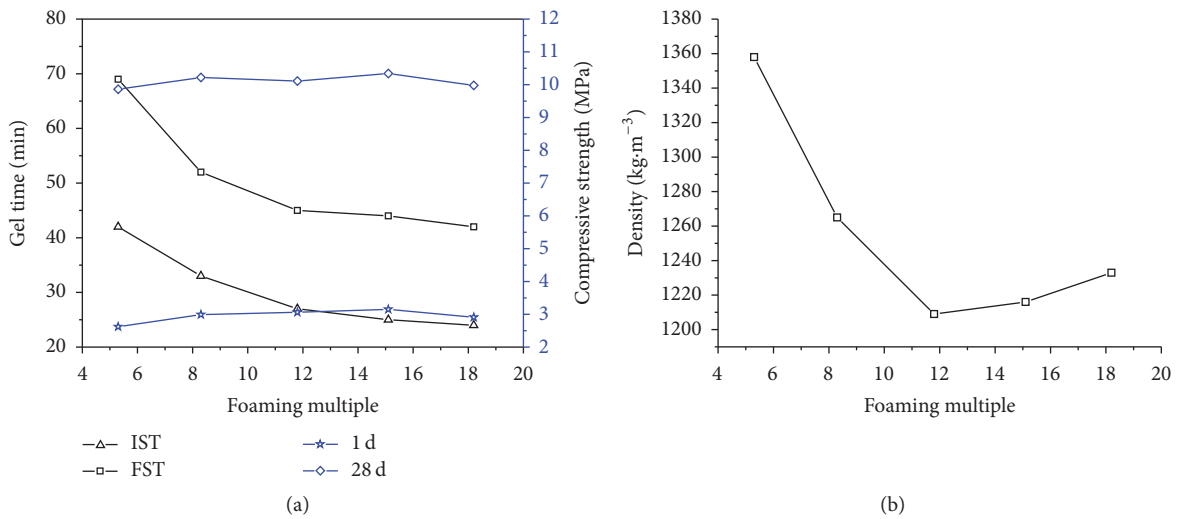


FIGURE 6: Effect of expansion ratio on the material.

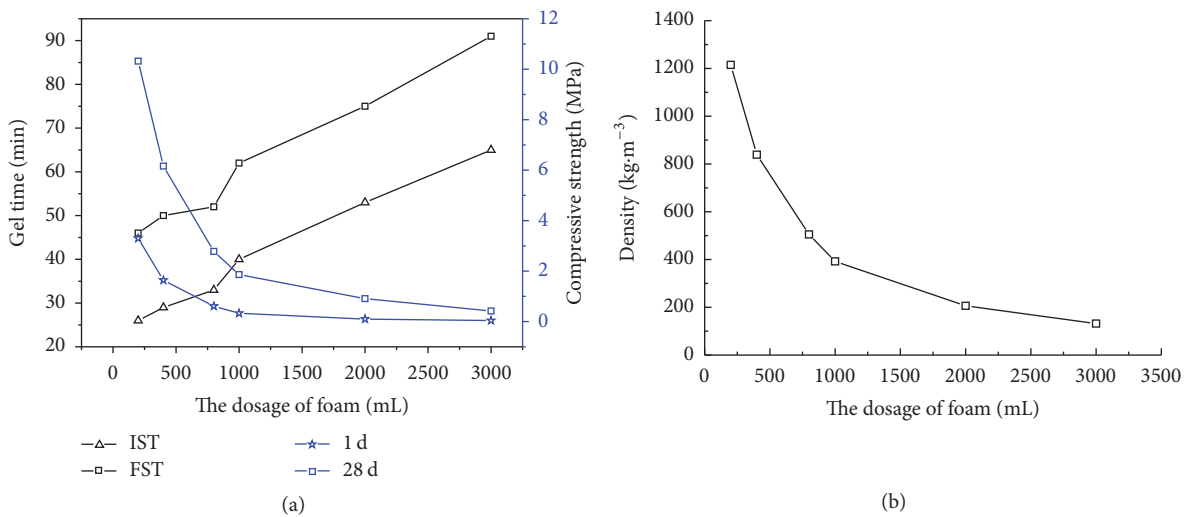


FIGURE 7: Effect of the dosage from foam on the material.

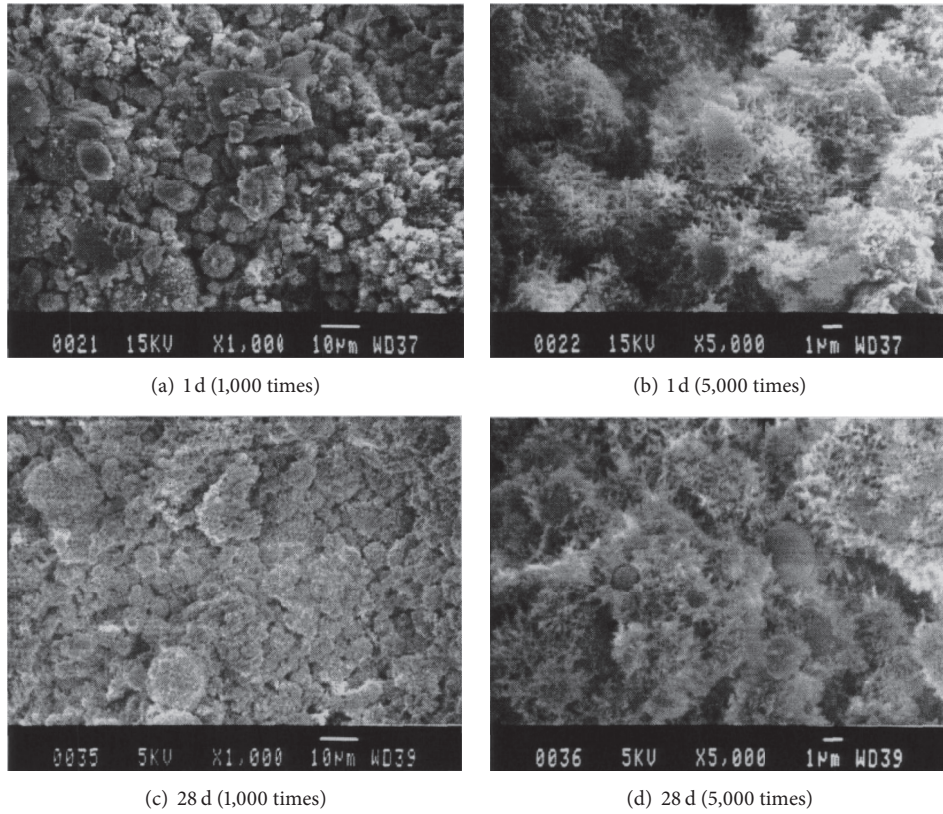


FIGURE 8: SEM scan grams on materials at different curing ages.

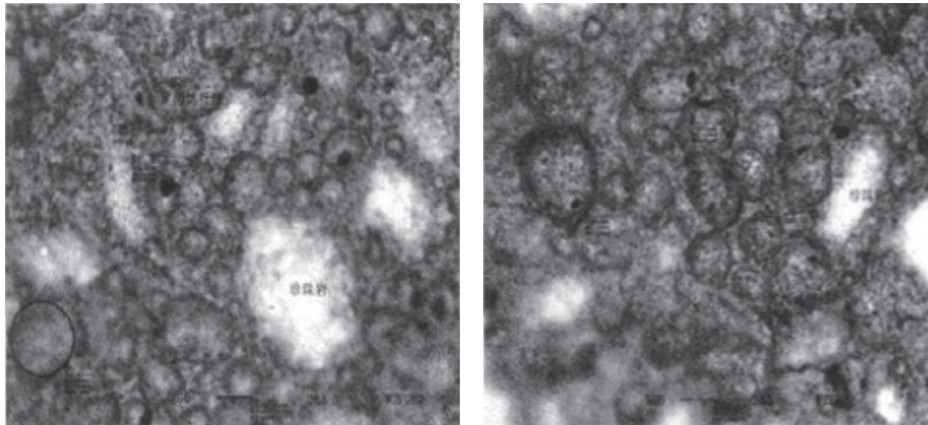


FIGURE 9: Pore structure of the filling material magnified by 60 times.

0.48:0.32:0.2; the water–cement ratio was 0.45; the water reducer content was 0.1%; the expansion ratio was 15; and there were equal volumes of foam and gelling slurry.

4.3. Grouting Equipment. On the basis of the performance of the filling material, we developed a special grouting machine, as shown in Figure 11. SC, fly ash, foam, and other raw materials were mixed in the ZMJ-F-type grout making machine and stirred into a foam slurry of a certain concentration. The slurry was pumped to seal the crossheading, and the slurry solidified after a period of time. The flow rate of

the foam slurry pump was $16 \text{ m}^3/\text{h}$ when the pressure was 0.6 MPa.

4.4. Filling Effect. Figure 12 shows how the external brick wall was removed to observe the filling effect after filling for 24 h. We found that the inorganic gelling foam cement had solidified; the inorganic gelling foam cement has well-known advantages, such as strength, airtightness, and being soundproof.

Figure 13 compares oxygen concentrations. After filling the 20 crossheadings with inorganic solidified gelling foam

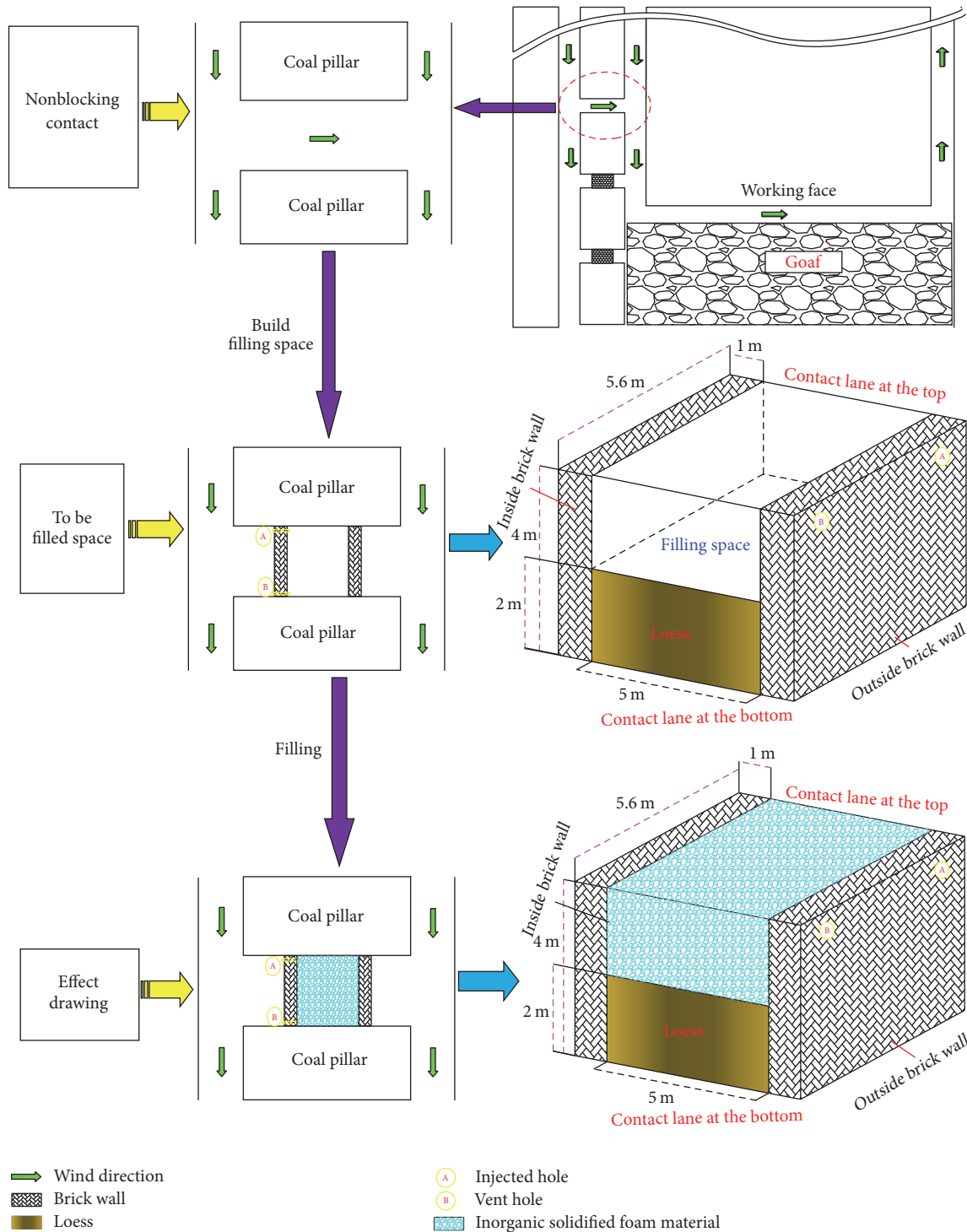


FIGURE 10: Sketch map of the grouting, filling, and sealing of the crossheading.

cement, we observed the oxygen concentration on the inlet side of the gob and compared the results with the oxygen concentration when loess was used as the filling material. After filling with foam cement material, the oxygen concentration at a point W that was 119.6 m from the working surface was 7.82%. In comparison, when loess was used to fill the

crossheading, the same oxygen concentration appeared at a point Q that was 233.8 m from the working surface. The distance between points W and Q was 114.2 m. This means that the inorganic foam cement filling material controlled effectively air leakage from the crossheadings to the gob and narrowed the width of the spontaneous combustion and

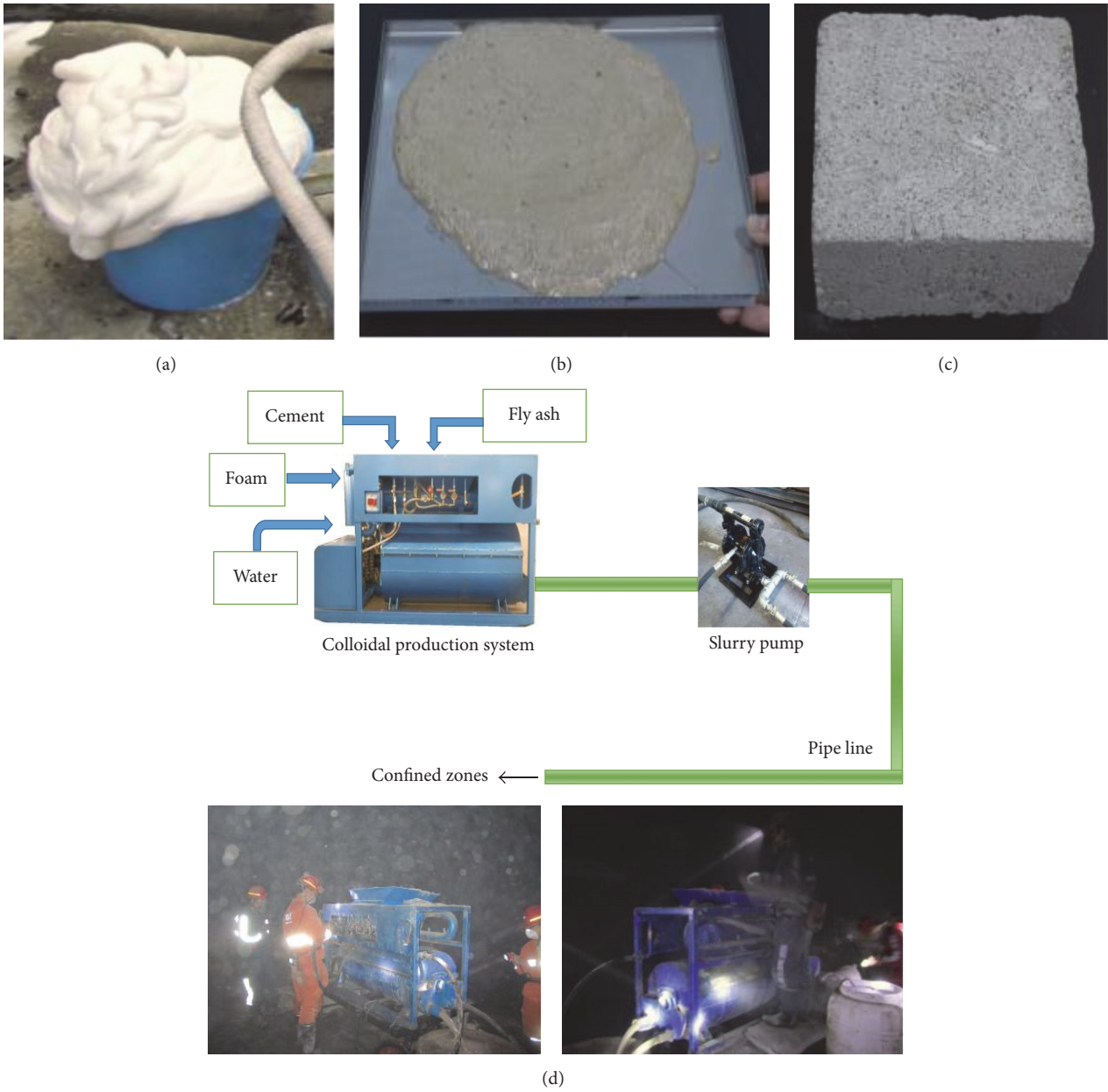


FIGURE 11: ZMJ-F grouting system: (a) foam, (b) foam slurry, (c) solidified filling material, and (d) inorganic foam filling equipment, including foam slurry production machine, transfer pump, and control system.

heat accumulation zone. Foam cement can therefore play an important role in preventing the spontaneous combustion of residual coal in the gob.

5. Conclusions

We conducted experiments to develop a type of inorganic solidified foam filling material for sealing crossheadings in coal mines and analyzed the effects of the dosage of SC, dosage of fly ash, water-cement ratio, expansion ratio, and foam dosage on the filling material.



FIGURE 12: The filling effect on mine.

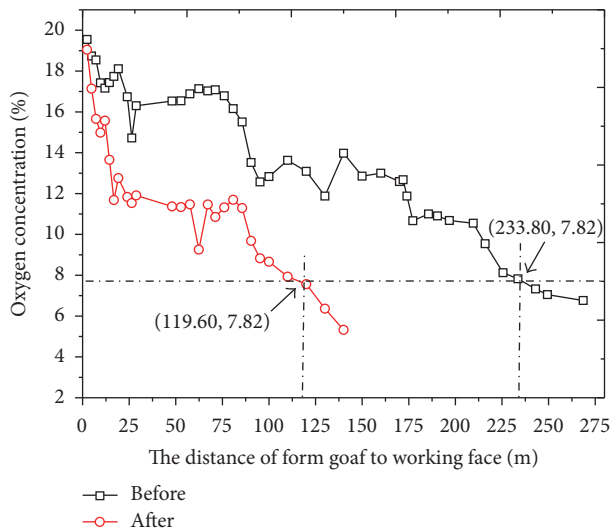


FIGURE 13: Comparison of oxygen concentrations. After: the oxygen concentration of the goaf after the crossheading was filled up with gelling foam cement material; before: the oxygen concentration of the goaf after the crossheading was filled up with loess.

The experimental results show that the solidification time shortened and the compressive strength grew with an increase in the content of SC. The fly ash dosage had little effect on the properties of the material if it was less than 20%, but the solidification time substantially lengthened if the dosage was greater than 20%. The compressive strength of the material on the 1st and 28th days decreased with an increase in the fly ash dosage. As the water–cement ratio increased, the initial setting time gradually lengthened. The final setting time shortened and then lengthened, and the compressive strength increased before decreasing. The solidification time shortened as the expansion ratio increased. However, the compressive strength did not vary after inorganic solidified foam filling material was added. With an increase in foam production, the solidification time increased and the compressive strength decreased exponentially.

On the basis of the experimental results, the best inorganic solidified foam filling material had a ratio of cement to SC to fly ash in the aggregate system of 0.48 : 0.32 : 0.20; a water–cement ratio of 0.45; a water reducer content of 0.10%; an expansion ratio of 15; and equal volumes of foam and gelling slurry.

We designed a special grouting machine to apply the filling material. The machine was air driven and easy to operate and relocate.

The field application demonstrated that the inorganic solidified foam filling material can seal crossheadings tightly and control the oxygen concentration in a gob effectively. As a kind of industrial waste, fly ash is readily available from thermal power plants in coal production regions. The proposed filling material therefore has broad application prospects owing to its low cost and suitability for large-area filling and plugging.

Conflicts of Interest

The authors declare that there are no conflicts of interest regarding the publication of this paper.

Acknowledgments

The present work was supported by the National Natural Science Foundation of China (Grants nos. U1361129 and 51504186) and China Postdoctoral Science Foundation (Program 2016-M-592820).

References

- [1] S. Dale, *Statistical Review of World Energy*, London, England, 2015.
- [2] The State Council of the People's Republic of China, "Medium and Long-term Development Plan for Energy (2004–2020), Beijing, China," 2004.
- [3] L. Lang and Z. Fu-bao, "A comprehensive hazard evaluation system for spontaneous combustion of coal in underground mining," *International Journal of Coal Geology*, vol. 82, no. 1-2, pp. 27–36, 2010.
- [4] S. Wang, K. Luo, X. Wang, and Y. Sun, "Estimate of sulfur, arsenic, mercury, fluorine emissions due to spontaneous combustion of coal gangue: an important part of chinese emission inventories," *Environmental Pollution*, vol. 209, pp. 107–113, 2015.
- [5] H. B. Sahu, S. S. Mahapatra, and D. C. Panigrahi, "An empirical approach for classification of coal seams with respect to the spontaneous heating susceptibility of Indian coals," *International Journal of Coal Geology*, vol. 80, no. 3-4, pp. 175–180, 2009.
- [6] S. Xue, B. Dickson, and J. Wu, "Application of 222Rn technique to locate subsurface coal heatings in Australian coal mines," *International Journal of Coal Geology*, vol. 74, no. 2, pp. 139–144, 2008.
- [7] O. I. Ogunsola and R. J. Mikula, "A study of spontaneous combustion characteristics of Nigerian coals," *Fuel*, vol. 70, no. 2, pp. 258–261, 1991.
- [8] C. Angle and N. Berkowitz, "Distribution of oxygen forms in Alberta low rank coals," *Fuel*, vol. 70, no. 7, pp. 891–896, 1991.
- [9] J. C. Jones, "Steady behaviour of long duration in the spontaneous heating of a bituminous coal," *Journal of Fire Sciences*, vol. 14, no. 2, pp. 159–166, 1996.
- [10] W. Bichler and L. Simon, "Phenolic resin foam for the sealing of loose hanging walls of mines," *Fuel and Energy Abstracts*, vol. 37, no. 4, p. 251, 1996.
- [11] S. L. Sarkar and J. Wheeler, "Important properties of an ultrafine cement-part I," *Cement and Concrete Research*, vol. 31, no. 1, pp. 119–123, 2001.
- [12] M. F. Gao, Q. L. Ma, Q. W. Lin, J. L. Chang, and H. Z. Ma, "Fabrication and adsorption properties of hybrid fly ash composites," *Applied Surface Science*, vol. 396, pp. 400–411, 2017.
- [13] J. Deng, Y. Xiao, J. Lu, H. Wen, and Y. Jin, "Application of composite fly ash gel to extinguish outcrop coal fires in China," *Natural Hazards*, vol. 79, no. 2, pp. 881–898, 2015.
- [14] A. Kesimal, B. Ercikdi, and E. Yilmaz, "The effect of desliming by sedimentation on paste backfill performance," *Minerals Engineering*, vol. 16, no. 10, pp. 1009–1011, 2003.
- [15] X. Yong-liang, W. De-ming, Z. Xiao-xing, T. Zhao-jun, and Q. Xu-yao, "Study of inhibition characteristic of sand suspending

- thickener for spontaneous combustion prevention,” in *Proceedings of the 6th International Conference on Mining Science and Technology (ICMST '09)*, pp. 336–340, October 2009.
- [16] B. T. Qin and Y. Lu, “Experimental research on inorganic solidified foam for sealing air leakage in coal mines,” *International Journal of Mining Science and Technology*, vol. 23, no. 1, pp. 151–155, 2013.
- [17] M. S. Yun and W. I. Lee, “Analysis of bubble nucleation and growth in the pultrusion process of phenolic foam composites,” *Composites Science and Technology*, vol. 68, no. 1, pp. 202–208, 2008.
- [18] X. Ni and N. E. Pereira, “Parameters affecting fluid dispersion in a continuous oscillatory baffled tube,” *AIChE Journal*, vol. 46, no. 1, pp. 37–45, 2000.
- [19] C. B. Sudhish, *Prevention and Combating Mine Fires*, Crc Press, Rotterdam, Netherlands, 2000.
- [20] G. J. Colaizzi, “Prevention, control and/or extinguishment of coal seam fires using cellular grout,” *International Journal of Coal Geology*, vol. 59, no. 1-2, pp. 75–81, 2004.
- [21] A. Sommer, *Foaming Agent for Making Cellular Concrete and Method of Making Same*, vol. 31, Hamburg-Wilhelsburg, Germany, 1964.
- [22] E. K. K. Nambiar and K. Ramamurthy, “Influence of filler type on the properties of foam concrete,” *Cement and Concrete Composites*, vol. 28, no. 5, pp. 475–480, 2006.
- [23] E. P. Kearsley and P. J. Wainwright, “The effect of high fly ash content on the compressive strength of foamed concrete,” *Cement and Concrete Research*, vol. 31, no. 1, pp. 105–112, 2001.
- [24] E. P. Kearsley and P. J. Wainwright, “Porosity and permeability of foamed concrete,” *Cement and Concrete Research*, vol. 31, no. 5, pp. 805–812, 2001.
- [25] E. P. Kearsley and P. J. Wainwright, “The effect of porosity on the strength of foamed concrete,” *Cement and Concrete Research*, vol. 32, no. 2, pp. 233–239, 2002.
- [26] E. P. Kearsley and P. J. Wainwright, “Ash content for optimum strength of foamed concrete,” *Cement and Concrete Research*, vol. 32, no. 2, pp. 241–246, 2002.
- [27] J. Jambor, “Pore structure and strength development of cement composites,” *Cement and Concrete Research*, vol. 20, no. 6, pp. 948–954, 1990.
- [28] T. Luping, “A study of the quantitative relationship between strength and pore-size distribution of porous materials,” *Cement and Concrete Research*, vol. 16, no. 1, pp. 87–96, 1986.
- [29] E. K. K. Nambiar and K. Ramamurthy, “Air-void characterisation of foam concrete,” *Cement and Concrete Research*, vol. 37, no. 2, pp. 221–230, 2007.
- [30] B. T. Qin and D. M. Wang, “Present situation and development of mine fire control technology,” *China Safety Science Journal*, vol. 12, no. 17, pp. 80–85, 2007.
- [31] Z. J. Feng, B. T. Qin, J. H. Wang, and J. P. Zhang, “Application of three phase foam fire extinguishing technology in Xinji Mine,” *Coal Engineering*, vol. 7, pp. 88–90, 2007.
- [32] H. Zhao and J.-S. Liu, “The feasibility study of extinguishing oil tank fire by using compressed air foam system,” in *Proceedings of the 2015 7th International Conference on Performance-Based Fire and Fire Protection Engineering (ICPFPE '16)*, vol. 135, pp. 61–66, December 2016.
- [33] “JG/T266-2011, Foamed concrete, The construction industry standard of the People’s Republic of China,” 2011.
- [34] M. R. Jones and A. McCarthy, “Utilising unprocessed low-lime coal fly ash in foamed concrete,” *Fuel*, vol. 84, no. 11, pp. 1398–1409, 2005.
- [35] G. M. Feng, Y. Ding, and H. J. Zhang, “Experimental research on a super high-water packing material for mining and its micromorphology,” *Journal of China University of Mining and Technology*, vol. 39, no. 6, pp. 814–818, 2010.
- [36] W. Zhao, Q. Zhu, and J. X. Zeng, “Fly ash-cement-based concrete performance test of the bubble,” *Sichuan Building Materials*, vol. 36, no. 4, pp. 28–29, 2010.
- [37] R. F. Feldman, G. G. Carette, and V. M. Malhotra, “Studies on mechanics of development of physical and mechanical properties of high-volume fly ash-cement pastes,” *Cement and Concrete Composites*, vol. 12, no. 4, pp. 245–251, 1990.
- [38] F. Cihangir, *Investigation of utilisation of alkali activated blast furnace slag as binder in paste backfill [Ph.D. thesis]*, Karadeniz Technical University, Trabzon, Turkey, 2011.
- [39] D. M. R. Stonr, “The optimization of mix designs for cemented rockfill,” in *Proceedings of the 5th Int. Symp. on Mining with Backfill Johannesburg (MINEFILL'93)*, pp. 249–253, SAIMM, 1993.

Research Article

An Investigation on Self-Compacting Concrete Using Ultrafine Natural Steatite Powder as Replacement to Cement

P. Kumar,¹ K. Sudalaimani,² and M. Shanmugasundaram³

¹Department of Civil Engineering, P.S.R. Engineering College, Sivakasi, Tamil Nadu 626140, India

²Department of Civil Engineering, Thiagarajar College of Engineering, Thiruparankundram, Madurai, Tamil Nadu 625015, India

³Structural Engineering Division, School of Mechanical and Building Sciences, VIT University, Chennai Campus, Chennai, Tamil Nadu 600127, India

Correspondence should be addressed to P. Kumar; kumarponnudurai.civil@gmail.com

Received 18 April 2017; Accepted 2 July 2017; Published 2 August 2017

Academic Editor: Prinya Chindapasirt

Copyright © 2017 P. Kumar et al. This is an open access article distributed under the Creative Commons Attribution License, which permits unrestricted use, distribution, and reproduction in any medium, provided the original work is properly cited.

An experimental investigation was made on flow properties and compressive strength of self-compacting concrete (SCC) with ultrafine natural steatite powder (UFNSP) as replacement to cement. The tests were conducted on specimens with 5%, 10%, 15%, 20%, and 25% of replacement of UFNSP to the weight of cement and compared to the control specimens. The flow properties of all specimens were tested and checked for their limit with the existing guidelines. The compressive strength test was done on all specimens for strength of 7 days, 14 days, 28 days, and 56 days. The hardened samples were tested for their microstructural behavior and the elements Mg, Ca, and Si were mapped. Through mapping, the formations of M-S-H along with C-S-H are observed. The results show that the addition of UFNSP influences the flow property, by reducing the flow, and increases the compressive strength till 20% replacement. Further the addition of UFNSP increases the denseness of microstructure of the specimens thus resulting in the strength increment.

1. Introduction

The self-compacting concrete (SCC), also known as self-consolidating concrete, is in the limelight for the last two decades in construction industry. Self-compacting concrete (SCC) is a concrete which can be placed and compacted into every corner of formwork purely by means of its self-weight by eliminating the need of external energy. So it does not require compaction at site or concrete plants. It has been developed in Japan to improve the durability and uniformity of concrete [1]. The mix composition is chosen to satisfy all performance criteria for the concrete in both the fresh and hardened states. To achieve this, fly ash and silica fume were used as mineral admixtures, and super plasticizers were used in mix as chemical admixtures for design of concrete. In this regard, mass of fine aggregate is typically equal or greater when compared to coarse aggregate. Selection of coarse aggregate size also has an impact on requirement of self-compacting concrete. The development of SCC and its results

on theoretical and experimental aspects were reviewed in various studies [2–4]. The methods of manufacturing of SCC initially had high content of paste; later on, researches were made to reduce the paste content and achieve strength [5, 6]. Due to the high content of water and voids, it has become important to look into the workability and segregation behavior of SCC [7, 8]. The important property of a SCC is to have workable and segregation resistant concrete which can flow through the reinforcement without any external vibrations or compactions [9]. The bond strength of reinforced bars and the SCC are higher when compared to that of normal concrete which also made the SCC more predominant material [10]. There were two types of usage of materials in SCC; one is as a pozzolanic replacement and the other one is filler. In this study ultrafine natural steatite powder (UFNSP) is used as cementitious replacement to cement. The steatite was used as insulators in ceramics, due to its high thermal resistivity. Its other major uses are in carving and sculpture industry. It is a proven durable raw material in refractory industry. In

TABLE 1: Properties of UFNSP.

	UFNSP	Cement
Physical properties		
Blaine surface area (m ² /Kg)	750	380
Particle mean Dia (μm)	<5	<32
Density	2.7	3.1
Loss of ignition	3.33%	2%
Chemical properties		
SiO ₂	62.67%	23%
Al ₂ O ₃	0.24%	4.20%
MgO	33.26%	0.20%
Fe ₂ O ₃	0.30%	1.20%
CaO	0.20%	62%

terms of steatite the grinded powder was already proved to be good replacement to cement until 15% [11, 12]. Durability and strength of concrete increase with replacement of steatite powder to certain limit [12–14]. The phase of steatite is crystalline which belongs to magnesium metasilicate from talc mineral based on the following reaction [15]:



And this reaction supports the M-S-H formation. Generally the earlier studies show that the M-S-H gel has amorphous phase [11, 12]. The magnesium-rich binders can lead to low pH binding system which has wide range of applications in adverse concreting condition, and also this magnesium richness leads to early strength development and durability [16]. The present proposal will cover the area on development of SCC based on magnesium-rich steatite powder replacement and its mechanical behavior.

2. Materials, Mix Proportions, and Experimental Investigation

2.1. Materials Used in This Study. Ordinary Portland cement of grade 43 conforming to Indian Standard (IS) 12269-1987 was used and the properties were listed in Table 1. The UFNSP of less than 5 microns similar to that of earlier studies [11–14] is used and the physical and chemical properties were presented in Table 1. UFNSP was used as pozzolanic replacement in this study. The river sand procured from Tamil Nadu Minerals Limited (TAMIN) with the specific gravity of 2.65 and passing through 2.36 mm sieve was used. Crushed granite was used as coarse aggregate with a maximum nominal size of 12 mm and bulk density of 1640 kg/m³. The normal potable water was used for mixing and curing process. Polycarboxylic ether based superplasticizer sky 8233 and viscosity modifier, Mastermatrix VMA 362, were used in this study as admixtures to maintain the workability.

2.2. Mix Proportion. The mix proportion was finalized based on trial and error process conforming to the EFNARC guidelines [17], and the target strength to be achieved was fixed as 25 MPa. The ratio of powder : fine aggregate : coarse

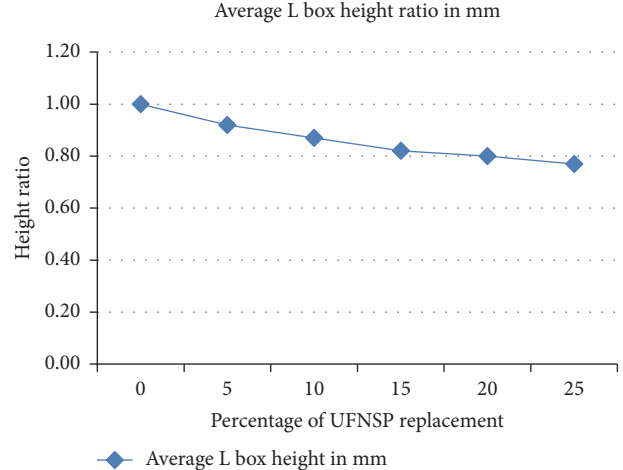


FIGURE 1: Results on L box test.

aggregate was maintained as 1:1.8:1.9. The water/powder ratio was fixed as 0.8 [17]. To achieve the workability 2% superplasticizer and 0.4% viscosity modifier were added, and the addition was carried out with respect to weight of cement.

2.3. Experimental Investigation. The workability and flow properties of the fresh concrete were examined by L box test, J-ring test, V-funnel flow test, slump flow test, and T50 flow timing conforming to EFNARC guidelines [17]. The compressive strength of the hardened specimens was tested on cubes of size 150 mm × 150 mm × 150 mm conforming to specification of Indian Standard (IS) 10086: 1982 and the tests were carried out in accordance with IS 516: 1959 (reaffirmed 2004) in hydraulic compression testing machine of 2000 kN capacity. The microstructural behavior of the specimens is studied by scanning electron microscopy. Samples for scanning electron microscopy (SEM) analysis are taken near the surface (0-1 mm depth) of specimens. Microstructural studies utilized SEM (ZEISS) equipped with EDAX analyzer for microstructural observations of the surfaces, which is coated with evaporated copper for examination. SEM analysis is done at a maximum magnification of 1000x with energy 20 keV and a high resolution of 3.5 nm. For this analysis, samples of size 10 mm cubes were cut with a saw cutter.

3. Results and Discussion

The results were observed on the fresh and hardened state of concrete. The tests were carried out to ascertain the flow properties of fresh concrete, compressive strength on hardened concrete, and its respective microstructural behavior.

3.1. Workability and Flow Properties of Fresh Concrete. The results for “L” box test were presented in Table 2 and Figure 1. The results show that the addition of UFNSP as replacement to cement increases the water requirement by reducing the height ratio. The average value of “L” box height for 25% UFNSP replacement crosses the safe limit of EFNARC permissible limit. In comparison with the control

TABLE 2: Results on flow properties of fresh concrete.

S. number	Mix Ids	Percentage replacement of UFNSP	Average L box height ratio	Average J-ring height (mm)	Average V-funnel flow time in sec	Average slump flow diameter in mm	Average T50 cm slump flow in sec
1	SCCCS	0	1.00	7.88	7.90	710.00	2.60
2	SCC5	5	0.92	7.93	9.20	700.00	2.70
3	SCC10	10	0.87	8.23	9.50	680.00	3.20
4	SCC15	15	0.82	8.45	10.40	672.00	4.00
5	SCC20	20	0.80	8.73	11.20	650.00	4.50
6	SCC25	25	0.77	9.33	11.80	630.00	5.00

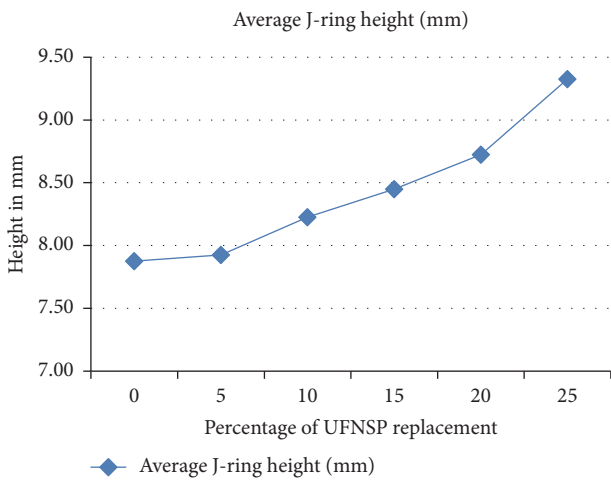


FIGURE 2: Results on J-ring test.

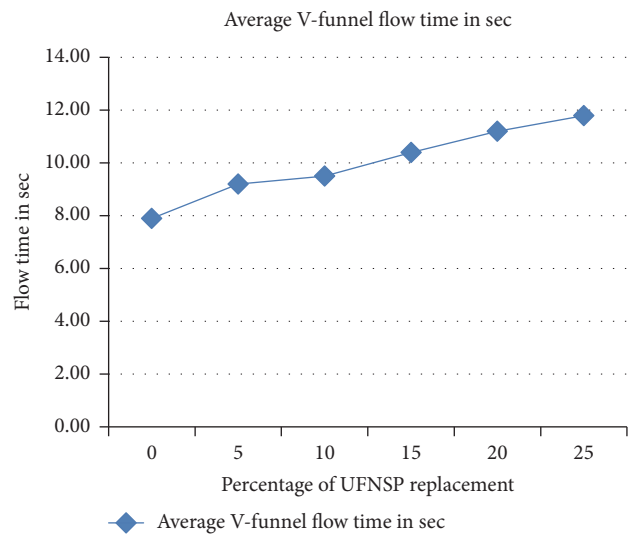


FIGURE 3: Results on V-funnel flow test.

specimen (SCCCS), specimens SCC5, SCC10, SCC15, SCC20, and SCC25 lose their height ratio by 8%, 13%, 18%, 20%, and 23%, respectively. The results show that there was a sudden reduction in height ratio between 0 and 15% replacements and then the ratio gets stabilized and this is due to the fact that after certain percentage of replacement the cement UFNSP reaction was lesser.

The results on J-ring test on fresh self-compacting concrete were presented in Table 2 and Figure 2. The test results shows that the height of fresh concrete in J-ring rises by 0.63%, 4.4%, 7.3%, 10.79%, and 18.41% for the specimens SCC5, SCC10, SCC15, SCC20, and SCC25, respectively, in comparison with SCCC. From Figure 2 it was observed that height increment is not notable for specimen with 5% of UFNSP replacement. From 5% to 20% of UFNSP replacement the height gradually increases from 7.93 mm to 8.73 mm; with the replacement of 25% the height gets a steep increase to 9.33 mm. Even though the height rises the values were within the permissible limit which is 0–10 mm.

The results on “V”-funnel test on fresh self-compacting concrete specimens were presented in Table 2 and Figure 3. The results show that the time period for flow of fresh concrete through the “V”-funnel increases as the replacement percentage of UFNSP increases. The minimum time is observed at SCCC specimen with flow period as 7.90 seconds and maximum time period for flow was observed

at SCC25 with 11.80 seconds. The flow timing increases almost linearly which can be observed from Figure 3. The flow period for SCC5, SCC10, SCC15, SCC20, and SCC25 increases by 16.46%, 20.25%, 31.65%, 41.77%, and 49.37% in comparison to SCCC specimen. The values lie well within the permissible limit for a typical self-compacting concrete. The actual permissible limit given by EFNARC is 0–25 Sec.

The slump flow values and the corresponding T50 cm test results were presented in Table 2 and Figures 4 and 5. The results show that the slump value reduces as the percentage replacement of UFNSP increases, which shows the UFNSP has an impact on the workability of SCC. The SCCC specimen has the maximum value as observed by the other tests earlier and the lowest value was observed at SCC25 measuring 630 mm. The flow of SCC5, SCC10, SCC15, SCC20, and SCC25 reduces by 1.41%, 4.23%, 5.35%, 8.45%, and 11.27% with reference to SCCC. The time period of flow for T50 test was presented in Figure 5. The time for spreading increases and the time for SCC25 is longer with its value as 5 sec. As the addition of UFNSP reduces the workability, the flow gets affected and hence the delay in spreading occurs. The spreading time increases as 3.85%, 23.08%, 53.85%, 73.08%, and 92.31% for SCC5, SCC10, SCC15, SCC20, and SCC25 in comparison with SCCC. Even though

TABLE 3: Compressive strength of hardened concrete cubes.

S. number	Mix Ids	Average compression strength in MPa			
		7 days	14 days	28 days	56 days
1	SCCCS	21.80	25.27	26.60	26.90
2	SCC5	27.95	31.20	32.50	32.65
3	SCC10	31.50	33.61	34.30	34.40
4	SCC15	34.20	35.90	36.20	36.30
5	SCC20	29.07	31.01	32.30	32.37
6	SCC25	22.80	25.44	26.50	26.80

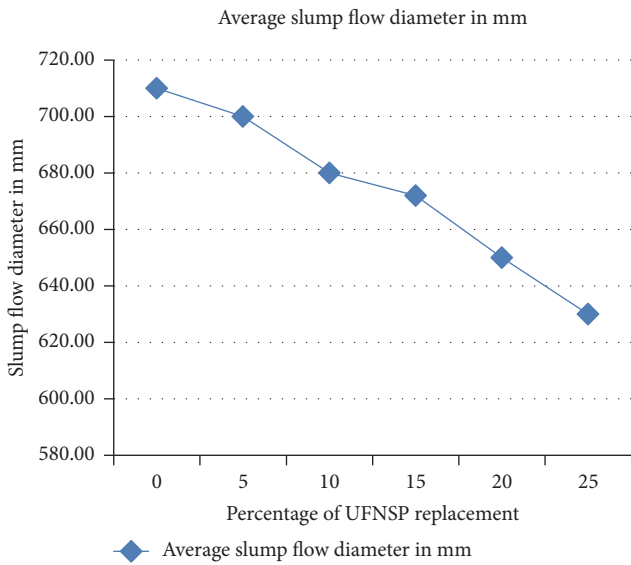


FIGURE 4: Results on slump flow test.

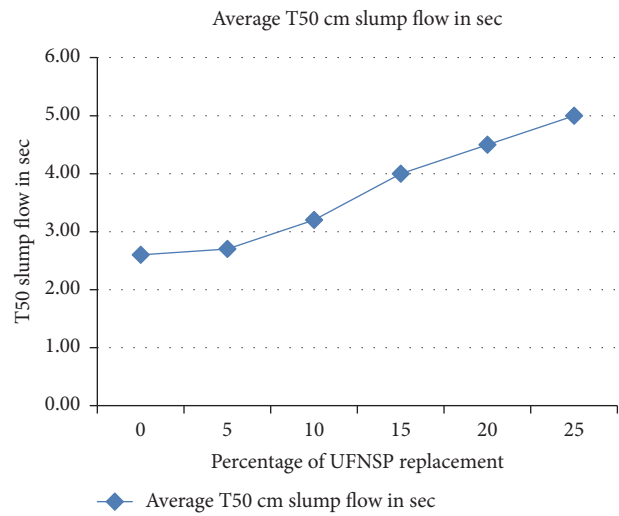


FIGURE 5: Results on T50 slump flow test.

the slump value decreases and the T50 test time increases the values are all well within the limit and show typical self-compacting concrete characteristics as indicated by EFNARC guidelines.

The observations shows that the water requirement was more in samples with UFNSP as replacement, and this is due to the fact that the M-S-H binder matrix with MgO presence has large water requirement due to texture, size, and shape of the particles [18]. This higher water requirement is also due to the reactive magnesia [19], a part in the UFNSP. From the tests on workability, even though it was observed that the replacement of UFNSP reduces the flow, almost all specimen lies within the typical limit as specified by EFNARC, and hence the replacement can be done until 25% without any effect on SCC limiting values.

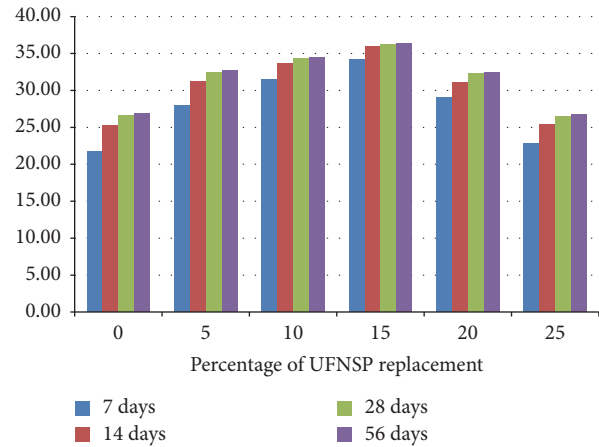


FIGURE 6: Results on average compressive strength test on 28 days.

3.2. Compressive Strength on Hardened Concrete at Various Ages. The compressive strength is tested on hardened concrete and the results are presented in Table 3 and Figure 6. The results show that at early ages all the replacement specimens show higher strength gain than the control specimens. The strength attainment of SCCCS, SCC5, SCC10, SCC15, SCC20, and SCC25 was 82%, 86%, 92%, 94%, 90%, and 86%,

respectively, on 7 days and 95%, 96%, 98%, 99%, 97%, and 95% on 14 days. Through this, the SCC5 and SCC10 specimens are attaining 90% and above of designed strength on 7 days, which may be a notable parameter. The 7 days' test shows that the SCC5, SCC10, SCC15, SCC20, and SCC25 has strength increment of about 28.21%, 44.50%, 56.88%, 33.35%, and 4.59%, respectively, when compared to SCCCS. From the

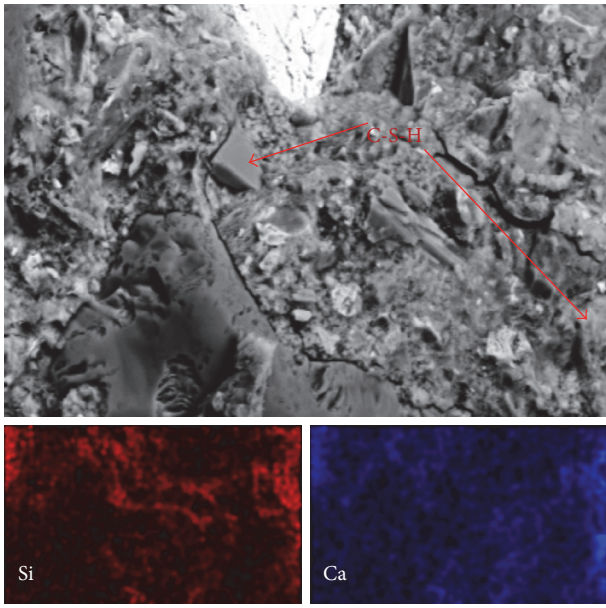


FIGURE 7: SEM image and its EDAX mapping on Si, Mg, and Ca of control specimen (CS).

results on 14 days' test it was evident that the SCC5, SCC10, SCC15, SCC20, and SCC25 have strength increment of about 23.47%, 33.30%, 42.07%, 22.71%, and 0.67%, respectively, in comparison with SCCCS. The 28 days' compressive strength for SCC5, SCC10, SCC15, and SCC20 has strength gain of about 22.18%, 28.95%, 36.09%, and 21.43%, respectively. The SCC25 specimens have a strength reduction of about 0.38% on 28 days in comparison with SCCCS. The 56 days' compressive strength for SCC5, SCC10, SCC15, and SCC20 has strength gain of about 21.38%, 27.88%, 34.94%, and 20.33%, respectively. The SCC25 specimens have a strength reduction of about 0.37% on 56 days in comparison with SCCCS. Through the observations it was evident that until 14 days the strength of all replacement specimens increases. From 28 days the strength of SCC25 is almost similar to that of SCCCS and there is very little strength loss for SCC25 on 28 and 56 days' tests. The strength gain is due to the presence of right proportion of M-S- and C-S-H [20]. The concrete attains its strength through the UFNSP; the reason behind this is the presence of Mg and reduced particle size of UFNSP, which facilitates the intrusion of particle in cement matrix [11-14]. The higher hydration rate is the main cause of early age strength attainment [21]. From the result it was clear that the strength attainment can be achieved until 20% replacement. The specimen with 25% UFNSP replacement is almost equal to and little lesser than SCCCS specimens on 28 days and 56 days.

3.3. Microstructure and Elemental Mapping on 56 Days' Hardened Specimens. The scanning electron microscopy analysis on the microstructure of the concrete specimen at 56 days and its relevant mapping for silica (Si), magnesium (Mg), and Calcium (Ca) of those specimens are presented through Figures 7-12. The elemental EDAX mapping is carried out

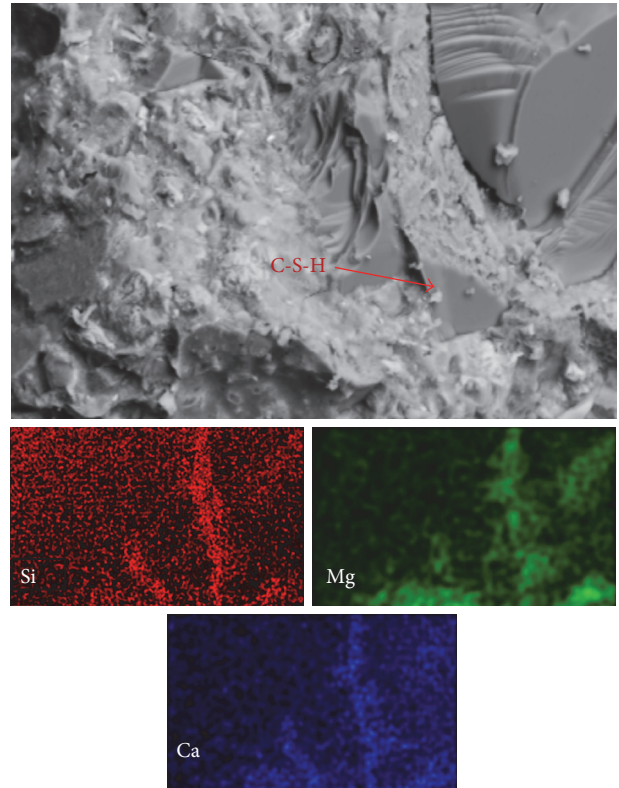


FIGURE 8: SEM image and its EDAX mapping on Si, Mg, and Ca of SCC-5.

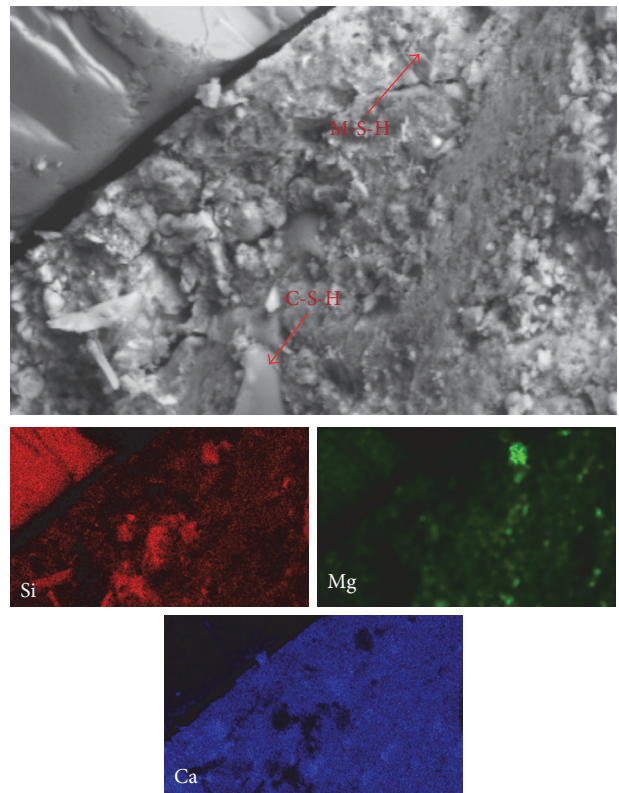


FIGURE 9: SEM image and its EDAX mapping on Si, Mg, and Ca of SCC-10.

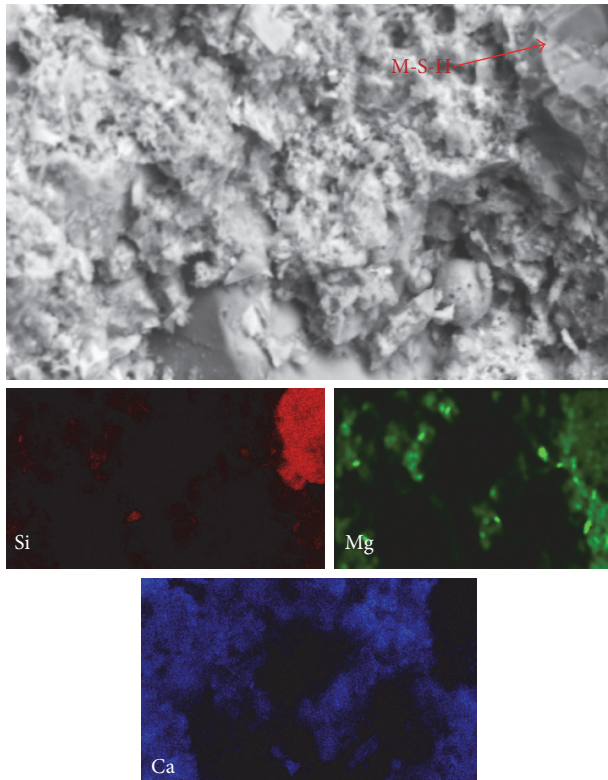


FIGURE 10: SEM image and its EDAX mapping on Si, Mg, and Ca of SCC-15.

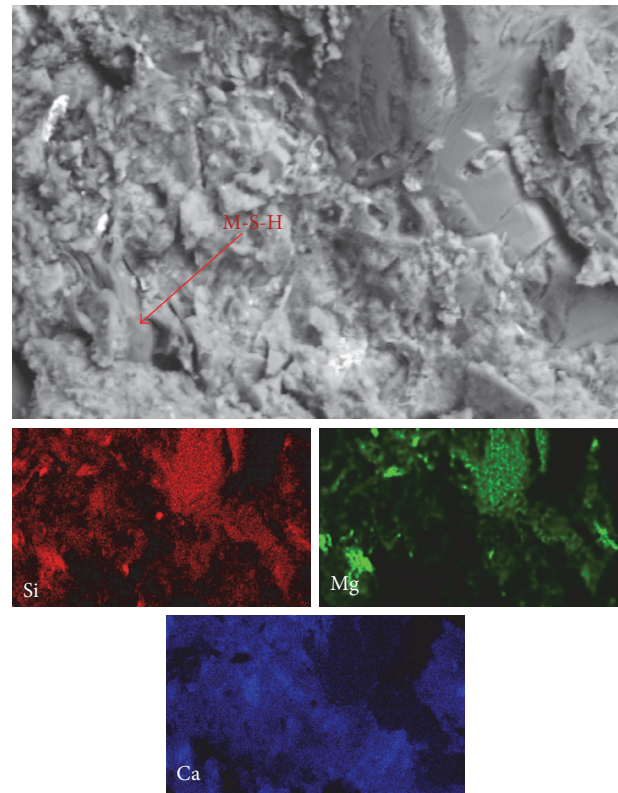


FIGURE 12: SEM image and its EDAX mapping on Si, Mg, and Ca of SCC-25.

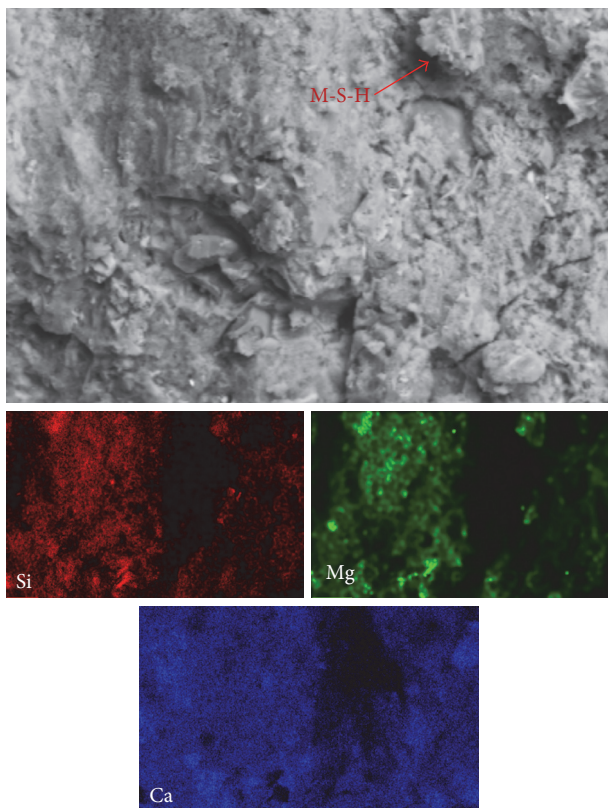


FIGURE 11: SEM image and its EDAX mapping on Si, Mg, and Ca of SCC-20.

to ascertain whether the addition of UFNSP has genuine effect on the strength development. The microstructural evolution was observed to be similar on all samples. Figure 7 shows the microscopy image of control specimen and its relevant mapping. This shows conventional specimen has no traces of magnesium elements. The formation of calcium silicate hydrates is noted. Figure 8 shows the images of SCC5 specimen has the traces of C-S-H along with M-S-H. The presence of magnesium is very limited when compared to calcium and this is due to the lesser replacement of UFNSP. The microscopy and mapping images were shown in Figure 9, and it is observed that the denseness of M-S-H formation is increasing and it is validated through the mapping, and a possible trace of magnesium hydroxide is also noted. Figure 10 shows the results of SCC15, and it is observed that the formation of M-S-H is more prominent and denser. The solidity of the magnesium silicate has increased widely in comparison with the specimens earlier, and also few spots of free calcium are traced which may cause a break point on strength gain. The maximum strength is observed at SCC15 which is to be noted at this point. Figure 11 shows the result images for SCC20 specimen and it shows large formation of magnesium silicate along with the calcium silicates, and the microstructure indicates positive attainment of microstructural evolution of control specimen, but not in comparison with SCC15 specimen. Figure 12 shows the microscopy and mapping images of SCC25 specimens; the microstructure of SCC25 was almost similar to that of SCCCS specimens.

In SCC25 it is noted that the magnesium silicates tend to break down to tiny M-S-H crystal which is identified through mapping, and this phenomenon causes the major strength reduction which is not observed in earlier specimens. In all the specimens it is noted that both magnesium based hydration products and calcium based hydration products have a vital role in establishing the strength gain.

From the above observations it can be ascertained that magnesium and magnesium based products are stable in all specimens, and it is also shown that when water exhausts the reaction of components end thus stabilizes its microstructure and attains early age strength in case of replacement up to 20%, this reaction product takes up space around magnesium compounds thus giving denser structure [22]. The magnesium based hydration products were found to be present in regions devoid of other elements, suggesting the presence of Mg crystals [23]. The observation shows that the M-S-H was less crystalline as observed and when this becomes more crystalline then the strength gain is reduced [24]. The process of increasing the $Mg(OH)_2$ and other magnesium hydration products improve the mechanical strength and specimen's microstructure as it is observed [21]. The addition of UFNSP has induced the magnesium based hydration products, and the results were little bit contrary to earlier studies [12, 13]. The contradiction is due to the increased water usage in current study through which the brucite development is accommodated in the pores. In this study as there are larger voids due to the higher water content and other admixtures, the $Mg(OH)_2$ which is higher in density than that of $Ca(OH)_2$ gets enough space to accommodate itself hence paving the way to good strength and microstructure, even at 25% replacement, which was not so in earlier studies [11, 12]. From the above study it can be ascertained that the usage of UFNSP will enhance the strength parameters and denser microstructural bond. The replacement percentage of UFNSP shall be maintained at 15% for maximum strength attainment, but still the 25% replacement gives strength similar to control specimen which shows that the replacement shall be carried out up to 25%.

4. Conclusions

From the present study it can be concluded that the replacement of UFNSP in self-compacting concrete system can have an influence on the workability, flow of fresh concrete, compressive strength of hardened concrete, and microstructural properties. There was decrease in flow properties of SCC with increase in addition of UFNSP. The entire replacement percentage exhibits safer limit for the SCC, but the specimens with 25% of UFNSP replacement reach the limit where the typical limit ends, which confirms that further replacement is not possible in terms of flow properties. The early age strength attainment is seen in samples SCC5, SCC10, SCC15, and SCC20 even on 7 days' test where more than the target strength is achieved. The maximum strength is achieved in SCC15 specimens. The strength enhancement is seen on all replacement specimens, wherein the strength of SCC25 specimens is almost equal to that of SCCCS. The microstructures of SCC10, SCC15, and SCC20 are denser and show

denser magnesium hydroxide which has an effect on strength improvement. Further magnesium and silicate are mapped, which shows the dispersion over the surface and forms denser structures. The reduced strength of SCC25 is due to the higher magnesium content. From the investigation and discussion it is concluded that the replacement of UFNSP should be maintained below 20% and the UFNSP will enhance the strength parameters of the SCC.

Conflicts of Interest

The authors declare that there are no conflicts of interest regarding the publication of this paper.

References

- [1] H. Okamura and M. Ouchi, "Self-compacting concrete," *Journal of Advanced Concrete Technology*, vol. 1, no. 1, pp. 5–15, 2003.
- [2] H. J. H. Brouwers and H. J. Radix, "Self-compacting concrete: Theoretical and experimental study," *Cement and Concrete Research*, vol. 35, no. 11, pp. 2116–2136, 2005.
- [3] P. L. Domone, "Self-compacting concrete: An analysis of 11 years of case studies," *Cement and Concrete Composites*, vol. 28, no. 2, pp. 197–208, 2006.
- [4] P. L. Domone, "A review of the hardened mechanical properties of self-compacting concrete," *Cement and Concrete Composites*, vol. 29, no. 1, pp. 1–12, 2007.
- [5] N. Su, K.-C. Hsu, and H.-W. Chai, "A simple mix design method for self-compacting concrete," *Cement and Concrete Research*, vol. 31, no. 12, pp. 1799–1807, 2001.
- [6] N. Su and B. Miao, "A new method for the mix design of medium strength flowing concrete with low cement content," *Cement and Concrete Composites*, vol. 25, no. 2, pp. 215–222, 2003.
- [7] M. F. Granata, "Pumice powder as filler of self-compacting concrete," *Construction and Building Materials*, vol. 96, pp. 581–590, 2015.
- [8] EFNARC, *Specifications and Guidelines for Self-compacting Concrete*, Association House, Surrey, UK, 2002.
- [9] E. Güneş, M. Geşoğlu, S. Al-Rawi, and K. Mermerdaş, "Effect of volcanic pumice powder on the fresh properties of self-compacting concretes with and without silica fume," *Materials and Structures/Materiaux et Constructions*, vol. 47, no. 11, pp. 1857–1865, 2014.
- [10] N. Verma and A. K. Misra, "Bond characteristics of reinforced TMT bars in self compacting concrete and normal cement concrete," *Alexandria Engineering Journal*, vol. 54, no. 4, pp. 1155–1159, 2015.
- [11] M. Shanmugasundaram and K. Sudalaimani, "An investigation on high performance concrete with ultra fine natural steatite powder," *Information*, vol. 17, no. 6 A, pp. 2267–2277, 2014.
- [12] K. Sudalaimani and M. Shanmugasundaram, "Influence of ultrafine natural steatite powder on setting time and strength development of cement," *Advances in Materials Science and Engineering*, vol. 2014, Article ID 532746, 6 pages, 2014.
- [13] M. Shanmugasundaram, S. Karthiyaini, and K. Sudalaimani, "Influence of ultrafine natural steatite powder on strength and permeability of high performance concrete," *International Journal of Applied Engineering Research*, vol. 10, no. 18, pp. 38967–38971, 2015.

- [14] M. Shanmugasundaram, R. Premkumar, R. Abinaya, KG. Arunya, M. Gowsalya, and M. Malathy, *A new cement free binding material based on steatite powder activated through alkaline solution*, Master Builder, 2016.
- [15] E. Vela, M. Peiteado, F. García, A. C. Caballero, and J. F. Fernández, "Sintering behaviour of steatite materials with barium carbonate flux," *Ceramics International*, vol. 33, no. 7, pp. 1325–1329, 2007.
- [16] T. Zhang, L. J. Vandeperre, and C. R. Cheeseman, "Formation of magnesium silicate hydrate (M-S-H) cement pastes using sodium hexametaphosphate," *Cement and Concrete Research*, vol. 65, pp. 8–14, 2014.
- [17] EFNARC, *Specification and Guidelines for Self-Compacting Concrete*, European Federation of Producers and Applicators of Specialist Products for Structures, 2002.
- [18] H. Tran and A. Scott, "Strength and workability of magnesium silicate hydrate binder systems," *Construction and Building Materials*, vol. 131, pp. 526–535, 2017.
- [19] W. R. EUBANK, "Calcination Studies of Magnesium Oxides," *Journal of the American Ceramic Society*, vol. 34, no. 8, pp. 225–229, 1951.
- [20] T. Zhang, L. J. Vandeperre, and C. R. Cheeseman, "Magnesium-silicate-hydrate cements for encapsulating problematic aluminium containing wastes," *Journal of Sustainable Cement-Based Materials*, vol. 1, no. 1-2, pp. 34–45, 2012.
- [21] C. Wu, W. Chen, H. Zhang et al., "The hydration mechanism and performance of Modified magnesium oxysulfate cement by tartaric acid," *Construction and Building Materials*, vol. 144, pp. 516–524, 2017.
- [22] H. Ma, B. Xu, and Z. Li, "Magnesium potassium phosphate cement paste: degree of reaction, porosity and pore structure," *Cement and Concrete Research*, vol. 65, pp. 96–104, 2014.
- [23] S. L. Sarkar, "X-ray mapping - A supplementary tool in clinker phase characterization," *Cement and Concrete Research*, vol. 14, no. 2, pp. 195–198, 1984.
- [24] C. Roosz, S. Grangeon, P. Blanc et al., "Crystal structure of magnesium silicate hydrates (M-S-H): The relation with 2:1 Mg-Si phyllosilicates," *Cement and Concrete Research*, vol. 73, pp. 228–237, 2015.

Research Article

Compression Behavior of Confined Columns with High-Volume Fly Ash Concrete

Sung-Won Yoo,¹ Young Cheol Choi,² and Wonchang Choi²

¹Department of Civil and Environmental Engineering, Gachon University, Seongnam-si, Gyeonggi-do 13120, Republic of Korea

²Department of Architectural Engineering, Gachon University, Seongnam-si, Gyeonggi-do 13120, Republic of Korea

Correspondence should be addressed to Wonchang Choi; wonchang.choi@gmail.com

Received 10 May 2017; Accepted 18 June 2017; Published 30 July 2017

Academic Editor: Prinya Chindaprasirt

Copyright © 2017 Sung-Won Yoo et al. This is an open access article distributed under the Creative Commons Attribution License, which permits unrestricted use, distribution, and reproduction in any medium, provided the original work is properly cited.

The use of fly ash in ordinary concrete provides practical benefits to concrete structures, such as a gain in long-term strength, reduced hydration heat, improved resistance to chloride, and enhanced workability. However, few studies with high-volume fly ash (HVFA) concrete have been conducted that focus on the structural applications such as a column. Thus, there is a need to promote field applications of HVFA concrete as a sustainable construction material. To this end, this study investigated the compressive behavior of reinforced concrete columns that contain HVFA with a 50 percent replacement rate. Six columns were fabricated for this study. The study variables were the HVFA replacement rate, tied steel ratio, and tie steel spacing. The computed ultimate strength by the American Concrete Institute (ACI) code conservatively predicted the measured values, and, thus, the existing equation in the ACI code is feasible for confined RC columns that contain HVFA. In addition, an analysis model was calibrated based on the experimental results and is recommended for predicting the stress-strain relationship of confined reinforced concrete columns that contain HVFA.

1. Introduction

Fly ash is an industrial byproduct of the electrical power industry. Recently, partially recycled fly ash has been used as supplementary cementitious material in the cement industry. Fly ash content that is less than 25 percent of the total cementitious content is now commonly used in concrete mixtures due to its apparent benefits for concrete, such as a gain in long-term strength, reduced hydration heat, improved resistance to chloride, and enhanced workability [1–4]. On a limited basis, an increase up to a 100 percent fly ash replacement rate in concrete mixtures has been attempted [5]. However, this increase in the replacement rate of cement has led to shortcomings, such as difficulties associated with adequate quality control and low early-age strength and inferior material properties [6].

Most of the previous studies on this topic have concentrated on evaluating the material properties of high-volume fly ash (HVFA) concrete and developing mix designs [3, 7]. For example, Huang et al. [8] investigated mix designs that incorporate HVFA and are associated with two types of “loss

on ignition” (LOI). Huang et al. [8] confirmed the superior mechanical properties of mixtures with low LOI fly ash and the feasibility of incorporating HVFA in concrete mixtures up to 80 percent. On the other hand, with similar water-to-binder ratio in the mix design of both HVFA concrete mix and the OPC mix, less compressive strength in HVFA concrete mix will be expected [6]. In addition, limited studies have been conducted that target the use of HVFA for structural applications [9–12].

Therefore, this study focused on the compressive behavior of confined reinforced concrete (RC) columns that contain HVFA. Numerous confinement models are available in the literature [13–15] to evaluate the axial capacity and to predict the envelope of the stress-strain relationship for RC columns. However, HVFA in concrete results in inferior structural performance in terms of early-age strength. To develop an accurate stress-strain model, the proper material properties must be considered. This paper presents the results of a series of tests of RC columns that contain HVFA and proposes an analysis model to predict the behavior of RC columns according to HVFA content.

TABLE 1: Chemical proportion for OPC and FA.

Types	Items							Physical properties	
	Chemical composition [%]							Specific gravity [g/cm ³]	Blaine [cm ² /g]
	SiO ₂	Al ₂ O ₃	Fe ₂ O ₃	CaO	MgO	SO ₃	Ig. loss		
NPC	21.96	5.27	3.44	63.41	2.13	1.96	0.79	3.16	3,214
FA	55.66	27.76	7.04	2.70	1.14	0.49	4.3	2.19	3,621

TABLE 2: Mix designs for OPC and HVFAC.

Binder type	W/B (%)	S/a (%)	Unit weight (kg/m ³)					Superplasticizer (% by cement weight)
			W	C	FA	S	G	
OPC	50.0	40.2	175	350	0	710	1,054	0.05
HVFAC	35.0	44.1	120	154	189	821	1,042	1.50

Note. S/a is the sand-to-aggregate ratio; W is water; C is cement; FA is fly ash; S is sand; G is gravel.

TABLE 3: Testing matrix.

ID	Longitudinal steel ratio (%)	Tied steel ratio (%)	Tied steel spacing (mm)	f_c (MPa)	Fly ash (%)
N-100	2.25	0.475	100	30.6	0
N-150		0.317	150		
N-250		0.190	250		
F-100	2.25	0.475	100	30	55
F-150		0.317	150		
F-250		0.190	250		

Six columns were manufactured for this study. The study variables are the replacement rate of the fly ash, the tied steel ratio, and tie steel spacing. In addition, based on the experimental results, an analysis model was developed to predict the compressive behavior of RC columns that contain HVFA. Comparisons of the model results with the test results were used to calibrate the accuracy of the proposed analysis model for HVFA RC columns.

2. Experimental Program

2.1. Test Parameters and Specimen Fabrication. Tests were conducted based on two replacement ratios of fly ash (0% and 50%) as the variables. The design compressive strength of the concrete was 30 MPa. The longitudinal rebar reinforcement ratio was fixed at 2.25 percent with three different spacings (100 mm, 150 mm, and 250 mm) of tie rebar in the column specimens. The rebar sizes of D13 ($\phi = 13$ mm) and D10 ($\phi = 10$ mm) were used for the longitudinal rebar and tie rebar, respectively. The measured yield strength of D13 rebar is 412 MPa. And the chemical composition of fly ash in the study was presented in Table 1. Extra process was performed to ensure quality control of fly ash and the loss of ignition values was controlled to 5% or less.

Table 2 shows the mix design for ordinary Portland cement (OPC) and high-volume fly ash concrete (HVFAC). Due to the low water-to-binder ratio (W/B), a relatively large

amount of superplasticizer was used in the HVFAC mix. The use of fly ash in OPC provides practical benefits to concrete, such as a gain in long-term strength, reduced hydration heat, improved resistance to chloride, and enhanced workability. The mix proportion used in this study has been developed based on the related research results by the authors [16]. To determine material properties of concrete, three cylindrical specimens (100 mm \times 200 mm) were made and cured in moisture condition for 28 days with $23^\circ\text{C} \pm 3$.

Table 3 shows the variables for the specimens: tie steel ratio, spacing of the tied steel, and the replacement rate of the fly ash. The specimen identification (ID) indicates the fly ash and tie steel spacing; for example, N-100 means that the specimen is fabricated with OPC with 100 mm of tie steel spacing.

Each specimen cross-section is 150 mm \times 150 mm at the midheight of the column and is 1,030 mm in height. The column specimens were cured in moisture for 28 days with $23^\circ\text{C} \pm 3$. Compression tests were performed at the age of 28 days after fabrication. Figure 1 presents the reinforcement details of a specimen, the installed gauge locations, and the test set-up used in this study.

2.2. Test Procedure. A universal testing machine (UTM) with 2,000 kN was used to apply monotonic axial compressive loading with displacement control at a rate of 0.5 mm/min (cross-head speed). To monitor the strain of the concrete

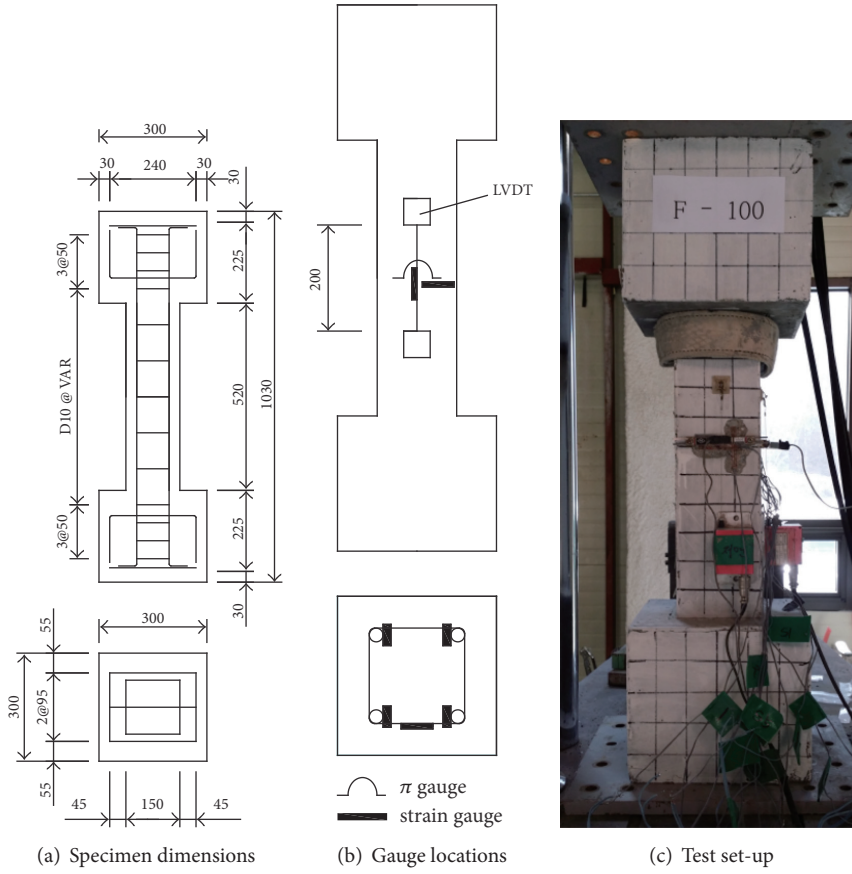


FIGURE 1: Specimen design and instrumentation.

TABLE 4: Material properties of concrete mixtures.

ID	f_c (MPa)	ϵ_c	Unit weight (kg/m^3)	E_c (MPa)		
				Measured	ACI 318	Meas./Pred.
OPC	30.6	0.00285	2,304	28,918	26,522	1.09
HVFAC	30.0	0.00287	2,102	21,173	23,058	0.92

surface and the displacement of the column, strain gauges, a pressure indicator (PI) gauge, and a linear variable displacement transducer (LVDT) were installed at the midheight of the column, as shown in Figure 1(b). Strain gauges also were installed on the longitudinal rebar and the tie rebar. Monotonic loading tests were terminated when an abrupt load drop was observed for each specimen.

3. Test Results and Discussion

3.1. Material Properties. Figure 2 presents the stress-strain relationship for the OPC and HVFAC specimens. Table 4 presents a summary of the test results, including the compressive strength, elastic modulus values, and the predicted values in accordance with the current American Concrete Institute (ACI) 318 specifications. The predicted elastic modulus value, $E_c = 0.077(m_c)^{1.5}(f_c)^{0.5}$, is computed based on the unit

weight of the concrete mixture (m_c) and the compressive concrete strength (f_c). A similar compressive concrete strength value was obtained for both concrete mixtures. However, a lower elastic modulus value was obtained for the HVFAC mixture than for the OPC mixture. This outcome was due to the low unit weight of the HVFAC mixture that is caused by the low unit weight of fly ash compared to the weight of cement. These results are in good agreement with those found in the literature [1].

3.2. Failure Mode and Load versus Displacement Relationship. Figure 3 presents typical failure modes of the axially loaded column specimens. No significant concrete spalling occurred during the axial load tests. Shear failure in specimens N-250 and F-150 occurred at failure. Similar failure patterns were observed for each specimen regardless of whether HVFA was present.

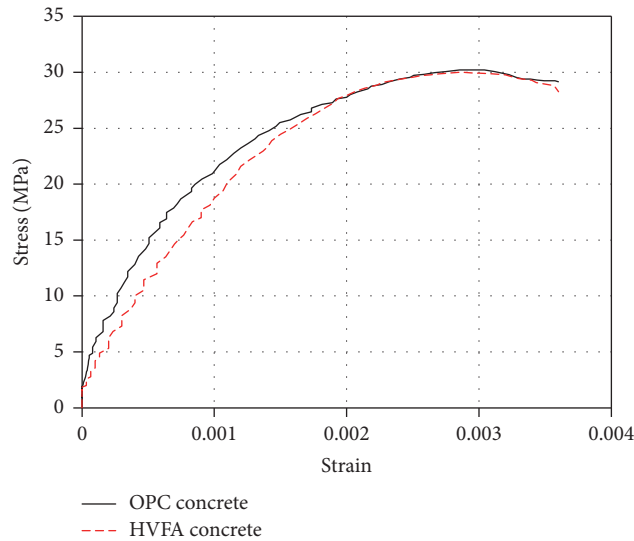


FIGURE 2: Stress-strain relationship in compression.

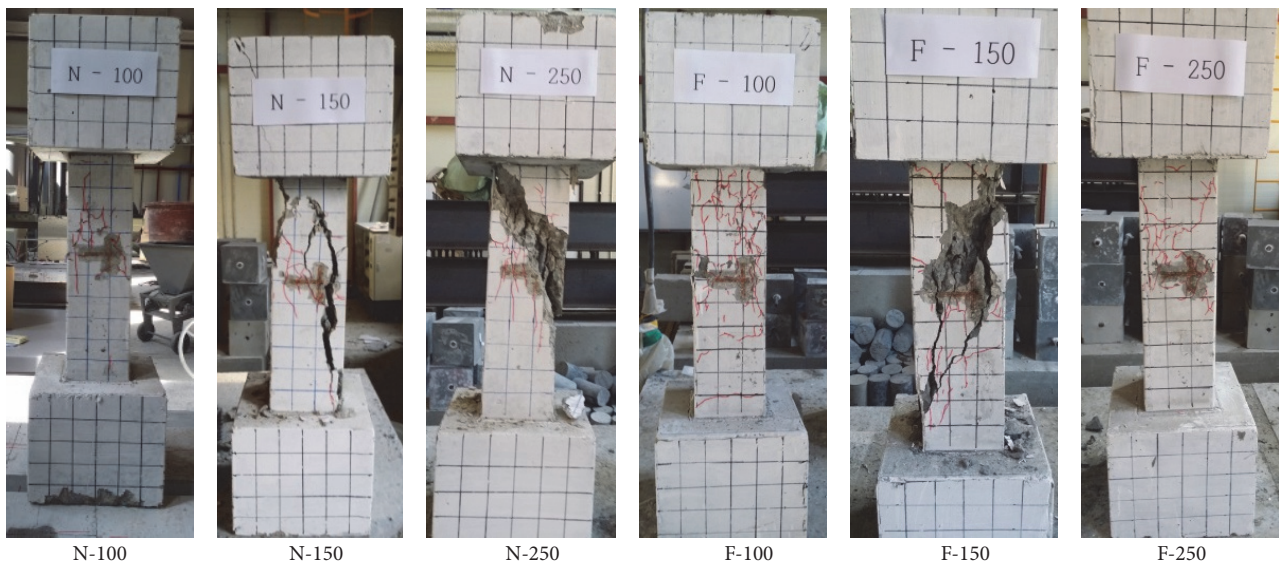


FIGURE 3: Failure modes of specimens.

Figure 4 shows the load versus displacement relation. The load-carrying capacity of the columns rapidly decreased after reaching the peak load. This behavior is consistent with that observed in similar RC columns with OPC. The ultimate load for the specimens, regardless of whether they contained HVFA, tended to decrease with an increase in the spacing of the transverse steel due to confining pressure.

Table 5 shows the measured axial loads at the yield of the longitudinal reinforcement and at the ultimate points. The ratio of the yield load to the ultimate load for the specimens with OPC is in the range of 0.73 to 0.79, and the ratio of the yield load to the ultimate load for the specimens with HVFA is in the range of 0.75 to 0.84. The ultimate load

for both series of tests tended to increase with an increase in the tie reinforcement ratio. The ultimate design axial strength of a column (ϕP_n) was computed using the equation found in ACI 318-16: $P_n = 0.8 * (0.85 f'_c (A_g - A_s) + f_y \cdot A_s)$. The measured longitudinal reinforcement strain levels reached the yield strain at the ultimate point, so the measured yield strength of the longitudinal reinforcement was used for the calculation. The predicted ultimate design strength of the RC columns with HVFA led to failure at loads ranging from 54 percent to 57 percent of the measured peak strength. The computed values conservatively predicted the measured values, and, thus, the existing equation in the ACI code is feasible for confined RC columns that contain HVFA.

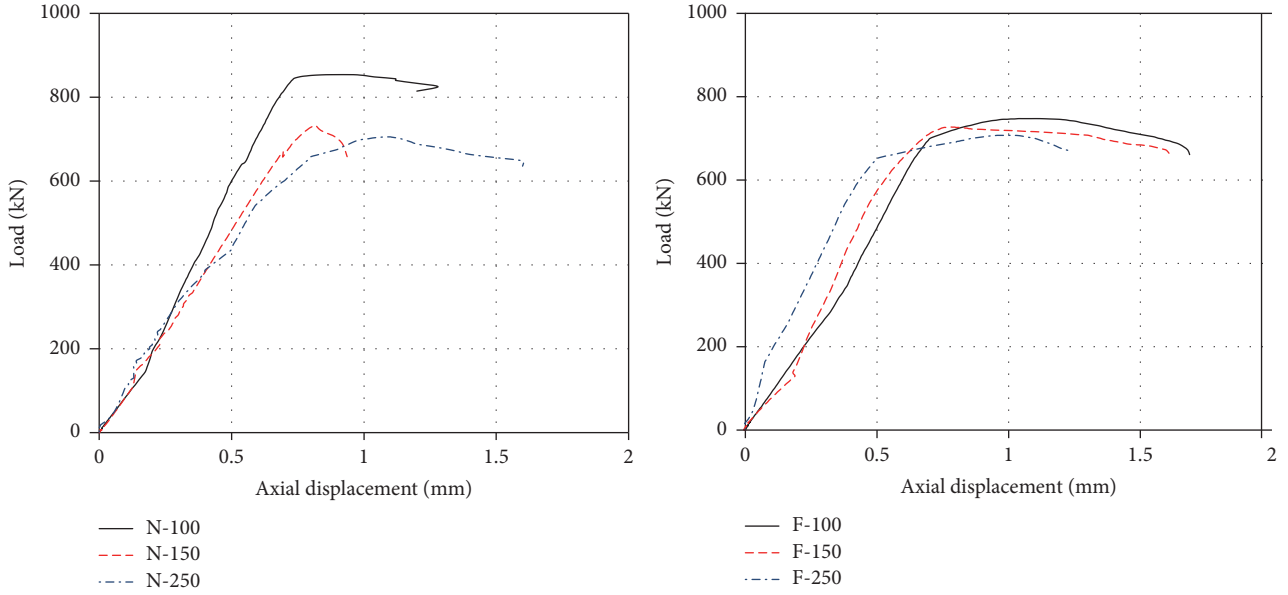


FIGURE 4: Load versus displacement relationship.

TABLE 5: Measured axial strength values at yield and ultimate points.

ID	P_y (kN)	P_{max} (kN)	P_y/P_{max}	ϕP_n (kN)	$\phi P_n/P_{max}$
N-100	626.8	854.0	0.73	406	0.48
N-150	548.8	732.8	0.75	406	0.55
N-250	559.0	705.8	0.79	406	0.58
F-100	625.5	747.2	0.84	400	0.54
F-150	673.5	727.1	0.93	400	0.55
F-250	531.6	707.7	0.75	400	0.57

3.3. *Concrete Strain of Specimens.* Figure 5 shows the measured concrete strain values in the axial and lateral directions. In the early stages, the response was a relatively linear relationship between the axial strain and the lateral strain of the concrete; subsequently, nonlinear responses in the lateral strain beyond $\epsilon_l = 0.0005$ were experienced. The axial strain at peak stress was assumed to be axial strain of 0.002 [17]; however, this lateral strain value varied depending on the tie reinforcement ratio.

3.4. *Effects of Tie Reinforcement Ratio.* Figure 6 shows the relation between the load and strain for the longitudinal steel, including the load when the longitudinal steel yielded. For all the tested columns, the longitudinal steel yielded. However, the strain of the transverse rebar for all the specimens did not reach yield strain, so a confinement effect for the columns hardly was observed in the study. Similar patterns were observed irrespective of the presence of HVFA.

4. Analytical Stress-Strain Models for Confined RC Columns

The modified Kent and Park model [18], which was developed based on the second-order parabola model, allows simplicity

and accuracy and thus is widely adopted in the literature. In the modified Kent and Park model, the monotonic concrete stress-strain relationship in compression is described as presented in

$$f_c = Kf_{cc} \left[2 \left(\frac{\epsilon_c}{\epsilon_{cc}} \right) - \left(\frac{\epsilon_c}{\epsilon_{cc}} \right)^2 \right] \quad \epsilon_c \leq \epsilon_{cc} \quad (1)$$

$$f_c = Kf_{cc} [1 - Z(\epsilon_c - \epsilon_{cc})] \geq 0.2Kf'_c \quad \epsilon_c \geq \epsilon_{cc},$$

where the concrete strain at the peak compressive stress is $\epsilon_{cc} = 0.002K$; $K = 1 + \rho_s f_{yh}/f_{cc}$ is a factor that accounts for the increase in strength that is due to confinement; the strain softening slope is $Z = 0.5/(((3 + 0.29f_{cc})/(145f_{cc} - 1000)) + 0.75\rho_s \sqrt{h'/S_h} - 0.002K)$; f_{cc} is the ultimate concrete compressive strength (MPa); f_{yh} is the yield strength of the transverse steel (MPa); ρ_s is the ratio of the volume of the transverse steel to the volume of the concrete core measured to the outside of the stirrups; h' is the width of the concrete core measured to the outside of the stirrups; and s_h is the center-to-center spacing of the stirrups.

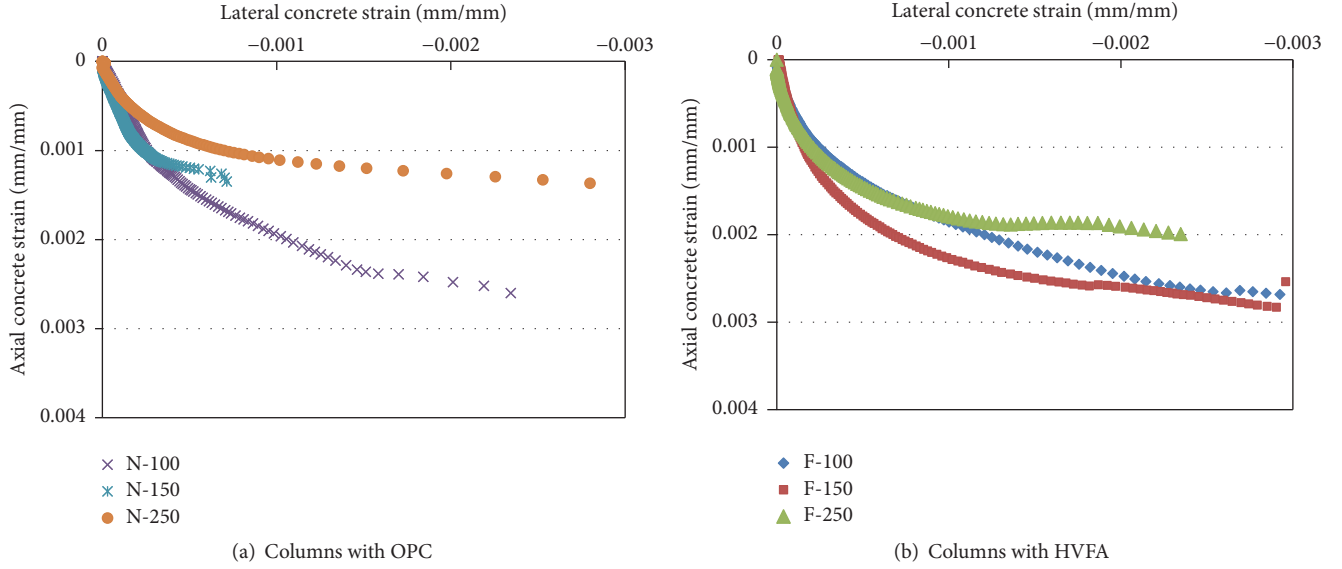


FIGURE 5: Axial versus lateral concrete strain of specimens.

Hoshikuma et al. [19] adopted an exponential function to simplify the expression for the ascending part, shown here as

$$f_c = E_c \varepsilon_c \left\{ 1 - \frac{1}{n} \left(\frac{\varepsilon_c}{\varepsilon_{cc}} \right)^{n-1} \right\}, \quad (2)$$

where ε_{cc} is the strain at peak stress, E_c is the initial stiffness (MPa), and n is a coefficient.

Also, the descending part of the stress curve can be modeled from the test results by a straight line, as expressed in

$$f_c = f_{cc} - E_{des} (\varepsilon_c - \varepsilon_{cc}), \quad (3)$$

where E_{des} is the gradient at the descending part (MPa) ($E_{des} = (11.2 \cdot f_{co}^2) / (\rho_s \cdot f_{yh})$).

Figure 7 presents comparisons of the experimental results and the analytical model results. The experimental results for the specimens with OPC are consistent with the results obtained from the analytical modified model proposed by Kent and Park [18] and the Hoshikuma et al. model [19] irrespective of the confinement spacing. On the other hand, the experimental results of the specimens with HVFAC were slightly overestimated by the analytical modified model of Kent and Park but matched relatively well with the proposed equation by Hoshikuma. Therefore, the Hoshikuma equation was employed in this study to develop a modified analytical model for confined RC columns with HVFAC.

The adopted Hoshikuma equation was calibrated by adjusting the initial stiffness value (E_c) of the HVFAC and the peak concrete strain that is due to the low unit weight of HVFA. Equations (4) and (5) are proposed for the initial

stiffness value (E_c) of RC columns with HVFA and the strain at peak stress (ε_{cc}), respectively.

$$E_c = 0.077 m_c^{1.5} \cdot \sqrt[3]{f_c} \quad (4)$$

$$\varepsilon_{cc} = 0.002 \left(\frac{2,300}{m_c} \right)^{1.5} + 0.033 \beta \frac{\rho_{sh} f_{yh}}{f_c}, \quad (5)$$

where β is a modification factor that depends on the section shape; for a square section, 0.4 is used by Hoshikuma et al. [19].

Figure 8 presents comparisons between the measured stress-strain values of the specimens using the proposed equations with modification of the elastic modulus values for the HVFAC mixture. The ascending part and descending part of the proposed stress-strain curves show good agreement with the measured envelopes.

Figure 9 shows that available experimental results in the literature [20] were compared with the proposed equation and confirmed that the stiffness of the specimen containing fly is less than that of the specimen without fly ash. The proposed equation properly predicts the stress-strain envelope for the column specimens containing fly ash.

The proposed equation was driven by limited experimental tests, and the results of the previous studies on HVFA concrete were insufficient for verification. Further study on the compressive behavior of HVFA concrete is needed. If a lot of experimental data are accumulated, it will be necessary to do further studies on the basis of the formula proposed.

5. Conclusions

Six specimens were tested in this study to develop an analytical stress-strain model for confined RC columns that contain HVFA. Based on the limited experimental results,

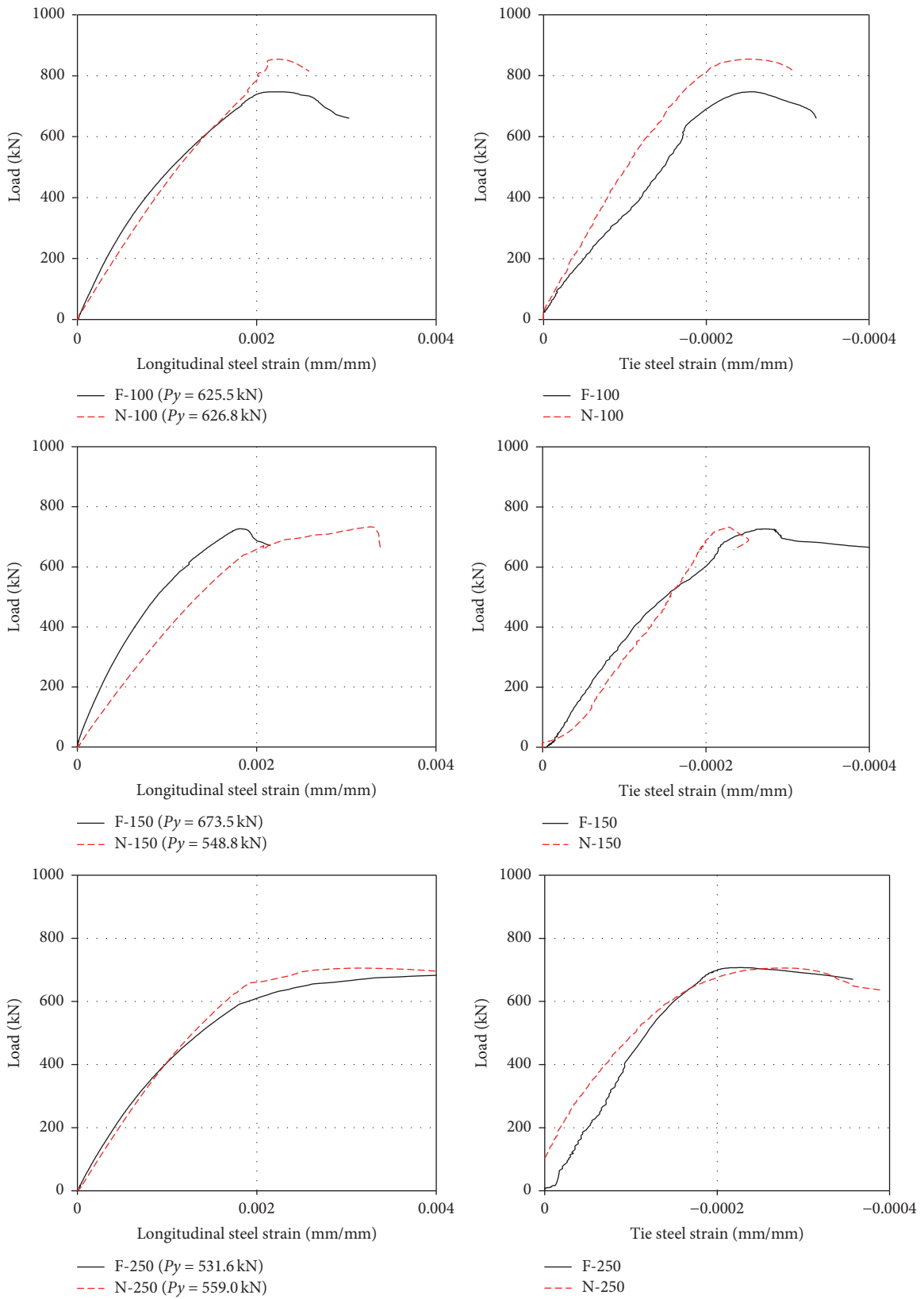


FIGURE 6: Load versus strain relationship of longitudinal steel for the specimens.

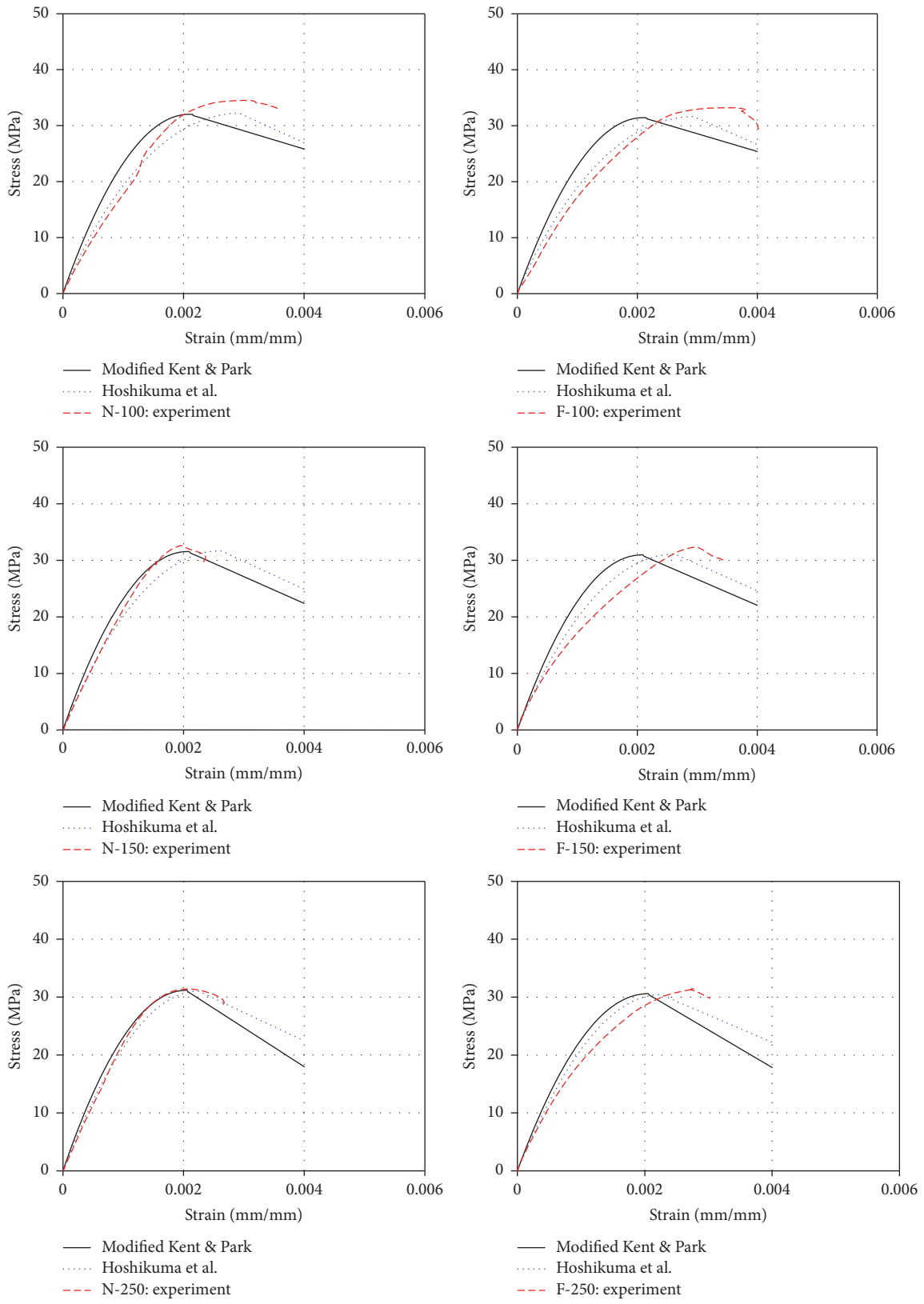


FIGURE 7: Comparisons of the experimental results and analytical model results.

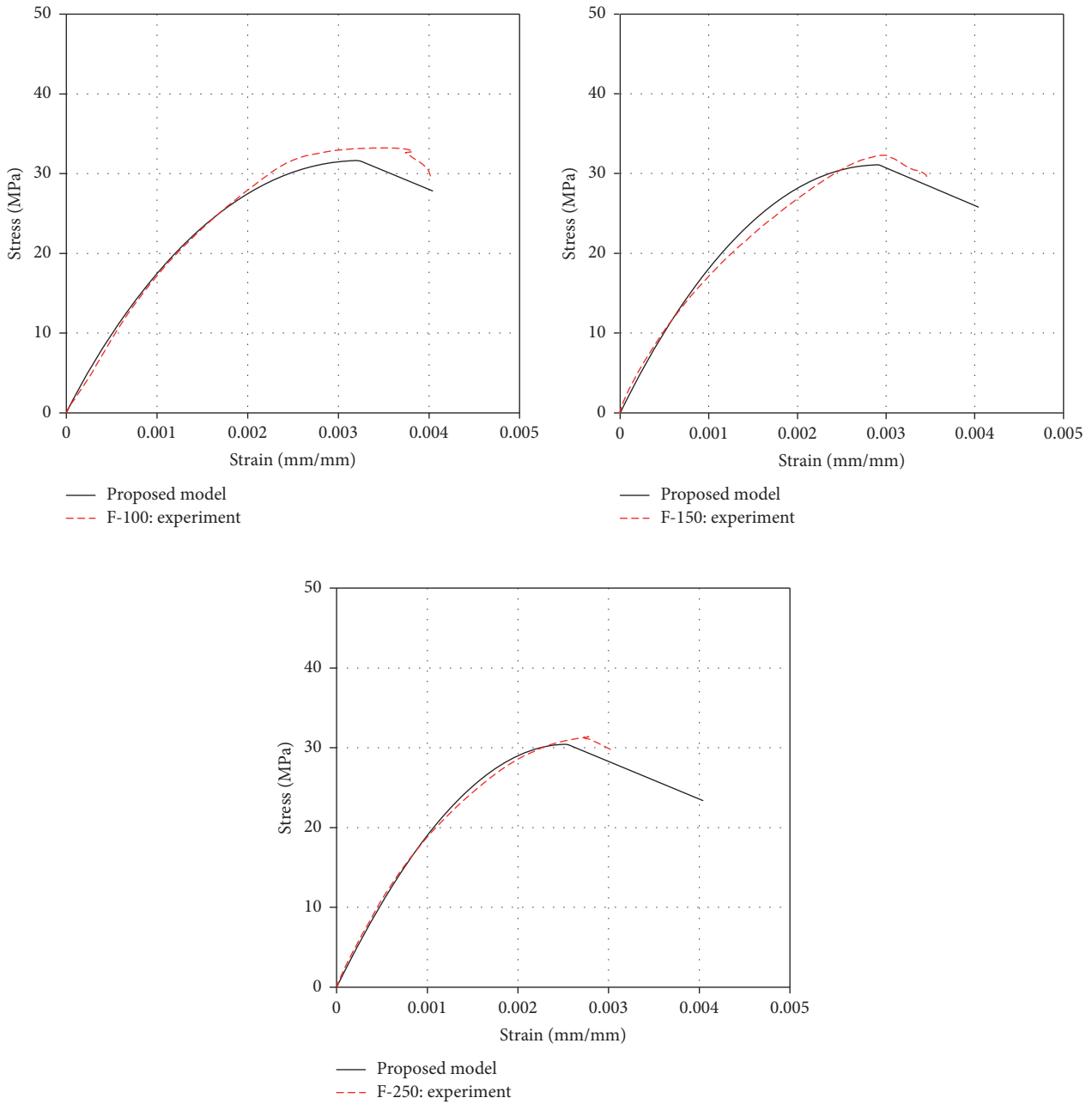


FIGURE 8: Comparisons between the experimental results and the proposed equation.

a stress-strain envelope for RC columns with HVFA was derived analytically and then calibrated using the experimental results. The following conclusions can be drawn with regard to the compressive behavior of the OPC and HVFAC mixes.

The elastic modulus values of the HVFAC mix were lower than those of the OPC mix. This outcome was due to the different water-to-binder ratio and low unit weight of the HVFAC mixture that is caused by the low specific gravity of its inherent fly ash compared to the weight of cement. Meanwhile, the compressive behavior of the HVFAC and OPC columns was similar with regard to

crack morphology and crack progression. The maximum load-carrying capacity of the columns with HVFA tended to decrease up to 14 percent compared to the columns with OPC. The RC column elements made with HVFA behaved similarly, as expected, based on the equation used to predict OPC column behavior. Existing design standards will conservatively predict the ultimate capacity of HVFAC columns.

The initial stiffness of a column affects the elastic modulus of HVFAC; therefore, the proposed modified elastic modulus equation allows for adjustment of the initial stiffness value of concrete columns that contain HVFA. The modified

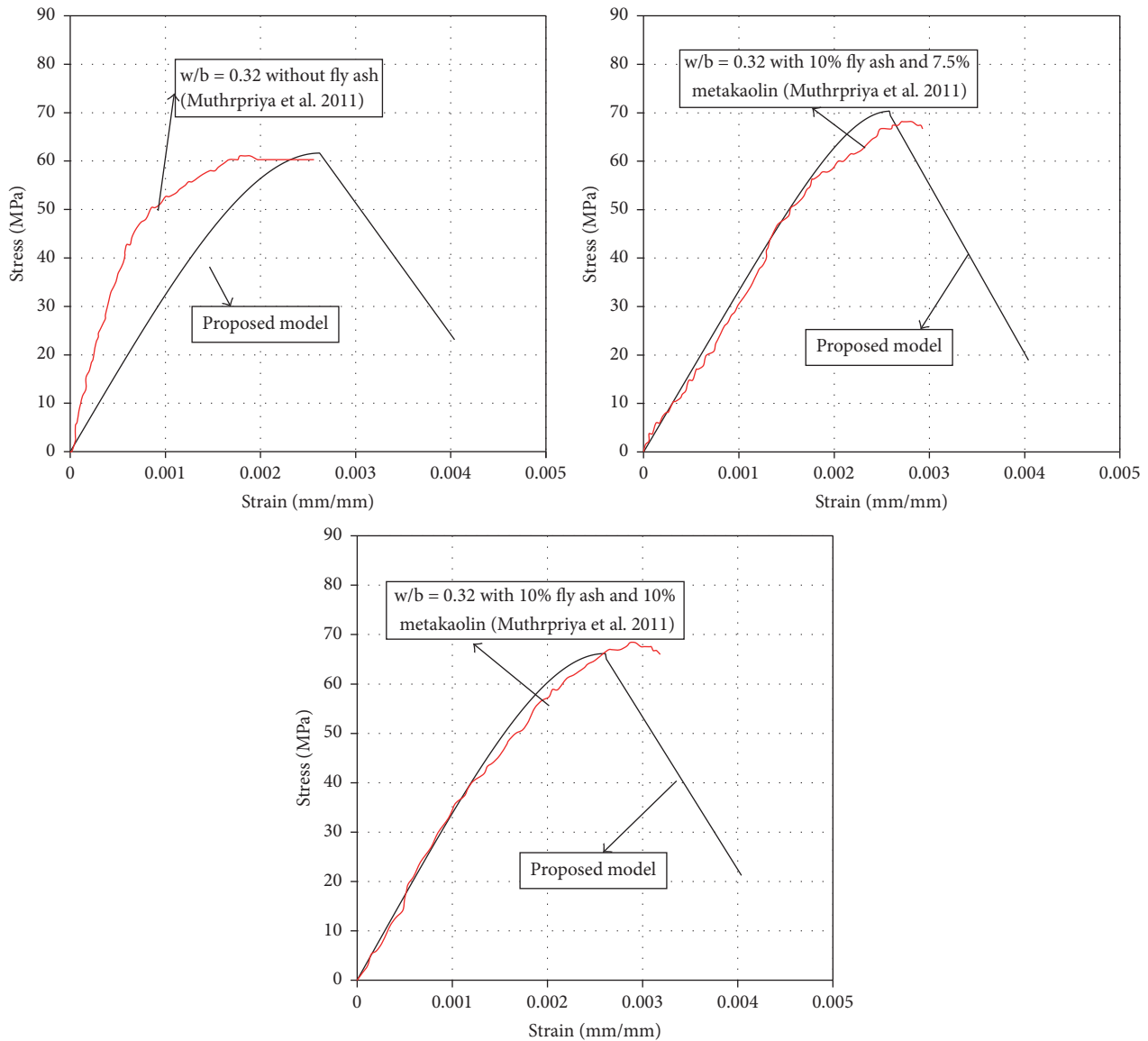


FIGURE 9: Comparisons between the available experimental result in the literature and the proposed equation.

stress-strain model can predict both the ascending and descending branches of the curve for confined RC columns with HVFA.

Conflicts of Interest

The authors declare that there are no conflicts of interest regarding the publication of this paper.

Acknowledgments

This research was financially supported by the Korean Ministry of Environment as “Public Technology Program Based on Environmental Policy” (no. 2016000700003).

References

- [1] R. Siddique, “Performance characteristics of high-volume Class F fly ash concrete,” *Cement and Concrete Research*, vol. 34, no. 3, pp. 487–493, 2004.
- [2] K. Mala, A. K. Mullick, K. K. Jain, and P. K. Singh, “Effect of relative levels of mineral admixtures on strength of concrete with ternary cement blend,” *International Journal of Concrete Structures and Materials*, vol. 7, no. 3, pp. 239–249, 2013.
- [3] V. M. Malhotra, “Durability of concrete incorporating high-volume of low-calcium (ASTM Class F) fly ash,” *Cement and Concrete Composites*, vol. 12, no. 4, pp. 271–277, 1990.
- [4] T. R. Naik, B. W. Ramme, and J. H. Tews, “Use of high volumes of Class C and Class F fly ash in concrete,” *Cement, Concrete and Aggregates*, vol. 16, no. 1, pp. 12–20, 1994.

- [5] D. Cross, J. Stephens, and J. Vollmer, "Structural applications of 100 percent fly ash concrete," in *Proceedings of the World of Coal Ash (WOCA)*, pp. 1–9, Springer, Lexington, Kentucky, USA, 2005.
- [6] J.-E. Kim, W.-S. Park, Y.-I. Jang et al., "Mechanical Properties of Energy Efficient Concretes Made with Binary, Ternary, and Quaternary Cementitious Blends of Fly Ash, Blast Furnace Slag, and Silica Fume," *International Journal of Concrete Structures and Materials*, vol. 10, no. 3, pp. 97–108, 2016.
- [7] T. R. Naik and S. S. Singh, "Influence of fly ash on setting and hardening characteristics of concrete systems," *ACI Materials Journal*, vol. 94, no. 5, pp. 355–360, 1997.
- [8] C. H. Huang, S. K. Lin, C. S. Chang, and H. J. Chen, "Mix proportions and mechanical properties of concrete containing very high-volume of Class F fly ash," *Construction and Building Materials*, vol. 46, pp. 71–78, 2013.
- [9] G. Venkatesan, S. Reghu Raman, and M. Chandra Sekaran, "Flexural behavior of reinforced concrete beams using high volume fly ash concrete confinement in compression zone," *Journal of Civil Engineering (IEB)*, vol. 41, no. 2, pp. 87–97, 2013.
- [10] M. Arezoumandi, C. A. Ortega, and J. S. Volz, "Flexural behavior of high-volume fly ash concrete beams-experimental study," *Transportation Research Record*, vol. 2508, pp. 22–30, 2015.
- [11] M. Arezoumandi, J. S. Volz, and J. J. Myers, "Shear behavior of high-volume fly ash concrete versus conventional concrete," *Journal of Materials in Civil Engineering*, vol. 25, no. 10, pp. 1506–1513, 2013.
- [12] R. Thangaraj and R. Thenmozhi, "Experimental study on rc beams using high volume fly ash," *IRA-International Journal of Technology & Engineering*, vol. 3, no. 2, pp. 71–85, 2016.
- [13] V. V. Cao and H. R. Ronagh, "A model for damage analysis of concrete," *Advances in Concrete Construction*, vol. 1, no. 2, pp. 187–200, 2013.
- [14] M. K. M. Reddar, *Stress-strain model of Unconfined and Confined Concrete and Stress-Block Parameters, Master Thesis [Master, thesis]*, University of Texas A & M, College Station, Tex, USA, 2009.
- [15] T. Tavio and A. Tata, "Predicting Nonlinear behavior ad stress-strain relationship of rectangular confined reinforced concrete columns with ANSYS," *Civil Engineering Dimension*, vol. 11, no. 1, pp. 23–31, 2009.
- [16] S. W. Yoo, S. H. Jung, and S.-J. Kwon, "Evaluation of compressive and shear strength characteristics in high volume fly ash concrete," *Applied Mechanics and Materials*, vol. 584–586, pp. 1282–1288, 2014.
- [17] M. H. Harajli, E. Hantouche, and K. Soudki, "Stress-strain model for fiber-reinforced polymer jacketed concrete columns," *ACI Structural Journal*, vol. 103, no. 5, pp. 672–682, 2006.
- [18] D. C. Kent and R. Park, "Flexural members with confined concrete," *Journal of the Structural Division*, vol. 97, no. 7, pp. 1969–1990, 1971.
- [19] J. Hoshikuma, K. Kawashima, K. Nagaya, and A. W. Taylor, "Stress-strain model for confined reinforced concrete in bridge piers," *Journal of Structural Engineering*, vol. 123, no. 5, pp. 624–633, 1997.
- [20] P. Muthupriya, K. Subramanian, and B. G. V. Vishnuram, "Investigation of Behaviour of high performance reinforced concrete columns with metakaolin and fly ash as admixture," *International Journal of Advanced Engineering Technology*, vol. 2, no. 1, pp. 190–202.

Research Article

Modifying Cement Hydration with NS@PCE Core-Shell Nanoparticles

Yue Gu,^{1,2} Qianping Ran,^{2,3} Wei She,¹ and Jiaping Liu^{1,2,3}

¹School of Materials Science and Engineering, Southeast University, Nanjing 211189, China

²State Key Laboratory of High Performance Civil Engineering Materials, Nanjing 210008, China

³Jiangsu Research Institute of Building Science, Nanjing, Jiangsu 210008, China

Correspondence should be addressed to Yue Gu; gubetter@163.com and Wei She; weishe@seu.edu.cn

Received 31 March 2017; Accepted 30 May 2017; Published 27 July 2017

Academic Editor: Kedsarin Pimraksa

Copyright © 2017 Yue Gu et al. This is an open access article distributed under the Creative Commons Attribution License, which permits unrestricted use, distribution, and reproduction in any medium, provided the original work is properly cited.

It is generally accepted that fine particles could accelerate cement hydration process, or, more specifically, this accelerating effect can be attributed to additional surface area introduced by fine particles. In addition to this view, the surface state of fine particles is also an important factor, especially for nanoparticles. In the previous study, a series of nano-SiO₂-polycarboxylate superplasticizer core-shell nanoparticles (NS@PCE) were synthesized, which have a similar particle size distribution but different surface properties. In this study, the impact of NS@PCE on cement hydration was investigated by heat flow calorimetry, mechanical property measurement, XRD, and SEM. Results show that, among a series of NS@PCE, NS@PCE-2 with a moderate shell-core ratio appeared to be more effective in accelerating cement hydration. As dosage increases, the efficiency of NS@PCE-2 would reach a plateau which is quantified by various characteristic values. Compressive strength results indicate that strength has a linear correlation with cumulative heat release. A hypothesis was proposed to explain the modification effect of NS@PCE, which highlights a balance between initial dispersion and pozzolanic reactivity. This paper provides a new understanding for the surface modification of supplementary cementitious materials and their application and also sheds a new light on nano-SiO₂ for optimizing cement-based materials.

1. Introduction

Concrete is still the most widely used construction material in our planet which contributed 8~10% of the worldwide anthropogenic CO₂ emission [1, 2]. To reduce the environmental footprint triggered by concrete, one effective strategy is to utilize supplementary cementitious materials (SCMs) to replace a portion of cement, the main binder component of concrete. This is particularly significant in a CO₂-penalized economy, where the reduced CO₂ impact of cement could bring about economic, social, and environmental benefits. SCMs commonly refer to fly ash, ground granulated blasted furnace slag, limestone, and calcined clays. Unfortunately, the addition of SCMs with a high volume would often adversely impact the development of mechanical property, especially at the early age. To overcome the undesired negative consequence, more recently, nanomaterials have been explored as

superior filler agents to improve the early age property [3–5]. For instance, Yehdego and Peethamparan [4] revealed that nanomaterials modified high volume fly ash concrete could obtain doubled compressive strength in comparison to pristine unmodified sample at 24 h.

Nanotechnology is in the forefront of materials research, as it changed the traditional vision about the synthesis, modification, and control of materials. To respond to constant curiosity around nanotechnology in cement and concrete research area, various nanoparticles, such as nano-SiO₂ [6], nano-Al₂O₃ [7], nano-TiO₂ [8, 9], nanoclay [10], and graphene [11], have been added to enhance the early age properties of cementitious materials. Among all the nanoparticles, the incorporation of nano-SiO₂ (NS) into cementitious materials has been most extensively studied and shows the high potential of commercial application, which may be attributed to two main reasons: (1) the affinity

TABLE 1: Chemical composition of cement.

SiO ₂	CaO	MgO	Al ₂ O ₃	Fe ₂ O ₃	SO ₃	NaOeq	Loss
19.98	61.86	2.02	4.61	3.07	4.43	0.68	0.9

with cement hydration products at molecular scale and (2) a reasonable price resulting from industrial-scale production. It is generally accepted that NS is very effective in accelerating cement hydration at early age. Several authors [12–15] have studied the interaction between NS and cement in depth to advance the understanding of mechanisms of NS. The dominant mechanisms that have been proposed include (1) filling effect, as NS could act as fillers to densify the microstructure; (2) seeding effect, as NS has much large surface area than cement; the additional surface area could serve as site for the precipitation of calcium-silicate-hydrate (C-S-H) nucleus; (3) pozzolanic effect, as NS consumes calcium hydroxide to form additional C-S-H which would decrease the micro defects and make hydration products more homogeneous. These mechanisms may operate in parallel or in some complicated combination.

Given acceleration of hydration triggered by nano-SiO₂ derived from seeding effect or filler effect, the proper dispersion is a critical problem for application and remains a big challenge. However, NS would inevitably agglomerate after mixing with cement and water, although it could be well dispersed in aqueous solution. This is because the calcium ion leaching from dissolution of cement breaks the stabilization controlled by the electrical double layer. To mitigate the degree of agglomeration, some physical methods, such as ultrasonic waves method [16], have been adopted, but efficiency of these methods only exists in pure water and not in cement pore solution containing high concentration of different ion species. Surface modification of NS has been studied and proven to be one of the most accepted methods to improve the dispersion stability of NS in complicated condition [17], while few attentions have been paid to it in the area of cement and concrete. The polymer on the surface could provide the steric hindrance for nanoparticles to generate significant repulsive force. Owing to the application of polycarboxylate (PCE) in concrete technology for over decades, in present work [18], PCE was chosen to graft on the NS surface, forming a kind of core-shell nanoparticles (NS@PCE). As expected, NS@PCE are more stable in synthetic pore solution, compared with pristine NS.

From the aspect of cement chemistry, the surface state of NS@PCE is an important factor for their ability to accelerate cement hydration, because the surface state of NS@PCE may decide (1) their dispersed state in cement paste matrix associated with the total addition of surface area and (2) the rate of reaction with calcium hydroxide which is related to the total number of C-S-H nuclei. To further elucidate the relationship between the surface state of NS@PCE and accelerating effect and obtain an optimal dosage, in this paper, we conducted a series of experiments by isothermal conduction calorimetry, mechanical property measurement, XRD, and SEM. The results show that the modified effect of NS@PCE has some new features, compared with that

of pristine NS. Whether intended explicitly as a message to application of NS@PCE in cement and concrete area or not, the move highlighted the possibility of the surface modification of supplementary cementitious materials and their application.

2. Materials and Methods

2.1. Materials

2.1.1. Cement. Ordinary Portland cement compliant with the Chinese National Standard GB8076-2008 was used in this study. The oxide analysis of the cement was performed by X-ray fluorescence spectrometry (XRF, Thermo Fisher ARL). The compositions of the cement are listed in Table 1.

2.1.2. Nanoparticles. Colloidal NS used in this study was supplied by Suzhou Nano-dispersion Co., Ltd (China) with an initial solid content of 30% by mass. This NS was produced by a sol-gel technique, which was formed through hydrolysis and condensation of tetraethyl orthosilicate ($\text{Si}(\text{OC}_2\text{H}_5)_4 + 2\text{H}_2\text{O} \xrightarrow{\text{NH}_3 \cdot \text{H}_2\text{O}} \text{SiO}_2 + 4\text{C}_2\text{H}_5\text{OH}$). Note that although commercial NS was dispersed into aqueous dispersion as received, it still needed purification to remove unreacted tetraethyl orthosilicate, alcohol, ammonia, and other impurities as much as possible before chemical synthesis.

The synthesis procedures of NS@PCE have been demonstrated in previous work [18]. A series of NS@PCE were synthesized from silanized polycarboxylate superplasticizer and colloidal nano-SiO₂ by “grafting to” method. Figure 1(a) demonstrates the chemical structure of NS@PCE. The particle size distribution of a series of PCE@PCE is determined by dynamic light scattering (ALV Co., CGS-3), as shown in Figure 1(b). Thermogravimetric analysis (TGA) quantified the content of PCE as the shell of NS@PCE using a thermal analyzer (TA Co., SDT-600). The shell-core ratio and hydrodynamic diameters of nanoparticles are listed in Table 2, which were calculated based on DLS and TGA experimental results.

2.2. Methods

2.2.1. Sample Preparation. To explore the effect of nanoparticles on cement hydration and mechanical property, cementitious paste mixtures with water to binder (cement + nanoparticles) ratio of 0.4 were prepared in this work. The dosages for each type of nanoparticles varied from 0% to 0.3%, 1%, 2%, and 3% by mass of the cement. For a series of NS@PCE, the nanoparticles mass is only considered as nano-SiO₂ mass in NS@PCE; hence, at a fixed dosage, the relative number of nanoparticles would remain consistent when introduced to cement paste mixture. It is worth pointing out that the content

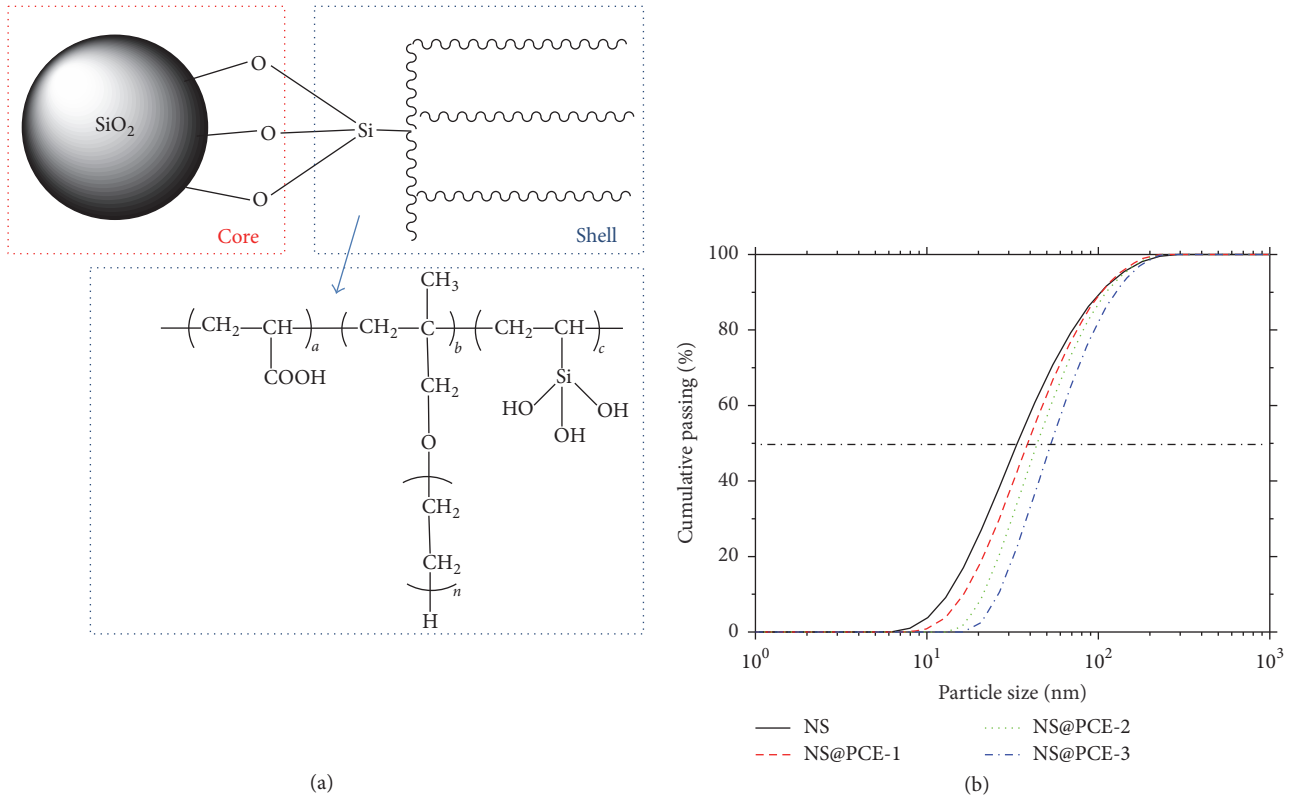


FIGURE 1: Schematic representation for NS@PCE: (a) chemical structure and (b) particle size distribution.

TABLE 2: The structural parameters of NS@PCE.

Items	Shell-core ratio (wt%)	Hydrodynamic diameter D50 (nm)
NS	0	33.84
NS@PCE-1	7.52	38.64
NS@PCE-2	9.99	44.48
NS@PCE-3	17.35	53.48

of PCE in NS@PCE can be determined by thermogravimetric analysis (TGA).

The mixing procedure is as follows: nanoparticle suspension and water were added to stainless steel mixer; cement was gradually added over a time span of 30 s at rotating rate of 60 rpm. After a 15 s interval, the cement paste was further mixed for another 60 s at 500 rpm and 60 s at 1500 rpm.

2.2.2. Rate of Cement Hydration. The influence of NS@PCE on the rate of cement hydration was tracked by isothermal conduction calorimetry. An isothermal calorimetry system (TA Co., TAM Air) was used to determine the heat evolved during the first 72 h at a constant temperature of 25°C. The thermal power and energy were used to assess reaction kinetics and the cumulative heat release of cementitious mixture. The paste of 10 g was placed on ampoules inserted

into the instrument within 5 min after initial cement and water contact. The heat data of hydration system was recorded every 60 s during test procedure.

2.2.3. Compressive Strength. Compressive strength of the composites was measured as described in ASTM C109. Cubic specimens for all mixtures (blank cement pastes, pastes containing NS, and pastes containing NS@PCE) were cast and stored in sealed condition at 25°C; after 12 h they were demolded and immersed in saturated limewater. Measurements were taken at 12 h, 24 h, 48 h, and 72 h. The strength value reported is the average of three replications.

2.2.4. XRD. X-ray diffraction analyses (XRD) were carried out on powdered paste mixtures after isopropyl alcohol solvent exchange at each desired age using a Bruker D8 Advance diffractometer in a θ - θ configuration using Cu-K α radiation. The scanning range was 5~70°C (2θ) with a scanning rate of 0.02°C/s.

2.2.5. SEM. The morphologies of the samples were examined by Quanta 250 Field Emission Scanning Electron Microscope (FEI, Hillsboro, OA, USA) using a FEI 3D microscope. The vacuum oven-dried sample was coated with 15 nm of gold to make it conductive before observation.

3. Results and Discussion

3.1. Cement Hydration

3.1.1. Stages of Cement Hydration. To better understand the influence of nanoparticles on the properties of the cementitious materials, it is essential to have a basic comprehension of the kinetic mechanisms for cement hydration. According to the classical theory, a typical cement hydration process can be divided into five stages, that is, the initial reaction period, the induction period, the acceleration period, the deceleration period, and the decline period, as shown in Figure 1. The initial hydration (*Stage I*) exothermic peak is the result of the wetting of granules surface, the fast dissolving of the hydrous phases, and the precipitation of ettringite due to the fast reactivity of the aluminates and calcium sulfate. The sharp peak is followed by the rapid decline; then an induction period (*Stage II*) occurs with a low heat flow rate. The mechanism of the induction period is still a subject of considerable debate. Compared to the traditional inhibiting layer theory, recent experimental evidences manifest that geochemistry dissolution theory seems a more reasonable explanation for the induction period [14]. The acceleration period (*Stage III*) presents an intensely exothermic rate, which is the result of the nucleation and growth of C-S-H. After the main heat evolution peak, there is an obvious shoulder peak that comes from the transformation of ettringite phase to AFm phase. At the end of acceleration period, the deceleration period (*Stage IV*) occurs with heat evolution rate dropping. While it is often assumed that the transition to diffusion rate control is responsible for this period, a new perspective was proposed as another interpretation that the inevitable impingement of region of growing hydration product reduced the surface available for nucleation and growth [19]. Finally, the hydration process steps into the decline period when heat release decreases to nearly zero (*Stage V*). The low activity is due to the slow diffusion of species in the hardened structure.

For further analysis of the influence of NS@PCE on cement hydration, in the subsequent presentation of the results, three points would be extracted from heat flow profile curves, that is, A, B, and C (Figure 2). A is the start point of acceleration period and also the end of induction period, B is the main peak point in acceleration period, and C is the shoulder peak. Heat flow value of these points and the time value at these points would be observed and correlated with characteristic parameters of NS@PCE.

3.1.2. Effect of Nanostructure of NS@PCE. Figure 3 shows the measured heat flow profiles of cement pastes prepared with different structures of NS@PCE at a dosage of 0.3 wt%. In general, it can be seen that three types of NS@PCE exhibit different influence on heat evolution. As noted by the upward shift of the rate curves, the rate of hydration increases after NS@PCE-1 and NS@PCE-2 added, while for NS@PCE-3, it only has a slight impact on cement hydration, the same as pristine NS. As reported in previous work [18], with shell-core ratio increasing, NS@PCE appeared to have

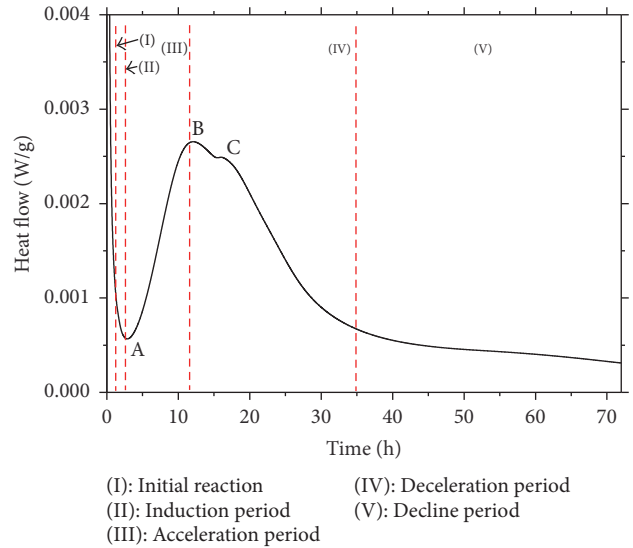


FIGURE 2: Typical heat flow profile of cement hydration.

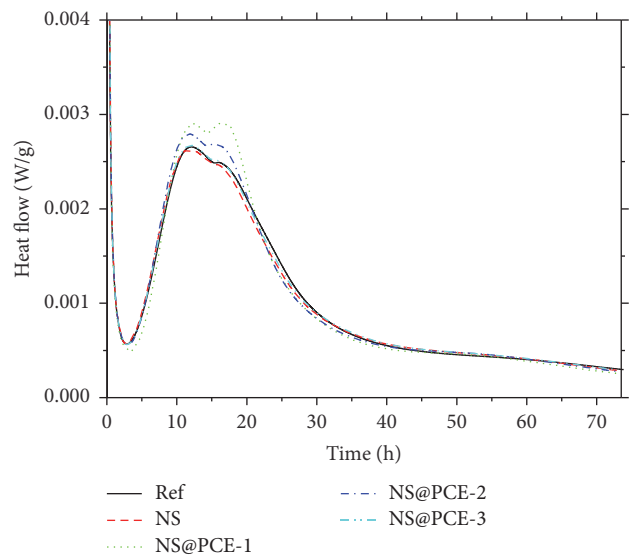


FIGURE 3: Measured heat flow profiles for cement pastes with nanoparticles at 0.3 wt%.

stronger dispersion stability in synthetic cement pore solution. Therefore, among a series of NS@PCE, NS@PCE-3 with highest shell-core ratio may appear to have best dispersion state in cement matrix; it can provide the largest surface area for the nucleation and growth of C-S-H. However, this deduction does not conform to the experimental result as shown in Figure 3. It means that, for a series of NS@PCE, the discrepancy in modification effect could not be explained by different dispersion states of nanoparticles in cement paste matrix, and a possible mechanism would be further elucidated in Section 3.4.

The higher the dosage of nanoparticles is, the more difficult it is for them to disperse in the matrix. This indicates that the dispersibility may become a dominant factor for

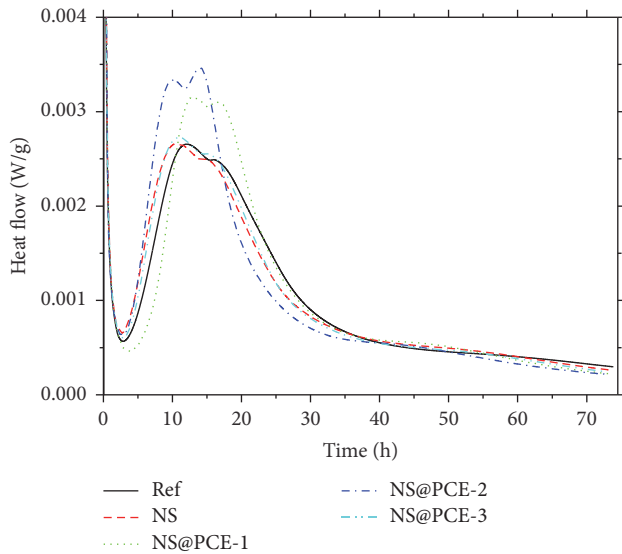


FIGURE 4: Measured heat flow profiles for cement pastes with nanoparticles at 1 wt%.

enhancing cement hydration at a higher dosage. To assess the sensitivity of effectiveness of NS@PCE to dosage, a higher dosage was carried out. The measured heat flow profile of cement pastes in the presence of various nanoparticles at a dosage of 1 wt% is shown in Figure 4. As noted in Figure 4, the NS@PCE with different structures have different influence on the heat evolution. To be more specific, NS@PCE-2 is the most effective one in enhancing cement hydration, as characterized by two aspects: (a) the initial time of acceleration period and (b) amplitude of the main heat peak. An obvious acceleration effect is also obtained by NS@PCE-1, although it is not so strong as NS@PCE-2, while for NS@PCE-3 and pristine NS, they only exhibit a slight disturbance. It is also very interesting that, in the heat flow profile of NS@PCE-2-added cement paste, the shoulder peak appears first; this is not conformed to the traditional curve of cement past where shoulder peak always follows the main peak [20].

According to the experimental results above, one can see that modification effects of nanoparticles could vary widely, even when they have similar particle size distributions and are added into cement pastes at the same dosage. This phenomenon should be related to the specific structures of nanoparticles or, in other words, the surface chemical properties of nanoparticles. Then, it is necessary to understand the relationship between the structures of nanoparticles and modification effects of nanoparticles on cement hydration. To further quantify the influence of NS@PCE in acceleration period, as mentioned earlier, some eigenvalues are extracted from heat flow profile curves to correlate with shell-core ratio of NS@PCE.

Figure 5(a) shows the evolution of T_A , T_B , and T_C as a function of shell-core ratio. As shown in Figure 5(a), T_B and T_C are sensitive to the change of shell-core ratio, while T_A is not. For T_B and T_C , at a certain ratio of 9.99 (NS@PCE-2), they reach a maximum which is higher than the reference time

from cement pastes without nanoparticles added. However, at other ratios, both T_B and T_C are lower than the reference. This indicates that only a moderate shell-core ratio could shorten the initial time of acceleration period. Figure 5(b) illustrates the correlation between the shell-core ratio and characteristic heat flow value at peak. As noted by Figure 5(b), H_A keeps a stable fluctuation as shell-core ratio increases. It is also clearly seen that H_B and H_C increase with the increase in shell-core ratio expect for the values at a ratio of 17.35. It means that the heat flow at peak could be enforced by rising shell-core ratio until reaching a threshold. A possible mechanism would be further discussed in Section 3.4. In addition, the analysis suggests that the impact of NS@PCE on cement hydration could be quantified very well by shell-core ratio, which is able to reflect surface properties of NS@PCE at some extent.

3.1.3. Effect of Dosages. Nanoparticles have been found to be effective in the stimulation of nucleation processes during the early cement hydration period [21]. The effect (so-called filler effect) is usually attributed to the provision of additional surface area by nanoparticles, of which particle size is approximately three orders of magnitude less than that of cement. In the traditional theoretical analysis, nanoparticles are considered to disperse in cement paste matrix in the form of monoparticle. Thus, the higher dosage was added, the larger surface area was got. However, if the serious agglomeration of nanoparticles appears, the dosage is no longer a scaling factor that can describe the change in solid surface area induced by nanoparticles addition.

To observe the sensitivity of modification effect of nanoparticles to the dosage, the dosages of 0.3%, 1%, 2%, and 3% were investigated. The results of pristine NS are presented in Figure 6. As shown in Figure 6, with the increase of dosage, the main hydration peak is shifted leftwards and the height of the curve is shifted upwards. For a low dosage of 0.3%, the modification effect is not very significant. For a high dosage of 3%, the change in the hydration curve is similar to the case of dosage of 2%. It may indicate that the agglomerations of nanoparticles appeared, which means the rise of surface areas could stay almost unchanged even if more nanoparticles were added to cement paste; thus hydration process is less responsive to the dosage increases.

According to the previous experimental results (Figure 4), among a series of NS@PCE, NS@PCE-2 is most effective in accelerating cement hydration at a dosage of 1%. Here, NS@PCE-2 (NP) was chosen to further test its modification effect at higher dosages. Figure 7 shows the measured heat flow profiles for NS@PCE-2-added cement pastes at different dosages. It is noted that, in general, an increase in the dosage acts to increase the hydration process. This increase manifests as an upshift of the heat flow curve. To be more specific, for a low dosage of 0.3%, the modification effect is unapparent, while it becomes significant at higher dosages. The accelerating effect seems no longer responsive to the dosage when the dosage exceeds a threshold, as compared with the curves at the dosage of 2% and that of 3%. What is more, compared with case of NS, it is interesting that there is hardly left-shift phenomenon presented in the curves.

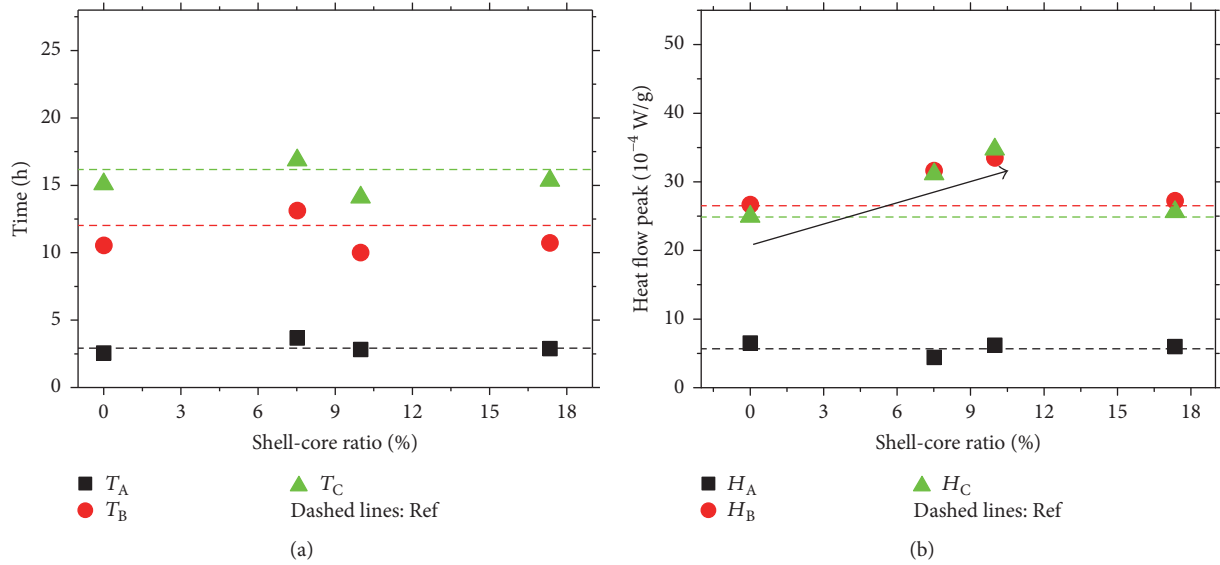


FIGURE 5: The relationship between the shell-core ratio and parameters corresponding to the measured heat flow profile at 1 wt%: (a) characteristic time at peak and (b) characteristic heat flow at peak.

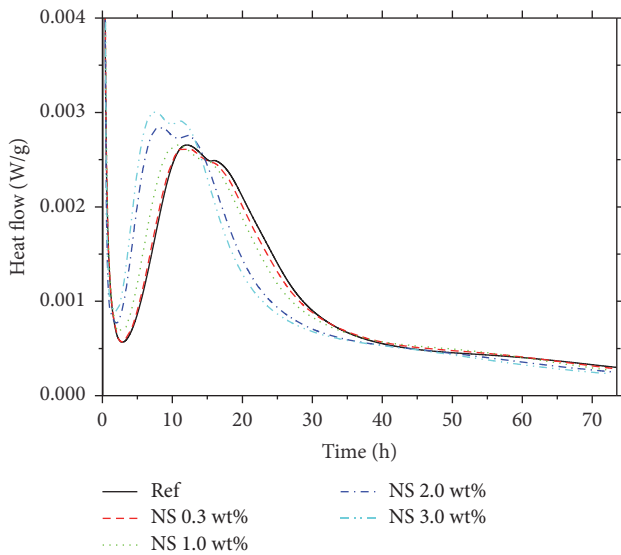


FIGURE 6: Measured heat flow profiles for NS-added cement pastes at different dosages.

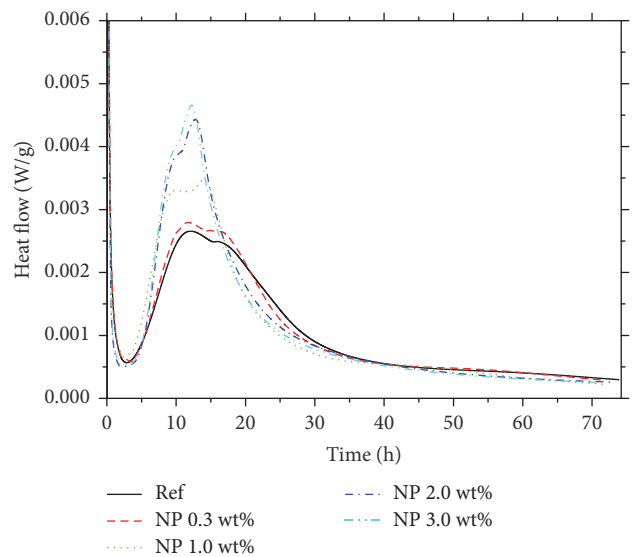


FIGURE 7: Measured heat flow profiles for NS@PCE-2-added cement pastes at different dosages.

To get a more detailed observation, as mentioned before, some characteristic values were extracted from heat flow profiles. Here, we utilize these extracted parameters to correlate with dosages. Figure 8 shows the evolution of T_A , T_B , and T_C as a function of dosages in the case of pristine NS and NP. For the case of NS (Figure 8(a)), it can be seen that there is clearly a linear regression between the dosage and T_A (or T_B or T_C). The slope of the curve associated with T_B (or T_C) is greater than that of the curve associated with T_A . This suggests that T_B or T_C is severely affected by dosages. Figure 8(b) illustrates the case of NP. From Figure 8(b), it is noted that T_A is inactive to the change in dosages, as opposed

to T_B and T_C . The trends of T_B and T_C are nearly identical; that is, they drop dramatically as dosage increases until stopping at a platform. This observation is unsurprising if we consider the hypothesis that the agglomeration of nanoparticles always existed at high dosage which makes the increase in the dosage no longer contribute to the growth in the total surface area of hydration system.

Figure 9 exhibits the relationship between the dosage and characteristic heat flow in the case of pristine NS and NP. For the case of NS, as shown in Figure 9(a), all of the three characteristic heat flows have a similar trend that escalates as a function of the dosage. They are all higher than the

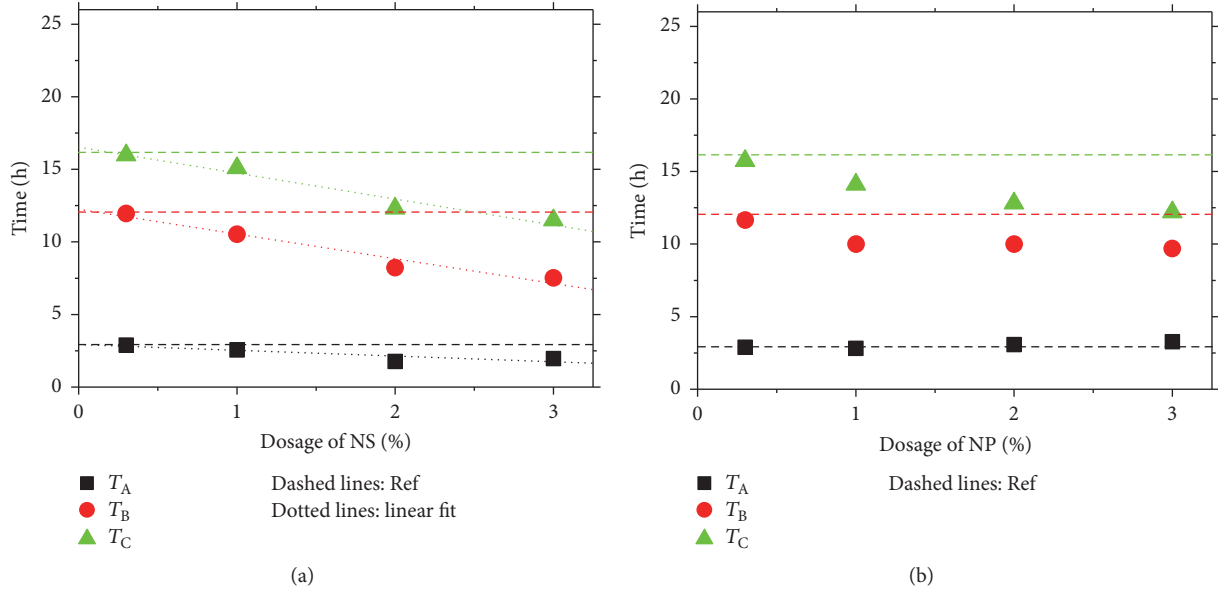


FIGURE 8: The relationship between dosage and characteristic time at peak corresponding to the measured heat flow profile: (a) NS and (b) NP.

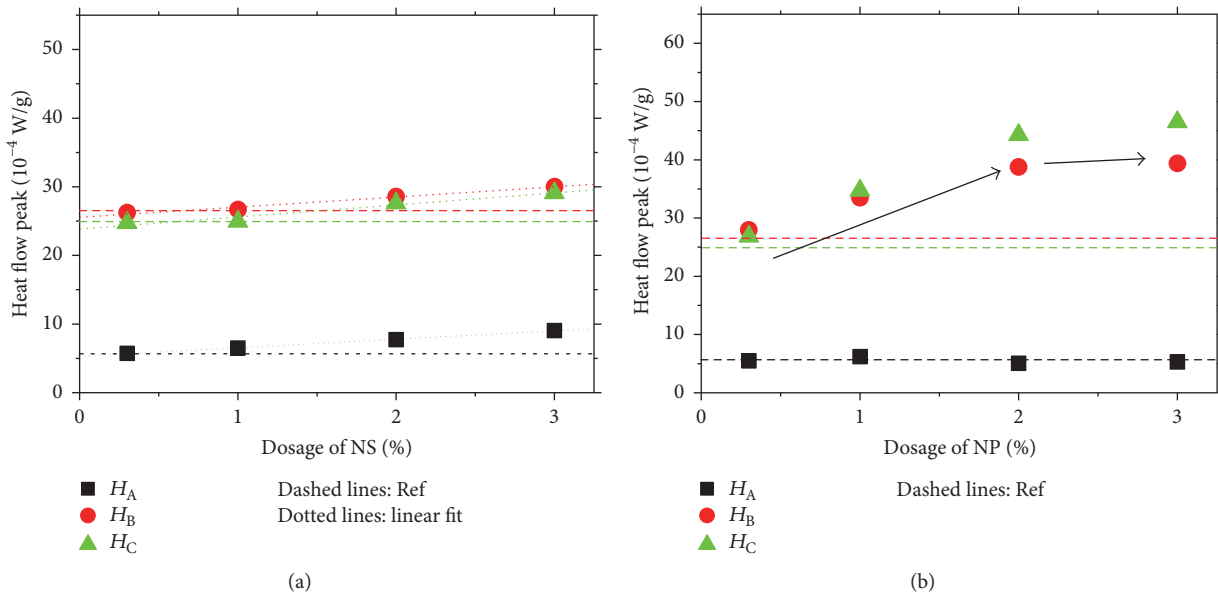


FIGURE 9: The relationship between dosage and characteristic heat flow at peak corresponding to the measured heat flow profile: (a) NS and (b) NP.

value of the reference cement pastes, if the dosage was higher than 1%, while for the case of NP, as noted in Figure 9(b), some different features could be found. For example, unlike H_A shown in Figure 9(a), H_A in Figure 9(b) seems more insensitive to the change in dosage. What is more, with the dosage rising, the fluctuations of H_B and H_C are more apparent. The linear regression seems to only exist before the dosage of 2%. These observations suggest that the physical or the chemical process of NS and NP may be controlled by different mechanisms, as the dosage increases.

3.2. Compressive Strength

3.2.1. *Effect of Nanostructure of NS@PCE.* Compressive strength is one of the most important mechanical properties of cementitious materials. Figure 10 shows the relative compressive strength evolution for cement paste prepared with four different types of nanoparticles. As noted by Figure 10, in general, regardless of the curing ages, all kinds of nanoparticles could produce an increase in the compressive strength. This effect is more prolific in the samples with NS@PCE-2.

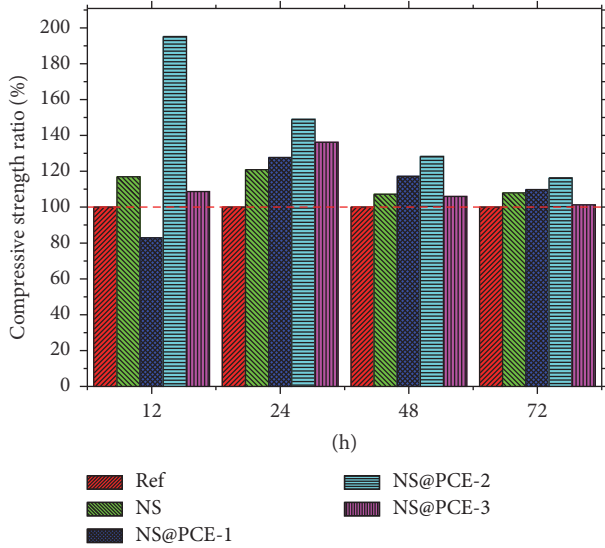


FIGURE 10: Relative compressive strength for cement pastes with nanoparticles at 1 wt%.

For example, the increase extent is as high as 125% at the age of 12 h and remains the highest at all ages. This observation may be partially ascribable to the assumption that NS@PCE-2 has the best-dispersed state in cement pastes matrix. In addition, the difference in enhancing compressive strength diminishes over time. Another interesting observation is that the strength of NS@PCE-1-added sample is lower than the reference at the age of 12 h. It is reported that NS addition would lead to high-polymerized C-S-H gels [22, 23]. For a series of NS@PCE, at specific time, they may produce C-S-H gels with different quantity or quality, which may be another mechanism accounting for compressive strength enhancement.

3.2.2. Effect of Dosage. To reveal the influence of the dosages of NS/NS@PCE-2 (NP) on the relative compressive strength, cement pastes with four dosages of 0.3, 1%, 2%, and 3% were measured. Figure 11 shows the results of samples with NS. From Figure 11, it is clearly seen that the relative compressive strength increases as a function of the dosage in all curing ages, with the maximum values produced by the dosage of 3%. This consequence is confirmed to other similar researchers reported by Nazari and Riahi [24] and Singh et al. [25]. It could be explained by the so-called filler effect or seeding effect; that is, additional surface area could offer more nucleation sites. However, the prerequisite for this interpretation is the ideal monodispersion of nanoparticles. Compared with the result of 72 h and that of 12 h, we can find that the improvement in strength is toned down over time. This may be due to the fact that the side effects of the formation of agglomeration become more obvious at later age including the following: (a) agglomeration would develop into the weakened zone which also generates many new interfacial transition zones [26] and (b) agglomeration can decrease active surface which would reduce the rate of the pozzolanic reaction.

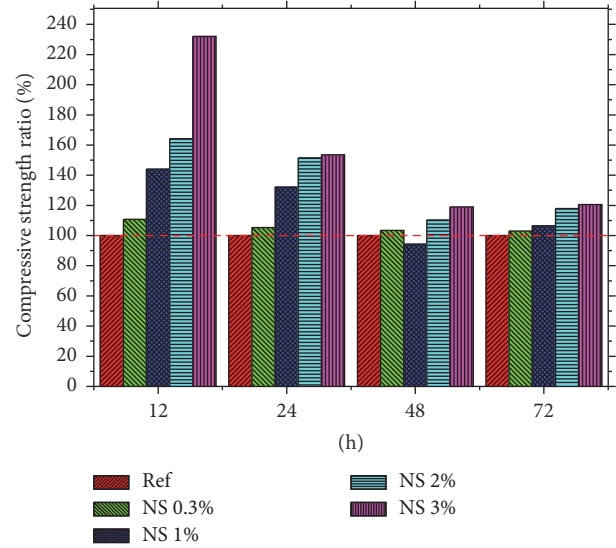


FIGURE 11: Relative compressive for NS-added cement pastes at different dosages.

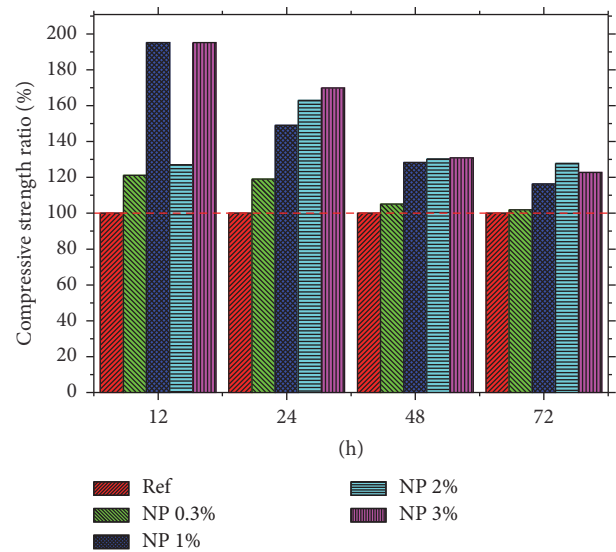


FIGURE 12: Relative compressive strength for NS@PCE-2-added cement pastes at different dosages.

The trends in strength development of samples with NP are shown in Figure 12. In general, apart from the result at the age of 12 h, the relative strength of samples increases with the dosage increasing up to 2%, while there is no appreciable disparity between the dosage of 2% and that of 3%. At the age of 12 h, the dosage of 1% has a similar improvement effect compared with that of 3%. This may be due to the fact that, at this curing time, NP fortunately achieves a better balance between lowering the agglomeration and enhancing the pozzolanic reaction. According to the previous research [18], it is rationalized that NP would have a better dispersion state in cement pastes matrix than NS. Then higher strength would be obtained by samples with NP at the same dosage.

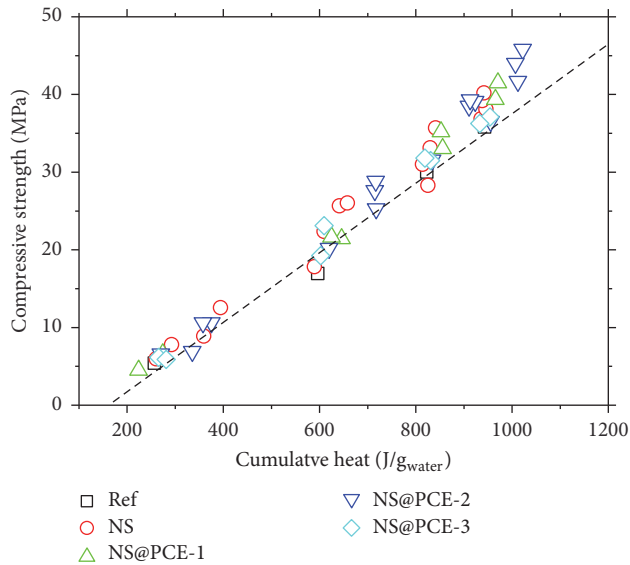


FIGURE 13: Measured compressive strength versus cumulative heat release, normalized by initial water content.

This speculation could be confirmed by comparing the results in Figures 11 and 12. Based on these results, it can be concluded that NP could enhance the strength of cement-based materials at lower dosage, especially at the early age, compared with pristine NS.

3.2.3. Relationship between Compressive Strength and Cumulative Heat. It is attractive to acquire the mechanical property development by adopting the data from calorimeter isothermal measurement. Some researchers [27–29] unambiguously showed that there is a strong correlation between the heat evolution and compressive strength in the hydration system with supplementary materials, such as fly ash and limestone. To verify this correlation in hydration system with nanoparticles, the relationship between compressive strength and cumulative heat releases is explored as shown in Figure 13. All the hydration heat data are extracted from the experimental results in Section 3.1. It should be noted that the measured heat is normalized by initial mixture water, which is a sign of the initial space surrounded by the cement grain and would be filled by hydration product over time. As noted in Figure 13, a reasonable correlation is achieved, where the majority of data points fall into the acceptable bound of the linear best fit line. No matter data come from NS-added sample or NS@PCE-added sample, they present a lower deviation when cumulative heat value is below 600 J/g. It is meaningful to get the information of linear correlation, because it suggests that the mechanical properties of samples with NS or NP can be inferred by heat evolution data. This is also a worthwhile complement to the research of the nanoparticles added hydration system.

3.3. Microstructure. To get some more details about modification effect, X-ray diffraction analysis was carried out to measure samples with 1 wt% NS and 1 wt% NP at the ages of

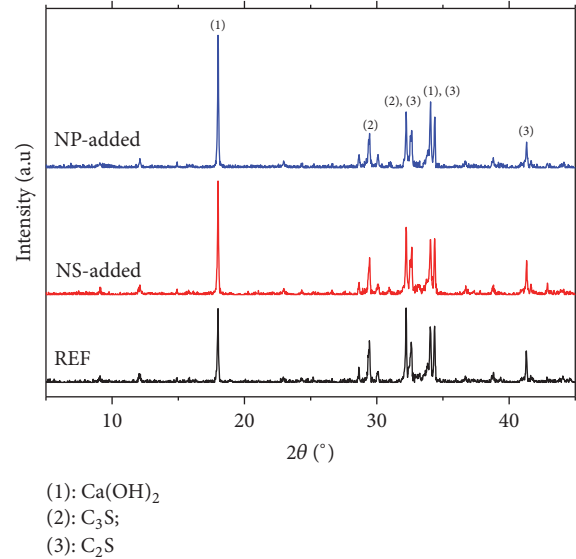


FIGURE 14: XRD patterns of cement pastes with nanoparticles at 6 h.

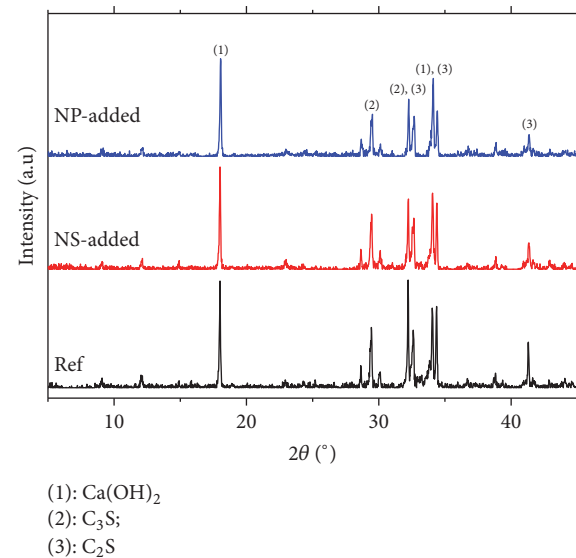


FIGURE 15: XRD patterns of cement pastes with nanoparticles at 12 h.

6 h and 12 h, and the results are shown in Figures 14 and 15, respectively. The main crystalline phases are identified and marked including calcium hydroxide (CH), dicalcium silicate (C_2S), and tricalcium silicate (C_3S). C_2S and C_3S are the two most important mineral phases of unhydrated cement. The source of CH is same for all samples as generated by the hydration process of cement. However, the final amount of CH is not just influenced by hydration process. For reference sample, the amount of CH is only controlled by hydration process of C_2S and C_3S , while for the samples with NS or NP, another chemical process, *that is*, pozzolanic reaction between nanoparticles and CH, should be considered because this reaction consumes CH. It has been documented that CH content disparity between NS-added sample and reference would first get a maximum point within few hours [26]. This

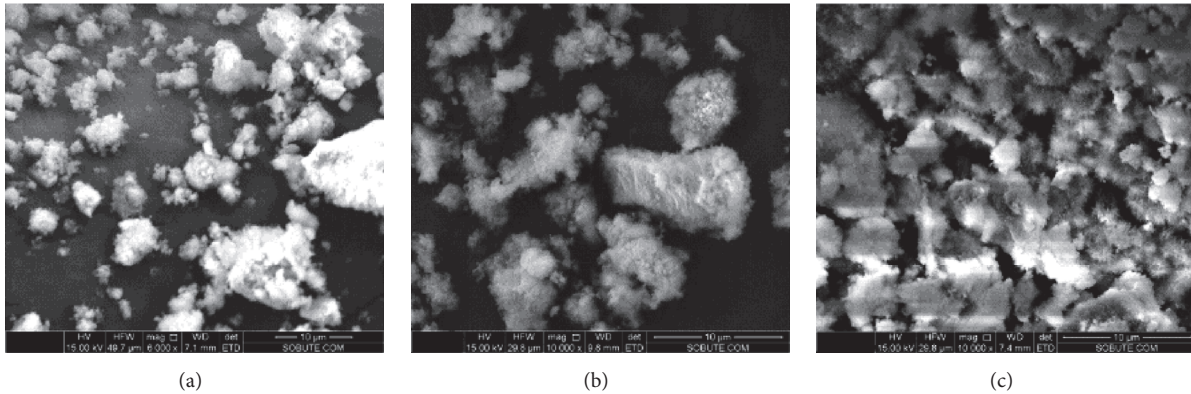


FIGURE 16: SEM images of cement pastes with nanoparticles at 6 h: (a) Ref, (b) NS, and (c) NP.

is due to the hydration acceleration effect of NS. After the maximum point, the CH content disparity would decrease steadily due to the effect of pozzolanic reaction. These trends are also observed in NP-added samples as noted in Figures 14 and 15. As shown in Figure 14, at 6 h, CH peak in the NP-added samples is more intense than that in other samples. This indicates again that both NS and NP could accelerate the hydration and the effect of NP could be more pronounced. For three type samples at 12 h (Figure 15), there is no significant difference in the CH peak. It suggests that pozzolanic reaction has been shown to be more apparent in the samples with NS or NP. From the fact that CH content in NP-added sample is higher than that in NS-added sample at 6 h while they are approximately equal at 12 h, we can infer that the NP may have a greater ability to consume CH by pozzolanic reaction at later age.

Since main hydration product C-S-H is hard to be detected by XRD due to its amorphous character, it can be identified by SEM. The morphology image of NP-added samples at 6 h was measured by SEM as shown in Figure 16 and compared with that of reference and NS-added samples. It can be seen from Figure 16(a) that irregular needle-like C-S-H appeared on the surface of cement grain resulting from the hydration of C_2S and C_3S . The amount of needle-like C-S-H improved after NS was added as shown in Figure 16(b). For sample with NP, more needle-like C-S-H can be found and some cement grains' surfaces have been filled with these products (see Figure 16(c)). The results further verify the discussion mentioned before demonstrating that NP could boost up cement hydration more effectively than NS.

3.4. Discussion

3.4.1. Seeding Effect. Fine particles are known to accelerate cement hydration. It is generally accepted that this acceleration effect has been attributed to additional surface which provides extra nucleation sites for C-S-H phases. In particular, as shown in Figures 17(a) and 17(b), in blank cement paste, it is usually hypothesized that the nucleus of C-S-H can only grow on the surface of cement grains, while, in the cement with NS, expect for cement grain surface, the

nanoparticle surface also can be the place where nucleus precipitated (see Figures 17(c) and 17(d)). Normally, the diameter of nanoparticle is about three orders of magnitude smaller than that of cement grain; therefore total surface area for nucleation sites would increase with the dosage of nanoparticles increasing. Oey et al. [30] and Costoya [31] have proposed that the seeding effect is proportional to the total surface of area. In this study, characteristic heat flow parameters are found to be in linearity with the dosage of NS (see Section 3.1.2); therefore it seems that seeding effect is still suitable for explaining the phenomenon of hydration acceleration by NS.

3.4.2. Relationship between Dispersion, Nucleation, and Surface Properties of Nanoparticles. According to the seeding effect theory, additional surface areas are responsible for acceleration effect, so the dispersion in cement matrix is the key problem for the application of nanoparticle. For NS, it is well monodispersed in water with a PH value of 7–9 by reason of hydrogen bonding between the surface silanol groups and the water molecules resulting in the formation of a water layer around nanoparticles [32]. Meanwhile in the solution with PH in excess of 12, the nanoparticles acquire a negative charge surface through partial deprotonation; then the hydrolyzed surface would produce electrostatic force to overcome the attractive force between nanoparticles. In cement pore solution, the dispersion issue would become more complicated with the presence of various ions such as Ca^{2+} , Na^+ , and K^+ . Among these cations, calcium ion is the most important factor affecting the stability of particles. Calcium ions of cement pore solution always present near the portlandite saturation point; in such concentration, calcium ion would affect the stability of NS by reducing the electrostatic repulsive potential. For above reasons, making a homogeneous dispersion of nanoparticles in cement paste matrix is a challenging task. In the worst condition, the so-called nanoparticles filled in cement pastes always contain certain of loosened clusters of particles, leading to properties even worse than blank cement pastes. For NS, it is difficult to further improve its dispersion by tuning DLVO interaction because of calcium ions constantly generated by hydration process.

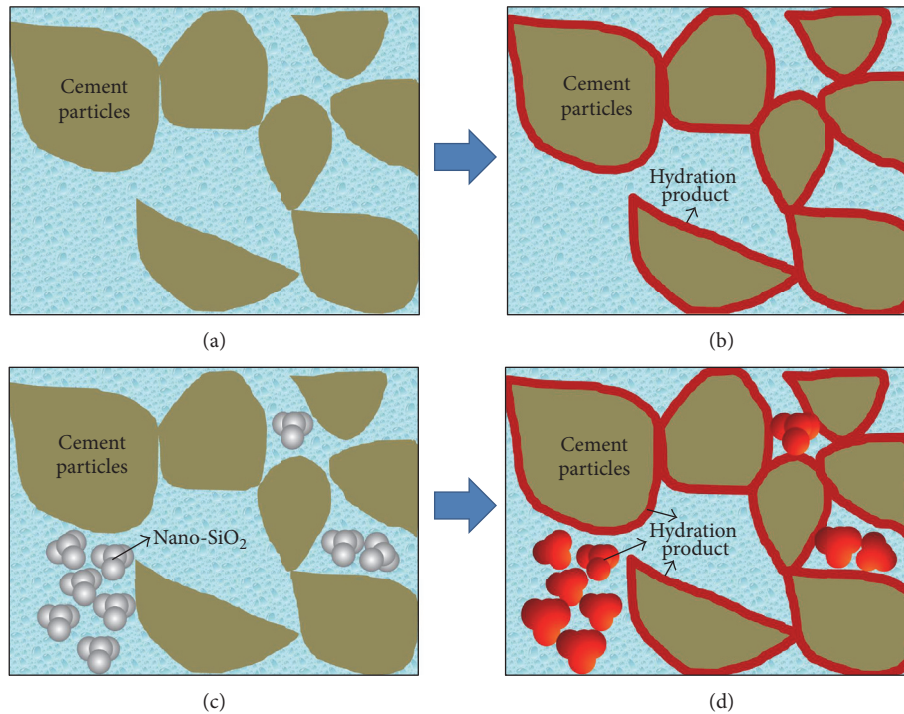


FIGURE 17: Schematic representation for seeding effect.

The surface modification method brings hope for NS to mitigate the agglomeration phenomenon in the solution with complex ions, because the polymer on particle surface could provide the extra potential barrier. This barrier comes from the steric repulsive force related to the conformation of polymer itself. For NS@PCE, it was designed based on the idea of surface modification. In previous study, as expected, NS@PCE could form a more stable nanosuspension than pristine NS in portlandite saturation, and the stability degree is improved with the shell-core ratio increasing [18]. Although the polymer on the surface could improve the dispersion property, on the other hand, the surface modification of NS also has the side effect that decreases pozzolanic reactivity of nanoparticles, which is due to the fact that the polymer on the surface would shield the attack of alkaline ion. As proposed by Thomas [13], NS itself is not regarded as the nucleating agent; it should first react with calcium hydroxide to generate the C-S-H nucleus. According to this theory, low pozzolanic reactivity accounts for low growth kinetics of C-S-H nucleus. That means that the benefit of good dispersion may be covered, if the pozzolanic reactivity of NS@PCE is too small. To be more specific, a high shell-core ratio would bring about a significant drawback for NS@PCE as verified by the hydration heat results of NS@PCE-3-added samples. Based on the discussion above, the schematic drawing for the dispersion and nucleation process of NS and NS@PCE is demonstrated in Figure 18.

In general, the effect of surface modification has two sides. It is important to keep in mind that if accelerating cement hydration is our core need, there is always a balance between initial dispersion and pozzolanic reactivity for NS@PCE.

We should balance trade-offs among those two effects to design an optimal shell-core ratio for NS@CPE. In addition, this interpretation about balance would also inspire us to engineer the NS@PCE with high shell-core ratio to make NS@PCE conforming to the requirement of retarding cement hydration.

4. Conclusions

This paper has described the generalized influence of NS@PCE on accelerating the rate of cement hydration. Factors of the dosage and disparity in surface properties (quantified by shell-core ratio) are distinguished and analyzed in the light of their influence on hydration rate. From this study, the following conclusions can be drawn:

- (1) Although a series of NS@PCE and NS have a similar particle size distribution, they exhibit different influences on cement hydration. This is not in agreement with the traditional viewpoint that the acceleration effect is proportional to the increase of surface area provided by nanoparticles.
- (2) A moderate shell-core ratio (NS@PCE-2) shows more effect in accelerating cement hydration among a series of NS@PCE at the dosage of 1%.
- (3) The optimal dosage of NS@PCE-2 is around 2%. At the same dosage, the accelerating effect of NS@PCE-2 is more pronounced than pristine NS.

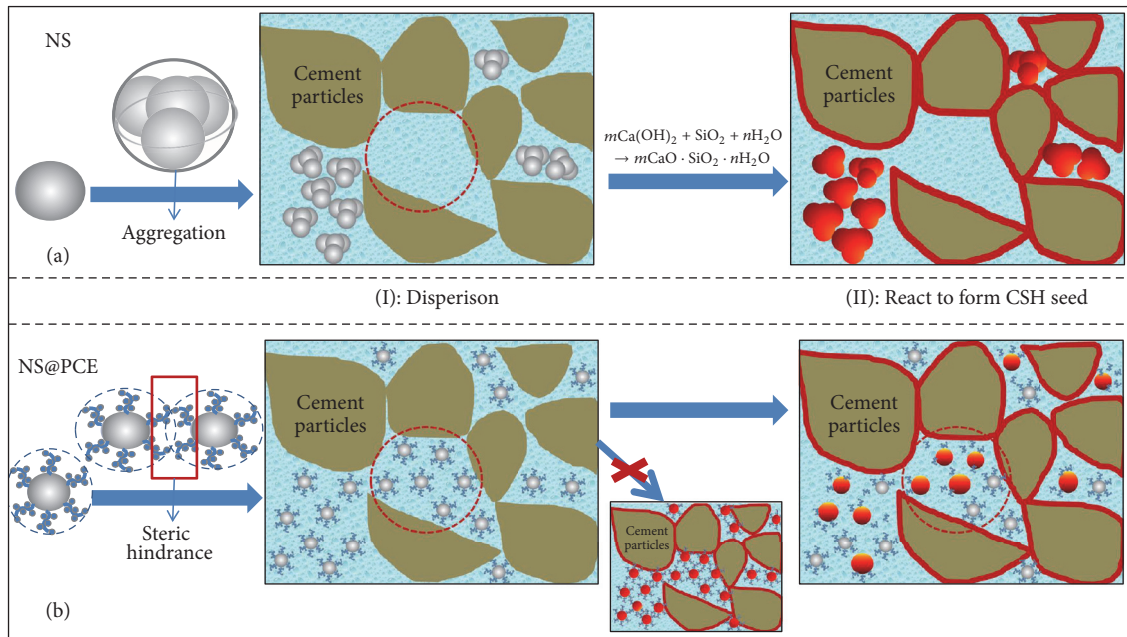


FIGURE 18: Schematic representation for dispersion and nucleation: (a) NS and (b) NS@PCE.

- (4) For cement paste with NS@PCE, there is a linear correlation between cumulative heat release and compressive strength. It suggests that the time-dependent evolution of mechanical properties in cementitious materials with NS@PCE could be estimated by heat evolution data.
- (5) A hypothesis is proposed to explain the effect of NS@PCE, which highlights a balance between initial dispersion and pozzolanic reactivity for NS@PCE. Based on this hypothesis, either accelerating effect or retarding effect could be achieved by controlling surface properties of NS.

Besides, the outcomes of this study provide new insight into controlling the cement hydration by modifying the surface property of supplementary cementitious materials.

Conflicts of Interest

The authors declare that there are no financial conflicts of interest.

Acknowledgments

The authors would like to acknowledge the financial support by the National Natural Science Foundation of China (Grants nos. 51408273 and 51438003), Excellent Doctoral Dissertations Cultivation Fund from Southeast University, and the China Scholarship Council.

References

- [1] F. Xi, S. J. Davis, P. Ciaia et al., "Substantial global carbon uptake by cement carbonation," *Nature Geoscience*, vol. 9, no. 12, pp. 880–883, 2016.
- [2] L. K. Turner and F. G. Collins, "Carbon dioxide equivalent (CO₂-e) emissions: a comparison between geopolymers and OPC cement concrete," *Construction and Building Materials*, vol. 43, pp. 125–130, 2013.
- [3] M. Liu, Z. Zhou, X. Zhang, X. Yang, and X. Cheng, "The synergistic effect of nano-silica with blast furnace slag in cement based materials," *Construction and Building Materials*, vol. 126, pp. 624–631, 2016.
- [4] T. Yehdego and S. Peethamparan, "The role of nano silica in modifying the early age hydration kinetics of binders containing high volume fly ashes," in *Nanotechnology in Construction*, pp. 399–405, Springer International Publishing, Cham, Switzerland, 2015.
- [5] P. Hou, K. Wang, J. Qian, S. Kawashima, D. Kong, and S. P. Shah, "Effects of colloidal nanoSiO₂ on fly ash hydration," *Cement and Concrete Composites*, vol. 34, no. 10, pp. 1095–1103, 2012.
- [6] Z. Rong, W. Sun, H. Xiao, and G. Jiang, "Effects of nano-SiO₂ particles on the mechanical and microstructural properties of ultra-high performance cementitious composites," *Cement and Concrete Composites*, vol. 56, pp. 25–31, 2015.
- [7] A. Nazari and S. Riahi, "Al₂O₃ nanoparticles in concrete and different curing media," *Energy and Buildings*, vol. 43, no. 6, pp. 1480–1488, 2011.
- [8] A. Nazari and S. Riahi, "The effect of TiO₂ nanoparticles on water permeability and thermal and mechanical properties of high strength self-compacting concrete," *Materials Science and Engineering A*, vol. 528, no. 2, pp. 756–763, 2010.
- [9] R. Zhang, X. Cheng, P. Hou, and Z. Ye, "Influences of nano-TiO₂ on the properties of cement-based materials: hydration and drying shrinkage," *Construction and Building Materials*, vol. 81, pp. 35–41, 2015.
- [10] M. Heikal and N. S. Ibrahim, "Hydration, microstructure and phase composition of composite cements containing nanoclay," *Construction and Building Materials*, vol. 112, pp. 19–27, 2016.

- [11] C. Lin, W. Wei, and Y. H. Hu, "Catalytic behavior of graphene oxide for cement hydration process," *Journal of Physics and Chemistry of Solids*, vol. 89, pp. 128–133, 2016.
- [12] J. J. Thomas, J. J. Biernacki, J. W. Bullard et al., "Modeling and simulation of cement hydration kinetics and microstructure development," *Cement and Concrete Research*, vol. 41, no. 12, pp. 1257–1278, 2011.
- [13] J. J. Thomas, H. M. Jennings, and J. J. Chen, "Influence of nucleation seeding on the hydration mechanisms of tricalcium silicate and cement," *Journal of Physical Chemistry C*, vol. 113, no. 11, pp. 4327–4334, 2009.
- [14] K. L. Scrivener, P. Juilland, and P. J. M. Monteiro, "Advances in understanding hydration of Portland cement," *Cement and Concrete Research*, vol. 78, pp. 38–56, 2015.
- [15] T. Oertel, U. Helbig, F. Hutter, H. Kletti, and G. Sestl, "Influence of amorphous silica on the hydration in ultra-high performance concrete," *Cement and Concrete Research*, vol. 58, pp. 121–130, 2014.
- [16] A. Bagheri, T. Parhizkar, H. Madani, and A. M. Raisghasemi, "The influence of different preparation methods on the aggregation status of pyrogenic nanosilicas used in concrete," *Materials and Structures*, vol. 46, no. 1-2, pp. 135–143, 2013.
- [17] M. Iijima and H. Kamiya, "Surface modification for improving the stability of nanoparticles in liquid media," *KONA Powder and Particle Journal*, vol. 27, pp. 119–129, 2009.
- [18] Y. Gu, Q. Ran, X. Shu, C. Yu, H. Chang, and J. Liu, "Synthesis of nanoSiO₂@PCE core-shell nanoparticles and its effect on cement hydration at early age," *Construction and Building Materials*, vol. 114, pp. 673–680, 2016.
- [19] J. W. Bullard, H. M. Jennings, R. A. Livingston et al., "Mechanisms of cement hydration," *Cement and Concrete Research*, vol. 41, no. 12, pp. 1208–1223, 2011.
- [20] H. Taylor, *Cement Chemistry*, Thomas Telford Publishing, London, UK, 1997.
- [21] G. Land and D. Stephan, "Controlling cement hydration with nanoparticles," *Cement and Concrete Composites*, vol. 57, pp. 64–67, 2015.
- [22] A. Ayuela, J. S. Dolado, I. Campillo et al., "Silicate chain formation in the nanostructure of cement-based materials," *The Journal of Chemical Physics*, vol. 127, no. 16, Article ID 164710, 2007.
- [23] J. S. Dolado, I. Campillo, E. Erkizia et al., "Effect of nanosilica additions on belite cement pastes held in sulfate solutions," *Journal of the American Ceramic Society*, vol. 90, no. 12, pp. 3973–3976, 2007.
- [24] A. Nazari and S. Riahi, "The effects of SiO₂ nanoparticles on physical and mechanical properties of high strength compacting concrete," *Composites Part B: Engineering*, vol. 42, no. 3, pp. 570–578, 2011.
- [25] L. P. Singh, D. Ali, and U. Sharma, "Studies on optimization of silica nanoparticles dosage in cementitious system," *Cement and Concrete Composites*, vol. 70, pp. 60–68, 2016.
- [26] P. Hou, S. Kawashima, D. Kong, D. J. Corr, J. Qian, and S. P. Shah, "Modification effects of colloidal nanoSiO₂ on cement hydration and its gel property," *Composites Part B: Engineering*, vol. 45, no. 1, pp. 440–448, 2013.
- [27] D. P. Bentz, T. Sato, I. De La Varga, and W. J. Weiss, "Fine limestone additions to regulate setting in high volume fly ash mixtures," *Cement and Concrete Composites*, vol. 34, no. 1, pp. 11–17, 2012.
- [28] A. Kumar, T. Oey, S. Kim et al., "Simple methods to estimate the influence of limestone fillers on reaction and property evolution in cementitious materials," *Cement and Concrete Composites*, vol. 42, pp. 20–29, 2013.
- [29] D. P. Bentz, A. S. Hansen, and J. M. Guynn, "Optimization of cement and fly ash particle sizes to produce sustainable concretes," *Cement and Concrete Composites*, vol. 33, no. 8, pp. 824–831, 2011.
- [30] T. Oey, A. Kumar, J. W. Bullard, N. Neithalath, and G. Sant, "The filler effect: the influence of filler content and surface area on cementitious reaction rates," *Journal of the American Ceramic Society*, vol. 96, no. 6, pp. 1978–1990, 2013.
- [31] M. Costoya, *Kinetics and Microstructural Investigation on the Hydration of Tricalcium Silicate*, École Polytechnique Fédérale de Lausanne, Lausanne, Switzerland, 2008.
- [32] Y. Gu, Z. Wei, Q. Ran, X. Shu, K. Lv, and J. Liu, "Characterizing cement paste containing SRA modified nanoSiO₂ and evaluating its strength development and shrinkage behavior," *Cement and Concrete Composites*, vol. 75, pp. 30–37, 2017.

Research Article

Flexural and Shear Behaviors of Reinforced Alkali-Activated Slag Concrete Beams

Kwang-Myong Lee,¹ Sung Choi,¹ Jinkyoo F. Choo,² Young-Cheol Choi,³ and Sung-Won Yoo⁴

¹Department of Civil and Environmental System Engineering, Sungkyunkwan University, 2066 Seobu-ro, Jangan-gu, Suwon 16419, Republic of Korea

²Department of Energy Engineering, Konkuk University, 120 Neungdong-ro, Gwangjin-gu, Seoul 05029, Republic of Korea

³Department of Architectural Engineering, Gachon University, 1342 Seongnamdaero, Sujeong-gu, Seongnam-si, Gyeonggi-do 13120, Republic of Korea

⁴Department of Civil and Environmental Engineering, Gachon University, 1342 Seongnamdaero, Sujeong-gu, Seongnam-si, Gyeonggi-do 13120, Republic of Korea

Correspondence should be addressed to Sung-Won Yoo; imysw@gachon.ac.kr

Received 4 April 2017; Revised 24 May 2017; Accepted 11 June 2017; Published 20 July 2017

Academic Editor: Tung-Chai Ling

Copyright © 2017 Kwang-Myong Lee et al. This is an open access article distributed under the Creative Commons Attribution License, which permits unrestricted use, distribution, and reproduction in any medium, provided the original work is properly cited.

The material properties of cement-zero concrete using alkali-activators have been studied extensively as the latest response to reduce the CO₂ exhaust of the cement industry. However, it is also critical to evaluate the behavior of reinforced concrete beams made of alkali-activated slag (AAS) concrete in terms of flexure and shear to promote the applicability of AAS concrete as structural material. Accordingly, nine types of beam specimens with various ratios of tensile steel and stirrup were fabricated and subject to bending and shear tests. The results show that the flexural and shear behaviors of the reinforced AAS concrete members are practically similar to those made of normal concrete and indicate the applicability of the conventional design code given that the lower density of slag is considered. In addition, a framework using the elastic modulus and stress-strain relation from earlier research is adopted to carry out nonlinear finite element analysis reflecting the material properties of AAS concrete. The numerical results exhibit good agreement with the experimental results and demonstrate the validity of the analytical model.

1. Introduction

The cement and concrete industries count among the primary producers of CO₂ and prediction forecasts that the worldwide consumption of cement will continue to increase yearly by 2.5 to 5.8% during the second and third decades of the 21st century [1]. As an attractive solution to prevent or at least delay the global warming caused by the emission of greenhouse gases, research was implemented worldwide to fabricate cement-zero concrete using slag powder, fly ash, and alkali-activators [2–4]. Experimental works especially reported that concrete using alkali-activated slag (AAS) instead of blast-furnace slag could develop high early strength higher than 50 MPa even at ambient temperature and resist chemical attack by sulfates [5, 6].

To date, studies focused essentially on the material properties of cement-zero concrete using AAS like the strength, drying shrinkage, autogenous shrinkage, and durability. For example, Oh et al. [7] studied the autogenous shrinkage of fresh AAS mortar according to the water-to-binder ratio to assess the effect of the rapid alkaline reaction occurring at early age caused by the introduction of large amount of AAS. Collins and Sanjayan [8] compared the workability and equivalent one-day strength of AAS concrete to those of Portland cement concrete at normal curing temperature and reported discrepancies in the mechanical properties like the compressive strength, elastic modulus, flexural strength, drying shrinkage, and creep. Sofi et al. [9] considered six inorganic polymer concrete (IPC) mixes to evaluate the effects of the inclusion of coarse aggregates and granulated

blast furnace slag. These authors carried out tests and found out that, in most cases, the engineering properties developed by the IPC mixes compared favorably to those predicted by the relevant standards for concrete mixtures. Atiş et al. [10] applied liquid sodium silicate, sodium hydroxide, and sodium carbonate (SC) at different sodium concentrations to produce AAS concrete mixes and recommended using SC as activator for slag mortar since it could achieve adequate strength and setting times and shrinkage comparable to Portland cement concrete. Using such SC activator, Melo Neto et al. [11] examined the relationship between the hydration, unrestrained drying, and autogenous shrinkage of AAS mortar specimens. These authors reported the critical influence of the amount of activator on the drying and autogenous shrinkages, and the significant contribution of the autogenous shrinkage on the total shrinkage. Besides, Puertas et al. [12] analyzed the behavior of AAS mortars after carbonation. The results indicated that AAS mortars were more intensely and deeply carbonated than Portland cement mortars.

These previous studies gave insight on the adequate mix to achieve AAS mortars exhibiting material properties comparable to Portland cement mortars. However, research shall also be implemented on the elastic modulus, stress-strain relations, and behavior of structural members to exploit AAS concrete as structural material. Recently, Lee and Seo [13] and Choi et al. [14] evaluated experimentally the flexural and shear behaviors of AAS concrete beams but without attempting to model these behaviors at once and analytically.

Accordingly, this study investigates experimentally and analytically the structural behavior of AAS concrete members and intends to verify the applicability of existing cement-based concrete design code to AAS concrete. To that goal, the behavior of reinforced concrete beams made of AAS concrete is evaluated experimentally in terms of both flexure and shear. In addition, the elastic modulus and stress-strain relation of AAS concrete for 50-MPa precast members obtained experimentally are used to perform the finite element analysis of the flexural members and shear members and the numerical results are compared to the experimental data.

2. Test Setup

2.1. Materials. Ground granulated blast furnace slag (GGBFS) with density of 2.90 g/cm^3 , fineness of $4,365 \text{ cm}^2/\text{g}$, and basicity of 1.78 is used as binder. River sand with density of 2.58 g/cm^3 and fineness modulus of 2.92 is used as fine aggregate. Crushed stone with density of 2.62 g/cm^3 and maximum size of 19 mm is adopted as coarse aggregate. Two types of alkali-activators that are sodium hydroxide (98% purity) and industrial water glass with $\text{SiO}_2 = 28.8\%$ and $\text{Na}_2\text{O} = 9.3\%$ are used to activate the GGBFS. These two products are added to realize $\text{Na}_2\text{O} = 6.0\%$ and alkali modulus $M_s (= \text{SiO}_2/\text{Na}_2\text{O})$ of 1.0 with respect to the mass of slag. Moreover, polycarbonate superplasticizer is adopted to secure the fluidity of AAS concrete.

2.2. Characteristics of Concrete and Reinforcement. Table 1 arranges the mix proportions of AAS concrete prepared for

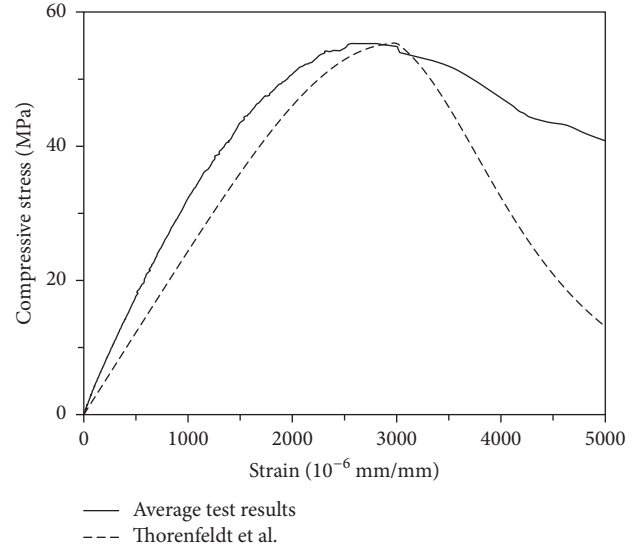


FIGURE 1: Stress-strain relationship of considered AAS concrete in compression.

50-MPa precast products and used for the fabrication of the beam specimens. In Table 1, W/B stands for water-to-binder ratio, S/a for fine-to-aggregate ratio, and W for water. Table 2 lists the properties of fresh AAS concrete together with the elastic modulus and strength of AAS concrete at 28 days. The compressive strength at 3 days is 32 MPa and the compressive strength and elastic modulus at 28 days are 55.3 MPa and 31.5 GPa, respectively.

Figure 1 plots the stress-strain relationship of AAS concrete in compression. The value of 0.003 obtained for the ultimate compressive strain of AAS concrete appears to be similar to that of ordinary Portland cement (OPC). The test results are also compared with the values given by the following analytical model suggested by Thorenfeldt et al. [16] for OPC.

$$f_c = f_{cm} \times \frac{\epsilon_c}{\epsilon_{cm}} \times \frac{n}{n - 1 + (\epsilon_c/\epsilon_{cm})^{nk}}, \quad (1)$$

where f_c and ϵ_c are strength and strain of concrete, respectively; f_{cm} is peak stress (MPa); ϵ_{cm} is strain at peak stress; and $n = 0.8 + (f_{cm}/17)$ with $k = 0.67 + (f_{cm}/62)$ if $\epsilon_c > \epsilon_{cm}$ and $k = 1$ if $\epsilon_c \leq \epsilon_{cm}$.

Figure 1 shows good agreement of the stress-strain relationship between the test results and the model of Thorenfeldt et al. [16] up to the ultimate strain. However, AAS concrete exhibits more ductile behavior than the analytical model beyond the ultimate strain.

Besides, the tensile reinforcement and stirrup are, respectively, made of steel SD500 and SD400 of which average yield strengths derived from direct tensile test are 499.6 MPa and 419.2 MPa [13, 14]. Tests were performed on $\phi 100 \times 200$ mm cylinders fabricated to examine the stress-strain relation and derive the elastic modulus of AAS concrete.

2.3. Test Variables. For the flexural test, three levels of reinforcement ratio (balanced steel ratio of 76, 58, and 43%) were

TABLE 1: Mix proportions of AAS concrete.

W/B (%)	S/a (%)	Unit mass (kg/m ³)						
		W	GGBFS	Fine aggregate	Coarse aggregate	Water glass	NaOH	Superplasticizer
45	50	165	367	855	869	73	19	3.67

TABLE 2: Properties of AAS concrete.

Fresh concrete			Hardened concrete (28 days)		
Slump (mm)	Air content (%)	Compressive strength (MPa)	Elastic modulus (GPa)	Splitting tensile strength (MPa)	
165	3.1	55.3	31.5	3.9	

selected as test variables to examine the flexural behavior of the AAS concrete specimens for 50-MPa precast products. Therefore, 3 types of beam specimens were fabricated. In the specimens, the stirrups (D10) are arranged densely with spacing of 70 mm to prevent shear failure. Moreover, three levels of tensile reinforcement ratio (balanced steel ratio of 76, 58, and 43%) and 2 levels of stirrup spacing ($(1/2)d$, no stirrup) were chosen as test variables of the beam specimens for the shear test. Here, six types of beam specimens were fabricated for the shear tests.

2.4. Details of Test Specimens. Table 3 lists the beam specimens with their designation and corresponding test variables for the examination of the flexural and shear behaviors. Figure 2 shows the reinforcement details and dimensions of the beam specimens. Table 3 gives the detailed dimensions of the specimens. Figure 2(b) illustrates the layout of the sensors for the measurement of the steel and concrete strains and the center deflection during the loading test. Figure 3 pictures a completed beam specimen installed for loading test.

3. Test Results and Discussion

3.1. Flexural Behavior of AAS Concrete Members. Table 4 lists the crack load, steel yield load, and ultimate load measured in the AAS concrete members during the bending test. All the specimens failed by flexure and the load bearing capacity increased with larger tensile steel ratio. The ratio of the ultimate load to the steel yield load ranges between 1.15 and 1.41. All the specimens exhibit similar crack load because the members were fabricated using the same AAS concrete.

Figure 4 plots the load-deflection curves of the flexural members. During the increase of the load, all the specimens develop deflection quasi-proportional to the load. Then, the slope of the curves experiences steep variation after the yielding of the tensile steel. The linear part of the curves especially becomes longer with higher tensile steel ratio. Finally, brittle failure occurs after the ultimate load with steep loss of the load. This indicates that the behavior of the AAS concrete beams depends sensitively on the steel ratio similarly to the beams made of normal concrete with OPC.

Figure 5(a) plots the load-strain curves of the tensile steel in the flexural members. The strain remains minimal under loading smaller than the crack load and increases linearly with larger load beyond the crack load. Moreover, the strain tends to enlarge significantly after yielding of the

tensile steel. Figure 5(b) plots the load-compressive strain curves of concrete in the flexural members. The strain ϵ_0 at maximum stress ranges between 0.00250 and 0.00285, and the ultimate strain ranges between 0.00250 and 0.00290. The ultimate strain is relatively smaller than the theoretical value of 0.0038 but the peak strain ϵ_0 is comparable to that of the experimental stress-strain curve.

Figure 6 compares the ultimate moments of the flexural members to those provided by the following equation. This equation assumes the yielding of steel.

$$M_u = 0.9d \times A_s \times f_y, \quad (2)$$

where d is effective depth of cross section; A_s is nominal area of reinforced bar; and f_y is yield stress.

Figure 6 shows good agreement between the experimental and computed ultimate moments with the experimental values larger by 3% to 9% than the predictions. This verifies the similar flexural behavior developed by the AAS concrete members and the OPC members.

3.2. Shear Behavior of AAS Concrete Members. Compared to a previous paper presented by the authors of [14], three additional members were fabricated and tested to complement erroneous data. Table 5 arranges the flexural crack and shear crack loads, the yield loads of the tensile steel and stirrup, and the ultimate loads obtained from the shear failure tests conducted at 28 days on the fabricated specimens. As shown in Figure 7, shear failure occurred in all the members except specimen S19-0.5d. The distinction between the shear failure and the flexural failure was done considering comprehensively the yielding of the stirrups, the eventual reaching of the ultimate strain by the flexural compressive strain of concrete, and the size of the shear strain of concrete.

The loads generating flexural cracking were similar in the six test members, which is attributable to the use of concrete with the same compressive strength in all the specimens. Besides, the members reinforced with stirrups experienced shear cracking at slightly larger load than the members without stirrup. Moreover, the shear crack load appears to be larger with higher tensile steel ratio. This can be explained by the Dowel action of the tensile steel. In other words, the Dowel action of the tensile steel delays the initiation of shear cracking as much as the tensile steel ratio is large. For the members with stirrups, the yield loads of the tensile steel become larger with higher tensile steel ratio and the ratio of

TABLE 3: Designation of beam specimen type and corresponding test variables.

Designation	Tensile steel (A_s)	Compression steel (A'_s)	D10 stirrup spacing (mm)	Tensile steel ratio
Flexure				
F25	3-D25			0.0304
F22	3-D22		70	0.0232
F19	3-D19			0.0172
Shear				
S25-0.5d	3-D25	2-D16		0.0304
S22-0.5d	3-D22		125	0.0232
S19-0.5d	3-D19			0.0172
S25-0	3-D25			0.0304
S22-0	3-D22		0	0.0232
S19-0	3-D19			0.0172

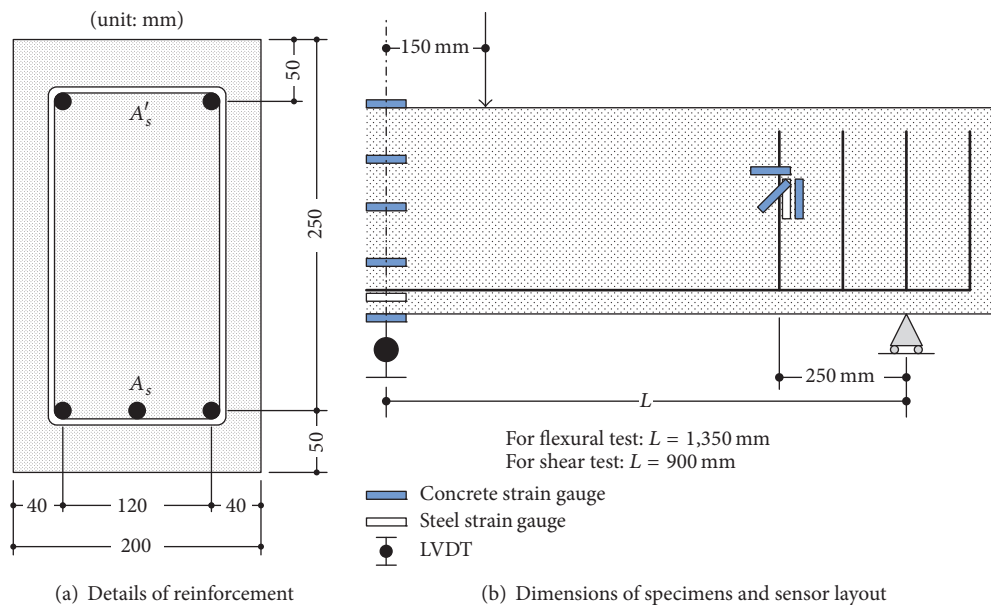


FIGURE 2: Cross-sectional details and sensor layout of AAS concrete beam specimens.



FIGURE 3: Setup for flexural test of AAS concrete beam specimen.

the ultimate load to the yield load of the tensile steel ranges between 1.09 and 1.58.

Figure 8 plots the load-deflection curves obtained from the shear test of the beam specimens. All the curves are quasi-linear before early cracking and, beyond that point, increase nonlinearly until the ultimate state. It appears that the tensile steel ratio has significant influence on the structural behavior of the beams. The shear behavior of the AAS concrete beam specimens is similar to that of the beams made of normal concrete. The specimens without stirrup especially failed as soon as the ultimate load was attained. Note that the specimens with stirrups experienced brittle failure practically without ductile behavior due to the minimum arrangement of stirrups adopted in this study. This means that, when shear failure occurs in absence of stirrup (specimens S25-0 and S22-0), the member shows common recovery of its resistance to shear owing to the Dowel action even after the first strength degradation. However, specimen S19-0 experienced flexural

TABLE 4: Crack, yield and ultimate loads and corresponding center displacement of flexural test specimens.

Member	Crack load (kN)	Yield		Ultimate		Ultimate/Yield		Failure mode
		Load (kN)	Deflection (mm)	Load (kN)	Deflection (mm)	Load ratio	Deflection ratio	
F25	20.6	272.5	13.8	313.4	18.1	1.15	1.31	Flexure
F22	24.4	171.9	10.8	242.3	24.5	1.41	2.27	Flexure
F19	22.4	155.6	10.9	188.4	23.3	1.21	2.14	Flexure

TABLE 5: Crack, yield, and ultimate loads of shear test specimens.

Member	Crack load (kN)		Yield load of tensile steel, a (kN)	Ultimate load, b (kN)	b/a	Failure mode
	Flexure	Shear				
S25-0.5d	34.6	163.2	228.5	249.6	1.09	Shear
S22-0.5d	30.9	152.2	144.6	228.3	1.58	Shear
S19-0.5d	25.1	134.0	127.5	176.5	1.38	Flexure
S25-0	30.7	125.9	—	85.3	—	Shear
S22-0	28.2	118.6	—	100.8	—	Shear
S19-0	32.9	112.9	94.3	111.2	1.18	Flexural shear

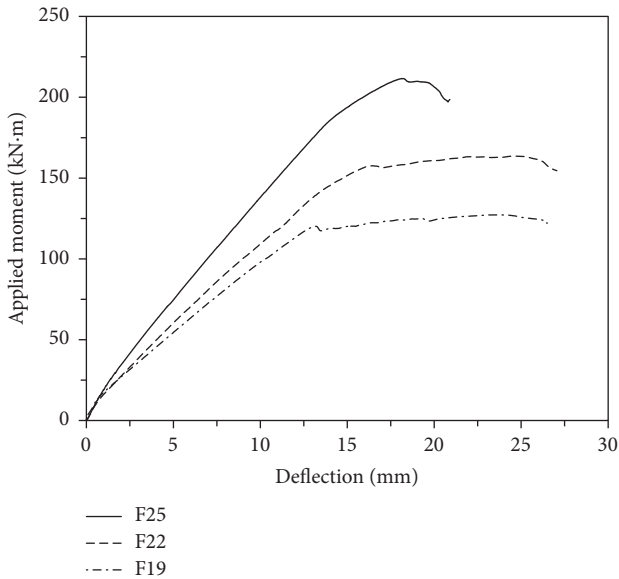


FIGURE 4: Comparison of load-deflection curves of flexural test specimens.

shear failure instead of pure shear failure due to the Dowel action of the tensile reinforcement. This explains the absence of strength recovery after the loss of early strength.

Figure 9 draws the load-strain curves of the tensile steel measured in the shear test specimens. In view of the results presented in Table 5 and Figure 9, specimens S25-0, S25-0.5d, and S22-0 experienced pure shear failure before yielding of the tensile reinforcement. Specimen S25-0.5d, as the one having the largest arrangement of tensile steel, exhibits small increase of the strain in the tensile steel because the specimen reached the ultimate load following the occurrence of shear failure immediately after yielding of the tensile reinforcement. Specimens S25-0 and S22-0 without stirrup and small arrangement of tensile steel experienced

sudden failure before yielding of the tensile steel once the load exceeded the shear strength due to the absence of stirrups.

On the other hand, the other specimens saw their tensile reinforcement deform at shear failure and without increase of the load because shear failure occurred after yielding of the tensile reinforcement. Specimens S22-0.5d and S19-0.5d with relatively small arrangement of tensile reinforcement experienced large deformation after yielding of the tensile steel and finally failed, respectively, through flexure/shear or flexure. Despite the absence of stirrups, specimen S19-0 failed through flexure/shear due to the small amount of tensile steel and developed relatively larger strain than the other specimens without stirrup.

Figure 10 plots the load with respect to the flexural compressive strain of concrete measured in the shear test specimens. Specimen S25-0.5d with large amount of tensile steel failed before concrete reached its ultimate strain due to the sudden occurrence of shear failure. Specimens S22-0.5d and S19-0.5d reinforced by stirrups and small amount of tensile steel were the only ones to develop relatively large concrete strain up to 0.0035 because of the following reasons. Specimen S22-0.5d experienced flexural failure at first due to its small amount of tensile steel and finally failed through shear due to its small amount of stirrup. Specimen S19-0.5d experienced flexural failure without shear failure due to its smaller amount of tensile steel. In addition, among the members without stirrup, specimens S25-0 and S22-0 developed small concrete strain due to the sudden occurrence of shear failure.

Figure 11(a) plots the load with respect to the shear strain measured in the stirrups. It appears that the stirrup yielded only in specimen S25-0.5d and not in the other two specimens. This is in agreement with the failure modes listed in Table 5, which indicated pure shear failure in specimen S25-0.5, flexure-shear failure in specimen S22-0.5d, and flexural failure in specimen S19-0.5d. Besides, specimens S22-0.5d and S19-0.5d that did not experience yielding of their stirrup recorded values of 0.00263 and 0.00262 for the

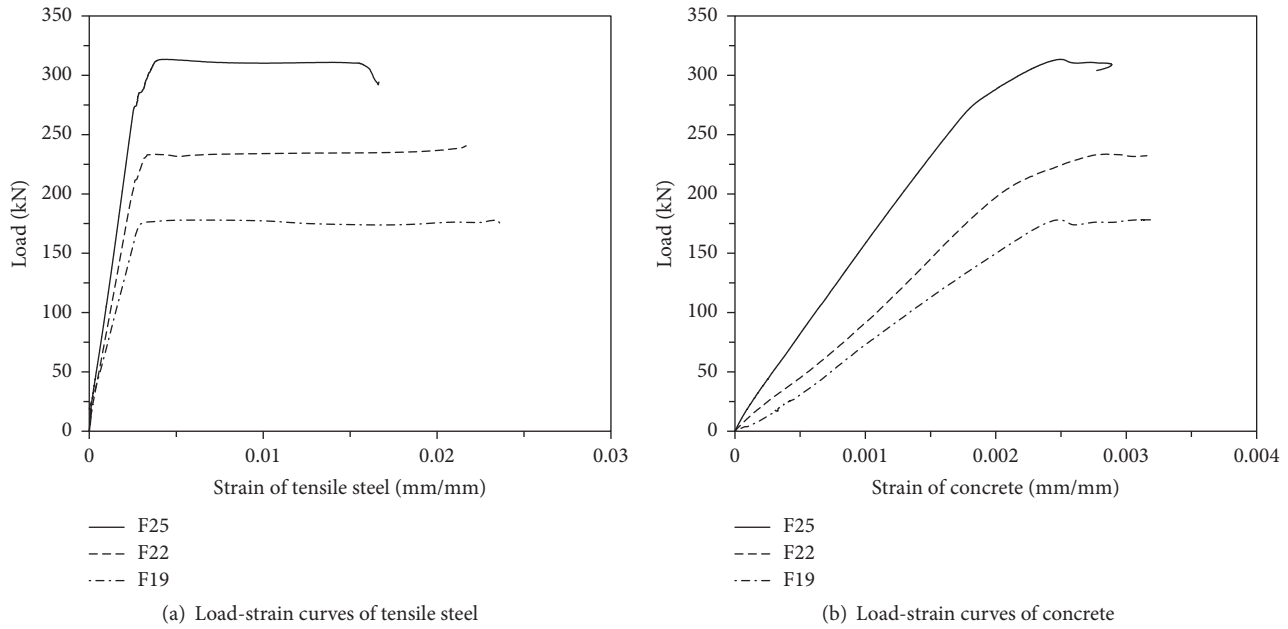


FIGURE 5: Load-strain curves of flexural test specimens according to steel ratio.

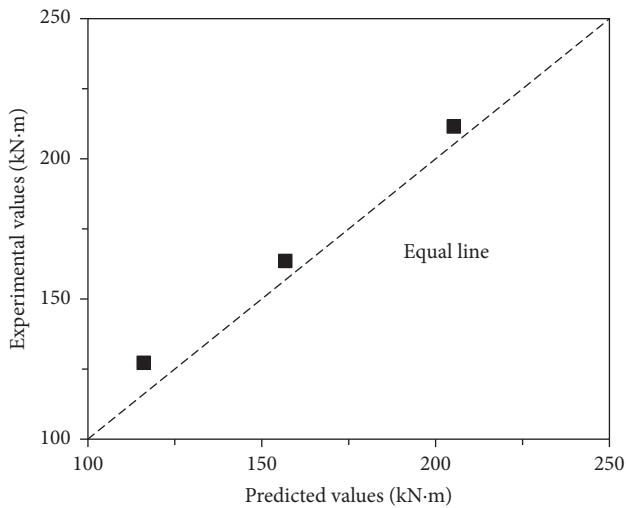


FIGURE 6: Comparison of experimental and predicted ultimate moments.

maximum strain of the stirrup, respectively. Accordingly, the stress in the stirrup based upon the uniaxial stress-strain relationship can be estimated to be 419 MPa for S25-0.5d, 367 MPa for S22-0.5d, and 366 MPa for S19-0.5d.

Figure 11(b) plots the load with respect to the principal strain measured in concrete. The members underwent shear cracking at shear strain of 0.000112 (specimen S19-0), 0.000113 (specimen S22-0), and 0.000121 (specimen S25-0). The values of the concrete principal strain were calculated by converting the strain measured by the strain gage rosette (Figure 2(b)) attached on the right-hand side of the critical section.

ACI 318-08 [17] proposes the following formulae for the calculation of the maximum shear stress v_{cr} of concrete.

Simplified Formula

$$v_{cr} = 0.16\sqrt{f_{ck}} \quad (3)$$

Elaborated Formula

$$v_{cr} = 0.16\sqrt{f_{ck}} + 17.6\frac{\rho Vd}{M} \leq 0.29\sqrt{f_{ck}}, \quad (4)$$

where f_{ck} is compressive strength of concrete; ρ is tensile steel ratio; V is shear force at the critical section; M is bending moment at the critical section; and d is effective depth.

If the compressive strength, steel ratio, shear force, and bending moment are substituted in (3), $v_{cr} = 1.19$ MPa, and v_{cr} takes values of 1.31 MPa (S19-0), 1.37 MPa (S22-0), and 1.39 MPa (S25-0) when (4) is used.

Assuming the common value of 0.17 for Poisson's ratio ν , the shear stress is calculated by multiplying the shear elastic modulus $G = E_c/[2(1 + \nu)] = 14.06$ GPa by the shear strain measured in the tests, where the experimental elastic modulus $E_c = 32.91$ GPa from Table 2. The corresponding shear stress becomes 1.58 MPa (S19-0), 1.59 MPa (S22-0), and 1.70 MPa (S25-0). This shows that the principal stress obtained experimentally is slightly larger than that predicted by the design formulae in (3) and (4).

3.3. Comparison of Experimental Shear Strength and Design Values. Table 6 compares the shear strengths obtained from the test with those suggested by the design code. In Table 6, "Test" indicates the values based upon the loads measured in the test and "Analysis" designates the values computed from the strain measured in the test. Recalling that specimen S19-0.5d failed through flexure, S19-0.5d and S19-0 are discarded because the comparison of the shear strength is meaningless

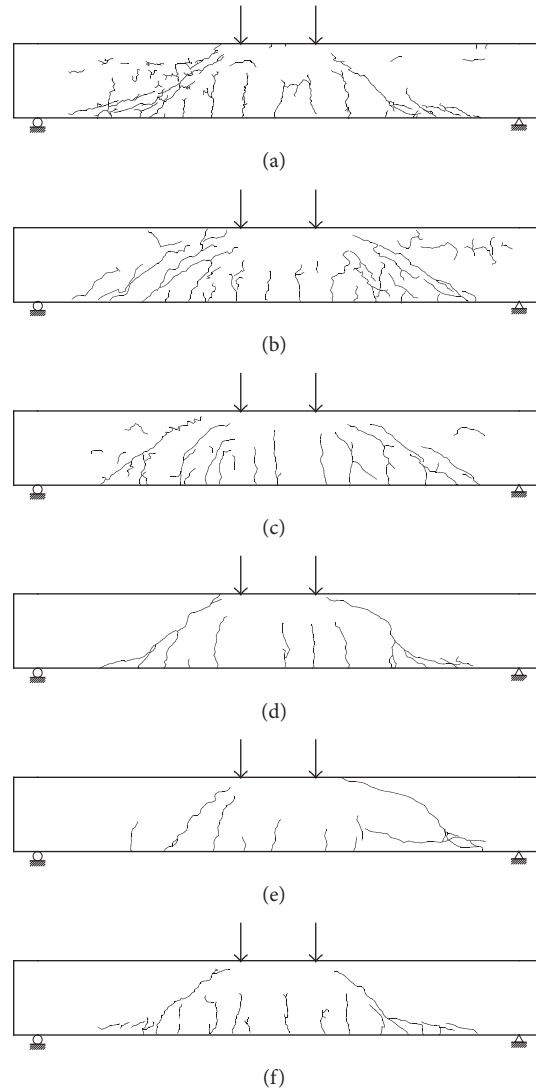


FIGURE 7: Crack pattern of shear test specimens (a) S25-0.5d, (b) S22-0.5d, (c) S19-0.5d, (d) S25-0, (e) S22-0, and (f) S19-0.

TABLE 6: Comparison of shear strengths from test and design code.

Shear strength	S25-0.5d	S25-0	S22-0.5d	S22-0
Test (kN)				
V_c	85.3	85.3	100.8	100.8
V_s	164.3	—	127.5	—
$V_u = V_c + V_s$ (incl. self-weight)	251.0	86.7	229.6	102.2
Design Code (kN)				
V_c	86.9	86.9	80.2	80.2
V_s	114.1	—	114.1	—
$V_n = V_c + V_s$	201.0	86.9	194.3	80.2
Test(V_u)/Code(V_n)	1.25	1.00	1.18	1.27
Analysis (kN)				
V_c	85.0	85.0	79.5	79.5
V_s	119.5	—	104.7	—
$V_n = V_c + V_s$ (incl. self-weight)	205.9	86.4	185.6	80.9
Test(V_u)/Analysis(V_n)	1.22	1.00	1.24	1.26

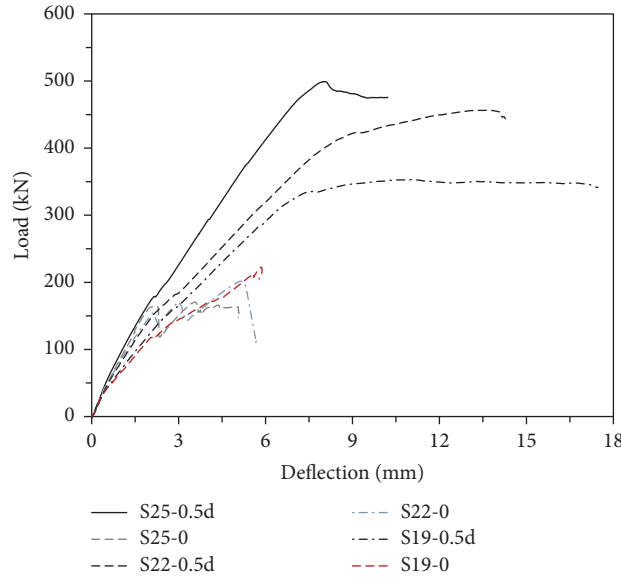


FIGURE 8: Load-deflection curves of shear test specimens.

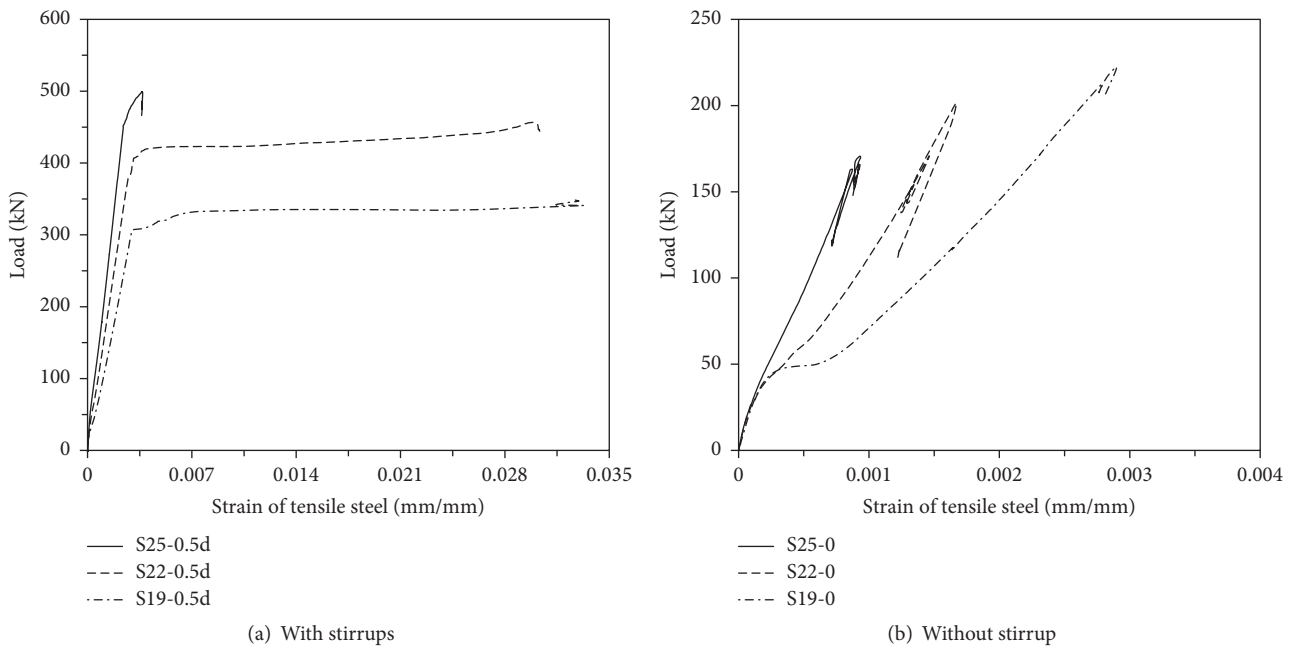


FIGURE 9: Load versus strain of tensile steel in shear test specimens.

for these members. In addition, the experimental shear force corresponds to the sum of the shear force obtained in the test and the self-weight ($1.35 \text{ kN} = 25 \times 0.3 \times 0.2 \times 1.8/2$); the shear strength V_c supported by concrete in the test is half of the ultimate load of the specimens without stirrup (S25-0, S22-0, S19-0); the shear strength V_c provided by the design code is the result of the application of (2); and the shear strength sustained by the stirrups is calculated by applying $V_s = A_v f_y d/s$, where s is the stirrup spacing. The values of V_c in “Analysis” are computed as the product of the principal

stress obtained in Figure 11(b) of Section 3.2 by the cross-sectional area of the specimen. The values of V_s in “Analysis” are calculated as the product of the strain in the stirrup obtained in Figure 11(a) of Section 3.2 by the cross-sectional area of the reinforcement.

The ratio of the experimental value to the value predicted by the design code ($\text{Test}(V_u)/\text{Code}(V_n)$) ranges between 1.00 and 1.27 and that of the experimental value to the analytic value calculated from the experimental strain ($\text{Test}(V_u)/\text{Analysis}(V_n)$) ranges between 1.00 and 1.26, which

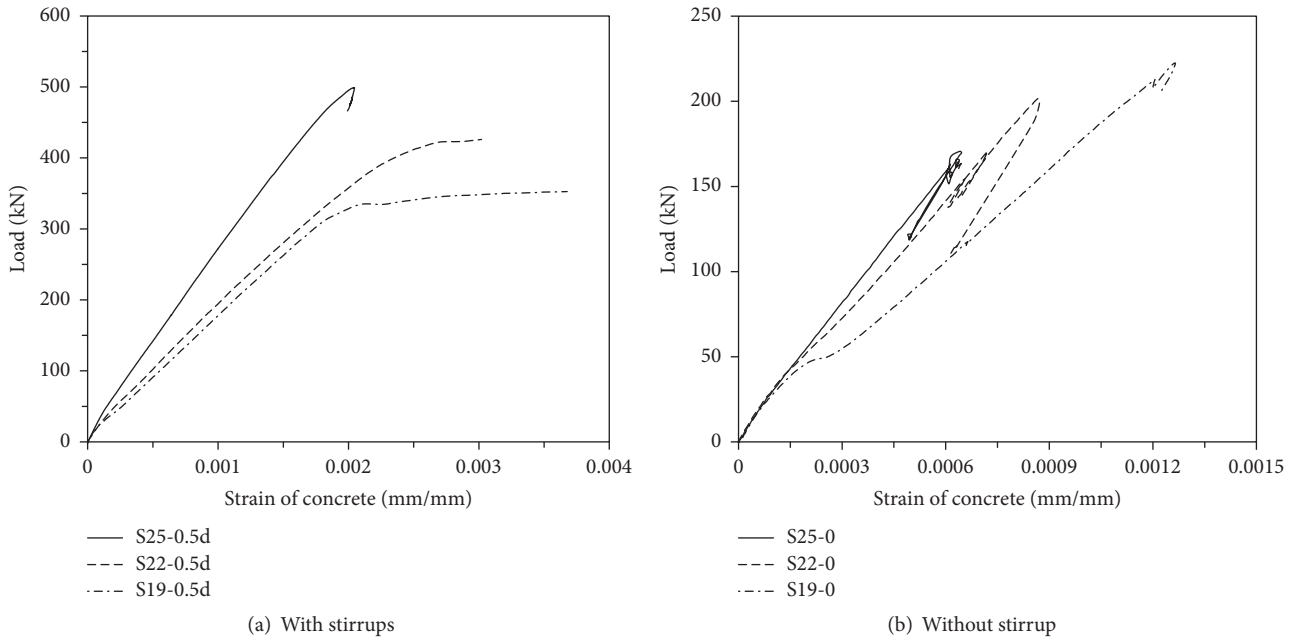


FIGURE 10: Load versus flexural compressive strain of concrete in shear test specimens.

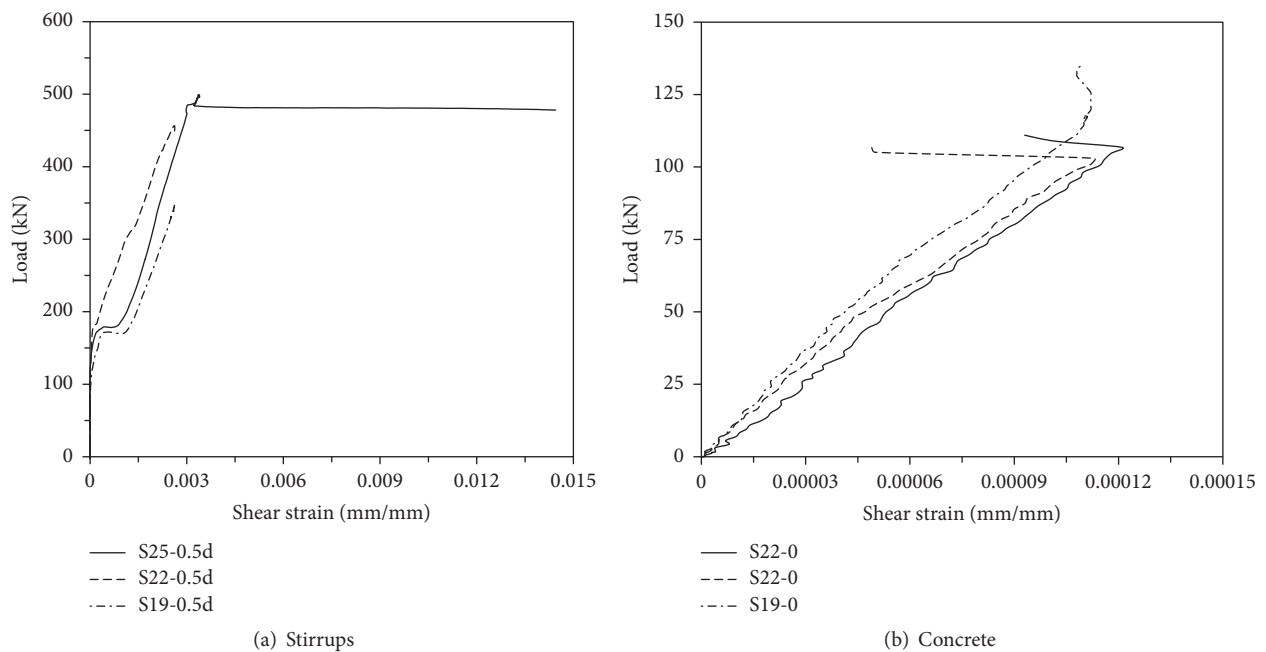


FIGURE 11: Load versus shear strain in shear test specimens.

indicate that the analysis provides values larger by maximum 26% and the similarity between the predictions of the design and the analysis.

4. Finite Element Analysis

4.1. Method of Analysis. The numerical analysis was carried out using the nonlinear finite element program, RCAST,

developed by Kim et al. [15]. The analysis models consist of a compression, tension stiffening, and shear transfer model for concrete and a model for embedded reinforcing steel. The concrete-reinforcement bond interaction is considered in both the tension stiffening model for concrete and the model for reinforcement. An earlier study [18] demonstrated that the above-mentioned analysis model agreed reasonably with the experimental data.

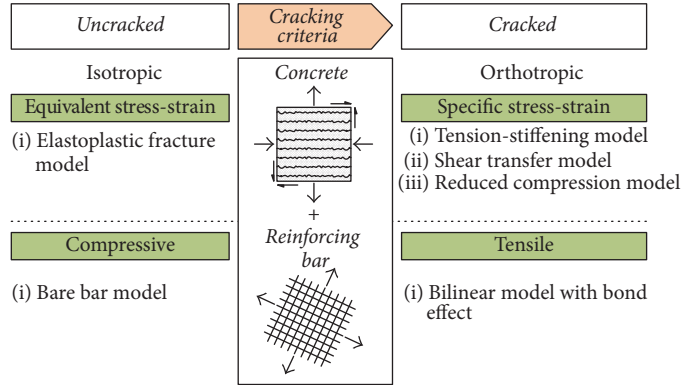


FIGURE 12: Outline of analysis model for reinforced high-strength concrete [15].

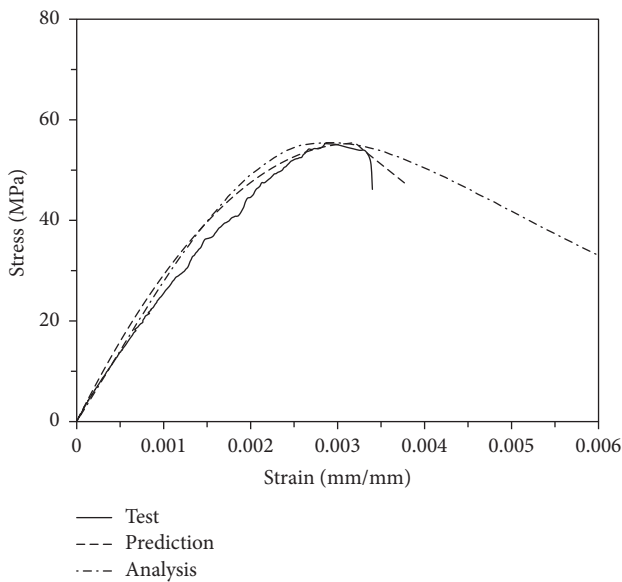


FIGURE 13: Comparison of experimental and predicted stress-strain curves.

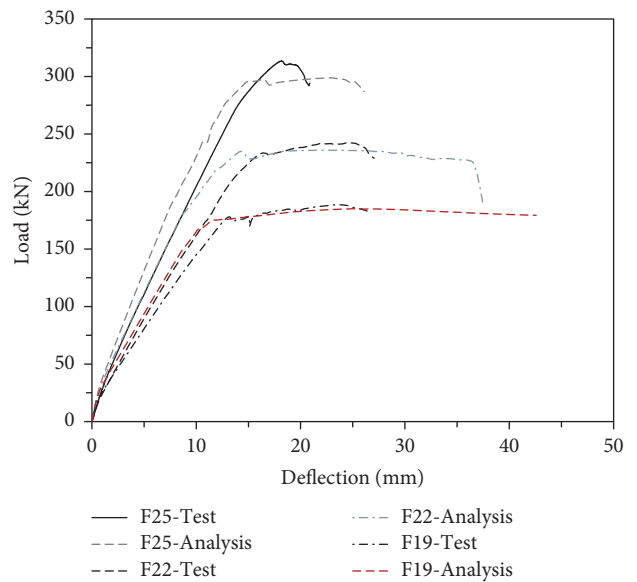


FIGURE 14: Comparison of experimental and analytical load-deflection curves for flexure test members.

4.2. *Material Models for Reinforced Concrete.* The nonlinear stress-strain relation of a reinforced concrete (RC) in-plane element is formulated based on the concept of space averaging on the control volume. The cracks and reinforcing bars are idealized as being distributed over the entire element. Although the local behavior of the cracked RC is not uniform, in practical terms it can be treated as a continuum having quasi-uniform stress and strain fields in a finite region. The material models aim to describe the overall behavior of a structure rather than a specific local behavior at the element level. In this paper, the term “crack” explicitly refers to the macrocrack perpendicular to the principal tensile direction.

According to the cracking criteria, the analysis models are divided into models before and after the initiation of cracks, as shown in Figure 12. The material model for concrete prior to cracking is based on the elastoplastic fracture model [19] given in Figure 13. The local coordinate systems of reinforcing bars are always assigned with respect to each bar axis, but those of cracked concrete are determined according

to the current major crack plane. Once a smeared crack is initiated, it is treated as fixed in a direction, and anisotropy is introduced. As loading step proceeds, the principal direction of the average stress can be changed, and the consequent shear transfer model is involved in the constitutive law.

5. Comparison of Experimental and Analytical Results

5.1. *Flexure.* Figure 14 compares the experimental and analytical load-displacement curves for specimens F25, F22, and F19. The analytical results are in relatively good agreement with the experimental values and indicate the validity of the analytic model. However, for F25 with the largest tensile ratio considered in this study, the test specimens exhibit slight brittle failure compared to the analytical prediction. The initial slope of the experimental curves is on the whole smaller than that of the analytical curves. The different initial slopes

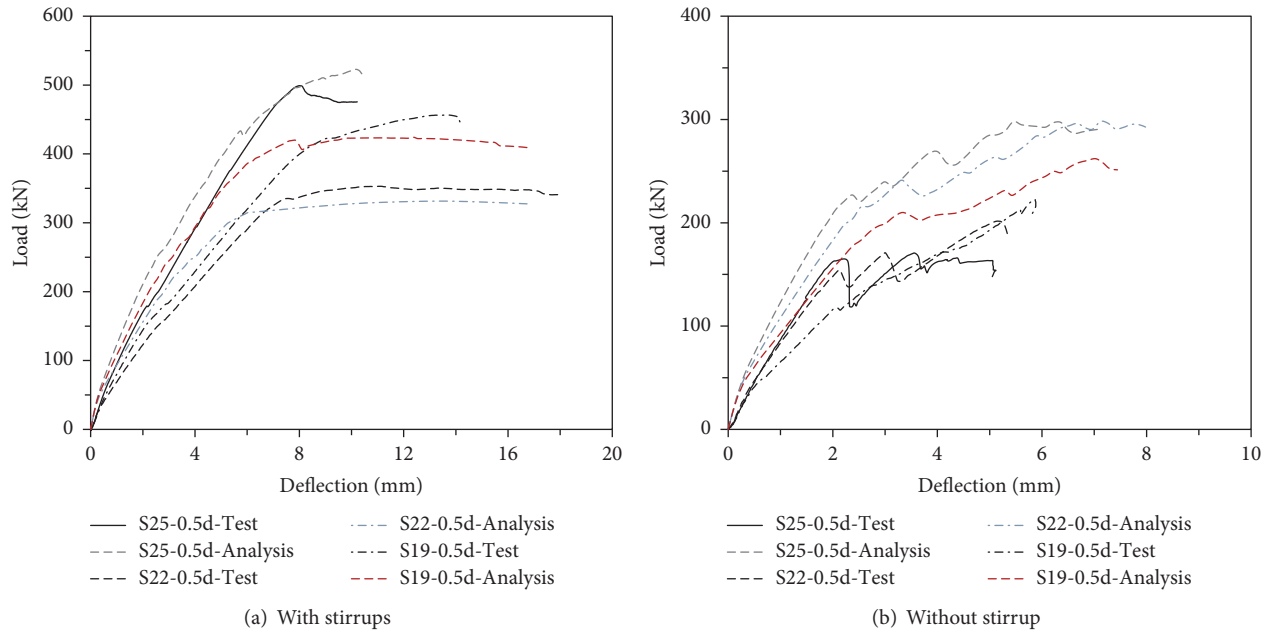


FIGURE 15: Comparison of experimental and analytical load-displacement curves for shear test members.

of the analytical and experimental results can be attributed partially to the stiffness adopted in the analytical model of the members and some experimental error. Moreover, the early completion of the tests explains the different maximum deflections of the analytical and experimental results. In fact, larger deflection would have been measured in the members that experienced failure through flexure but the tests were interrupted prematurely due to limitations in the capacity of the testing equipment and for the sake of safety.

5.2. Shear. Figure 15 compares the experimental and analytical load-displacement curves of the shear test specimens. The analytical results are in relatively good agreement with the experimental values for the specimens with stirrups. Here also, slight difference in the initial slope occurred as explained above in Section 5.1. Specimen S25-0.5d experienced sudden brittle failure due to the clear occurrence of shear failure. Values near the maximum load could not be measured because of the delay in the acquisition of the data. Besides, the specimens without stirrup showed smaller maximum loads in the test than those of the analysis. However, considering the large experimental errors that are generally observed in the shear test of specimens without stirrup, the results presented here demonstrate to some extent the good execution of the tests performed in this study.

Here also, the early ending of the tests explains the different maximum deflections of the analytical and experimental results. The members without stirrup in Figure 15(b) experienced sudden failure but the tests were interrupted prematurely due to limitations in the capacity of the testing equipment and for the sake of safety. In addition, it is extremely difficult to measure precisely the behavior of the members without stirrup after the ultimate state when the failure test is conducted using an actuator and through

displacement control. On the other hand, the similarity of the experimental and analytical maximum deflections observed in Figure 15(a) was achieved because the members suffered shear failure and reached a state close to their ultimate state at the completion of the tests thanks to the presence of stirrups.

6. Conclusions

This study evaluated experimentally and analytically the structural behavior of reinforced concrete beams made of AAS concrete. The following conclusions can be drawn from the results.

- (1) The elastic modulus and the strain at maximum stress of AAS concrete were slightly smaller than those predicted for normal concrete. This difference could be explained by the reduction in the unit mass of AAS concrete caused by the smaller density of slag compared to cement. Further study shall propose adequate models for the elastic modulus and stress-strain relation of AAS concrete.
- (2) The test results of the flexural members showed that the ratio of the ultimate load to the yield load of steel ranged between 1.15 and 1.41 and the load bearing capacity improved with higher tensile steel ratio. The flexural behavior of the reinforced AAS concrete members appeared thus to be very similar to that of the reinforced concrete beam made of normal concrete because the reinforcing bars govern the flexural behavior of the members. A nonlinear flexural analysis model was proposed using the elastic modulus and stress-strain relation of AAS concrete. The analytical results were in good agreement with the

experimental results and demonstrated the validity of the analytical model.

- (3) The experimental shear strength obtained for the members without stirrup was significantly higher than that predicted by the design code, which indicated the conservativeness of the design code. The shear behavior of the reinforced AAS concrete members varied according to the amount of tensile steel.
- (4) In view of the finite element analysis results reflecting the nonlinear model of AAS concrete used in previous studies, the flexural and shear behaviors of the AAS concrete specimens were in relatively good agreement with those predicted analytically.
- (5) Consequently, the test results show that the flexural and shear behaviors of the reinforced AAS concrete members are very similar to those of the reinforced concrete beam made of normal concrete and render it possible to apply conventional design code for flexure and shear in the design of reinforced AAS concrete members. Further studies are required for the practical use of AAS concrete since this experimental study was limited to specimens with specific dimensions.

Conflicts of Interest

The authors declare that they have no conflicts of interest.

Acknowledgments

This research was financially supported by the Korean Ministry of Environment as “Public Technology Program Based on Environmental Policy” (no. 2016000700003). This research was also supported by a grant (Code 11-Technology Innovation-F04) from Construction Technology Innovation Program (CTIP) funded by Ministry of Land and Transport of Korean government.

References

- [1] S.-D. Wang, X.-C. Pu, K. L. Scrivener, and P. L. Pratt, “Alkali-activated slag cement and concrete: a review of properties and problems,” *Advances in Cement Research*, vol. 7, no. 27, pp. 93–102, 1995.
- [2] A. Palomo, M. W. Grutzeck, and M. T. Blanco, “Alkali-activated fly ashes: a cement for the future,” *Cement and Concrete Research*, vol. 29, no. 8, pp. 1323–1329, 1999.
- [3] C. Shi, P. V. Krivenko, and D. Roy, *Alkali-activated cement and concrete*, vol. 376, Taylor & Francis, Abingdon, UK, 2006.
- [4] C. Shi, A. F. Jiménez, and A. Palomo, “New cements for the 21st century: the pursuit of an alternative to Portland cement,” *Cement and Concrete Research*, vol. 41, no. 7, pp. 750–763, 2011.
- [5] A. R. Brough and A. Atkinson, “Sodium silicate-based, alkali-activated slag mortars part I. Strength, hydration and microstructure,” *Cement and Concrete Research*, vol. 32, no. 6, pp. 865–879, 2002.
- [6] S. Aydin and B. Baradan, “Effect of activator type and content on properties of alkali-activated slag mortars,” *Composites Part B: Engineering*, vol. 57, pp. 166–172, 2014.
- [7] S. H. Oh, S. H. Hong, and K. M. Lee, “Autogenous shrinkage properties of high strength alkali activated slag mortar,” *Journal of the Korean Recycled Construction Resources Institute*, vol. 2, no. 1, pp. 60–65, 2014.
- [8] F. G. Collins and J. G. Sanjayan, “Workability and mechanical properties of alkali activated slag concrete,” *Cement and Concrete Research*, vol. 29, no. 3, pp. 455–458, 1999.
- [9] M. Sofi, J. S. J. van Deventer, P. A. Mendis, and G. C. Lukey, “Engineering properties of inorganic polymer concretes (IPCs),” *Cement and Concrete Research*, vol. 37, no. 2, pp. 251–257, 2007.
- [10] C. D. Atiş, C. Bilim, Ö. Çelik, and O. Karahan, “Influence of activator on the strength and drying shrinkage of alkali-activated slag mortar,” *Construction and Building Materials*, vol. 23, no. 1, pp. 548–555, 2009.
- [11] A. A. Melo Neto, M. A. Cincotto, and W. Repette, “Drying and autogenous shrinkage of pastes and mortars with activated slag cement,” *Cement and Concrete Research*, vol. 38, no. 4, pp. 565–574, 2008.
- [12] F. Puertas, M. Palacios, and T. Vázquez, “Carbonation process of alkali-activated slag mortars,” *Journal of Materials Science*, vol. 41, no. 10, pp. 3071–3082, 2006.
- [13] K. Lee and J. Seo, “Evaluation of flexural behavior of reinforced concrete beams using alkali activated slag concrete,” *Journal of the Korea Concrete Institute*, vol. 27, no. 3, pp. 311–317, 2015.
- [14] S. Choi, K. Lee, and S. Yoo, “Shear behavior of RC beams using alkali activated slag concrete,” *Journal of the Korean Recycled Construction Resources Institute*, vol. 3, no. 1, pp. 58–63, 2015.
- [15] T.-H. Kim, K.-M. Lee, C. Yoon, and H. M. Shin, “Inelastic behavior and ductility capacity of reinforced concrete bridge piers under earthquake. I: Theory and formulation,” *Journal of Structural Engineering*, vol. 129, no. 9, pp. 1199–1207, 2003.
- [16] E. Thorenfeldt, A. Tomaszewicz, and J. J. Jensen, “Mechanical properties of high strength concrete and application in design,” in *Proceedings of the Symposium Utilization of High Strength Concrete*, T. Trondheim, Ed., vol. 40, pp. 149–159, Stravanger, Norway, 15–18 June 1987.
- [17] S.-W. Shin, S. K. Ghosh, and J. Moreno, “Flexural ductility of ultra-high-strength concrete members,” *ACI Structural Journal*, vol. 86, no. 4, pp. 394–400, 1989.
- [18] T.-H. Kim, K.-M. Lee, C. Yoon, and H. M. Shin, “Inelastic behavior and ductility capacity of reinforced concrete bridge piers under earthquake. II: Numerical validation,” *Journal of Structural Engineering*, vol. 129, no. 9, pp. 1208–1219, 2003.
- [19] K. Maekawa and H. Okamura, “Deformational behavior and constitutive equation of concrete using the elasto-plastic and fracture model,” *Journal of the Faculty of Engineering, University of Tokyo, Series B*, vol. 37, no. 2, pp. 253–328, 1983.

Research Article

Influence of Palm Oil Fuel Ash and W/B Ratios on Compressive Strength, Water Permeability, and Chloride Resistance of Concrete

Wachilakorn Sanawung,¹ Tieng Cheewaket,²
Weerachart Tangchirapat,¹ and Chai Jaturapitakkul¹

¹Department of Civil Engineering, Faculty of Engineering, King Mongkut's University of Technology Thonburi, Bang Mod, Thung Khru, Bangkok 10140, Thailand

²Department of Civil Engineering, Faculty of Engineering, Burapha University, Chonburi 20131, Thailand

Correspondence should be addressed to Weerachart Tangchirapat; weerachart.tan@kmutt.ac.th

Received 20 March 2017; Accepted 23 May 2017; Published 4 July 2017

Academic Editor: Tung-Chai Ling

Copyright © 2017 Wachilakorn Sanawung et al. This is an open access article distributed under the Creative Commons Attribution License, which permits unrestricted use, distribution, and reproduction in any medium, provided the original work is properly cited.

This research studies the effects of W/B ratios and palm oil fuel ash (POFA) on compressive strength, water permeability, and chloride resistance of concrete. POFA was ground until the particles retained on sieve number 325 were less than 5% by weight. POFA was used to partially replace OPC at rates of 15, 25, and 35% by weight of binder. The water to binder (W/B) ratios of concrete were 0.40 and 0.50. The compressive strength, water permeability, and chloride resistance of concrete were investigated up to 90 days. The results showed that POFA concrete with W/B ratio of 0.40 had the compressive strengths ranging from 45.8 to 55.9 MPa or 82–94% of OPC concrete at 90 days, while POFA concrete with W/B ratio of 0.50 had the compressive strengths of 33.9–41.9 MPa or 81–94% of OPC concrete. Furthermore, the compressive strength of concrete incorporation of ground POFA at 15% was the same as OPC concrete. The water permeability coefficient and the chloride ion penetration of POFA concrete were lower than OPC concrete when both types of concrete had the same compressive strengths. The findings also indicated that water permeability and chloride ion penetration of POFA concrete were significantly reduced compared to OPC concrete.

1. Introduction

Palm oil fuel ash (POFA) is a by-product from biomass power plants, in which palm oil residues such as fibers, shells, and empty fruit bunches are burned to generate electricity. In 2013, approximately 6.25 million tons of palm oil residues were produced in Thailand. After combustion, approximately 312,500 tons of POFA were obtained or approximately 5% by weight of palm oil residue [1]. Since the palm oil is the main material in the production of biodiesel, the by-product of palm oil fuel ash is tended to increase annually, whereas the application of POFA remains to be very limited. Thus, most POFA is disposed as waste in landfills, which causes many environmental problems. The main chemical composition of palm oil fuel ash is silicon dioxide (SiO₂), and previous studies have shown that POFA in its original size is not

suitable as a good pozzolan due to its large particle and high porosity [1]. However, high fineness POFA is a good pozzolanic material. Therefore, the POFA should be ground to higher fineness before it is used to partially replace OPC in concrete [2–4].

Previous researchers have reported that blast furnace slag or pozzolans such as fly ash, silica fume, rice husk ash, and bagasse ash can be used to partially replace OPC in concrete mixture [5–10]. POFA has been introduced as a pozzolanic material in concrete and most studies of POFA have focused on the mechanical properties of concrete such as compressive strength and modulus of elasticity of concrete [1–4]. Moreover, POFA has been used to replace cement as a binder in the geopolymer mortar and concrete to improve the compressive strength [11–13]. Some studies have considered the durability of concrete in terms of chloride

TABLE 1: Physical properties of the materials.

Sample	Specific gravity	Retained on a 45 μm sieve (number 325) (%)	Median particle size, d_{50} (μm)
Type I Portland cement	3.14	13.5	14.7
POFA (before grinding)	1.89	94.4	183.0
Ground POFA	2.52	1.7	10.7

TABLE 2: Chemical compositions of the ground POFA and Type I Portland cement.

Sample	SiO ₂	Al ₂ O ₃	Fe ₂ O ₃	CaO	MgO	K ₂ O	Na ₂ O	SO ₃	LOI
Cement	20.9	4.8	3.8	65.4	1.2	0.4	0.2	2.7	1.0
Ground POFA	55.4	9.1	5.5	12.4	4.6	—	—	2.3	7.9

TABLE 3: Mixture proportions of the types of concrete.

Sample	Mix proportion (kg/m ³)						Slump (mm)
	Cement	Ground POFA	Sand	Crushed limestone	Effective water	Super P.	
40CT	475	0	765	935	190	2.38	85
40P15	404	71	765	910	190	2.85	72
40P25	357	118	765	895	190	3.09	80
40P35	309	166	765	875	190	3.33	75
50CT	385	0	765	1012	190	0.39	90
50P15	327	58	765	990	190	0.58	85
50P25	289	96	765	980	190	0.77	75
50P35	250	135	765	965	190	1.16	80

ion penetration [14, 15] and corrosion resistance of high-strength, high workability concrete [16]. Once chloride ions penetrate into concrete and their concentrations around the reinforcing steel exceed a critical level, they will break down the protective film, which leads to the beginning of steel corrosion.

However, few studies have jointly considered the three main properties for durability in concrete, that is, compressive strength, water permeability, and chloride ion penetration. Moreover, POFA concrete with different W/B ratios was also considered in this study. In addition, the results obtained from this study would be beneficial to understand the POFA concrete's properties and to apply POFA concrete in the future.

2. Experimental Programs

2.1. Materials. Palm oil fuel ash (POFA) used in this study was collected from a power plant in Thailand. The POFA obtained from the power plant was in a dry condition and had a low pozzolanic reaction due to its large particle sizes and high porosity; therefore, it was ground with a ball mill to improve its reactivity. The POFA was ground by ball mill to a required level of fineness until the retained particles were on a number 325 sieve of 1.7% by weight.

Ordinary Portland cement (OPC), natural river sand with a fineness modulus of 3.09, crushed limestone with a maximum size of 19 mm, and a type-F superplasticizer (SP)

were used in this study. The physical properties of the OPC and POFA are shown in Table 1.

As shown in Table 2, the chemical compositions indicate that the sums of SiO₂, Fe₂O₃, and Al₂O₃ in the ground POFA were 70% (55.4 + 9.1 + 5.5) by weight, whereas the values of LOI and SO₃ were 7.9 and 2.3%, respectively. Awal and Hussin [17] found that the sum of SiO₂, Fe₂O₃, and Al₂O₃ in POFA from Malaysia was 59.7% and the values of LOI and SO₃ were 18.0 and 2.8%, respectively, which were not much different from the results of this study (except LOI).

2.2. Mix Proportions of Concrete. To investigate the effects of W/B ratios on properties of concrete containing ground POFA, two values of W/B ratio were used. The concrete was designed to have binder contents of 475 and 385 kg/m³, corresponding to the W/B ratios of 0.40 and 0.50, respectively. The mixture proportions of the control types of concrete (40CT and 50CT) and the types of concrete containing ground POFA (40P15, 40P25, 40P35, 50P15, 50P25, and 50P35) are summarized in Table 3. The compressive strengths of the 40CT and 50CT control types of concrete (types of concrete using OPC as a binder) were designed to be 50 and 40 MPa at 28 days, respectively. A type-F superplasticizer was used to produce concrete having roughly the same slump between 50 and 100 mm which was the typical workability for general concrete. The cement replacements with ground POFA in the concrete mixtures were at rates of 15, 25, and 35% by weight of binder (ground POFA + OPC). The effects of W/B ratios

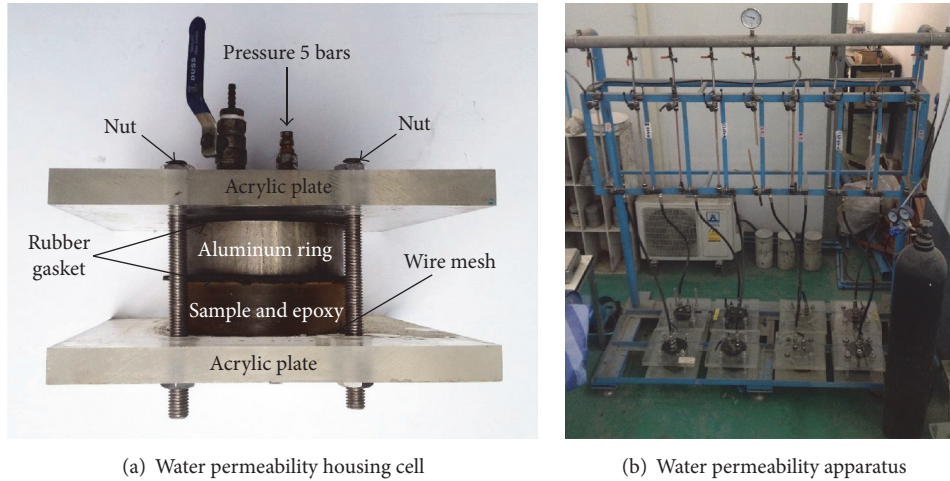


FIGURE 1: Water permeability coefficient test.

and ground POFA on the properties of the concrete were investigated and compared to the control concrete.

2.3. Tests for the Compressive Strengths of Concrete. Cylindrical concrete specimens with a diameter of 100 mm and a height of 200 mm were used to determine the compressive strengths. To prepare the concrete specimens, cylindrical molds were filled with fresh concrete in three equal layers, and each layer was rodded 25 times using a standard rod. After casting, the concrete specimens were allowed to set for 24 h before being removed from the molds and were cured in fresh water. The concrete specimens were tested for compressive strengths at 7, 28, 60, and 90 days according to ASTM C39 [18]. At each testing age, three samples were used to obtain an average value.

2.4. Tests for the Water Permeabilities of the Concrete. The steady flow method was applied to test the water permeability of the concrete. Each of the 100 × 200 mm cylinder types of concrete at the middle was cut to have 2 sliced pieces of 100 mm in diameter and 40 mm in thickness. Epoxy resin with a thickness of 25 mm was coated around the perimeter of the sliced concrete specimen. The concrete sample, after the epoxy resin set for 24 h, was installed in housing cells and a water permeability test apparatus, as shown in Figure 1, which was suggested by Chan and Wu [19]. The test of water permeability of concrete followed the procedure used by Tangchirapat et al. [20]. The concrete was conducted to determine water permeability coefficient (WPC) at the ages of 28 and 90 days. The water permeability coefficient of concrete was calculated from the following equation [21]:

$$K = \frac{\rho L g Q}{P A} \quad (1)$$

K is the water permeability coefficient, WPC, (m/s); ρ is the density of water (kg/m^3); g is the acceleration due to gravity, $9.81 \text{ (m/s}^2\text{)}$; Q is the constant flow rate (m^3/s); L is the length of the concrete sample (m); P is the water pressure

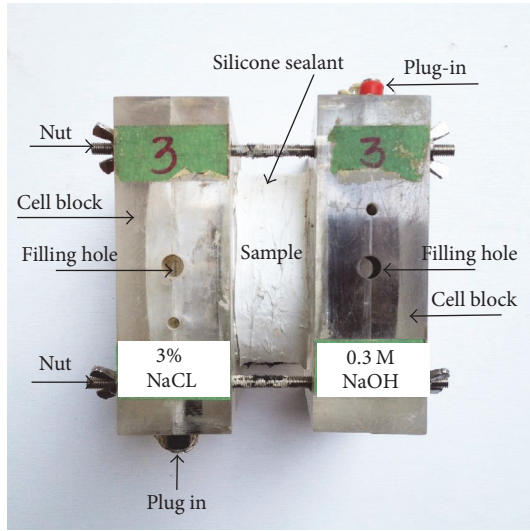
(0.5 MPa); and A is the cross-sectional area of the concrete sample (m^2).

2.5. Tests for the Electrical Indication of the Concrete's Ability to Resist Chloride Ion Penetration. At ages of 28 and 90 days, a 100 mm diameter and 50 mm height concrete specimen was cut from a 100 × 200 mm concrete cylinder, coated with epoxy resin, and tested for rapid chloride ion penetration in accordance with ASTM C1202 [22]. This test method covers the determination of the electrical conductance of concrete to provide a rapid indication of its resistance to the penetration of chloride ions. The total passed charge (in coulombs) was recorded by application of a 60 V voltage (DC) across the specimen during a 6 h period. The set-up for the rapid chloride ion penetration test apparatus is shown in Figure 2.

3. Results and Discussion

3.1. Compressive Strength of Concrete. Figure 3 shows the compressive strengths of the control concrete and the POFA concrete with OPC replacements of 15, 25, and 35% by weight of binder. The development of the compressive strengths of the POFA concrete was compared to that of the 40CT and 50CT types of concrete, from which the effects of the different W/B ratios on the compressive strengths and durability properties of the concrete were investigated.

The 40CT and 50CT types of concrete gained compressive strengths of 45.5 and 31.5 MPa at 7 days, respectively. At 28, 60, and 90 days, the 40CT concrete developed strengths up to 50.2, 54.1, and 55.9 MPa, respectively, whereas the 50CT concrete developed lesser strengths, which were 39.6, 41.4, and 41.9 MPa, respectively. At the same W/B ratios, the POFA concrete produced lower compressive strengths than those of the control concrete up to 90 days. At 7 days, the 40P15 concrete had compressive strength of 38.9 MPa and increased to 46.2 MPa at 28 days. At the later ages of 60 and 90 days, the 40P15 concrete had compressive strengths of 49.1 and 52.8 MPa, respectively. The compressive strengths of the

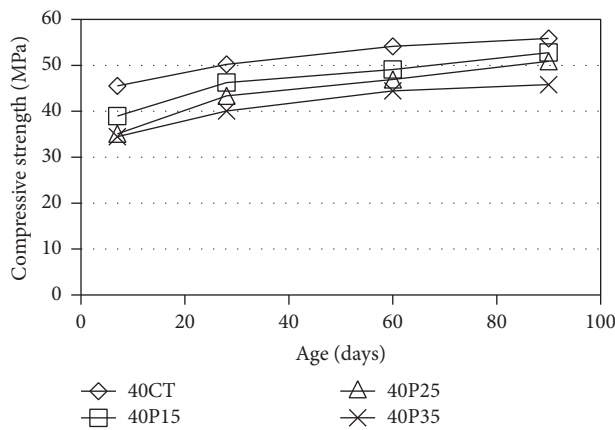


(a) Chloride ion penetration housing cell

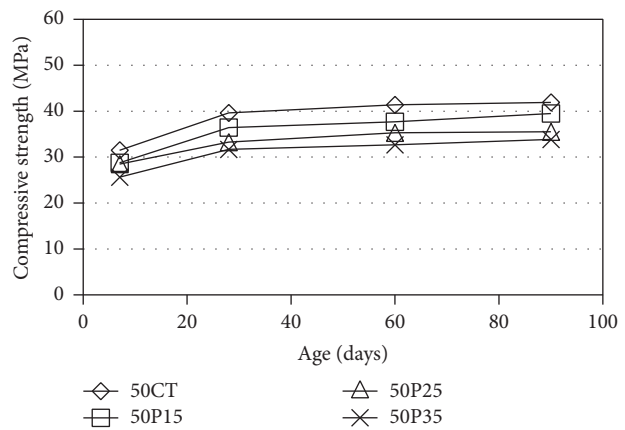


(b) Chloride ion penetration apparatus

FIGURE 2: Installation test for the electrical indication of a concrete's ability to resist chloride ion penetration.



(a) W/B ratio of 0.40



(b) W/B ratio of 0.50

FIGURE 3: Compressive strengths of the concrete at different ages.

40P25 concrete were 35.1, 43.3, 46.9, and 50.9 MPa at 7, 28, 60, and 90 days, respectively. At ages of 7, 28, 60, and 90 days, the 40P35 concrete had compressive strengths of 34.5, 40.0, 44.4, and 45.8 MPa, respectively.

The results indicated that the use of ground POFA to replace OPC at rates of 15 to 35% by weight of binder slightly decreased the compressive strength of the concrete. The 40P15 concrete had a compressive strength of 92% of the 40CT concrete at 28 days and developed to 94% of the 40CT concrete at 90 days, whereas the 50P15 concrete had a compressive strength of 92% of the 50CT concrete at 28 days and developed to 94% of the 50CT concrete at 90 days. When the ground POFA was used to replace OPC in concrete, it resulted in a decrease in the compressive strength, and the results conformed to those of Sata et al. [23]. The decrease in the compressive strengths of the POFA concrete could be attributed to the lower quantity of OPC, such that the

compressive strength obtained from the pozzolanic reaction of the ground POFA was not high enough to compensate for the loss in strength due to the hydration of the cement. However, the use of ground POFA to replace OPC can reduce the usage of OPC in concrete mixtures and the compressive strength is not much different from the control concrete at the same W/B ratio.

3.2. *Water Permeability.* Table 4 shows the water permeability coefficients (WPCs) and the compressive strengths of concrete at 28 and 90 days. The ratio of WPC (k/k control) is the normalized WPC of POFA concrete as compared with the control concrete at the same testing age and W/B ratio (40CT or 50CT concrete). The 40CT and 50CT types of concrete at 28 days had the WPC of 3.01×10^{-13} and 4.81×10^{-13} m/s and reduced to 1.96×10^{-13} and 3.2×10^{-13} m/s at 90 days, respectively, which was similar to the previous research [24]

TABLE 4: Compressive strengths and water permeability coefficients of the types of concrete at 28 and 90 days.

Mix	Compressive strength (MPa)-normalized (%)		Water permeability (k) $\times 10^{-13}$, k (m/s) - k/k control	
	28 days	90 days	28 days	90 days
40CT	50.2-(100)	55.9-(100)	3.01-1.00	1.96-1.00
40P15	46.2-(92)	52.8-(94)	2.26-0.75	1.08-0.53
40P25	43.3-(86)	50.9-(91)	3.33-1.11	2.04-1.04
40P35	40.0-(80)	45.8-(82)	4.52-1.50	2.86-1.46
50CT	39.6-(100)	41.9-(100)	4.81-1.00	3.20-1.00
50P15	36.4-(92)	39.5-(94)	5.06-1.05	2.91-0.91
50P25	34.6-(88)	35.5-(85)	6.67-1.39	3.86-1.21
50P35	31.7-(80)	33.9-(81)	7.03-1.46	4.51-1.41

demonstrating that the WPCs of cement concrete were between 10.00×10^{-13} and 1.00×10^{-13} m/s at 28 days.

This study showed that the WPCs of the POFA concrete decreased as the curing age increased. For example, at 28 and 90 days, the 40P15 concrete had the WPCs of 2.26×10^{-13} and 1.08×10^{-13} m/s or 0.75 and 0.53 of the 40CT concrete at 28 and 90 days, respectively, which were lower than those of the control concrete. It should be noted that the 40P15 concrete had a lower compressive strength than that of the 40CT concrete and still had a lower WPC than the 40CT concrete too.

The POFA concrete with 15% cement replacement had the WPCs lower than those of the control concrete and had higher WPCs than those of the control concrete at replacement rates of 25 and 35%. For example, at 28 days, the 40P25 and 40P35 types of concrete had the WPCs of 3.33×10^{-13} and 4.52×10^{-13} m/s or 1.11 and 1.50 of the 40CT concrete, respectively. The WPCs of the concrete with W/B ratios of 0.40 at 90 days were slightly lower than those at 28 days. The WPCs of the 40P25 and 40P35 types of concrete were 2.04×10^{-13} and 2.86×10^{-13} m/s or 1.04 and 1.46 of the 40CT concrete at 90 days, respectively. It should be noted that the compressive strengths of the 40P25 and 40P35 types of concrete at 90 days were 91 and 82% of the 40CT concrete, respectively.

The WPC ratios of the 50P15, 50P25, and 50P35 types of concrete at 90 days were 0.91, 1.21, and 1.41 of the 50CT concrete, respectively. At 90 days, the WPC ratios of the POFA concrete were slightly lower than the values at 28 days. This denotes that the WPCs of the POFA concrete at 25 and 35% OPC replacement were slightly higher than those of the control concrete. However, the POFA concrete at 15% OPC replacement can produce concrete with lower WPC than that of the control concrete.

Considering the types of concrete with the same ranges of WPCs, it was found that the concrete with lower W/B ratio can replace OPC with ground POFA at a higher rate. For example, at 90 days, the WPCs of the 40P35 and 50P15 types of concrete were 2.86×10^{-13} m/s and 2.91×10^{-13} m/s, respectively, but the 40P35 concrete had a ground POFA replacement of 35% by weight of binder. Note that the 40P35 and 50P15 types of concrete had compressive strengths of 45.8 and 39.5 MPa, respectively.

Considering the same ranges of compressive strengths but for types of concrete of different ages, the 40P35 and 50P15 types of concrete had compressive strengths of 40.0 MPa at 28 days and 39.5 MPa at 90 days, respectively. It was found that the 50P15 concrete had a WPC of 2.91×10^{-13} m/s, whereas that of the 40P35 concrete was 4.52×10^{-13} m/s. This suggested that the age of concrete has more influence on reducing water permeability compared to the compressive strength.

Table 4 also indicates that the increase in the compressive strength of POFA concrete could be attributed to the lower WPC. This is due to the incorporation of ground POFA, which made the concrete denser by pozzolanic reaction and packing effect was an effective way to reduce the water permeability of the POFA concrete. However, the WPCs of POFA concrete tended to increase as the POFA replacement increased to same extent, that is, 25 or 35% replacement. This result agreed with that of Chindaprasirt et al. [25] who reported that the water permeability of concrete containing pozzolans such as fly ash and rice husk-bark ash tended to increase as the fly ash and rice husk-bark ash replacement increased.

3.3. Chloride Ion Penetration. The results of the chloride ion penetration of concrete determined by ASTM C1202 [22] are given in Figure 4. At the same W/B ratios, the total passed charges (coulombs) for the control concrete were much higher than those of the POFA concrete. The 40CT and 50CT types of concrete (W/B ratios of 0.40 and 0.50) had total passed charges of 3236 and 4507 coulombs at 28 days and reduced to 1891 and 3590 coulombs at 90 days, respectively. From the obtained results, the total passed charges for the control concrete decreased as the curing age increased and decreased as the W/B ratio decreased.

Figure 4 also suggests that, at the age of 28 days, the control concrete with W/B ratios of 0.40 and 0.50 can be classified as moderate and high for chloride ion penetration as specified by ASTM C1202 [22] because the values of the total passed charges of the 40CT and 50CT types of concrete were greater than 2000 and 4000 coulombs, respectively. However, at 90 days, the 40CT and 50CT types of concrete were classified as low and moderate for chloride ion penetration because the

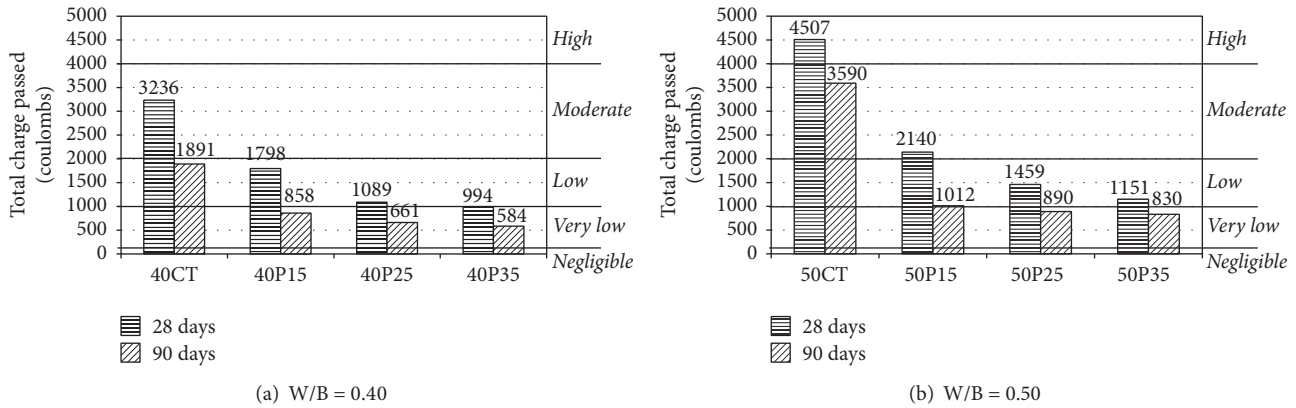


FIGURE 4: Chloride ion penetration and the replacement of ground POFA in concrete for W/B ratios of 0.40 and 0.50.

TABLE 5: Compressive strengths and chloride ion penetrations of the types of concrete.

Mix	Compressive strength (MPa)-normalized (%)		Total charge passed (coulombs)-normalized (%)	
	28 days	90 days	28 days	90 days
40CT	50.2-(100)	55.9-(100)	3236-100	1891-100
40P15	46.2-(92)	52.8-(94)	1798-56	823-44
40P25	43.3-(86)	50.9-(91)	1089-34	661-35
40P35	40.0-(80)	45.8-(82)	994-31	584-31
50CT	39.6-(100)	41.9-(100)	4507-100	3590-100
50P15	36.4-(92)	39.5-(94)	2140-47	1012-28
50P25	34.6-(88)	35.5-(85)	1459-32	890-25
50P35	31.7-(80)	33.9-(81)	1151-26	830-23

values of the total passed charges were less than 2000 and 4000 coulombs, respectively.

For the POFA concrete, the values of total passed charges for the 50P15, 50P25, and 50P35 types of concrete were 2140, 1459, and 1151 coulombs at 28 days and declined to 1012, 890, and 830 coulombs at 90 days, respectively. For the 40P15, 40P25, and 40P35 types of concrete, the values were only 1798, 1089, and 994 coulombs at 28 days and declined to 858, 661, and 584 coulombs at 90 days, respectively. It should be noted that the values of total passed charges of the POFA concrete at 28 days were classified as low for chloride ion penetration because the value of total passed charges was less than 2000 coulombs, except for the 50P15 concrete, which had total passed charges of 2140 coulombs. When the age of the POFA concrete reached 90 days, all the POFA concrete could be classified as very low for chloride ion penetration because the total passed charges were approximately 1000 coulombs or less. The results suggested that ground POFA could be used very effectively to reduce chloride ion penetration in concrete.

Table 5 shows the compressive strength and chloride ion penetration results of the types of concrete. The results suggested that the chloride ion penetration of the POFA concrete tended to decrease as the replacement of ground POFA and curing age increased. Use of ground POFA is effective in reducing chloride ion penetration in concrete, which is the same as the result of using fly ash and silica fume

in concrete [26]. This improvement in concrete resistivity was due to the pozzolanic reaction, which improved the interfacial bonding between the aggregates and pastes [27, 28], resulting in impermeable and dense concrete [29].

The types of concrete with the same replacement of ground POFA, that is, the 25% replacement of OPC in the 40P25 and 50P25 types of concrete at 90 days, had the total passed charges of 661 and 890 coulombs, respectively. The 40P25 concrete had lower total passed charges because of its higher compressive strength and lower W/B ratio and it was denser than the one with a higher W/B ratio. These results have also been reported by many researchers [30, 31] who used fly ash or silica fume to replace OPC in concrete.

Considering the same ranges of compressive strengths but for POFA types of concrete with different W/B ratios, that is, the 40P35 concrete and 50P15 concrete, which had the compressive strengths of 40.0 MPa at 28 days and 39.5 MPa at 90 days, respectively, it was found that the 40P35 and 50P15 types of concrete had the total passed charges of 994 and 1012 coulombs, respectively, which were approximately the same. Note that the total passed charges of the 40P35 concrete were considered at 28 days, whereas those of the 50P15 concrete were considered at 90 days.

Considering types of concrete cured at the same age and approximately the same total passed charges, the types of concrete to be considered are 40P15 and 50P35 at 90 days, which had total passed charges of 858 and 830 coulombs,

respectively. The results suggested that the replacement with ground POFA at 35% in 50P35 yielded a compressive strength of 33.9 MPa compared with that of 40P15 concrete (ground POFA of 15%), which was 52.8 MPa, but both types of concrete had almost the same total passed charges. This means that the replacement of POFA was more effective to reduce the total passed charges compared to the increase in the compressive strength. When the replacement of ground POFA in the concrete increased, the chloride ion penetration of concrete tended to decrease. This was due to the higher pozzolanic reaction in 50P35, which reduced $\text{Ca}(\text{OH})_2$ content, produced more C-S-H gel [32], reduced porosity, and thus increased the resistance of the chloride ion penetration. The results conformed to a large amount of researches demonstrating that the increased replacement of blast furnace slag or pozzolan such as fly ash or silica fume in concrete can increase the resistance of chloride ion penetration when compared to types of concrete with lower replacement of pozzolan [33, 34].

4. Conclusions

The following can be concluded:

- (1) The effects of W/B ratios on the compressive strengths of the POFA concrete were similar to those of conventional concrete; that is, the compressive strength of POFA concrete increased as the W/B ratio was decreased. Moreover, the POFA concrete (W/B ratios of 0.40 and 0.50) had approximately the same percentages of compressive strength compared to the control concrete with the same W/B ratios.
- (2) The replacement of ground POFA in OPC at 15 and 35% by weight of binder had strengths of 94–80% of the control concrete at 28 and 90 days. In addition, the use of ground POFA in the concrete required slightly higher amounts of superplasticizer than those required by the control concrete.
- (3) The replacement of ground POFA in OPC at 15% by weight of binder (40P15 and 50P15) produced good water permeability resistance results, although the compressive strengths of the POFA concrete were lower than those of the control concrete. In addition, the water permeability of the ground POFA concrete decreased as the compressive strength and curing age of the concrete increased.
- (4) From the results of the rapid chloride ion penetration test, ground POFA can be used very effectively to reduce chloride ion penetration in concrete. Moreover, the replacement of ground POFA (15 to 35%) is more important for increasing the chloride ion penetration resistance of concrete than for increasing its compressive strength.

Conflicts of Interest

The authors declare that they have no conflicts of interest.

Acknowledgments

The authors gratefully acknowledge the financial support from the Office of the Higher Education Commission, Thailand, under the National Research University (NRU) Project, King Mongkut's University of Technology Thonburi.

References

- [1] W. Tangchirapat, T. Saeting, C. Jaturapitakkul, K. Kiattikomol, and A. Siripanichgorn, "Use of waste ash from palm oil industry in concrete," *Waste Management*, vol. 27, no. 1, pp. 81–88, 2007.
- [2] A. S. M. Abdul Awal and I. A. Shehu, "Performance evaluation of concrete containing high volume palm oil fuel ash exposed to elevated temperature," *Construction and Building Materials*, vol. 76, pp. 214–220, 2015.
- [3] J.-H. Tay, "Ash from oil-palm waste as concrete material," *Journal of Materials in Civil Engineering*, vol. 2, no. 2, pp. 94–105, 1990.
- [4] J.-H. Tay and K.-Y. Show, "Use of ash derived from oil-palm waste incineration as a cement replacement material," *Resources, Conservation and Recycling*, vol. 13, no. 1, pp. 27–36, 1995.
- [5] P. Chindaprasirt, C. Chotithanorm, H. T. Cao, and V. Sirivivatnanon, "Influence of fly ash fineness on the chloride penetration of concrete," *Construction and Building Materials*, vol. 21, no. 2, pp. 356–361, 2007.
- [6] P. Chindaprasirt, S. Rukzon, and V. Sirivivatnanon, "Effect of carbon dioxide on chloride penetration and chloride ion diffusion coefficient of blended Portland cement mortar," *Construction and Building Materials*, vol. 22, no. 8, pp. 1701–1707, 2008.
- [7] W. Deboucha, M. N. Oudjit, A. Bouzid, and L. Belagraa, "Effect of incorporating blast furnace slag and natural pozzolan on compressive strength and capillary water absorption of concrete," *Procedia Engineering*, vol. 108, pp. 254–261, 2015.
- [8] W. Wongkeo, P. Thongsanitgarn, A. Ngamjarurojana, and A. Chaipanich, "Compressive strength and chloride resistance of self-compacting concrete containing high level fly ash and silica fume," *Materials and Design*, vol. 64, pp. 261–269, 2014.
- [9] W. Tangchirapat, R. Buranasing, C. Jaturapitakkul, and P. Chindaprasirt, "Influence of rice husk-bark ash on mechanical properties of concrete containing high amount of recycled aggregates," *Construction and Building Materials*, vol. 22, no. 8, pp. 1812–1819, 2008.
- [10] N. Chusilp, C. Jaturapitakkul, and K. Kiattikomol, "Utilization of bagasse ash as a pozzolanic material in concrete," *Construction and Building Materials*, vol. 23, no. 11, pp. 3352–3358, 2009.
- [11] I. I. Bashar, U. J. Alengaram, M. Z. Jumaat, and A. Islam, "The effect of variation of molarity of alkali activator and fine aggregate content on the compressive strength of the fly ash: palm oil fuel ash based geopolymer mortar," *Advances in Materials Science and Engineering*, vol. 2014, Article ID 245473, 13 pages, 2014.
- [12] T. O. Yusuf, M. Ismail, J. Usman, and A. H. Noruzman, "Impact of blending on strength distribution of ambient cured metakaolin and palm oil fuel ash based geopolymer mortar," *Advances in Civil Engineering*, vol. 2014, Article ID 658067, 8 pages, 2014.
- [13] M. Y. J. Liu, C. P. Chua, U. J. Alengaram, and M. Z. Jumaat, "Utilization of palm oil fuel ash as binder in lightweight oil palm shell geopolymer concrete," *Advances in Materials Science and Engineering*, vol. 2014, Article ID 610274, 6 pages, 2014.

- [14] S. O. Bamaga, M. A. Ismail, and M. W. Hussin, "Chloride resistance of concrete containing palm oil fuel ash," *Cement and Concrete Research*, vol. 1, pp. 158–166, 2010.
- [15] P. Chindapasirt, S. Rukzon, and V. Sirivivatnanon, "Resistance to chloride penetration of blended Portland cement mortar containing palm oil fuel ash, rice husk ash and fly ash," *Construction and Building Materials*, vol. 22, no. 5, pp. 932–938, 2008.
- [16] P. Chindapasirt, C. Chotetanorm, and S. Rukzon, "Use of palm oil fuel ash to improve chloride and corrosion resistance of high-strength and high-workability concrete," *Journal of Materials in Civil Engineering*, vol. 23, no. 4, pp. 499–503, 2011.
- [17] A. S. M. A. Awal and M. W. Hussin, "The effectiveness of palm oil fuel ash in preventing expansion due to alkali-silica reaction," *Cement and Concrete Composites*, vol. 19, no. 4, pp. 367–372, 1997.
- [18] ASTM C39/C39M, "Standard test method for compressive strength of cylindrical concrete specimens, American Society for Testing and Materials, 2015".
- [19] W. W. J. Chan and C. M. L. Wu, "Durability of concrete with high cement replacement," *Cement and Concrete Research*, vol. 30, no. 6, pp. 865–879, 2000.
- [20] W. Tangchirapat, S. Khamklai, and C. Jaturapitakkul, "Use of ground palm oil fuel ash to improve strength, sulfate resistance, and water permeability of concrete containing high amount of recycled concrete aggregates," *Materials & Design*, vol. 41, pp. 150–157, 2012.
- [21] R. P. Khatri and V. Sirivivatnanon, "Methods for the determination of water permeability of concrete," *ACI Materials Journal*, vol. 94, no. 3, pp. 257–261, 1997.
- [22] ASTM C1202-12, Standard test method for electrical indication of concrete's ability to resist chloride ion penetration. American Society for Testing and Materials, 2012.
- [23] V. Sata, C. Jaturapitakkul, and K. Kiattikomol, "Utilization of palm oil fuel ash in high-strength concrete," *Journal of Materials in Civil Engineering*, vol. 16, no. 6, pp. 623–628, 2004.
- [24] L. Zongjin and C. C. Kong, "New water permeability test scheme for concrete," *ACI Materials Journal*, vol. 97, no. 1, pp. 84–90, 2000.
- [25] P. Chindapasirt, S. Homwuttiwong, and C. Jaturapitakkul, "Strength and water permeability of concrete containing palm oil fuel ash and rice husk-bark ash," *Construction and Building Materials*, vol. 21, no. 7, pp. 1492–1499, 2007.
- [26] H. Yazici, "The effect of silica fume and high-volume Class C fly ash on mechanical properties, chloride penetration and freeze-thaw resistance of self-compacting concrete," *Construction and Building Materials*, vol. 22, no. 4, pp. 456–462, 2008.
- [27] G. C. Isaia, A. L. G. Gastaldini, and R. Moraes, "Physical and pozzolanic action of mineral additions on the mechanical strength of high performance concrete," *Cement and Concrete Composites*, vol. 25, no. 1, pp. 69–76, 2003.
- [28] W. Tangchirapat and C. Jaturapitakkul, "Strength, drying shrinkage, and water permeability of concrete incorporating ground palm oil fuel ash," *Cement and Concrete Composites*, vol. 32, no. 10, pp. 767–774, 2010.
- [29] W. Tangchirapat, C. Jaturapitakkul, and K. Kiattikomol, "Compressive strength and expansion of blended cement mortar containing palm oil fuel ash," *Journal of Materials in Civil Engineering*, vol. 21, no. 8, pp. 426–431, 2009.
- [30] A. R. Boa and L. B. Topu, "Influence of fly ash on corrosion resistance and chloride ion permeability of concrete," *Construction and Building Materials*, vol. 31, pp. 258–264, 2012.
- [31] Q. Yuan, C. Shi, G. de Schutter, K. Audenaert, and D. Deng, "Chloride binding of cement-based materials subjected to external chloride environment—a review," *Construction and Building Materials*, vol. 23, no. 1, pp. 1–13, 2009.
- [32] N. M. Altwair, M. A. M. Johari, and S. F. S. Hashim, "Influence of treated palm oil fuel ash on compressive properties and chloride resistance of engineered cementitious composites," *Materials and Structures*, pp. 1–16, 2013.
- [33] O. Sengul and M. Ali Tasdemir, "Compressive strength and rapid chloride permeability of concretes with ground fly ash and slag," *Journal of Materials in Civil Engineering*, vol. 21, no. 9, pp. 494–501, 2009.
- [34] A. A. Ramezani-pour and V. M. Malhotra, "Effect of curing on the compressive strength, resistance to chloride-ion penetration and porosity of concretes incorporating slag, fly ash or silica fume," *Cement and Concrete Composites*, vol. 17, no. 2, pp. 125–133, 1995.